STARS

Electronic Theses and Dissertations, 2020-

2020

Development of Facile Microfabrication Technologies for the Fabrication and Characterization of Multimodal Impedimetric, Plasmonic, and Electrophysiological Biosensors

Cacie Hart
University of Central Florida

University of Central Florida

STARS
Showcase of Text, Archives, Research & Scholarship

DEVELOPMENT OF FACILE MICROFABRICATION TECHNOLOGIES FOR THE
FABRICATION AND CHARACTERIZATION OF MULTIMODAL IMPEDIMETRIC,
PLASMONIC, AND ELECTROPHYSIOLOGICAL BIOSENSORS

by

CACIE HART
B.S./M.S. Towson University, 2011/2015

A dissertation submitted in partial fulfillment of the requirements
for the degree of Doctor of Philosophy
in the Department of Materials Science and Engineering
in the College of Engineering and Computer Science
at the University of Central Florida
Orlando, Florida

Fall Term
2020

Major Professor: Swaminathan Rajaraman

ABSTRACT

The objective of this dissertation was to develop novel methods of patterning inorganic and organic materials, develop biocompatibility evaluations, and subsequently apply these methods toward developing biosensors and lab-on-a-chip devices, such as Interdigitated Electrodes (IDEs) and Microelectrode Arrays (MEAs) on non-traditional (such as nanostructured and plasmonic) polymer substrates or deploy these methods to enhance precision cellular placement on traditional (glass) MEA substrates. It was hypothesized that a combination of such facile microfabrication techniques and patterning technologies on traditional and non-traditional substrates would increase the sensitivity and selectivity of such sensor platforms by several orders of magnitude, and potentially introduce new modalities for cell-based biosensing. In order to demonstrate the biological functionality of these new IDEs and MEAs, a variety of cell cultures were used (cardiac, stem cell, and endothelial cells) to study the growth, proliferation, modes of increasing sensitivity and response to various compounds *in vitro* (outside the body).

I dedicate this to Kevin, Riley, Sara, my mom, and Bob. You have supported me throughout this

more than you could ever know. I could not have finished without you.

ACKNOWLEDGMENTS

I would like to thank my advisor Swami for all the guidance provided over the past several years. You have shown me side of engineering that I never knew and that I have fallen in love with! I would also like to thank my committee members Dr. Kevin Coffey, Dr. Ellen Kang, Dr. Stephanie Florczyk, and Dr. Kaitlyn Crawford. Thank you to Frank for teaching me everything I know about the basics of cell culture. Thank you to my lab members Chuck, Nilab, Julia, and Avra for putting up with my terrible jokes and providing me with much needed encouragement. Finally, I would like to thank the College of Graduate Studies for awarding me with the Doctoral Research Support Award, which allowed me to buy the HL-1 cell line that really made this work come to life.

TABLE OF CONTENTS

LIST OF FIGURES

LIST OF TABLES

LIST OF ABBREVIATIONS

2D	Two-dimensional
3D	Three-dimensional
AAO	Anodic aluminum oxide
AC	Alternating current
AFM	Atomic force microscopy
ANF	Atrial natriuretic factor
ATP	Adenosine triphosphate
CAD	Computer-aided design
CI	Cellular index
CO_2	Carbon dioxide
DI	De-ionized
DIV	Days *in vitro*
DLP	Digital light processing
DPBS	Dulbecco's phosphate-buffered saline
DRIE	Deep reactive ion etching
DSMO	Dimethyl sulfoxide
DXF	Drawing exchange format
ECIS	Electric cell-substrate impedance sensing
ECM	Extracellular matrix
EDM	Electrical discharge machining
EDTA	Ethylenediaminetetraacetic acid
EIS	Electrochemical impedance spectroscopy
EURL ECVAM	European Union Reference Library European Centre for Validation of Alternative Methods
FDM	Fused deposition modeling
FIB	Focused ion beam
IC50	Half maximal inhibitory concentration

IDE	Interdigitated Electrode
IPA	Isopropyl alcohol
IR	Infrared
ISO	International organization for standards
iPSC-CM	Induced pluripotent stem cell derived cardiomyocytes
LCD	Liquid crystal display
LED	Light emitting diode
MEA	Microelectrode array
MEMS	Micro-electro-mechanical Systems
MSDS	Material safety data sheets
μSLA	Micro stereolithography
Nd: YAG	Neodymium-doped yttrium aluminum garnet
nIDE	Nanostructured interdigitated electrode
NIL	Nano imprint lithography
NRVM	Neonatal rat ventricular myocytes
PAN	Polyacrylonitrile
PBS	Phosphate-buffered saline
PDMS	Polydimethylsiloxane
PET	Polyethylene terephthalate
pIDE	Plasmonic interdigitated electrode
PLA	Polylactic acid
pMEA	Plasmonic microelectrode array
PMMA	Poly (methyl methacrylate)
PS	Polystyrene
RFU	Relative fluorescence units
RIE	Reactive ion etching
SEM	Scanning electron microscopy
SNAP	Spin-on nanoimprinting process

SNR	Signal-to-noise ratio
SPR	Surface plasmon resonance
SS	Stainless steel
THF	Tetrahydrofuran
UV	Ultraviolet

CHAPTER 1: INTRODUCTION

The objective of this dissertation was to develop facile patterning technologies for organic and inorganic materials such as metal layers, insulation, extracellular matrix (ECM) materials, micro/nanoparticles, and cells to simplify the processes and provide sensitivity/selectivity enhancements to these processes in order to develop cell-based biosensors, such as Interdigitated Electrodes (IDEs) and Microelectrode Arrays (MEAs). The focus was on shadow or stencil mask fabrication technologies, 3D bioprinting techniques, and the demonstration of cell-based biosensors using these techniques.

Shadow mask (or stencil mask) fabrication technology is a fundamental component in the fabrication of micro/nanostructures for prototyping in microelectronics, optical, microfluidics, micro-electro-mechanical systems (MEMS), packaging, and biomedical lab-on-a-chip applications, including IDE and MEA fabrication. Conventional shadow mask fabrication techniques are expensive and require cleanroom-based fabrication [1]. This factor has led to the demand for alternative shadow mask fabrication technologies. Many groups have explored non-cleanroom-based shadow mask fabrication technologies including inkjet printing of transparent masks [2], gravure [3], shadow mask [3], and stamping [4]. While these methods can create functional shadow masks, they tend to have highly limited resolution and little reusability. Multimodal laser micromachining, on the other hand, provides the possibility of fabricating shadow masks in a makerspace microfabrication environment with reduced costs, reduced capacity, the ability to integrate a variety of materials, one-step, non-contact processing, and universal applicability. Chapter 2 reports on the development of multimodal laser-based shadow (or stencil) masks and on the definition of organic and inorganic materials with these masks.

Since the turn of the century, cell printing has gained considerable traction in the field of biology. The widespread adaptation of 3D printing has revolutionized manufacturing, specifically in medical product design. In the field of cellular patterning, this version of 3D printing is known as bioprinting. Here biomaterials are deposited through a computer controlled dispensing system that places the material in designated areas with high accuracy in the micrometer scale [5]. A variety of 3D printing technologies have been adapted for bioprinting applications including powder bed fusion [6, 7], binder jetting [8], and vat photopolymerization [9], but the three main techniques that have proven to be most suited for bioprinting are inkjet printing, laser-assisted printing, and microextrusion [10, 11]. Each of these techniques has its advantages and disadvantages, but inkjet bioprinting is the most popular despite having some major disadvantages, and its less than ideal ability to translate to the clinical environment. Laser-assisted and extrusion bioprinting have retained a reliance on costly commercial printing systems, which makes them far less attractive for already strained research budgets in academic laboratories. Two-dimensional fused deposition modeling (FDM)-based cell printing, or cell plating can be a viable approach to enhance cell-electrode coupling in cell-based biosensors. Considering the relatively high cost of human derived stem cells, cell printing can bring this additional benefit, as it reduces the cost of each experiment by placing cells only where they are needed. Due to the extensive printing work performed in this dissertation, electrogenic HL-1 cells were selected for this purpose because of their ability to be serially passaged. Chapter 3 further describes the rationale for this selection, as well as the preliminary characterization and biocompatibility testing using these cells. Chapter 4 reports the construction and characterization of a sterile bioprinter for printing HL-1 cells and the characterization of droplet cellular prints using this printer. This chapter further reports on the

utilization of extrusion printing to precisely couple human neurons and cardiomyocytes atop standard MEAs and the characterization results from such assays.

The simplest cell-based biosensor is an IDE which has remained remarkably unchanged over several decades. Classic IDEs consist of two individually addressable interwoven electrode structures. IDEs are one of the most commonly used micro/nanosensors for chemical and biological sensing because of their low cost, high sensitivity, and ease of fabrication [12]. IDEs can easily be fashioned into a biosensor by incorporating a culture well into the design and attaching wires to the contact pads. Monitoring changes in impedance of the IDEs over time allows for the assessment of cell growth and proliferation. IDE and impedance-based biosensors are currently available in the marketplace, but many of them require the use of expensive commercial systems [13-20] for data analysis and involve complex and expensive cleanroom-based fabrication approaches for micro- and nanostructuring [21] of the electrode design. These systems often use densely packed electrodes, which cover much of the substrate surface, resulting in increased device sensitivity but prohibits the optical tracking of cells, which is required for most biological assays. Other approaches integrate MEAs with IDEs, which allows for more comprehensive measurements, but also involves a much more complex fabrication process that are not reproducible [22]. Additionally, they report on just electrical measures. Chapter 5 describes a new take on IDEs where IDEs fabricated on nanoscale substrates for dramatically enhanced sensitivities are reported for the first time. Further, the nanoscale substrate offers plasmonic sensing mode and the evaluation of this mode, as well as the characterization of the sensitivity of electrical, geometric, and optical modes for cell based biosensing are investigated. Up to 6 orders of magnitude improved sensitivity with these devices are reported.

Utilizing the developed facile micro/nanofabrication technologies, such as shadow or stencil masking and FDM extrusion bioprinting, in this dissertation efforts have focused on truly revolutionizing a standard IDE and MEA cellular biosensor. As a part of this dissertation, rapid nanofabrication technologies have been utilized to develop IDEs on a nanostructured substrate with a sensing modality in addition to impedance measurement that allows for optical probing with plasmonics. Additionally, initial steps to develop a multimodal MEA that would allow for both electrophysiological measurements and optical probing with plasmonics have begun.

CHAPTER 2: LASER MICROMACHINING OF SHADOW MASKS

Laser micromachining is a direct write microfabrication technology that has several advantages over traditional micro/nanofabrication techniques. This chapter presents a comprehensive characterization of a QuikLaze 50ST2 multimodal laser micromachining tool by determining the ablation characteristics of six (6) different materials and demonstrating two applications. Both the thermodynamic theoretical and experimental ablation characteristics of stainless steel (SS) and aluminum are examined at 1064 nm, silicon, and polydimethylsiloxane (PDMS) at 532 nm, and Kapton® and polyethylene terephthalate at 355 nm. It was found that the experimental data aligned well with the theoretical analysis. Additionally, two applications of this multimodal laser micromachining technology were demonstrated: shadow masking down to approximately 1.5 µm feature sizes and Interdigitated Electrode (IDE) fabrication down to 7 µm electrode gap width.

Hypothesis and Publications

Laser micromachining could be used to fabricate shadow masks with features in the single micron range for use in interdigitated electrodes and other Micro-Electro-Mechanical Systems (MEMS) applications.

The work presented in this chapter has previously been presented at the 22nd International Conference on Miniaturized Systems for Chemistry and Life Sciences (µTAS 2018) in Kaohsiung, Taiwan [23] and has been published in Micromachines [24].

Introduction

Material ablation via pulsed light sources has been researched since the invention of the laser [25, 26]; however, in 1982, reports of polymers etched by ultraviolet excimer lasers launched

more widespread investigations into using the process for micromachining [27, 28]. In recent years, laser technology has been examined as an exciting material processing method for both industrial and academic researchers [29-32]. The high quality of laser beams allows for improved micromachining precision for a variety of materials [33, 34]. Additionally, the compact size, high efficiency, cost-effectiveness, direct machining, 3D fabrication, and ease of integration are appealing to academic researchers with limited benchtop area and lean budgets.

Laser micromachining, specifically, involves the ablation of materials where the features produced by the laser are in the micro-scale [33, 35]. Laser micromachining techniques are currently employed in the automobile [36], medical [30, 37], semiconductor [38, 39], and solar cell industries [40]. Lasers used in micromachining are available in a wide range of wavelengths (ultraviolet to infrared), pulse durations (micro- to femtosecond), and repetition rates (single pulse to megahertz) [33, 36]. Because of this flexibility, laser micromachining allows for the processing of a variety of materials.

Figure 1 compares laser micromachining to three commonly used direct-write microfabrication methods [41-47]. All these methods involve a mechanism for removing material directly from a substrate in a desired pattern using computer-controlled machinery. While other patterning methods, such as photolithography are often used, they are not direct-write techniques and involve several steps to pattern materials; thus, a comparison to these other methods is not provided in this figure. Photolithography is of course required for one of the methods depicted (Reactive Ion Etching or RIE) for performing feature definition followed by RIE to "engrave" the feature in the substrate beneath [43-46]. Since RIE requires photolithography, the process involves more steps when compared to the other methods depicted in Figure 1 [45]. Micromilling is a technically simple process; however, this simplicity comes at the expense of frequent drill bit

brakeage and the inability to produce features in the sub-100 μm range [42]. As with some RIE technologies, Focused Ion Beam milling can define nanoscale features; however, the write process can take days depending on the pattern complexity. Additionally, in FIB-based milling processes, the material surface may become amorphous due to the implantation of gallium ions [41, 44-47]. The comparison depicted in Figure 1 is by no means comprehensive and has been included to show the characteristics of laser-based micromachining with some other commonly used technologies for patterning materials in micromachining and MEMS. Several other techniques for direct subtractive fabrication of micromachined features are available such as Electrical Discharge Machining (EDM) [48], ultrasonic drilling [49], water jet cutting [50] etc.

The lasers used in the above-reported research can produce shadow masks for MEMS applications, but they are unable to micromachine highly precise features on the scale of a single micron, unless they operate in the femtosecond regime [31, 35, 51-54]. The higher power of these lasers allows for the processing of thicker materials in a more reasonable time scale; however, this capability comes at the price of benchtop machining, high costs, space, high power usage (GW), and absence of multimodality to micromachine several materials with the same tool. Characterization of lasers used for materials processing is necessary for the proper use of such tools. By understanding the necessary energy, repetition rate/frequency, spot size, and depths that can be micromachined with various processing conditions in specific materials, users can subsequently optimize their experiments for successful results in different applications.

Categories	Reactive Ion Etching	Micromilling	Focused Ion Beam Milling	Laser Micromachining
Schematic				
Materials	Glass, Silicon, Polymers	Polymers, Metals, Composites, Ceramics	Glass, Silicon, Metals	Polymers, Metals, Glass, Oxides, Ceramics, Silicon, Biomaterials
Scale	nanometers	100's of microns	10's of nanometers	micron
Characteristics	Precise feature definition Toxic gases used Expensive photomasks required High initial investment	Suitable for machining thicker materials Moderate-to-high initial investment Unable to define small features	Precise nanoscale features Long write time (up to days depending on pattern complexity) Modifies surface by implanting Gallium ions and making it amorphous High initial investment	Precise feature definition Moderate-to-high initial investment Safety hazard from reflected laser light

Figure 1 Comparison of three widely used direct-write fabrication methods (RIE [49, 51], micromilling [48], and FIB [47,50,53]) to laser micromachining. Each of these methods allows for high aspect ratio, serial, single-substrate fabrication. In the case of RIE multi-wafer/multi-substrate parallel processing is also possible as with some laser micromachining examples as well for higher throughput micro/nanofabrication.

In this dissertation chapter, the full characterization of a multimodal laser micromachining tool and two applications of the usage of microstructures fabricated using the tool is reported. Multimodal laser micromachining allows for a wide range of materials processing capabilities; however, this comes at the price of limited power and nanosecond ablation. These tools allow users to operate at specific laser wavelengths (1064 nm, 532 nm, and 355 nm, in the case of the QuikLaze) and reduced powers (2.6 mJ maximum energy). These conditions however provide greater control over the material selectivity for laser micromachining and ablation depths. Specifically, one can remove a material from a device while leaving the remainder of the constituent materials unaffected [55].

Typically, such laser micromachining tools are employed in LCD repair, semiconductor failure analysis, and removing shorts and passivation layers in integrated circuits [33, 56]. In this chapter, the multimodal tool for the laser micromachining of six (6) different materials was characterized: Stainless Steel (SS) and aluminum - machined with IR mode, Polyethylene terephthalate (PET) and Kapton® - machined with UV mode, and Poly dimethylsiloxane (PDMS) and Silicon - machined with green mode. Subsequent shadow mask patterning allowed for the definition of organic and inorganic layers and the development of fully functional Interdigitated Electrode (IDE) devices. These devices are further characterized in this chapter.

<div align="center">State of the Art</div>

As previously stated, shadow mask, or stencil mask, technology is an integral part of the fabrication of micro/nanostructures in microelectronics, optical, microfluidic, MEMS, packaging, and biomedical lab-on-a-chip applications [57]. Typical shadow mask fabrication techniques, such as photolithography and deep reactive ion etching, are expensive and rely on cleanroom-based

<div align="center">9</div>

fabrication, expensive vacuum equipment, ultra-pure air filtration, and advanced know-how [58-62].

Laser micromachining provides an alternative solution to these cleanroom-based fabrication technologies. Laser micromachining is a subtractive microfabrication technique, i.e. you start with a bulk piece of material and selectively remove material based on a defined design. The laser ablates away the substrate material in desired areas to produce a pattern. This method is also known as direct-write patterning. Laser micromachining offers high precision, design flexibility, material flexibility depending on the wavelength of laser light used, and requires no chemicals (harsh acids, bases etc.) to produce features in the micro and the nanoscale in a variety of materials. The laser can further be housed in a chemistry lab without the need for advanced facilities and ultra-pure air providing an intimidation-free environment for accessing and producing results with the tool. However, there is an inherent safety hazard from the laser light which can be alleviated with appropriate safety equipment. Additionally, there is an initial investment in laser systems, but being a one-time investment can offer advantages over other microfabrication technologies that require continuous investments in terms of gases, chemicals, mass flow controllers, etc.

Laser micromachining has occasionally been used for shadow mask fabrication; however, the state of the art in laser micromachining (minimum feature size of 10 μm) [51] (to date) has relied entirely on single-wavelength excimer, CO_2, and Nd:YAG lasers [29, 31, 40, 49, 52, 53, 63-73]. To the best of my knowledge, multimodal laser micromachining has not been used for shadow mask fabrication. While the term "multimodal" in the laser field typically means that the laser contains multiple transverse electromagnetic modes, the laser micromachining tool used in this

work has the ability to operate at several wavelengths in the same tool, a rare capability not afforded by many lasers.

Specifically, with respect to shadow mask microfabrication with lasers, several impressive research efforts are reported in literature: Tahir et. al. used a 1064 nm Nd:YAG laser to fabricate 250 µm channels in wood, glass, plastic, and rubber [40]. Chung, et. al. fabricated shadow masks with minimum feature sizes of 200 µm with a 785 nm Ti: Sapphire laser [64]. Shiu, et. al. machined 140 µm channels in low-carbon steel for use as a shadow mask using an excimer laser [71]. Yang, et. al. fabricated nickel shadow masks with millimeter scale features for use in pulsed laser deposition of thin film thermocouple sensors [74].

Kumar, et. al. used an excimer laser to make chromium shadow masks. They deposited a 1000 nm layer of Cr onto a glass slide and micromilled an aluminum mask that was 10X the desired feature size of their final desired mask. This Al mask was then mounted to the laser and a demagnified image of the mask was projected over the Chrome film. This demagnified image was used to etch away the chromium layer and produce a shadow mask that was to be used for 2D lithography. This work showed a minimum feature size of 10 µm [75].

Fan et. al. also fabricated shadow masks using laser micromachining. Here, a CO_2 laser was used to make wax shadow masks. The resultant mask has overly rough edges and minimum feature sizes of only 500 µm. In addition, these masks are not reusable [59].

Other examples of laser micromachining feature sizes include a CO_2 laser micromachined 85 µm microfluidic channel [76], CO_2 laser micromachined cuts (100-190 µm) in PMMA substrates [63], 10 µm microelectrode structures fabricated via excimer laser ablation [77], 10-65 µm microdevice channels in polymeric substrates [78], 10-150 µm laser micromachined feature

sizes in alumina and stainless steel shadow masks [79], and 25 µm laser micromachined features in Permalloy for a shadow mask [80]. The lowest resolution of these efforts was limited to ~10 µm.
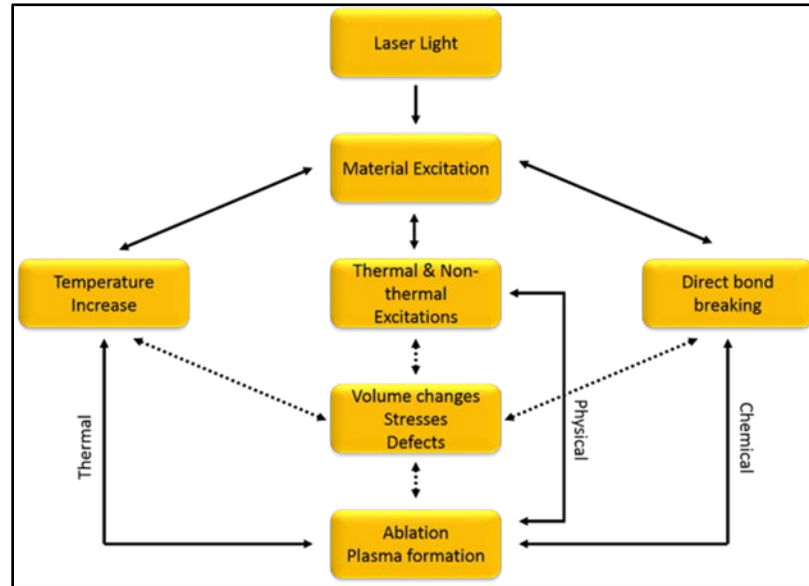
Figure 2 Mechanisms of ablation in laser micromachining. Substrate removal can be a result of thermal ablation, physical ablation, chemical ablation, or a combination of these mechanisms.

Microfabrication Method Overview

In laser micromachining, a laser beam is collimated into a small spot and patterning is achieved by either moving the substrate within a fixed beam or rastering the laser across a surface [33]. The desired machining patterns simply need to be drawn in a CAD program (such as AutoCAD) and imported as a DXF file into the control program of the laser micromachining tool. Once the program is executed with the laser, substrate material removal can be a result of photochemical, photothermal, or photophysical ablation [81], as shown in Figure 2. Commonly used processes include laser cutting, scribing, drilling, or etching to produce relief structures or holes on a substrate in ambient temperatures [31, 36, 51, 63, 81-83]. The power of this technique lies in the ability to construct desired patterns on arbitrarily shaped surfaces, with the only

limitation being the degrees of freedom and the resolution of the motion controller. Laser micromachining is considered a rapid prototyping technique because designs can be changed immediately without the need to fabricate new molds or masks.

Every laser micromachining system is comprised of three parts, as shown in Figure 3a for the multimodal laser micromachining tool: (1) the source laser, (2) the beam delivery system, and (3) the substrate mounting stage. Obviously, the laser source is at the heart of the system, as it determines which substrates and feature sizes can be micromachined [36]. The system used in this work has a multimodal laser source that allows for switching between three wavelengths of light: 1064 nm infrared (IR mode), 532 nm visible green (Visible mode), and 355 nm ultra-violet (UV mode). This wavelength switching allows for greater substrate compatibility and a wide array of feature sizes in an extremely compact benchtop system. The laser source used in this work is depicted in Figure 3b with greater detail.

Beam delivery involves optical components, including fixed focusing objects and mirrors, galvanometric scanners, optical fibers, waveguides, apertures, and q-switches, that are used to focus the laser spot. The selection of these optical components depends on the working distance, desired spot size, and required energy [33, 36, 82, 84]. The combination of the laser source and optical components of the beam delivery system determines the ultimate properties of the laser beam.
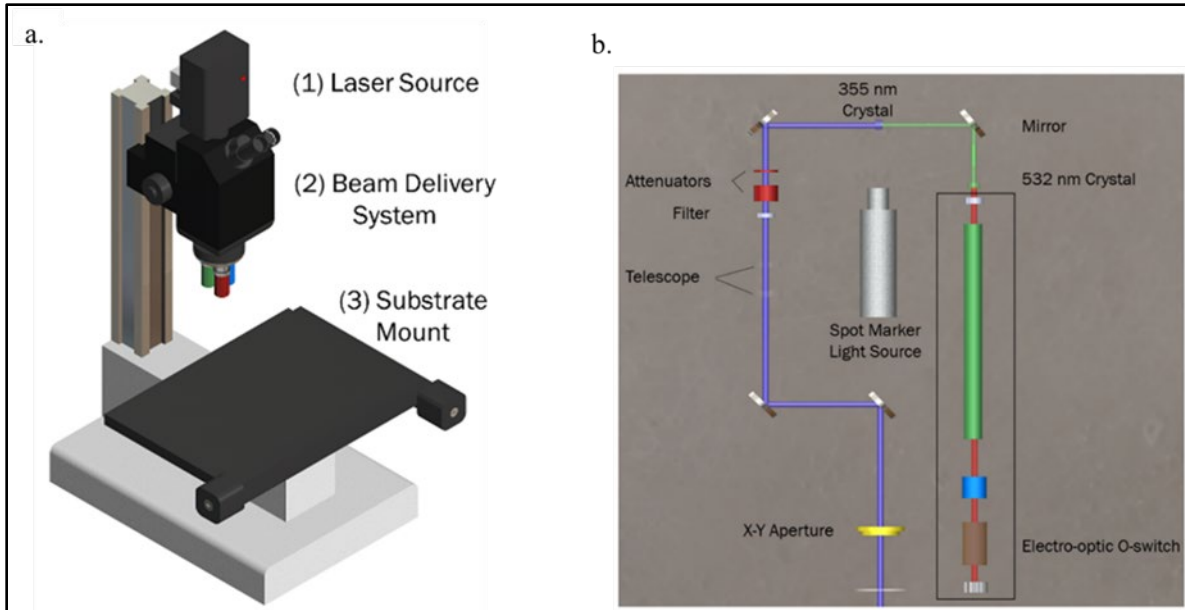
Figure 3 Laser Schematic a. External schematic of a QuikLaze 50ST2 Multimodal Laser Micromachining System. The three components of every laser micromachining system are shown. (1) The laser source box. (2) The beam delivery system. (3) The motorized substrate mount. b. Internal schematics of the laser source box. This shows the three crystals and a switch that create the different wavelengths of light the system produces with the ability to switch between three wavelengths.

Lastly, the substrate mounting system depends on how the rastering occurs on the tool. If the laser beam is to be rastered over the substrate surface, then a stationary substrate mount may be used. In most cases, including the system used in this work, it is more desirable to raster the substrate itself within a laser beam. In this instance, the substrate mount is manipulatable in the x- and y-directions, and even in the z-direction in some cases.

In the multimodal laser system used in this work, the laser beam is initially generated as a 1064 nm IR mode, shown in Figure 3b. The IR laser beam is subsequently passed through two crystals in the beam delivery system that produce the two additional wavelengths. The beam delivery system employs filters prior to the microscope optics to filter out the unnecessary wavelengths, allowing only the desired wavelength to interact with the substrate surface.

Theoretical Background

A thermodynamic approach to calculating the theoretical "depth of cut" for the materials tested in this work was adapted from Schütz, et. al. [39]. This formula is based solely on material properties and laser energy. Examining the depth of cut in this manner allows for a more fundamental understanding of the interaction between the laser and the material with fewer assumptions when compared to a molecular approach used for photochemical ablation [39, 83, 85].

$$a_p = \frac{\Phi}{\rho \int_{T_{room}}^{T_v} c_p(T)dT + \sum_{i=1}^{n} H_{ph}^v} - d \qquad (1)$$

Equation 1 shows the relationship between the depth of cut per pulse (a_p), the laser fluence (Φ), and involved material properties, including density (ρ), vaporization temperature (T_v), heat capacity (c_p), and the phase change enthalpy (H_{ph}^v). The d term (right-hand side of the equation) is a correction term that includes optical and thermal losses. This equation represented schematically (Figure 4) balances intrinsic energy and enthalpy, which are state variables and omits fundamental process parameters that are not state variables (i.e. particle dynamics) [86, 87].
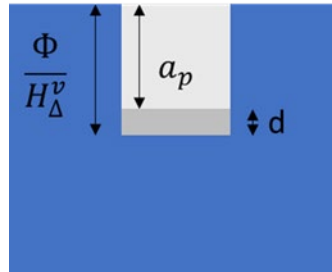
Figure 4 Schematic showing the variables in the thermodynamic theory for evaluation of the depth of cut.

While the inclusion of these fundamental process parameters could lead to a more accurate theoretical solution, the complexity would be vastly increased due to the use of non-linear partial differential equations, as well as the need for sophisticated simulation software to solve such

equations [33, 34, 39, 81, 85, 88]. Additionally, since this laser micromachining setup does not operate in the femtosecond regime, ablation occurs through melt expulsion and redeposition driven by the vapor pressure and the recoil pressure of light [85, 88, 89]. As a result, a simple thermodynamic analysis was performed to extract the relationship between the "depth of cut" and laser fluence which can be compared to the results obtained through experiments.

Materials and Methods

This section details the materials and methods used within this chapter.

Multimodal Laser

A QuikLaze 50ST2 multimodal laser (New Wave Research Inc., Freemont, CA) was used for all the laser micromachining performed in this dissertation. A selection of three wavelengths as mentioned in the previous sections allows the laser to be tailored to a specific application. The microscope of the laser system is equipped with 10X, 50X, and 100X lenses, each with specific wavelength limitations. Because of additional filters in the microscope lenses, the green wavelength can be used through any of the lenses, while the UV and the IR can only be used through the 50X and 100X lenses, respectively.

The laser outputs a 5 mm diameter Gaussian beam, which is then shaped into a rectangle by the XY aperture. The size of this rectangle is determined by user inputs into the control software. The maximum pulse duration of the laser is 5 ns for all wavelengths; however, it can be adjusted by the user in the program. Additionally, the laser fluence depends on the user specifications in the control software and the wavelength of light used, as the laser output energy can be adjusted by the user. The fluence ranges from a maximum of 27,000 J/cm^2 to a minimum of 1.08 J/cm^2.

Materials Used

To ensure a comprehensive study of multimodal laser micromachining, several materials were machined. Success in laser micromachining for a given material is typically determined only by the choice of wavelength because each material reacts differently to a specific wavelength. In general, metals absorb shorter wavelengths more effectively than longer wavelengths [33, 36]; however, there are limitations to how effectively material is removed at shorter wavelengths determined by the microscope optics used. Because the amount of light transmitted through the microscope objectives required for each wavelength varies, the "effective" absorption of the material at a given wavelength is changed.

As shown in Table 1, 12.5 µm thick Stainless Steel (type 304) (Trinity Brand Industries, Countryside, IL) and 16 µm thick Aluminum Foil (Reynolds Group Holdings, Auckland, NZ) were machined using the 1064 nm IR wavelength through the 100X microscope lens. The absorbances of these materials at this wavelength is 37% and 5%, respectively [61]. Kapton® of thickness 12.5 µm (DuPont, Wilmington, DE) and 25 µm thick polyethylene terephthalate (PET) (McMaster-Carr, Elmhurst, IL) were machined using the 355 nm UV wavelength through the 50X microscope lens. The absorbances of these materials at this wavelength are 22.5% and 12%, respectively [59, 62]. Finally, Silicon (University Wafer, Boston, MA) and polydimethylsiloxane (PDMS) (Dow Corning, Midland, MI) were micromachined using the 532 nm green wavelength through the 10X microscope lens. The absorbances for these materials at this wavelength are 25% and 72%, respectively [17, 18, 68].

Table 1 Materials characterized for use with the multimodal laser

Wavelength (nm)	Material	Thickness (μm)
1064	Stainless Steel	12.5
	Aluminum	16
532	Silicon	275
	Polydimethylsiloxane	100
355	Kapton®	12.5
	Polyethylene terephthalate	25

<u>Laser Characterization</u>

To establish protocols for processing each material, characterization grids were machined for all six (6) materials. These grids consisted of 100 spots, as shown schematically in Figure 5, and were designed in SolidWorks (Dassault Systems, Waltham, MA).

DXF pattern files were subsequently uploaded into the New Wave Laser program, and each spot was assigned a specific frequency (range of 5 Hz to 50 Hz) increasing by 5 Hz increments along the x-axis of the grid, and a specific energy from 10% (0.27 mJ) to 100% (2.7 mJ) increasing along the negative y-axis of the grid by 10%. The laser spot size was varied for each grid to provide full characterization of the laser's capabilities over a wide range of fluence. Grids were then patterned in all 6 materials using the multimodal laser.

All grids were imaged using Scanning Electron Microscopy (JEOL JSM-6480, Tokyo, Japan). Full images of the grids were obtained, as well as images of the individual spots in both

flat and 45º angled orientations. ImageJ (NIH, Bethesda, MD) was used to characterize the depth of the laser cut, as well as the resultant spot size.

		Frequency (Hz)									
		5	10	15	20	25	30	35	40	45	50
Energy (mJ)	0.27	■	■	■	■	■	■	■	■	■	■
	0.54	■	■	■	■	■	■	■	■	■	■
	0.81	■	■	■	■	■	■	■	■	■	■
	1.08	■	■	■	■	■	■	■	■	■	■
	1.35	■	■	■	■	■	■	■	■	■	■
	1.62	■	■	■	■	■	■	■	■	■	■
	1.89	■	■	■	■	■	■	■	■	■	■
	2.16	■	■	■	■	■	■	■	■	■	■
	2.43	■	■	■	■	■	■	■	■	■	■
	2.70	■	■	■	■	■	■	■	■	■	■

Figure 5 Layout of the grid of spots laser cut into the materials. The grid was designed to have 100 μm distances between the spots.

Shadow Masks

Shadow masks for the patterning of materials were fabricated from Kapton®, stainless steel, PET, and aluminum substrates. These materials were chosen because they are all commonly available in most microfabrication laboratories and it was determined that they could be ablated all the way through the material using the multimodal laser, a necessity for shadow masks. Full coverage, circle-on-line IDE shadow masks were designed using SolidWorks and machined using the multimodal laser and the appropriate wavelength for the substrate material. The shadow masks

19

were then imaged using the SEM (JEOL JSM-6480, Tokyo, Japan) to characterize the design (CAD dimensions) to device (fabricated shadow mask) translation. These shadow masks were subsequently used to pattern both metal and gelatin for design to device studies, as described below.

Additionally, traditional interwoven comb IDE shadow masks were fabricated to test the lowest feature size limits of the multimodal laser. These structures allow for more rapid shadow mask fabrication at the lowest possible widths ensuring higher sensitivity in IDE assays; thus, allowing for any necessary adjustments to achieve the desired electrode gap width. Due to the size of these structures, Atomic Force Microscopy (AFM) (Anasys Instruments, Santa Barbara, CA) and SEM (JEOL, Tokyo, Japan) were used to characterize the electrode gap widths of these shadow masks.

Lastly, because of the widespread use of PDMS in microfluidics, several lines of 2 mm length were laser micromachined into this material to determine the depth of cut for a given number of laser passes. All lines were micromachined through the IR microscope lens with the green laser at 2.7 mJ with an X-Y aperture area of 50 μm^2. The number of laser passes was varied from 5 to 40 passes. In this mode of operation, the laser beam is continuously scanned across the surface of the material in the desired pattern.

The process flow for the shadow mask fabrication and subsequent patterning of organic and inorganic layers is depicted in Figure 6.

Patterning of Organic and Inorganic Layers

To access the accuracy of low power, multimodal laser micromachining, material patterning through multimodal laser micromachined shadow masks was performed.

20
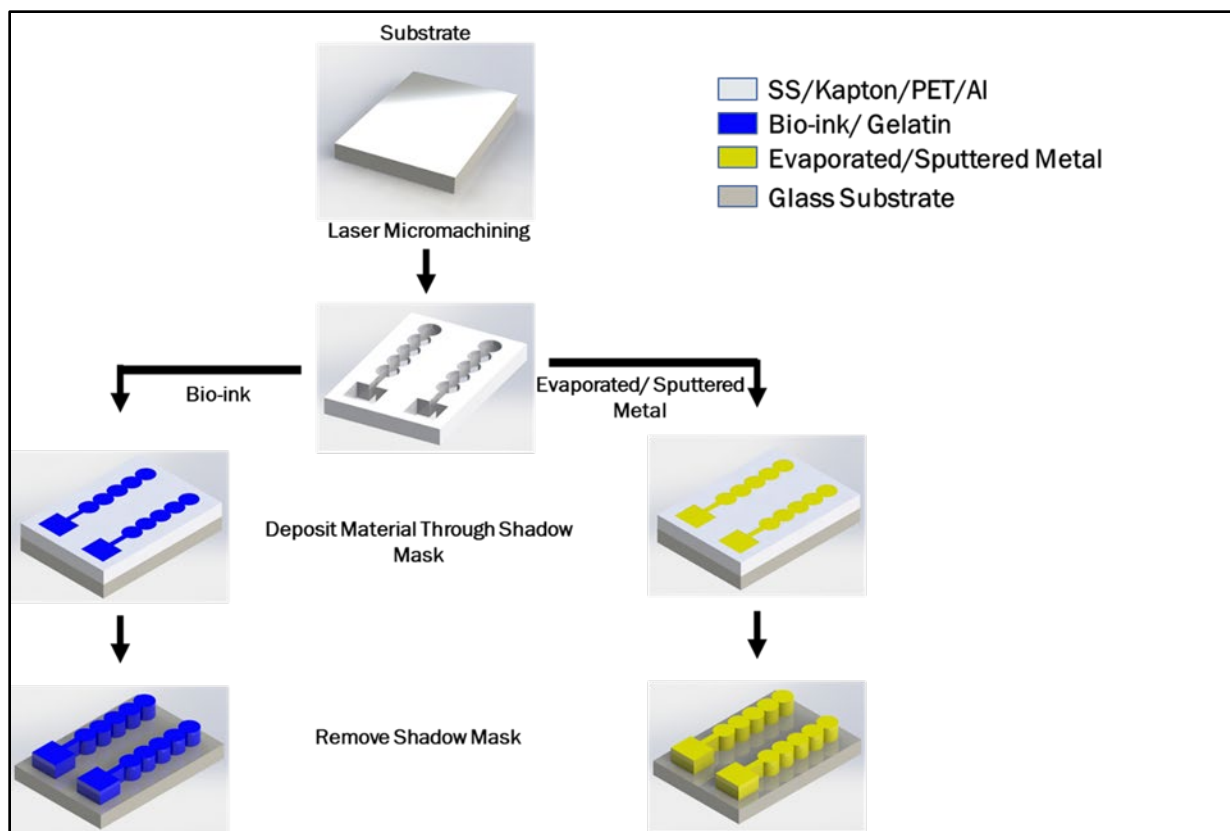
Figure 6 Schematic of laser micromachined shadow mask fabrication and subsequent materials patterning demonstration.

Gelatin Patterning

Gelatin (Millipore Sigma, St. Louis, MO) and deionized (DI) water were mixed to make a 5%-wt. gelatin solution to act as a sample bioink. Kapton® IDE shadow masks were dipped in DI water to allow for better adherence to the glass microscope slide substrates. The 5%-wt. gelatin solution was subsequently pipetted onto the glass slides through the shadow masks. The gelatin solution was allowed to set, then the shadow masks were carefully removed to expose the gelatin IDE patterns. The resultant gelatin structures were imaged using a Nikon TS2 inverted microscope.

Metal Patterning

The Kapton®, stainless steel, aluminum, and PET multimodal laser micromachined shadow masks were affixed onto glass microscope slides (Fisher Scientific, Hampton, NH) with Kapton®

tape (DuPont, Wilmington, DE). Titanium-Gold (Ted Pella, Redding, CA) electrodes, traces, and contact pads of 5 nm-30 nm thickness respectively were subsequently deposited (Deposition rate: 1 Å/sec at 1 x 10^{-6} Torr) through these shadow masks onto glass microscope slides via electron beam evaporation (Thermionics, Port Townsend, WA). After metal patterning, the shadow masks were removed by carefully detaching the Kapton® tape from the glass slide with tweezers. Transmitted light microscopy (TS2 Inverted Microscope, Nikon, Tokyo, Japan) was used to image the patterned metal structures. ImageJ (NIH, Bethesda, MD) was used for further optical analysis of the captured images and measurement of the electrode structures.

Impedance Characterization of Metal Patterns

The full frequency spectrum impedance of each of the resultant patterned metal IDE structures was measured with a BODE 100 impedance measurement system (Omicron Labs, Klaus, Austria) in series-thru impedance measurement mode, as shown in Figure 7. Series-thru organization of the system was chosen because the impedance of the sensors exceeded 1 kΩ at all frequencies, meaning that the impedance is in the mid-to-high range that is ideal for this measurement setup. The measurement is swept through a frequency range of 10 Hz to 10 MHz with the voltage ranging from 14 mV to 2 V depending on the frequency.

Dulbecco's phosphate buffered saline (DPBS) (Gibco, Waltham, MA) acted as the electrolyte solution and Platinum-Titanium wire (eDAQ, Deniston East, NSW, Australia) was used as a counter electrode used during the impedance measurements. Impedance data was extracted and plotted with Origin 2016 (OriginLab, North Hampton, MA).
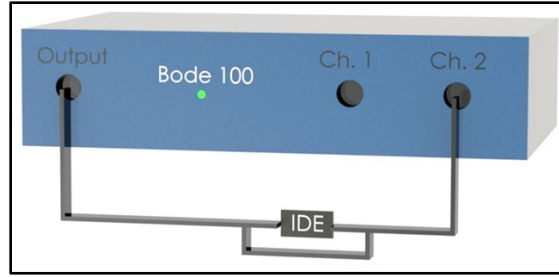
Figure 7 Schematic of a Series-Thru impedance measurement on the Bode 100.

Figure 8 SEM images of the laser characterization grids for each of the six materials. Kapton®, SS, PET, and aluminum are all at the maximum spot size for their respective wavelengths. Silicon and PDMS are both at 50% spot size to show the grid in its entirety. All scale bars are 200 μm.

Results and Discussion

Here, we present and discuss the results of the experiments.

Laser Characterization

Laser characterization grids were fabricated for each of the six materials for a range of spot sizes as described in Materials and Methods section. The spot sizes for the materials depended on the microscope objective that was used for the ablation. The spot sizes ranged from 50 μm down

to 2 µm for IR ablation through the 100X lens for stainless steel and aluminum, 60 µm down to 4 µm for UV ablation through the 50X lens for Kapton® and PET, and 250 µm down to 20 µm for green ablation though the 10X lens for silicon and PDMS. SEM imaging of these grid structures, and subsequent processing in ImageJ was used to calculate the depth of cut for each spot micromachined by the laser. Figure 8 shows examples of the characterization grids for each of the six materials at the maximum spot size for each wavelength. For PET, Kapton®, stainless steel, and aluminum, full ablation (through vias, all the way through the substrate) is achieved for the full range of power and frequency combinations shown in Figure 5. Since these materials were fully ablated within the 10 pulses used, the ablation depth was averaged over the number of spots. Some deviation from the theoretical calculation for these materials was observed. Ablation rates of 46.3 µm/mJ for Kapton® and stainless, 92.6 µm/mJ for PET, and 59.3 µm/mJ for aluminum were achieved. Neither silicon nor PDMS were able to be fully ablated through for any power and frequency combination. Silicon began measurable ablation at a minimum of 35 Hz and 2.43 mJ and had an ablation rate of 1.4 µm/mJ. PDMS began measurable ablation at a minimum of 35 Hz and 2.16 mJ, which gives an ablation rate of 1.5 µm/mJ.

Traces (lines) were scribed in PDMS using the green laser through the IR lens with between 5 and 40 passes and a 50 µm laser spot size. Cross sectioning the scribed lines carefully using a razor blade, followed by SEM imaging of the cross section, resulted in the measurement of the depth of cut for each number of laser passes. Figure 9 shows the linear relationship that was found between the depth of cut and the number of laser micromachining passes. Characterizing this relationship allows for the fabrication of microchannels of specific depths in PDMS by varying the number of laser passes.
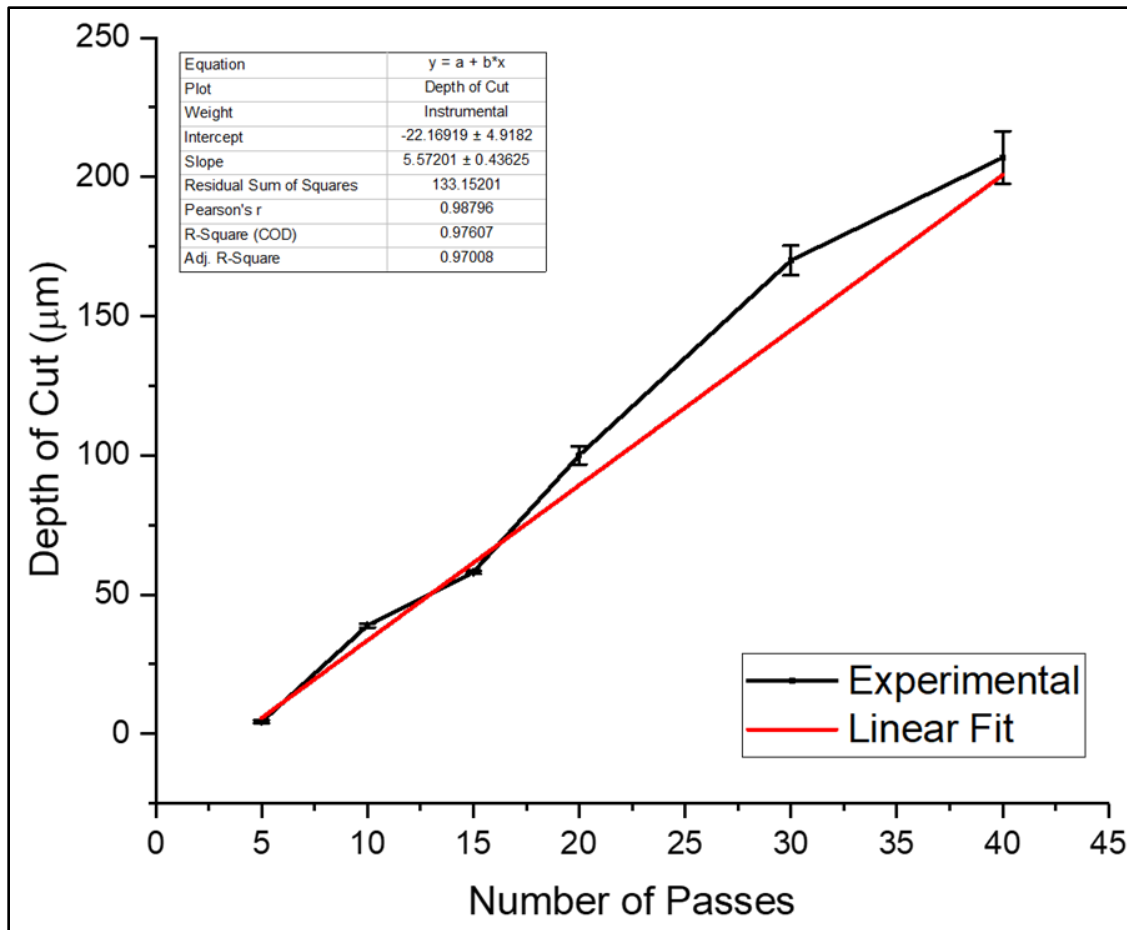
Figure 9 Results from scribing lines in PDMS with a varied number of laser passes. The depth of cut increases linearly with the number of laser passes as expected. This allows for the direct tuning of channel depth by selecting the number of passes the laser makes to cut PDMS.

<u>Comparison to Theoretical Values</u>

Figure 10 and Table 2 show the comparison between the theoretical ablation depth model and the experimental results. For silicon and PDMS, the thermodynamic model fits well. The comparison in ablation depth per pulse for both materials between theory and practice is in the same order of magnitude. Further, the ablation depth per pulse/ depth of cut plots for both materials show a clear correlation between the experimental and theoretical data. Neither one of these materials are ablated all the way through by the laser.
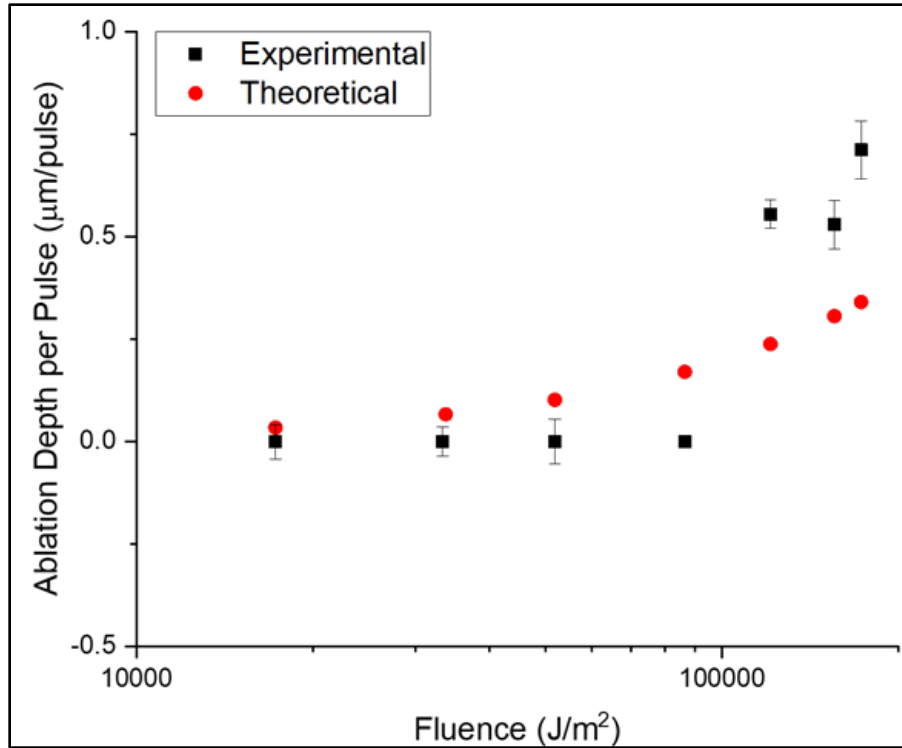
Figure 10 Comparison of theoretical and experimental ablation depth for a range of fluences in silicon.

Conversely, deviation from theory is observed in the experimental ablation depth per pulse comparison for Kapton®, stainless steel, PET, and aluminum. Kapton® and stainless steel perform similar to silicon and PDMS as observed in Table 2 with both the theoretical and experimental values in the same order of magnitude with experimental values being smaller than theoretical values. The discrepancy between PET and Aluminum is roughly an order of magnitude higher predicted theoretical values. The laser ablated through these materials at some point (difficult to measure experimentally in our current setup), so deviation is expected in all these materials. For example, both Kapton® and stainless steel could have shown an average ablation depth of ~3 μm per pulse, and both PET and aluminum could have shown an average ablation depth of approximately ~16 μm per pulse. Because of the thickness of these materials, when the normalization of the ablation depth to the number of pulses is performed, the experimental values are determined to be substantially lower. The key results from the experimental data in this case is

26

that the laser is capable of fully ablating these thicknesses and that a reasonable number of pulses can be used to ablate even thicker samples of these materials. These results also show the limitations of a thermodynamic approach, as the material thickness is not considered in the calculations.

Table 2 Comparison of theoretical and experimental ablation depths. *Limited due to full ablation of materials in less than 10 pulses.

Material	Thickness (μm)	Maximum Theoretical Ablation Depth per Pulse (μm/pulse)	Experimental Ablation Depth per Pulse (μm/pulse)	Ablated Through After 10 Pulses?
Kapton	12.5	2.65	1.25*	Yes
Stainless Steel	12.5	3.18	1.25*	Yes
PET	25	15.6	2.5*	Yes
Aluminum	16.3	16.3	1.63*	Yes
Silicon	500	0.34024	0.7112	No
PDMS	100	0.25783	0.6481	No

Applications

Two applications of this multimodal laser micromachining technique were additionally demonstrated in this work namely the microfabrication of shadow masks and IDEs.

Shadow Masks

Shadow masking technology is an integral part of fabricating micro/nanostructures for prototyping in microelectronics, optical, microfluidic, Micro-Electro-Mechanical Systems (MEMS), packaging, and biomedical lab-on-a-chip applications [38, 51]. Typical methods for producing shadow masks, such as photolithography and Deep Reactive Ion Etching (DRIE) or Ion Beam Milling, are expensive, require cleanroom-based fabrication, expensive vacuum equipment,

ultra-pure air filtration, and advanced know-how [1, 31]. Multimodal laser micromachining, on the other hand, is simple, cost effective, and makerspace-compatible, all vital attributes for cell-based assays and microfluidics applications.
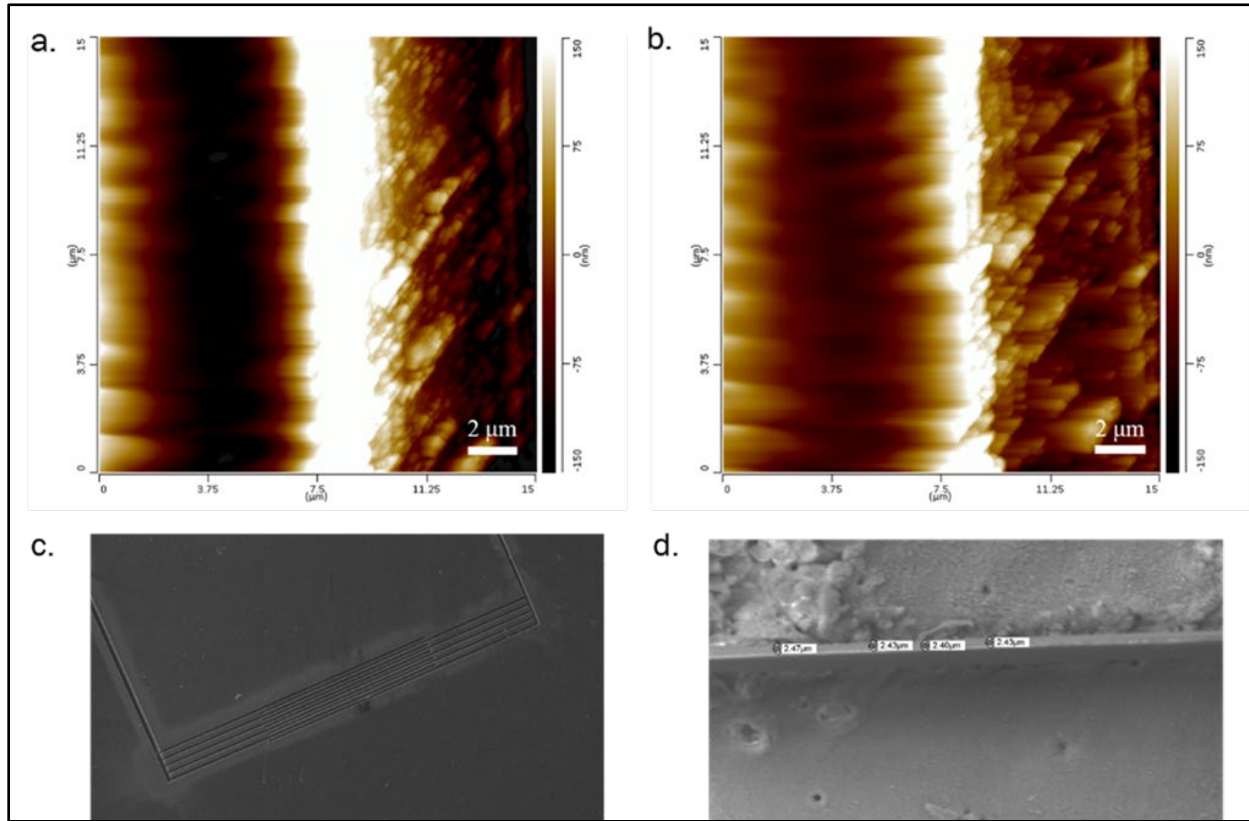
Figure 11 Images of sub-5 µm trace widths in Kapton®. a. AFM image of 3.5 µm trace width (white area). b. AFM image of 1.5 µm trace width (white area). c. SEM image of full comb finger electrode structure (approx. 5 µm trace width). d. SEM image of shadow mask feature of approximately 2.43 µm trace width.

Fabrication of the shadow masks down to ~1.5 µm was successfully demonstrated, as shown in Figure 11. To the best of my knowledge, this is the lowest feature size demonstrated for laser defined shadow masks [31, 51]. Previous work with laser micromachining has produced feature sizes down to ~10 µm. As a result, patterns that are an almost an order of magnitude better than the state of the art are reported in this dissertation.

Patterning Through Shadow Masks

The laser micromachined shadow masks were further used to pattern both metal and gelatin/bio-ink. The organic and inorganic layer patterning can be utilized for applications such as accurate cell placement in single cell and culture assays, precision confinement and growth of cellular constructs, tissue engineering, metal micro/nanoelectrodes, definition of organic insulation layers, and other lab-on-a-chip and diagnostic applications [31, 51, 82, 90, 91].
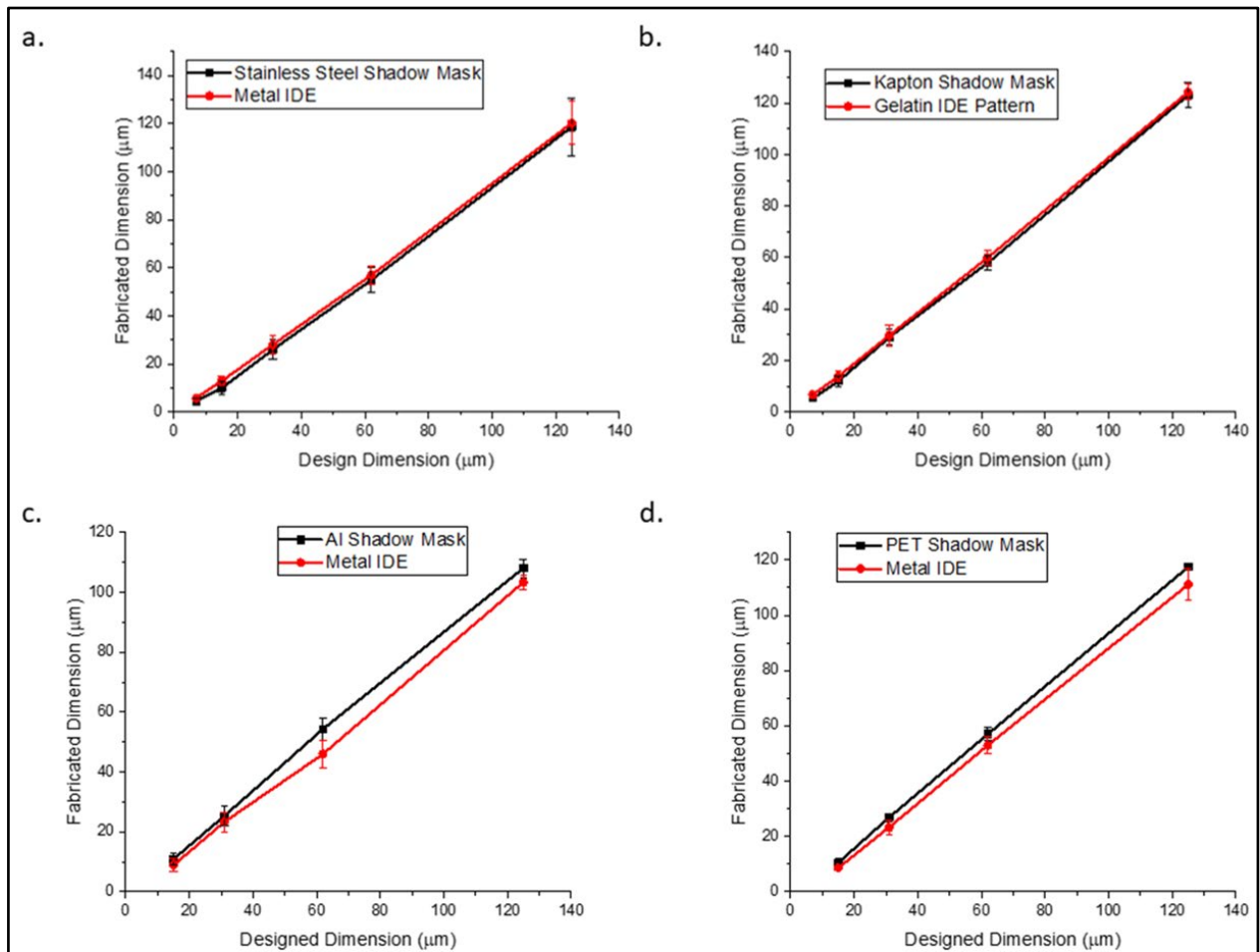
Figure 12 Design to shadow mask to device (IDE on glass) for the four materials that cut all the way through the substrate. a. Stainless steel to Ti-Au metal IDE, b. Kapton® to gelatin IDE pattern, c. Aluminum to Ti-Au metal IDE, and d. PET to Ti-Au metal IDE.

Design of a shadow mask to microfabricated device translation for the four materials that the multimodal laser was completely able to micromachine through are shown in Figure 12.

Aluminum, PET, and stainless-steel shadow masks were used to fabricate metal IDEs while Kapton® shadow masks were used for fabricating a gelatin/bio-ink IDE. It was observed that Kapton® and stainless steel demonstrated the best design to device translation for 125 µm to 7 µm. Both stainless steel and Kapton® showed minimal thermal damage from laser microfabrication at their respective laser wavelengths (1064 nm and 355 nm). Additionally, both materials have coefficients of thermal expansion (both approximately 20×10^{-6} K^{-1}) which are 2x larger than the thermal expansion of glass (9×10^{-6} K^{-1}) [46] theoretically suggesting better translation results and experimentally verified in Figure 12 (for N = 3 measurements at the various design values). The best design to device translation was observed to be ~98% for the 7 µm gelatin features due to the rapid deposition and curing of the gelatin. The worst design to device translation for stainless steel was observed to be 95% for 125 µm metal IDE on glass due to the higher run-off possibilities during the electron beam evaporation process [34]. PET and aluminum demonstrated a deviation from the designed IDE pitch by 11.2% and 25.8% at maximum pitch, respectively. PET has a coefficient of thermal expansion (80×10^{-6} K^{-1}) [87] that is nearly an order of magnitude larger than that of glass, so some deviation from the design dimensions is expected due to thermal mismatch effects during e-beam evaporation. The aluminum shadow mask exhibited physical melting during the laser micromachining process, which could explain the large deviation from design dimensions.

Figure 13 shows the design schematic, SEM images of the shadow masks, and transmitted light microscope images of both Ti-Au metal patterning and gelatin bioink patterning for circular fill IDE patterns with electrode gaps from 125 µm to 7 µm. Metal patterning appeared to work best with Kapton® or stainless-steel shadow masks because their coefficients of thermal expansion are closer to that of glass. Kapton® and PET shadow masks worked best for gelatin patterning. Both

shadow mask materials allowed for simple adhesion to the glass substrate utilizing surface tension effects by simply dipping the mask in DI water prior to attachment on glass substrates. Allowing the gelatin to fully set prior to shadow mask removal was key in preventing the patterns from bleeding.

Figure 13 Results of laser micromachining of the shadow masks, as well as inorganic and organic layer patterning. The design of an Interdigitated Electrode (IDE) was translated into metal (titanium-gold) and bioink (gelatin).

The impedance of the metallized IDEs (Figure 14) was found to decrease with decreasing electrode gap width as is expected [92] with the 1 kHz impedance decreasing by 33.47% between the extremities of the designs tested. Table 3 further illustrates impedances at key frequencies, clearly depicting resistive behavior at the lower and upper ends of the spectra and capacitive behavior in the mid-band with increasing impedance values as expected [92].
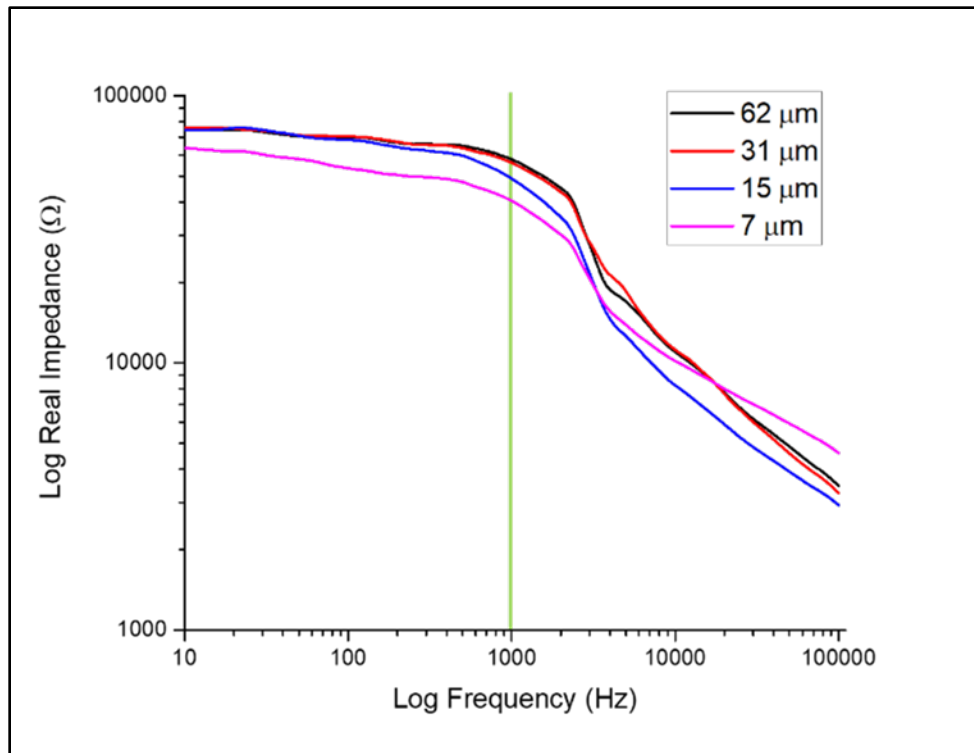
Figure 14 Full spectrum impedance measurements of several IDEs of varying pitch. The electrophysiologically significant frequency of 1 kHz (green line) reports impedances from approximately 39 kΩ (7 μm) to 56 kΩ (62 μm).

Table 3 Values of the real part of the impedance at significant frequencies

				Real Impedance (kΩ)		
	Frequency	10 Hz	100 Hz	1 kHz	10 kHz	100 kHz
	7	63.76	53.50	40.40	10.17	4.60
	15	74.21	68.37	48.91	8.24	2.90
Electrode Gap (μm)	32	76.06	70.29	56.06	11.19	3.26
	62	74.77	70.05	57.74	10.99	3.46
		Resistive	Capacitive	Capacitive	Resistive	Resistive

32

Conclusions

Complete characterization of the laser micromachining processes for six (6) commonly used microfabrication materials was developed in this chapter using a multimodal laser micromachining tool. Characterization of the QuikLaze 50ST2 multimodal laser for the laser micromachining of six (6) different materials demonstrated that the ablation depth that were experimentally obtained fit relatively well with a simple thermodynamic theory for most of the materials. While more complex theories or analysis [88] one could improve the discrepancy, this technique is accurate enough to allow one to readily calculate possible ablation depths of a new material using such a laser micromachining tool. Additionally, two applications of multimodal laser micromachining were demonstrated: shadow mask fabrication in the sub-5 μm range and patterning of organic and inorganic materials in the sub-10 μm range. The ability for such a technique which allows for rapid prototyping of shadow masks and devices, combined with the compact, benchtop-friendly design gives multimodal laser micromachining tremendous promise as an efficient fabrication method in both academic and industrial research settings.

CHAPTER 3: HL-1 CELL LINE ESTABLISHMENT AND MATERIAL BIOCOMPATIBILITY

The work presented in this chapter has been published in *Biosensors* in October 2020 [93]. This cell line also helped the group to report on its first electrophysiological data acquisition from a 3D Microelectrode Array (3D MEA), which was the subject of a paper accepted in RSC Advances in November 2020 [94] and a presentation in NanoFlorida 2019 [95].

Introduction

Since the development of cell-based biosensors was the focus of the work in this dissertation, preliminary cell studies were needed. Initially, the idea was to rely on collaborators (such as Prof. Hickman) for the cell studies and some of these collaborative results are presented in the bioprinting chapter. Two things became evident as the facile biosensor micro/nanofabrication methodologies were developed: (1) bioprinting on cell-based biosensors required a lot of cell experiments; (2) biocompatibility of materials being used in the biosensors was paramount and needed specific attention. As a result, it was decided to pursue a separate cell line in the lab to facilitate these experiments.

Since a majority of *in vitro* biosensor research focuses on human induced pluripotent stem cells [14, 16, 90, 96-98], specifically cardiomyocytes, this was where the cell studies had originally focused. The requirements for handling and costs of these cells were researched and found to be beyond what was required in this dissertation [99]. Additionally, further increase in cellular population, known as passaging, is not possible with these cells [98]. The original idea was that any intermittent testing could be done with lower overheads of handling, care, and costs with human induced pluripotent stem cell derived retinal pigment epithelial cells. While these cells were not electrogenic, they grew rapidly and, in a brick-like pattern, which quickly allowed for

34

identification of any biocompatibility, impedance changes, or process issues that may have been present.

As the work in this dissertation progressed, it became clear that extensive cell experiments with passaging of a cell line would be needed. The promising results presented in the nIDE chapter which follows later, as well as the cell consumption involved with developing a bioprinter made it clear that we would need to establish a cell line in our lab.

To test material biocompatibility, a cell type that has been well studied and has predictable growth patterns should be used. HL-1 cells are derived from rat atrial cardiac myocytes and are the only cardiomyocyte cell line currently available that can continuously divide, spontaneously contract, and maintain a differentiated adult cardiac phenotype [100, 101]. Additionally, this cell line has been widely characterized using optical, electrophysiological, immunohistochemical, and pharmacological methods [100, 101].
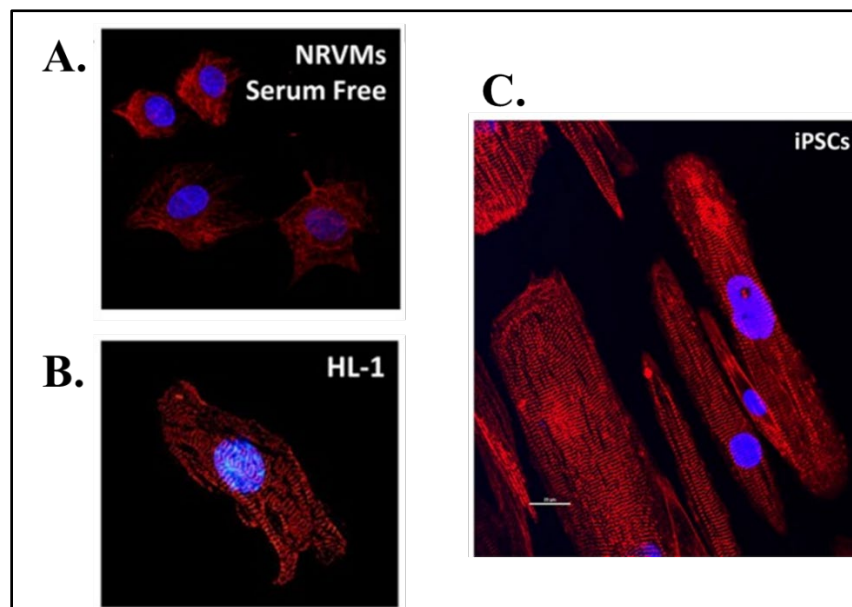
Figure 15 Fluorescent microscopic images taken from Peter et. al. of the three most employed cardiomyocytes. a. Neonatal rat ventricular myocytes: the immaturity of the cells can be seen when compared to the b. HL-1 cells and c. human induced pluripotent stem cell derived cardiomyocytes. [102]

<u>Cell Line Selection</u>

Several decisions were to be made when choosing a cell line to establish in the lab. Since we were interested in morphological and electrophysiological measures, electrogenic cells addressed all our needs. A choice was subsequently made between neurons and cardiomyocytes. Cardiomyocytes tend to be slightly easier to manage [103, 104], which was ideal for our lab since cell biology experience was minimal and not the focus of the lab. Three cardiomyocyte cell types are commonly used in biosensor research: the aforementioned human induced pluripotent stem cell derived cardiomyocytes (hiPSC-CM), neonatal rat ventricular myocytes (NRVM), and HL-1 cells [104, 105]; and a decision needed to be made about which cell line would be the best choice for our needs. Figure 15 shows fluorescent microscope images from Peter et. al. comparing the three cell types [102].

The first cell type of the three is the most popular, and the ideal choice as far as clinical translation, human induced pluripotent stem cell derived cardiomyocytes (hiPSC-CMs). These are intrinsically heterogeneous consisting of three subpopulations: atrial-, ventricular-, and nodal-like cardiomyocytes [106, 107]. This is beneficial because these cell types are all present in the heart, meaning that any drug dosing experiments give a more realistic picture of potential reactions. Additionally, these cells are human, which means that direct clinical translation of drugs is easier to realize as reactions are human [102, 106]. These cells also set the tone for future "personalized" medicine where cells from a patient can be used to determine any potential side effects or reactions to treatments.

While hiPSC-CMs are the ideal choice, some significant downsides still exist. Despite the successful differentiation of human induced pluripotent stem cells into spontaneously beating cells with active cardiogenic marker genes, the resulting cardiomyocytes are an immature and highly

variable cardiac phenotype [107]. Electrophysiology measurements have shown that the shapes of the action potentials have varied significantly between studies and even within studies among the same cell lines (derived from a different set of stem cells) and with different differentiation methods [106]. An example of these different action potential morphologies, from He, et. al. is presented in Figure 16 [98]. This high heterogeneity requires that many cells be analyzed to generate statistically meaningful conclusions. The high cost of stem cell derived cardiomyocytes makes maintaining such a cell line for a non-biology-based lab prohibitive.
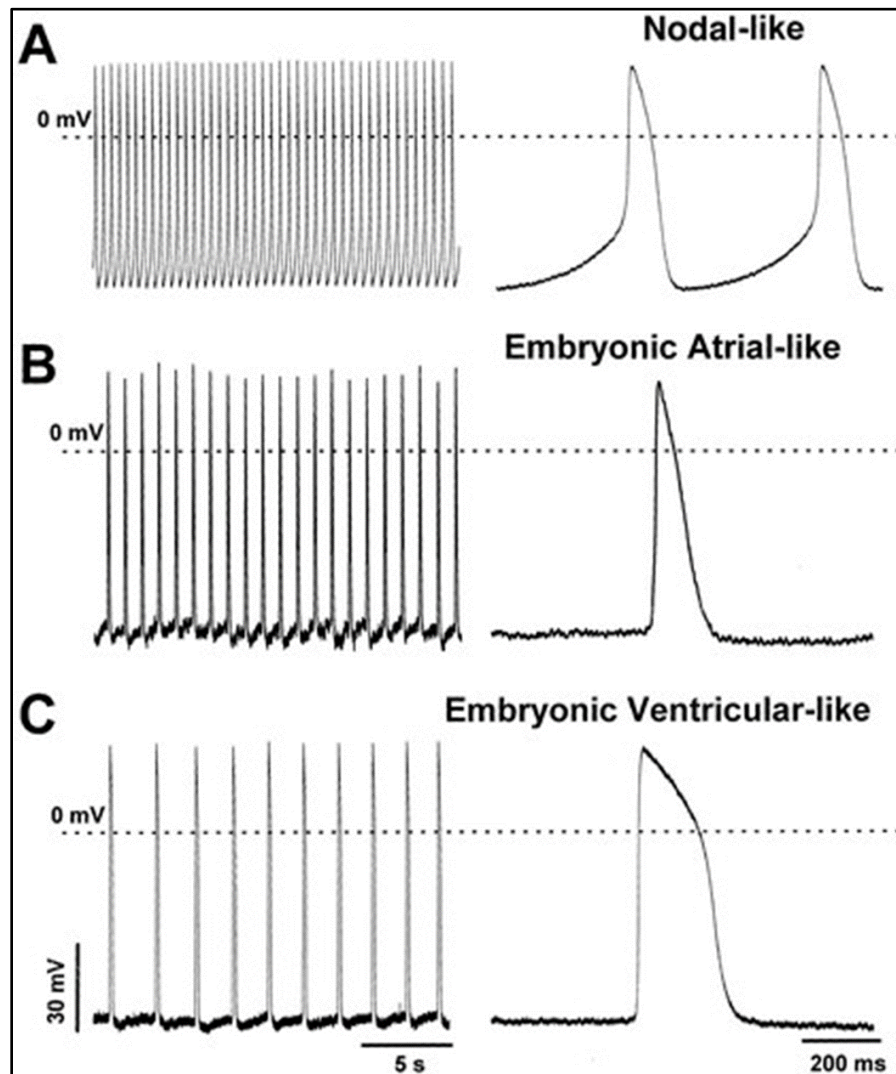
Figure 16 Different shapes of action potentials that can be generated from stem cell-derived cardiomyocytes [98]

Because human cells were not realistic for our needs, animal models needed to be explored. There is no ideal animal model available for cardiac research [108]. The use of every animal model is accompanied by its own set of advantages and disadvantages. Many disadvantages come in the form of ethical questions of the use of animals that many consider pets in laboratory settings. For this reason, only rodent models were considered, as people are generally more inclined to accept this. Cardiac excitation, contraction, and relaxation of small rodents and humans many similarities (Figure 17) [102, 106, 108-111]. Both groups express proteins with similar functions and roles [108, 110]. Genetically modified mouse and rat models can be used to probe the function of various genes in cardiac physiology and disease, which can address vital questions in physiology and disease modelling. Despite their similarities, there are important differences in human and small rodent models, mouse/rat models allow for rapid establishment of proof-of-principle that can later be extended to human models [108].
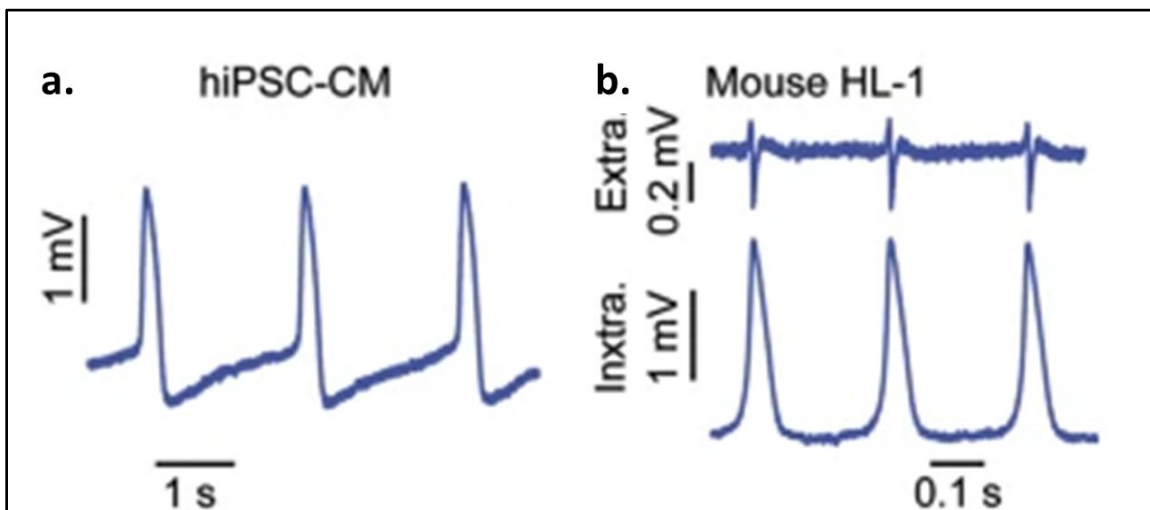
Figure 17 Comparison of action potentials for human and mouse derived cardiomyocytes. The action potentials are of similar amplitude, but the pulse duration differs by an order of magnitude. From Lin et. al. [106]

Neonatal rat ventricular myocytes (NRVM) solve some of the issues with hiPSC-CMs [104, 105]. They are all ventricular-like, which means that the action potentials that they exhibit

are homogeneous [103]. These cells are primary cardiomyocytes meaning they are terminally differentiated cells and they are difficult to transfect [102]. While you can purchase primary cells from several companies, it is much more economical to procure them yourself directly from the rat [102]. This brings in a whole host of new institutional and ethical protocols since it involves live animals, as well as the need for expensive new equipment. Additionally, their use is somewhat limited because they lack many adult cardiomyocyte characteristics, such as becoming overgrown by non-myocytes after a few days in culture, ceasing to divide after the neonatal period, and difficult genetic manipulation [102, 108, 110].

HL-1 cells were the third option. The HL-1 cell line was derived from AT-1 cardiac myocytes, which are atrial cardiac muscle cells obtained from transgenic mice in which the expression of the SV40 large T antigen was controlled by the atrial natriuretic factor (ANF) promoter [100, 101]. These cells can continuously divide, spontaneously contract, and maintain a differentiated adult cardiac phenotype through indefinite passages in culture [100, 101]. HL-1 cells have been characterized using microscopic, immunohistochemical, electrophysiological, and pharmacological methods [101]. The cells contain highly organized sarcomeres necessary for mediating contraction and intracellular ANF granules characteristic of atrial myocytes [101, 102, 106]. Additionally, they exhibit an adult cardiomyocyte-like gene expression profile, meaning that they should respond to chemical stimulation as typical adult cardiomyocytes would [101, 102, 106]. HL-1 cells spontaneously depolarize and express the necessary ion channels required for generating action potentials characteristic of primary cardiomyocytes [101], which makes them a good candidate for electrophysiological experiments. Some disadvantages of HL-1 cells include their rapid uninhibited growth and their homogeneous atrial phenotype makes the cell line incompatible with ventricular studies [101, 102, 106].

Table 4 lays out the advantages and disadvantages of these cell lines [101, 102, 106, 108]. Because of the frequency of cell culture in our lab (often, but not continuous), HL-1 cells seemed to be the optimal choice. The low cost and maintenance of this cell line combined with the possibility for serial propagation gave the flexibility to bank billions of cells for future use to be thawed as needed. Additionally, we already had much of the required labware. The support for the cell line as well as a BioCane for cryogenic storage came from a generous UCF Doctoral Research Support Award provided by CECS.

Table 4 Comparison of the advantages and disadvantages of the three most common cardiomyocyte cultures used in the biosensor community

Cell Type	Advantages	Disadvantages
Human Induced Pluripotent Stem Cell derived Cardiomyocytes (hiPSC-CM)	Easily manipulated Spontaneously beat in ideal culture conditions Human cells – easier clinical translation Easily manipulated	Expensive Technically challenging Multiple differentiation protocols make data comparison across studies difficult Heterogeneous
Neonatal Rat Ventricular Cardiomyocytes (NRVM)	Cost-effective when obtained in-house Spontaneously beat in culture Can be maintained in serum-free culture medium	Terminally differentiated Difficult to transfect Immature phenotype
HL-1 cells	Immortalized Homogeneous Rapid expansion Spontaneously beat in culture Low-cost	Require specialized medium Do not recapitulate ventricular cells in culture

Materials and Methods

In this section of the chapter, the methods for establishment of the cell line and biocompatibility testing of the cells follow.

Establishment of HL-1 Cell Line and Protocols

HL-1 cells were purchased from Millipore Sigma. The cells arrived in a cryovial and were immediately thawed into prepared cell culture flasks. The following sections detail the protocol

for thawing, passaging, and freezing the cells, as well as the recipes for the various mediums needed for these protocols. All protocols and recipes were adapted from Dr. Claycomb's original paper and one that followed [100, 101]. Everything has been adapted to fit the specific needs of our lab without sacrificing the health of the HL-1 cells. Significant trial and error have allowed for the development of this protocol. The initial establishment of the cell line required nearly 24/7 lab work, which was thankfully shared with my colleague Dr. Frank Sommerhage. By combining our time, we were able to establish an impressive cell bank, as well as determine to nearly the half-hour when we could expect the number of cells to have doubled.

Prior to starting the cell experiment, the centrifuge, water bath, and microscope were all turned on. Additionally, the IPA/Ethanol bottle was filled, and the inside of the biosafety cabinet was been sprayed and wiped down. Finally, it was determined that all needed consumables were present inside the biosafety cabinet.

Most of the solutions used in culturing the cells required pre-mixing or aliquoting.

Gelatin/Fibronectin Solution

To make gelatin/fibronectin solution, 10 mL of 0.1% gelatin solution were added to 40 mL of sterile water in a 50 mL centrifuge tube. This made a 0.02% gelatin solution. 250 µL of fibronectin (1 mg/mL) was added to the 50 mL centrifuge tube of 0.02% gelatin solution and mixed gently. The mixture was then sterile filtered using a 0.2 µm syringe filter aliquoted into 15 mL centrifuge tubes. Aliquots were kept frozen at -20°C.

Norepinephrine

To make 10 mM stock norepinephrine, 0.59 g of ascorbic acid was added to 100 mL of cell culture grade distilled water (30 mM ascorbic acid). Then 80 mg of norepinephrine was added to

25 mL of the 30 mM ascorbic acid and filter sterilized using a 0.2 µm syringe filter. The solution was then aliquoted into 1 mL working volumes in sterile microtubes and stored at -20°C. 1 mL of stock solution was used per 100 mL of Claycomb medium for a final concentration of 0.1 mM of norepinephrine.

L-Glutamine

L-glutamine came as a 100X solution. It was aliquoted into working volumes in sterile 1 mL microtubes and stored at -20°C.

Supplemented Claycomb Medium

Supplemented Claycomb Medium was required to maintain the desirable characteristics (beating, differentiation, phenotype) of HL-1 cells. To make supplemented Claycomb medium in working volumes for our needs, 87 mL of Claycomb medium, 10 mL of Fetal Bovine Serum, 1 mL of penicillin/streptomycin, 1 mL of 10 mM stock norepinephrine, and 1 mL of L-Glutamine were mixed to make 100 mL of medium. The medium was stored in amber glass media bottles and protected from light at 4°C.

Wash Medium

Wash medium was used to wash the cells of trypsin and trypsin inhibitor or freezing medium during centrifuging by supplying them with necessary nutrients they may have been lacking for a short time. To make 100 mL of wash medium, 94 mL of Claycomb medium, 5 mL of fetal bovine serum, and 1 mL of penicillin/streptomycin were mixed in a glass amber media bottle and protected from light. Wash medium was stored at 4°C.

Freezing Medium

Freezing medium was used for cryogenic storage of cells. To make freezing medium, 9.5 mL of fetal bovine serum was mixed with 500 µL of dimethyl sulfoxide (DMSO) in a 15 mL

centrifuge tube. DMSO was used to prevent the formation of ice crystals during the freezing process, which would kill the cells.

Soybean Trypsin Inhibitor

Soybean trypsin inhibitor was necessary to stop the trypsinization of cells in culture. It was necessary to use trypsin to remove the cells from the surface from which they were adhered, but if the action of the trypsin was not halted, the cell surface proteins would begin to be digested and cell functioning would be impacted.

To make soybean trypsin inhibitor, 25 mg of soybean trypsin inhibitor was weighed out and placed into a beaker containing 100 mL of phosphate buffered saline. The solution was mixed until the soybean trypsin inhibitor was dissolved. The solution was then filter sterilized using a 0.2 µm syringe filter and placed into a 50 mL centrifuge tube. Soybean trypsin inhibitor was stored at 4°C for up to 1 month.

Pre-Coating Flasks with Gelatin/Fibronectin Solution

The required number of frozen 15 mL tubes of gelatin/fibronectin solution were thawed in the 37°C water bath. Once thawed, sterile tissue culture flasks were coated with the required volume of the gelatin/fibronectin solution. T25 flasks required 1 mL and T75 flasks required 3 mL. The flasks were capped and incubated at 37°C for at least one hour, preferably overnight. The gelatin/fibronectin solution was removed from the flask via aspiration just prior to adding the cells.

Initial Cell Culturing and Banking of Cells

Two T25 flasks were prepared for cell culture using the coating protocol above. The gelatin/fibronectin solution was aspirated from the culture flasks and replaced with 4 mL of supplemented Claycomb medium in each flask. The flasks were placed back in the incubator. A

volume of 10 mL of wash medium was added to an empty 15 mL centrifuge tube and incubated in a 37°C water bath. The cells were quickly thawed in the 37°C water bath (approximately 2 minutes). The cells were immediately transferred to the 15 mL centrifuge tube containing the wash medium and centrifuged for 5 minutes at 500 x G. When centrifuging was complete, the tube was removed from the centrifuge and the wash medium was aspirated while being careful not to disturb the cell pellet. The cell pellet was resuspended in 2 mL of supplemented Claycomb medium. 1 mL of the mixture was transferred into each of the two culture flasks. The medium in each flask was replaced with 5 mL of fresh medium approximately 4 hours later after the cells had attached. Figure 18 presents this procedure sequentially with optical images.
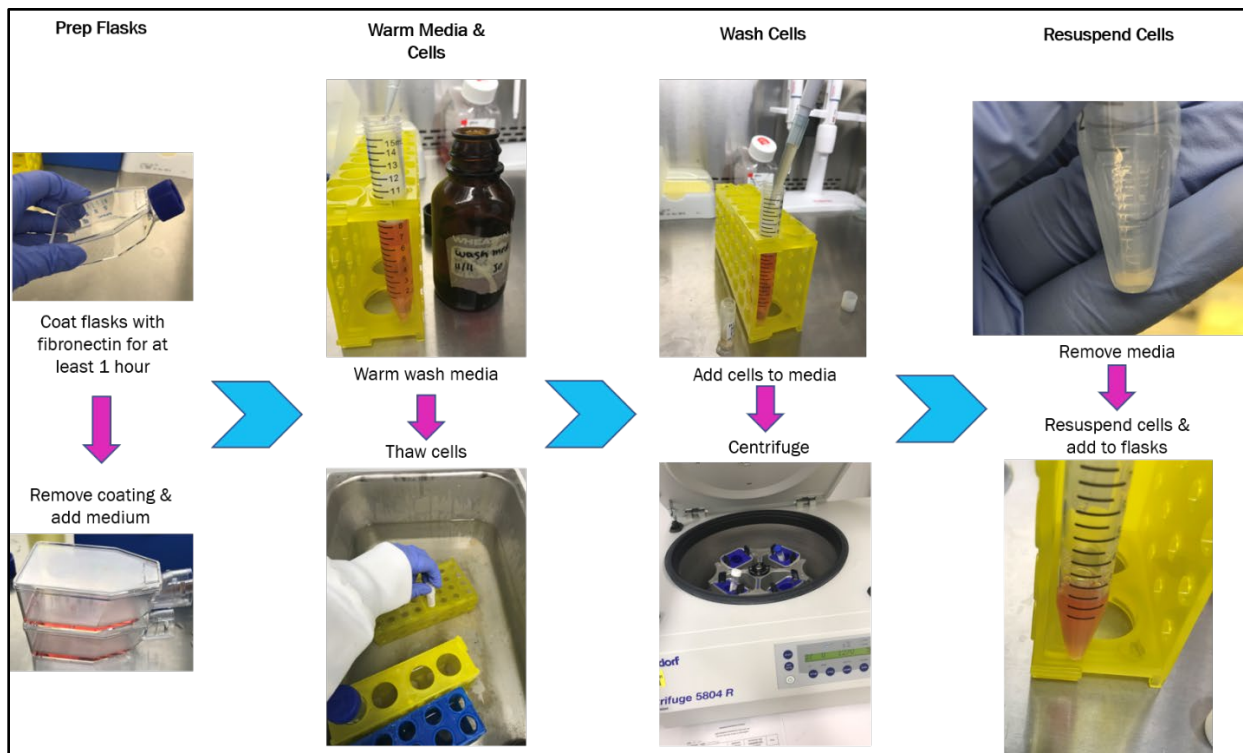
Figure 18 Schematic of the process for thawing and plating HL-1 cells.

After the cells first arrived, it was recommended that they were split when they reached confluency, that was when most of the surface became covered with cells. Each of the T25 flasks was split 1:2, which resulted in four T25 flasks.

When the cells became confluent, they needed to be passaged to proceed further. The procedure for passaging cells from a T25 flask follows and is shown in Figure 19. First, medium was aspirated from the flasks. A volume of 3 mL of DPBS warmed to 37°C was added to each flask by pipetting the DPBS onto the base of the flask (the side opposite the cap) trying not to injure the cells. The cells were rinsed gently and the DPBS was removed via aspiration. Next, 1 mL of pre-warmed 0.05% trypsin/EDTA was added to each flask and incubated at room temperature for 1 minute. The trypsin was then removed and fresh 0.05% trypsin/EDTA was added and incubated at room temperature for an additional 2 minutes. The flasks were then examined microscopically to confirm that cells were detached, as shown in Figure 20. If the cells were still adhered, the flask was gently perturbed with hands on the benchtop to dislodge the remaining cells. To inactivate the remaining trypsin, 1 mL of soybean trypsin inhibitor was added to the flask. Cells and solution from the flask were transferred to a 15 mL centrifuge tube. The empty flask was rinsed with 5 mL of wash medium, which was then aspirated and added to the cells already in the 15 mL centrifuge tube. The total volume of 15 mL of cells and solution was then centrifuged at 500 x G for 5 minutes. Meanwhile, the gelatin/fibronectin solution was removed from each T25 flask that was previously prepared and 4 mL of supplemented Claycomb medium was added to each T25 flask. The cells were removed from the centrifuge and the supernatant was carefully aspirated as to not disturb to cell pellet. The cell pellet was resuspended in 2 mL of supplemented Claycomb medium. Subsequently 1 mL of the cell suspension was transferred into each of the two labeled gelatin/fibronectin-coated flasks.

These flasks were then grown to confluency. Three of the flasks were passaged to T75 flasks and frozen as passage one (1). The fourth flask was kept as the working flask and further passaged. It was important to try to freeze a flask or two from each passage in case an issue arose with the cells at some point. This allowed us to return to that earlier, error-free passage. The protocol for passaging to the T75 flasks was largely the same as passaging to the T25 flasks, except the volume of supplemented Claycomb medium added after the gelatin/fibronectin was aspirated was 9 mL.

Generally, the contents of one confluent T75 flask were frozen into 3 cryovials (approximately 2.0 x 10^6 cells/vial). When cells were needed, one cryovial was thawed into one T75 flask. The T75 flask containing the Hl-1 culture was briefly rinsed with 5 mL of DPBS warmed to 37°C and removed by aspiration. Further 3 mL of 0.05% trypsin/EDTA was added into the flask and incubated at 37°C for one minute. The trypsin/EDTA was removed from the flask, replaced with 3 mL of fresh 0.05% trypsin/EDTA, and incubated at 37°C for 2 minutes. After 2 minutes, the flask was checked under the microscope to ensure that the cells were dislodged. If they were not, the flask was gently perturbed on the benchtop to dislodge any cells that remained adhered to the flask surface. A volume of 3 mL of soybean trypsin inhibitor were added to the flask and transferred the 6 mL of solution into a 15 mL centrifuge tube. The empty flask was then rinsed with 5 mL of wash medium, which was aspirated and transferred to the 15 mL centrifuge tube containing the cells. The cells and solution were centrifuged at 500 X G for 5 minutes, then removed and the wash medium was aspirated. The cell pellet was gently resuspended in 4.5 mL of freezing medium. A volume of 1.5 mL of resuspended cells were pipetted into labeled cryovials. The cryovials containing the cells were placed into a Nalgene freezing jar containing room temperature isopropyl alcohol (IPA). The freezing jar was immediately placed into a -80°C

freezer, which allowed the cells to freeze at a rate of -1°C/minute. Six to twelve hours later, the vials were transferred into a liquid nitrogen dewar.

Maintaining the Cell Culture

Cells were fed with supplemented Claycomb medium every weekday. The media was fully replaced every day. T25 flasks received 5 mL of fresh supplemented Claycomb medium daily, while T75 flasks received 10 mL of fresh supplemented Claycomb medium daily. To avoid feeding the cells on the weekends, double the supplemented Claycomb medium was added to each flask on Friday afternoon. This medium was fully exchanged on Monday morning.
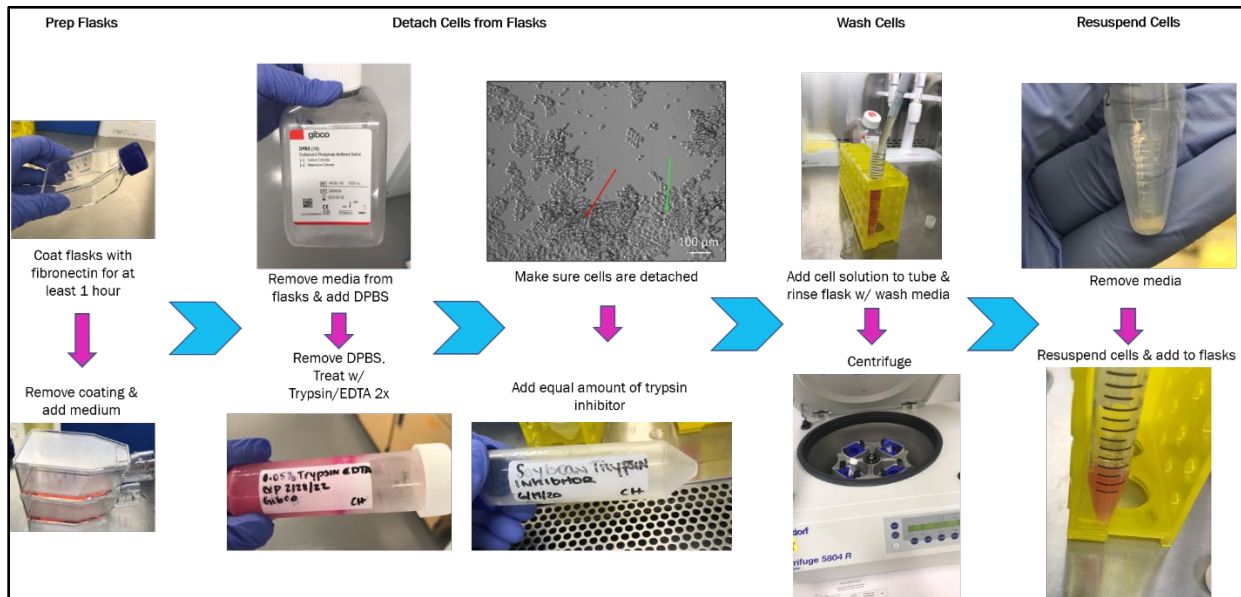
Figure 19 Schematic of the process for passaging HL-1 cells

Cell Counting

Cell counting is an extremely important part of maintaining a cell bank. It is pertinent to know how many cells are being frozen away in cryovials. It is also important to keep track of cell counts as this is one way to tell if there is a problem with your culture. When building our cell bank, cell counts were also used to determine the doubling time of our cell cultures. This allowed

us to eventually be able to time cell cultures so overnight and weekend passaging would no longer be necessary.
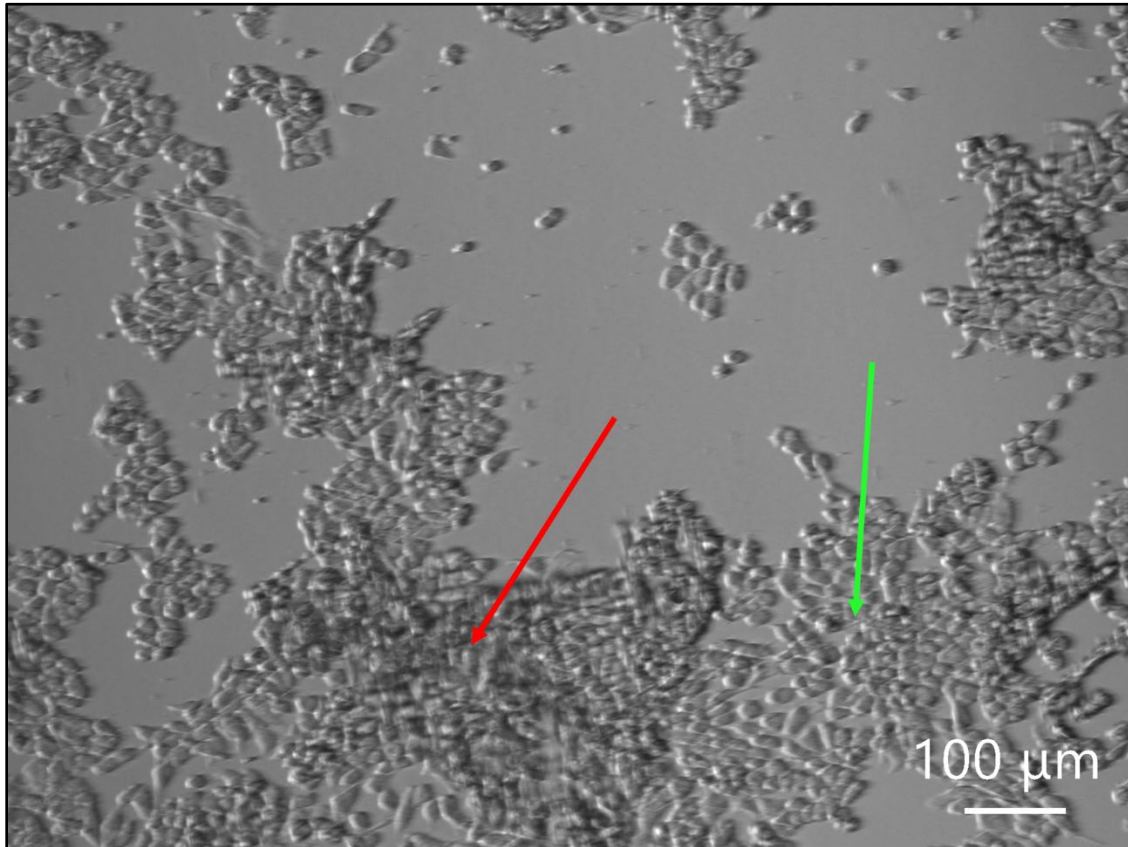
Figure 20 Cells being trypsanized to dislodge them from the surface of a flask to which they are adhered. The red arrow shows a layer of cells that have detached from the flask. The green arrow shows an area of cells which are still attached to the flask surface. (Image taken with Keyence BZ-X800 All-in-One Confocal Microscope at 10X magnification)

Several methods are available for cell counting. The most common method is cell counting using a hemocytometer. This protocol is an extremely common practice used in every cell biology lab [112]. To use a glass hemocytometer, along with a coverslip, it was cleaned with alcohol before use. The coverslip was then moistened with water and affixed to the hemocytometer. The presence of Newton's refraction rings under the coverslip indicated proper adhesion. Typically, cells were counted after cells were resuspended after trypsinization and centrifugation.

To count the cells, 100 µL of cells were pipetted into an Eppendorf tube. A volume of 400 µL of 0.4% Trypan Blue was then pipetted into the same tube and mixed gently, giving a final trypan blue concentration of 0.32%. Using a pipette, 100 µL of the trypan-blue treated cell suspension was applied to the hemocytometer. Both chambers were gently filled under the coverslip, which allowed the cell suspension to be drawn out by capillary action. Using an inverted microscope, the grid lines of the hemocytometer were focused on with a 10X objective. Using a hand tally counter, the live, unstained cells (live cells do not up-take trypan blue) in one of 4 sets of 16 squares on the corners were counted, as labeled in Figure 21. When counting, a system where cells are only counted when they are within a square or on the right-hand or bottom boundary line was used. The hemocytometer was then moved to the next set of 16 corner squares and counting was continued until all four sets of 16 corners were counted.
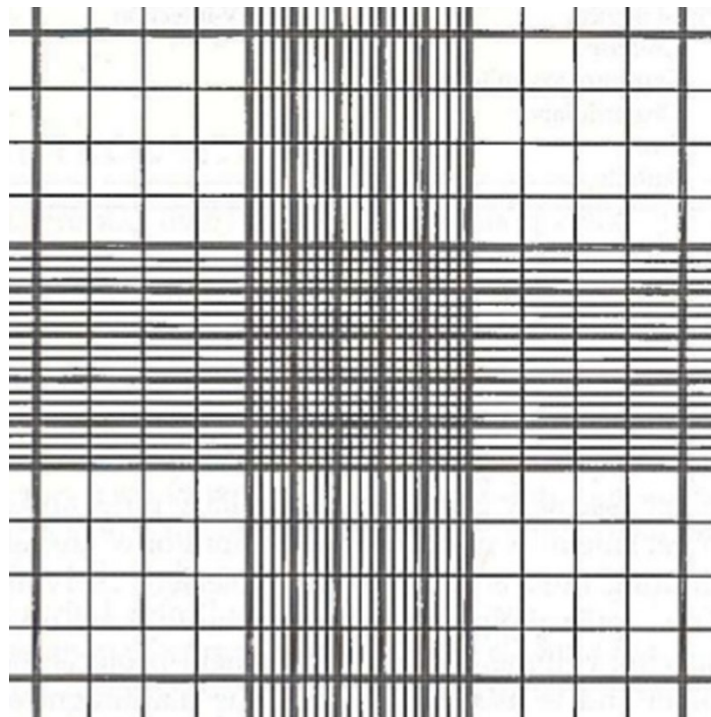
Figure 21 Hemocytometer chamber: the four sets of sixteen squares in which cells are counted are labeled 1 to 4. The densely gridded area is not counted.

49

To calculate the number of live cells per milliliter the average cell count from each of the sets of 16 corner squares was taken and multiplied by 10,000. Then, this number was multiplied by 5 to correct for the 1 to 5 dilution from the trypan blue addition. This final number was the number of viable cells per milliliter in the original cell suspension. When splitting an entire centrifuge tube into flasks of cryovials, the entire volume of cells and medium needed to be considered.

Cell Doubling Time

By maintaining stringent counts of each flask that was passaged while establishing the culture in our lab, pinpointing how long it took for the cells to double was determined. By using this information, the timeline for passaging was ascertained. Having this control allowed us to avoid passaging over the weekends, as well as at odd times of the night. It was determined that our HL-1 cells double in approximately 2.1 days. Given the number of cells typically seeded in a flask, this means that flasks, whether T25 or T75, are typically ready to be passaged after approximately 72 hours.

Necessity of Determining the Biocompatibility of 3D Printing Resins with HL-1 Cells

Once the HL-1 cell line was established in the lab, it was necessary to understand the limitations of its biocompatibility with non-traditional materials that are often used in our group. Specifically, in order to achieve the desired feature sizes to enhance biosensor sensitivity using our 3D bioprinter that we developed in house in Chapter 4 it was necessary to develop our own printer micro-nozzles, with openings ranging from 500 μm to 100 μm. To ensure the viability of the cells was not further reduced in the printing process, it was necessary to select the proper 3D printer resin to print the nozzles. An extensive study of the biocompatibility of HL-1 cells with six 3D printer resins follows. The results of this study also led to improved fabrication of the

culture wells utilized in the packaging of the nanointerdigitated electrodes and plasmonic interdigitated electrodes as discussed later in this dissertation.

Biocompatibility of Blank, Post-Processed and Coated 3D Printed Resin Structures with Electrogenic Cells

The widespread adaptation of 3D printing in the microfluidic and bio-MEMS community has been stifled by the lack of investigation into the biocompatibility of commercially available printer resins. By introducing an in-depth post-printing treatment of these resins, their biocompatibility can be dramatically improved up to that of a standard cell culture vessel (99.99%). Additionally, encapsulating less biocompatible resins with materials that are common constituents in biosensors further enhances the biocompatibility of the material. This investigation provides a clear pathway toward enhancing extrusion bioprinting methodologies and developing fully functional and biocompatible biosensor devices especially for interfacing with electrogenic cells utilizing benchtop-based microfabrication and post-processing techniques.

Biocompatibility Testing of 3D Printed Resins

Conventional micro/nanofabrication techniques allow for the realization of micron- and nanoscale features; however, these techniques have several disadvantages, including expensive and time-consuming processes when altering the design of a device, difficulty in scaling up from prototyping to bulk manufacturing, and 3D geometric design requirements [113-119]. 3D printing, also known as additive manufacturing or rapid prototyping, has recently become an important technology for revolutionizing biosensor and microfluidic device development because of its ability to overcome most of the disadvantages associated with traditional microfabrication techniques [113-120]. Unlike traditional microfabrication techniques, 3D printing does not require the need for a cleanroom facility, thus allowing for simple implementation, low costs, and rapid fabrication [118].

3D printers generally define a three-dimensional object from a computer-aided design (CAD) model layer-by-layer in an additive process [117, 119]. The most prevalent types of 3D printing utilize polymers, and these types are namely fused deposition modelling (FDM), micro-stereolithography (μSLA), and digital light processing (DLP). FDM printing involves the extrusion of small streams or beads of a material, such as polylactic acid (PLA), that immediately harden to form the structural layers of the final device [117, 119]. FDM printing is the easiest to implement and the most cost-efficient of these three methods; however, limitations exist in the shapes and feature sizes that can be fabricated [117, 119]. Both μSLA and DLP printing produce objects in a layer-by-layer fashion via the photopolymerization of a liquid resin. These technologies may also be referred to as vat photopolymerization or resin 3D printing [117, 119, 121]. Both μSLA and DLP printing can produce highly accurate, isotropic objects with microscale feature sizes and a smooth surface finish. The difference between these two types of printing lies in how the layers are cured. In μSLA printing, a laser beam and digital mirrors are used to photocure each portion of every single layer of the object, whereas in DLP printing, the entirety of each layer of the object is cured at once using a projected display [116, 117, 119, 121, 122]. With respect to the application of these types of 3D printed interfaces in biology, especially in the realm of *in vitro* studies, μSLA and DLP 3D printing lend supplemental benefits outside of the ease of microfabrication. Many cell types prefer micro/nano textured surfaces, which can be easily achieved by these methods. Such surfaces allow cells to better sense and respond to their environment [123-125]. It is important to note that the mechanical properties of such commercial resins are not suited for every application in the space of biomedical micro-electromechanical systems (BioMEMS) devices, and the choice of commercial resins can be motivated by a variety of factors, including the ability to rapidly structure microsystems, access to ready-to-use materials and well mechanically characterized materials, as

well as cost, consistency, and ease of procurement. If other material properties are desired such as conformability, silcones and hydrogels remain as alterative 3D-printable materials potentially of interest [126-128].

3D printing allows for the accurate and rapid design and fabrication of monolithic devices. Although this technology has revolutionized MEMS and microfluidics fields, little investigation into the biocompatibility of the most commonly used commercial 3D printing resins has been performed to date. This is especially true for electrogenic or electrically active cells (e.g., neurons, cardiomyocytes) where no biocompatibility reports have been published as far as our knowledge goes [113, 114, 120-122, 129-139]. Many of these "off-the-shelf" 3D printing liquid resins can be purchased directly from the individual printer manufacturers, and as a result their compositions are proprietary. Thus, the constituent materials, specifically the photoinitiators, surfactants, solvents, and shelf-life extending compounds, are unknown. This lack of information is a barrier to wider adaptation of 3D printing in the bioelectronic, biosensor, and microfluidic communities, as material biocompatibility is of utmost concern for cells interfacing with these materials. Some groups have studied some of these resins with little luck in having any extended cell viability, except for the few groups that add prolonged UV treatment to the usual post-print processing [100, 101, 113, 114, 116, 119, 120, 130, 131]. Several of these materials are methacrylate-based as deduced from their materials safety data sheets (MSDS) [140-144]; however, their exact compositions remain proprietary. Studying these resins in cell culture and improving their biocompatibility through post-process treatments is of immense interest to the community and provides multiple advantages. First, the ability to design constructs for *in vitro* biological work solely based on 3D-printing microfabrication strategies means that novel and monolithic design approaches can be explored. Second, the application of post-processing treatments begins to reveal

a larger concept of compound material biocompatibility, by posing the questions of the exact material changes occurring during each step. While some effects are readily known and the effects of certain treatments can be hypothesized, these steps could allow for the identification of the exact components of each resin.

In this section of this chapter, the feasibility of using resin 3D printing for *in vitro* biological

To test material biocompatibility, a cell type that has been well studied and has predictable growth patterns should be used. HL-1 cells are derived from rat atrial cardiac myocytes and are the only cardiomyocyte cell line currently available that can continuously divide, spontaneously contract, and maintain a differentiated adult cardiac phenotype [100, 101]. Additionally, this cell line has been widely characterized using optical, electrophysiological, immunohistochemical, and pharmacological methods [100, 101].

In this section of this chapter, the feasibility of using resin 3D printing for *in vitro* biological applications by testing the biocompatibility of several commercial resins was explored. By utilizing commercially available resins and standard BioMEMS coatings, it was demonstrated how several standard processes can be combined to provide enhanced biocompatibility, which in turn will create higher accessibility to 3D printed BioMEMS fabrication for the creation of novel, *in vitro* electrogenic assays. With respect to the selection of postprocess treatments for 3D printed constructs, the treatments themselves should also be accessible. To that end, coatings that are known to enhance biocompatibility and are accessible to all labs, i.e., SU-8 [96, 145], gold [90, 96, 146], polystyrene [147], Medco/polyethylene terephthalate (PET) [148], and polydimethylsiloxane (PDMS) [149] to enhance biocompatibility, were tested for each material. With respect to postprocessing surface treatments, we examined isopropyl alcohol (IPA) treatment (a common solvent for cleaning freshly printed Methacrylate-based resin parts to remove the uncured monomer [150]); ultraviolet (UV) post-curing (a common step to improve 3D printed final

structural properties due to enhanced crosslinking, as well as a common sterilization method prior to cell culture [121, 151, 152]); thermal baking (a common post-treatment for achieving final, post-print properties [121]), and autoclaving (a common sterilization technique [153] that may encourage further polymerization due to the high-pressure environment [154-156]). Additionally, several resins were tested, as each offers varying mechanical and optical properties, which lends themselves to be useful in multiple applications. Indirect and direct characterization of the biocompatibility of these resins was then thoroughly characterized.

3D Printed Chips

Computer-aided design (CAD) of the sample chips (4 mm x 4 mm x 1 mm) was performed in SolidWorks (Dassault Systems, Velizy-Villacoublay, France). The chips were subsequently sliced and printed (Figure 22A) using Preform and a desktop Form2 μSLA 3D printer (both from FormLabs, Somerville, MA) or Composer and an Asiga MAX UV27 DLP 3D printer (both from Asiga, Sydney, Australia) depending on the resin type used. The Form2 uses a 405 nm laser with a 140 μm spot size for curing, while the Asiga uses 385 nm LED light with a pixel size of 27 μm.

The resins tested for biocompatibility were Clear Resin (FLGPCL04), Flexible Resin (FLFLGR02), Dental LT Clear Resin (DLFLCL01), and High Temp Resin (FLHTAM01) from FormLabs (Somerville, MA, USA) and the GR-10 Clear from Pro3dure (Iserlohn, Germany). All resins tested were printed on the Asiga printer, except for Flexible Resin, which was printed on the Form2.

After printing, the 3D-printed chips were subjected to numerous treatments to increase cell viability (Figure 22B). Figure 22B demonstrates the order in which the treatments were performed. The post-processing treatment steps ranged from no treatment to a full treatment comprising all the different steps, but they were always performed sequentially. The full regimen of the post-

processing treatments that could be combined is as follows, and the detailed methods are listed as the following: sonication rinse in fresh 70% isopropyl alcohol (IPA), ultraviolet light (UV) postprint curing, dry thermal postbaking at 80 °C, and full autoclaving cycle at 135 °C. The individual variations were performed solely for the FormLabs Clear Resin, to rapidly and efficiently idenitfy the major changes in efficacy of post-process treatments to biocompatibility, which were then to be applied to all resins.
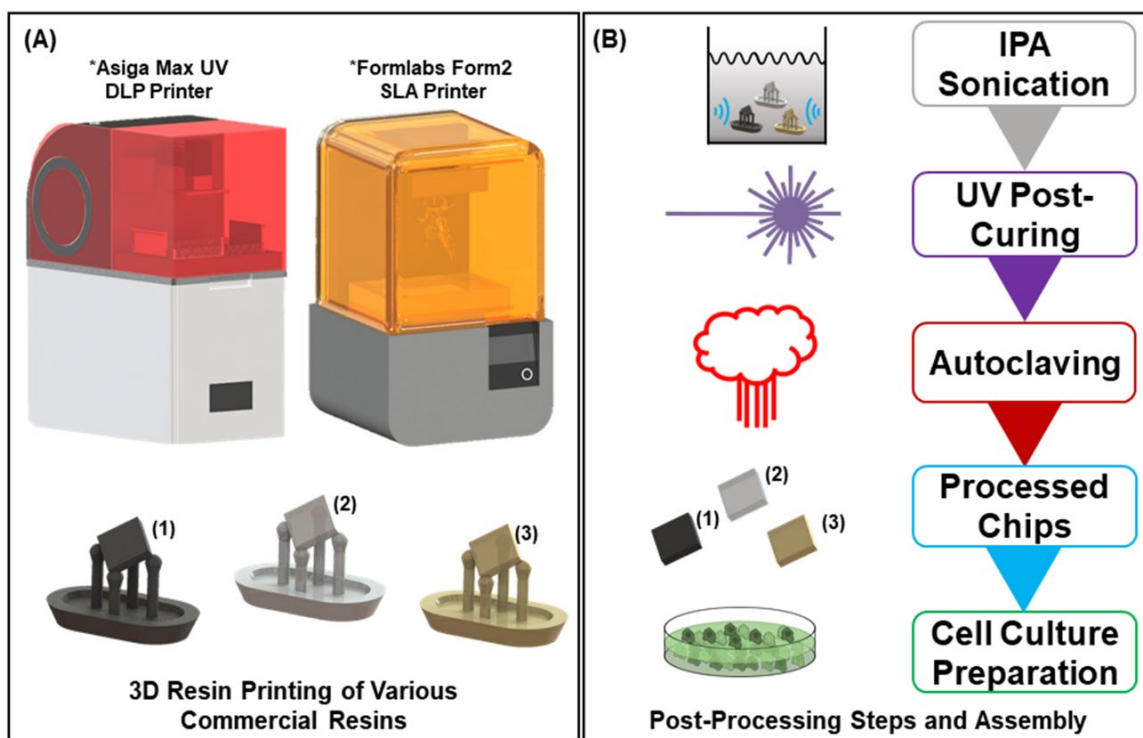
Figure 22 Resin chip fabrication: a. Schematic of the Asiga Max UV DLP 3D printer and the Form2 SLA 3D printer and associated printed resin chips (flexible in black, clear/high temperature in grey and dental in brown). The printer can cure many different commercial methacrylate-based photopolymer resins, allowing for a variety of sampling materials, provided the photo-initiator absorbs between 385-405 nm. Each chip comes printed on a raft and support structure (as shown in the schematic) and must be singulated before post-processing. b. Resin chip post-processing stages. Each of the indicated steps and the order was the final sequence used for a full regiment of resin treatment. After fully post-processing, the chips can then be assembled in 48-well plates and sterilized for cell culture.

IPA-treated chips were washed and sonicated at 40 kHz in fresh 70% IPA (Cole Parmer, Vernon Hills, IL, USA) for 15 min in a sonication bath (Fisher Scientific, Hampton, NH, USA). UV-cured chips were cured for 6 minutes at 60 °C in the Form Cure UV postcuring station (FormLabs, Somerville, MA, USA), which operates at a wavelength of 405 nm. The extended UV

treated chip was cured for an additional 30 minutes in the same curing station. Thermally treated chips (not shown in Figure 22B) were baked in a benchtop oven (Fisher Scientific, Hampton, MA, USA) at 80 °C for 1 hour. Autoclave treated chips were affixed to glass slides (Fisher Scientific, Hampton, NH, USA) using biocompatible Kapton® polyimide tape (Dupont, Wilmington, DE, USA) and autoclaved in a SterilElite16™ autoclave (Fisher Scientific, Hampton, NH, USA) for a two-hour cycle, which comprised one-hour heating followed by an one-hour drying cycle at 135 °C. Since autoclaving includes a thermal step, resin thermal treatment is not depicted in Figure 22B. As a measure between the negative controls (listed in the Negative and Positive Controls section) and the post-treated resin samples described in the section above, we also prepared resin chips that were not cleaned or treated in any way after removal from the 3D printers, aside from gently wiping away of any excess uncured resin.

After the postprinting treatments, some of the chips were coated with materials that are prevalent in BioMEMS and microfluidic devices. These coatings included 10 µm thick polydimethylsiloxane (PDMS) (Sylgard-184, Dow Corning, Midland, MI, USA) mixed in the standard 10:1 polymer to curing agent ratio; 5 µm thick polystyrene (PS, Millipore Sigma, St. Louis, MO, USA) mixed into tetrahydrofuran (THF) (Fisher Scientific, Hampton, NH, USA) to create a 10% w/v solution; 20 µm thick SU-8 (Gersteltec, Pully, Switzerland); 100 µm thick biolaminate layer consisting of a polyethylene terephthalate (PET) film with a single side coated with a Medco adhesive (Medco/PET) (Medco Labs, Bedford Heights, OH, USA); and 75 nm thick gold (Ted Pella, Redding, CA, USA). Chips with PDMS, PS, and SU-8 were dip-coated and cured at 60 °C for 1 hour. Gold coated chips were sputter coated in a Quorum Q150T Sputter Coater (Quorum Technologies, Lewes, UK), and the biolaminate sheet was cut to size and applied to the chips, with the Medco adhesive acting as the adhesive layer. All thickness measurements were

performed using a scanning electron microscope (SEM) (JEOL, JSM-6480, Tokyo, Japan). FormLabs Clear Resin chips were coated with each of the afforementioned materials to evaluate the effect on biocompatibility as stated earlier, while each of the other resins were only coated with PDMS.

The fabricated and post-processed chips were subsequently adhered to a sterile 48-well cell culture plate (Fisher Scientific, Hampton, NH, USA) with biocompatible 353ND epoxy [157] (Epotek, Billerica, MA, USA) mixed at a 50:1 epoxy to curing agent ratio for increased transparency. The chips were placed in one side of the well (Figure 23A) in order to expose sufficient area for the plate reader analysis. The plate was subsequently placed into an oven overnight at 45 °C to allow the epoxy to cure. For each experimental set, $n = 6$ samples were prepared.

The plates were then sterilized, first, by washing each well two times with phosphate buffered saline (DPBS) (Gibco, Waltham, MA) for five minutes. As the next step, the wells were washed with 70% ethanol (Fisher Scientific, Hampton, NH) for 10 minutes. The plate was subsequently UV sterilized in a biosafety cabinet (NuAire, Plymouth, MN) for 30 minutes and then washed with sterile water four times for five minutes each.

HL-1 Cell Culture for Biocompatibility Testing

A sterile 48-well plate with the chips affixed was first coated with a fibronectin/gelatin (both Millipore Sigma, Burlington, MA) extracellular matrix solution to allow for cell adhesion to the surface and incubated at 37°C with 5% CO_2 overnight, as previously outlined. The fibronectin/gelatin solution is aspirated just prior to cell plating and replaced with 500 µL of supplemented Claycomb medium (Millipore Sigma, Burlington, MA).

HL-1 cells were thawed from a cryovial stored in liquid nitrogen and resuspended in supplemented Claycomb medium via the protocol mentioned in the Materials and Methods section. The cells were then counted using a standard hemocytometer protocol with trypan blue (Gibco, Waltham, MA). Typically, each cryogenic vial contains around 1.5 million cells. Since the optimal plating density for a 48-well plate is approximately 30,000 cells/well [25], approximately 20 µL of the cell suspension was added to each well. The exact amount depends on the cell density in a specific vial and is typically determined at this step in the process.
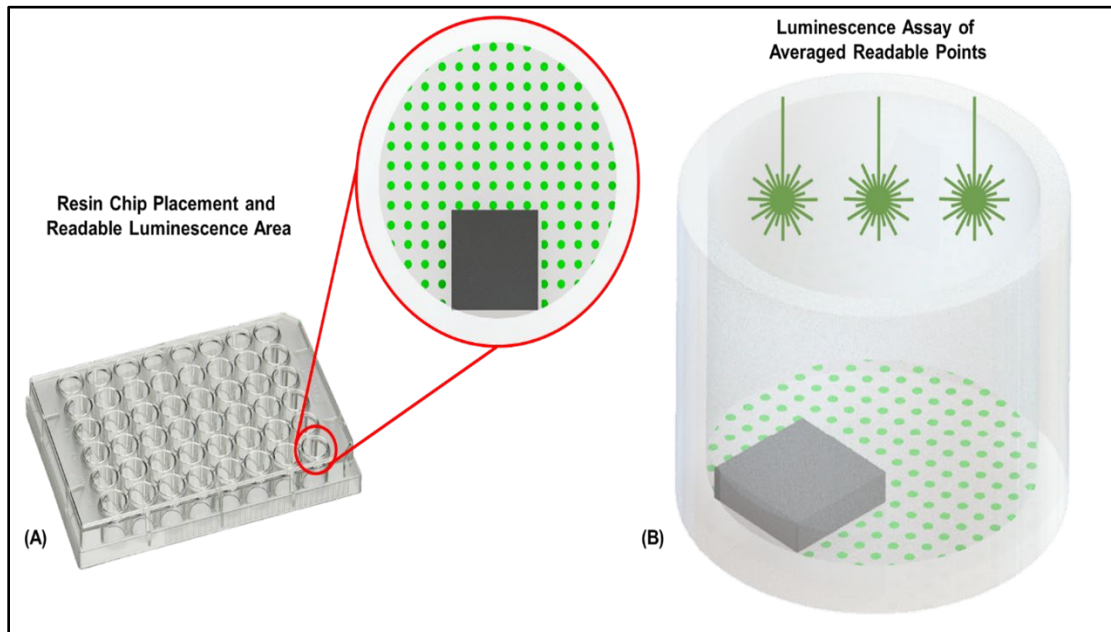
Figure 23 Luminescence assay: a. Image of 48-well plate with schematic close-up demonstrating the placement and relative size of the resin chips in the wells. The grid of green dots represents the sampling points of the luminescence assay. b. Schematic view of the luminescence assay process, illustrating the averaged luminescence leading to an output of percent viability.

Culture plates were incubated at 37°C with 5% CO_2 and allowed to reach confluency (3 days). Cell culture medium was exchanged daily. After the cells reached confluency, an ATP assay was performed to assess cell viability [158]. Promega CellTiter-Glo (Promega, Madison, WI) ATP assay was prepared according to their protocol [158]: 200 µL of supplemented Claycomb medium, along with an equal amount of the ATP assay reagent were added to each well, mixed

for two minutes to induce lysis, and then incubated at room temperature for ten minutes to stabilize the luminescent signal. Luminescence was then recorded for each well using a SpectraMax i3x microplate reader (Molecular Devices, San Jose, CA) in a 48-point well scan mode (Figure 23A and B).

HL-1 cells were also optically observed using inverted microscopy (Nikon TS2, Nikon, Tokyo, Japan). Images of the cell growth over time and during beating were procured using a camera (Amscope, Irvine, CA). Live/dead fluorescence images were taken of the cells plated on standard microscope slide-sized (25 mm x 75 mm x 1 mm) treated resin pieces adhered to a glass microscope slide using 353ND epoxy to make the resin transparent at DIV05 using a Keyence BZ-X800 All-in-One Confocal Microscope (Tokyo, Japan). Invitrogen Live/Dead Cell Imaging Kit (Carlsbad, CA, USA) was used for fluorescent staining, where live cells fluoresced green (488 nm) and dead cells fluoresced red (470 nm).

Negative and Positive Controls

To ensure the validity of the experimental protocol, both negative and positive controls were designed to clearly demonstrate uninhibited cell death and growth, respectively. For the negative controls, 6 mL of each uncured resin was mixed with 24 mL of supplemented media to create a 1/4 (v/v) solution. The purpose of this solution was to "leach" the resin into the media, leaving potential cytotoxic compounds (which are normally removed during curing and post-processing steps), in the media. Cells were plated as described in the previous section until adhered to the culture well surface (N=6 for each resin), at which time point the leached media was used (moving forward) to supplement the cultures. For the positive control, cells were plated until adherent as above, and cultured for the duration of each experimental protocol without any resin (cured or uncured) present in the wells.

<u>Results and Discussion</u>

The positive and negative controls each serve to highlight the findings of the biocompatibility study described in the dissertation. Positive control wells were consistently 99.99% viable as expected. The negative control wells were nonviable (0% viability) within 12 hours of the "leached" supplemented media being introduced in culture. This result held for all instances of every uncured resin leached media that was used. Uncured resin would most certainly never be used in the fabrication of a BioMEMS construct, as uncured resins contain shelf-life stabilizers, solvents, monomers, UV-blockers, and photoinitiators [139, 140, 159], and these are likely polymerized with the solvent evaporating out of the construct as the 3D structure is cured. Again, it is important to note that commercial resins are largely proprietary, so exact chemical compositions remain unknown and are an area of interest for future studies. These controls serve to demonstrate the necessity of the postcuring steps, including sufficient UV/thermal curing of the resin, which would ensure the removal of these overtly cytotoxic compounds [160, 161] that may still be present in trace quantities after the initial structural curing of the resin during 3D printing.

The resins selected were based on both their commercial availability and recommended base resins (by the manufacturer) for the respective 3D printing platforms. These resins according to the manufacturers are the most used products in BioMEMS, microfluidics, dentistry, artistic endeavours, and other fields. As a starting basis for comparison, the various iterations of printed materials are deemed biocompatible with HL-1 cells if cell viability exceeded 85.00% [162]. This viability marker extends from both the ISO 10993-5 standard and the European Union Reference Library European Centre for Validation of Alternative Methods (EURL ECVAM) [162], as well as visual observations of cell growth and beating. The percentages shown are based on arbitrary luminescence units, corresponding directly to a culture's population viability (average $n = 6$). Each experimental group was accompanied by a set of positive controls (no resin; $n = 6$; 99.99% average

viability across experiments) that demonstrated the healthy viable nature of the cells used in a culture experiment. For each of the resins as mentioned previously, a negative control consisting of the uncured resin leached media ($n = 6$; 00.00% average viability) was performed.
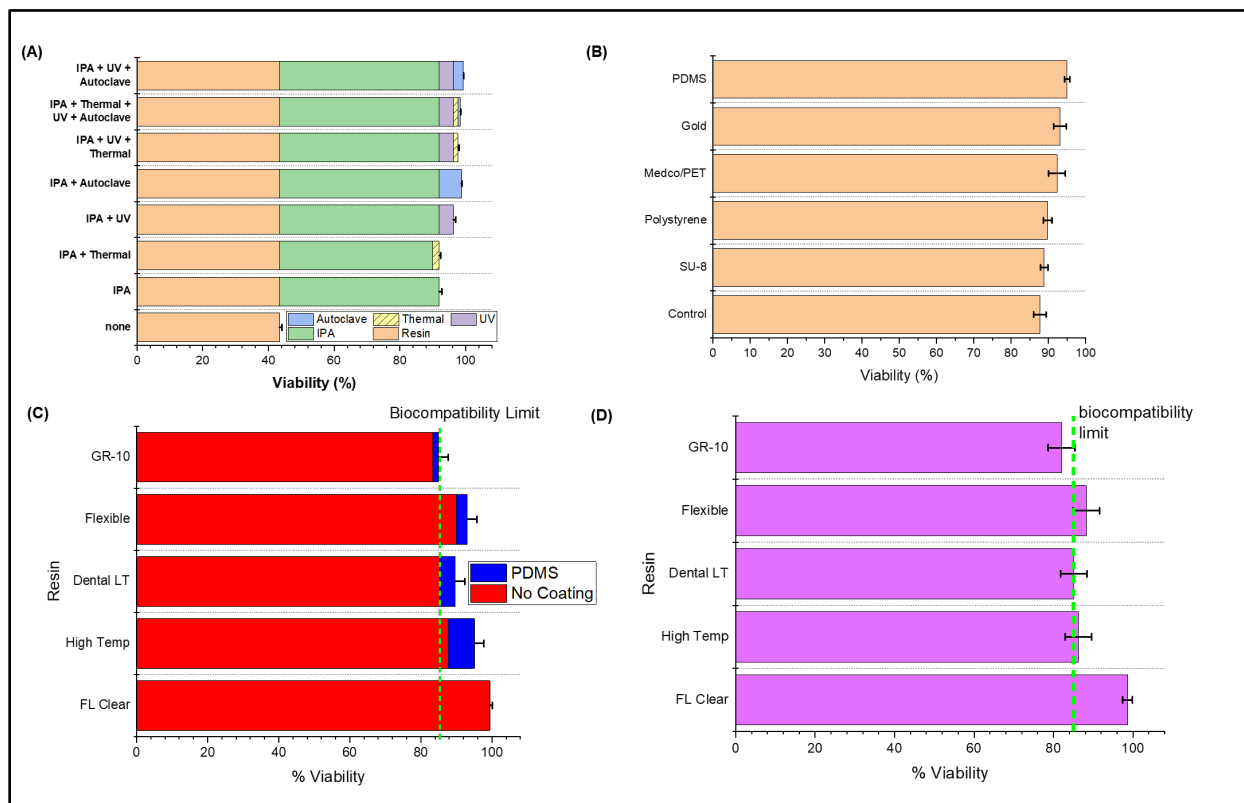
Figure 24 a. Biocompatibility results of incremental improvements in biocompatibility during post-processing for FormLabs Clear V4: Clear resin alone showed the lowest survival rate, while washing with IPA resulted in the greatest increase of survival. Surprisingly, thermal treatment after IPA washing reduced the biocompatibility slightly even through the result was above the accepted values for HL-1 cells. The combination of IPA + UV + Autoclave resulted in the greatest collective viability. b. Coatings encapsulation of FormLabs High-Temp resin to improve biocompatibility: All samples were washed with IPA, exposed to UV for 6 minutes, and subsequently autoclaved. SU-8 and polystyrene had a rather small impact on the biocompatibility. Medco/PET and gold resulted in slightly better biocompatibility, and encapsulation in PDMS provided the best results and was subsequently used. c. Biocompatibility of the different resins before and after PDMS coating encapsulation. d. Biocompatibility results of the different resins where the chips were only coated with fibronectin/gelatin solution as opposed to the entire culture well.

Experimentally, the FormLabs Clear Resin [140] was tested first (Figure 24A), as it is the simplest and most widely available resin accessible for this type of work. All viability numbers mentioned in this section are an average of $n = 6$ samples. Untreated (printed; no wash or post-processing) FormLabs Clear Resin (FLGPCL04) was first tested as a basis of comparison and demonstrated a 43.39% ± 0.70% (mean ± standard deviation for all such numbers from now on)

viability. Such a high cytotoxicity was expected because of the presence of the various moities as hypothesized earlier [52,53]. Next, the postprocessing treatments were tested in a compound manner, beginning with the sonication in fresh 70% IPA, a step routinely recommended to clean a resin-based 3D printed structure. The IPA wash alone resulted in a 91.99% ± 0.76% viability, a dramatic increase in biocompatibility for this resin. This dramatic increase in viability was expected as well, as the IPA rinse removes any uncured resin and other particles that remain on the structure after the printing process [42]. Next, an IPA and a UV postcure was tested, resulting in a 96.35% ± 0.71% viability. The combination of the IPA rinse and UV curing likely results in an increase in viability due to the combination of the removal of uncured resin [42] and further crosslinking of the polymer in the UV curing station due to free radical initiated polymerization [9,43,44]. IPA and a thermal bake were then tested together resulting in 89.98% ± 0.39% viability, prompting a comparison with an IPA and autoclave regimen, which resulted in a viability of 98.71% ± 0.24%. From this result, it was hypothesized that while the addition of only thermal baking enhances the mechanical properties of the resin [9], no further crosslinking is achieved; however, the high pressure environment of an autoclave step may in fact further crosslink methacrylate-based resins, as previously mentioned in literature [46–48]. The clear benefits from combining IPA washing with UV postcuring and IPA with autoclaving prompted the final compound postprocessing treatment regimen comprising IPA sonication, UV postcuring, and subsequently autoclaving, which resulted in the highest reported HL-1 cell culture viability for this type of resin of 99.31% ± 0.17%.

Although the combined treatments greatly increased the overall viability of the cultures, the Clear Resin itself suffered some minor visible damage from the heat and pressure inherent in an autoclave step. Due to this, the next resin tested was the FormLabs High Temp Resin

(FLHTAM01), which can withstand temperatures of approximately 200 °C [141]. The similar base composition of these resins (both being methacrylate-based) [140, 141] allowed for the extrapolation of the benefits of the full regiment of post-curing processes used in Clear Resin (FLGPCL04). High Temp Resin showed a similar untreated performance viability as Clear Resin at 45.26% ± 0.85% and was also able to be converted to be fully biocompatible (meeting the established HL-1 biocompatibility metric [162]) with the full postprint treatment regimen and with a viability of 87.74% ± 1.6%. Although this resin was significantly less biocompatible after treatments than Clear Resin, it was obvious due to the lack of mechanical damage as observed using optical microscopy that it qualitatively withstood the autoclaving process far better.

In order to assess the ability to improve this viability further, several common BioMEMS and microfluidics materials coatings that are typically used in conjunction with 3D printing of resins in microfabrication were added to the fully postprocessed FormLabs High Temp Resin chips (Figure 24B). These coatings served to enhance biocompatibility: SU-8 demonstrated 88.89% ± 1.0% viability, polystyrene with 89.80% ± 1.2% viability, Medco/PET lamination with 92.31% ± 2.2% viability, gold with 93.1% ± 1.7% viability, and PDMS with 95.05% ± 0.75% viability. The polystyrene coating was found to be porous [163], perhaps causing its lower viability numbers. SU-8 was deposited in the same manner, so we suspect that it may be porous as well. The Medco/PET lamination had a tendency to be detached from the surface of the chips after extended exposure to the culture media, which could have influenced the viability obtained. Gold had surprisingly good viability, which is ideal for exposed electrodes on a 3D-printed polymer surface. PDMS demonstrated the highest viability of all of the coatings for the FLHTAM01 resin structures, which resulted in its subsequent use as a coating for the remaining experiments.

As an additional test for increasing the viability, this resin was subjected to an extended 30-min UV treatment to assess the possibility of potentially increasing the UV postcure time for enhanced crosslinking of dangling polymer chains. The resulting viability of 92.09% ± 0.46% (without any material coatings) suggests this is a potential course of action (result not shown in Figure 24). The FormLabs Clear Resin, when fully treated and PDMS-coated, did demonstrate a 99.42% ± 0.11% culture viability, but it still suffered from failures in the structural integrity of the material that were induced during the autoclaving cycle. As a result, the usage of High Temp Resin is preferred for 3D printed architectures.

Other 3D-printing resins may additionally be options in the development of novel BioMEMS, wearable, and microfluidics devices. In order to enhance the material palette FormLabs Dental LT (DLFLCL01) [143], FormLabs Flexible (FLFLGR0) [142], and Pro3dure GR-10 resins [144] were additionally tested after being subjected to post-treatment (IPA wash, 6 min of UV exposure, and autoclave) and material coating (Figure 24C). These resins were selected because of their commercial availability, and because they are all designated as biocompatible according to ISO standards [122, 129, 130, 132-136, 138, 139, 151, 152, 164-167]. Since PDMS showed the best biocompatibility results among all the coatings used with High Temp Resin, it was used as the coating in the abbreviated evaluation of these other resins. Surprisingly, the Dental LT Resin, reported as a Class IIA long-term biocompatible resin [143], demonstrated a lower assessed viability of 85.29% ± 3.4% when compared to the other two resins. Even with the PDMS coating, the viability was found to be 89.66% ± 2.8%. Flexible Resin demonstrated biocompatibilities of 90.00% ± 1.7% and 93.10% ± 2.7% respectively for post-treatment and PDMS-coating, respectively. The drawback for Flexible Resin overall is its opacity, which limits its use in *in vitro* biological research requiring transmitted light microscopy, but this resin could

find applications in wearable microfluidics, for instance [168]. Finally, the GR-10 resin demonstrated minimal biocompatibility both when fully post-treated (83.33% ± 5.2%) or coated with PDMS (85.00% ± 2.9%). Biocompatibility with respect to HL-1 [162] is met with all of these conditions with the exception of post-treated GR-10 structures. The reason for this result is currently being evaluated.

Additional testing was performed to demonstrate that the reported results were from the resin chips alone and material interactions with HL-1 cells, and not the result of the cells in the surrounding well area. Six fully post-treated chips of each of the resins above were adhered to a well in a 48-well plate and then carefully coated with gelatin/fibronectin solution so that only the chip was coated. Cell viability was subsequently determined using trypan blue exclusion [169]. The resulting cell viabilities, shown in Figure 24D, mirror those shown in Figure 24C.

Surprisingly, the FormLabs Clear Resin and High Temp Resin performed better overall than the commercial resins marketed as biocompatible. Obviously, nuanced differences in the composition of both resins exist; however, the high temperature resin can meet the viability threshold of 85.00% [162] while maintaining its integrity under higher heat and pressure, a necessary requirement in microfabrication. The viability of this material can be further improved with the addition of coating materials such as PDMS. This material appears to be a promising material for BioMEMS, bioelectronics, wearable, and microfluidics researchers.

HL-1 cells are separated when seeded but grow to form mats (Figure 25A). These mats subsequently begin to spontaneously beat, a direct measure of healthy, active cardiomyocyte layers. This can be observed optically and can be interpreted as a direct measure of biocompatibility since the cells will not grow or beat if their viability is compromised [170]. Cells were found to spontaneously beat on all the resins except for the GR-10. Cells grown on the

flexible resin were not optically observed due to the opacity of the material. Images of the cell growth and matting over the course of the five-day testing period are shown in Figure 25A. Expected cell growth and matting was observed for Clear Resin, High Temp Resin, and Dental LT Resin; however, the GR-10 resin showed extensive cell death and minimal growth. Live/dead fluorescence imaging of the cells on top of the Clear Resin, High Temp Resin, Dental LT Resin, and the GR-10 resin was performed using a Keyence BZ-X800 Confocal Microscope (Figure 25B). Cells on top of the Clear Resin and High Temp Resin showed excellent viability, while those on top of the Dental LT Resin and the GR-10 resin showed less desirable viability. This is expected from the results presented above.
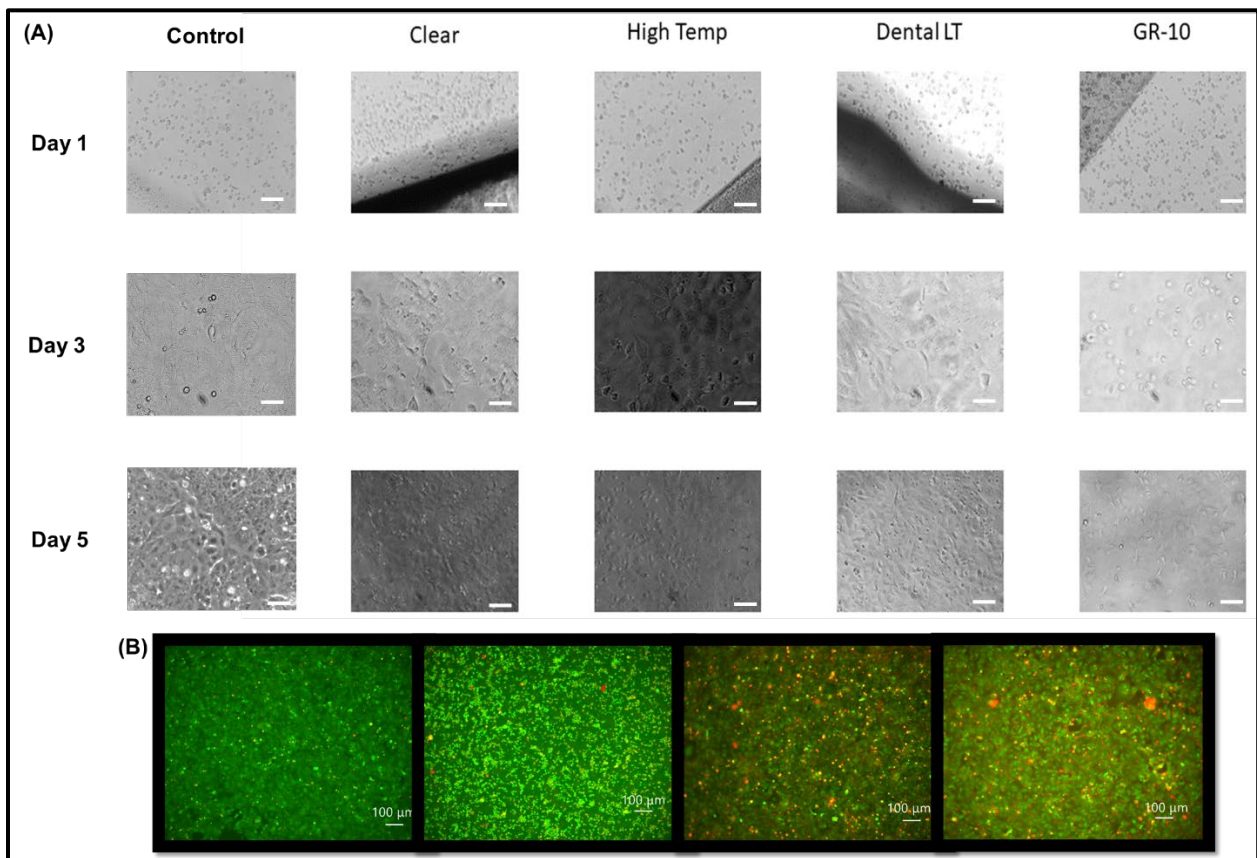
Figure 25 a. Images of HL-1 cell growth over the course of 5 days. Clear, High Temp, and Dental LT resins all demonstrated the expected cell growth and matting. GR-10 resin, however, had extensive cell death with minimal growth. Confluency, or full cell coverage of the surface is reached after DIV 5 (five Days in vitro). After this time, the cells begin to overgrow and die. b. Live/Dead Fluorescence imaging of the HL-1 cells on top of the Clear, High Temp, Dental LT, and GR-10 resins. The cells show excellent viability on both the Clear and High Temp resins, but poor viability on the Dental LT and GR-10 resins. All scale bars are 100 μm.

Conclusions

Through the establishment of the HL-1 cell line, the NanoBioSensors and Systems laboratory now has a bank of several billion cells. This allows for further passaging of the HL-1 cell line, as well as an extensive future of cellular testing on a variety of biosensors. Biocompatibility testing can easily be performed on new materials on an as needed basis. These are being continually performed by the group.

The expansion of 3D printing into the microfluidic and BioMEMS fields has been suppressed by the lack of transparency in the chemical compositions of commercially available resins, as well as the minimal amount of biocompatibility data currently available in literature. First steps towards establishing biocompatibility of various resins with respect to electrogenic cells, utilizing both post-processing treatments and material coatings have been taken. Specifically, the results presented here provide a clear pathway toward applying these resins toward 3D printing-based 2D and 3D microelectrode array (MEA) devices [145, 163, 171], as well as cell culture wells for use in biosensors [90, 146] and 3D printer extrusion micro-nozzles.

CHAPTER 4: EXTRUSION PRINTING OF BIOMATERIALS

A portion of the work presented in this chapter has been previously published in IEEE JMEMS in 2019 [96]. The "home made" bioprinter work has not yet been published but expected to be submitted to IEEE Transducers 2021.

Introduction

In recent years, 3D printing has been widely accepted as a viable manufacturing technique and has the potential to revolutionize micro/nanomanufacturing and medicine. In the field of cellular patterning, 3D printing is known as bioprinting. Using several approaches, biomaterials are deposited through a computer-controlled dispensing system in designated areas with high accuracy in the micrometer scale [5] [172]. A variety of 3D printing technologies have been adapted for bioprinting applications, but the three main techniques that have proven to be most suited for bioprinting are inkjet printing, laser-assisted printing, and microextrusion (Figure 26) [173-177]. Each of these techniques has advantages and disadvantages. Laser-assisted bioprinting is accurate and reliable, but it is suitable only for cell deposition and prone to heating problems which can cause cell damage [178-180]. Inkjet bioprinting is the most used bioprinting technique. It is inexpensive, easy to set up because it typically involves the modification of off-the-shelf printers, easily expandable, high-throughput compatible, digitally controlled, and non-contact; however, print heads are prone to clogging, shear forces from printing can lead to cell damage, bioink flexibility is limited because bioinks must fall within a specific viscosity and surface tension range, and cells are comparable in size to inkjet channels [10, 178, 181-188]. Microextrusion bioprinting, which is the focus of this work, has a larger nozzle size which leads to less clogging, is capable of printing bioinks with a large range of viscosities and surface tensions, and is the most

promising technique for clinical translation; however, it is a higher-pressure printing technique, which leads to higher stresses, and thus, a possible decrease in cell viability [173, 189, 190].
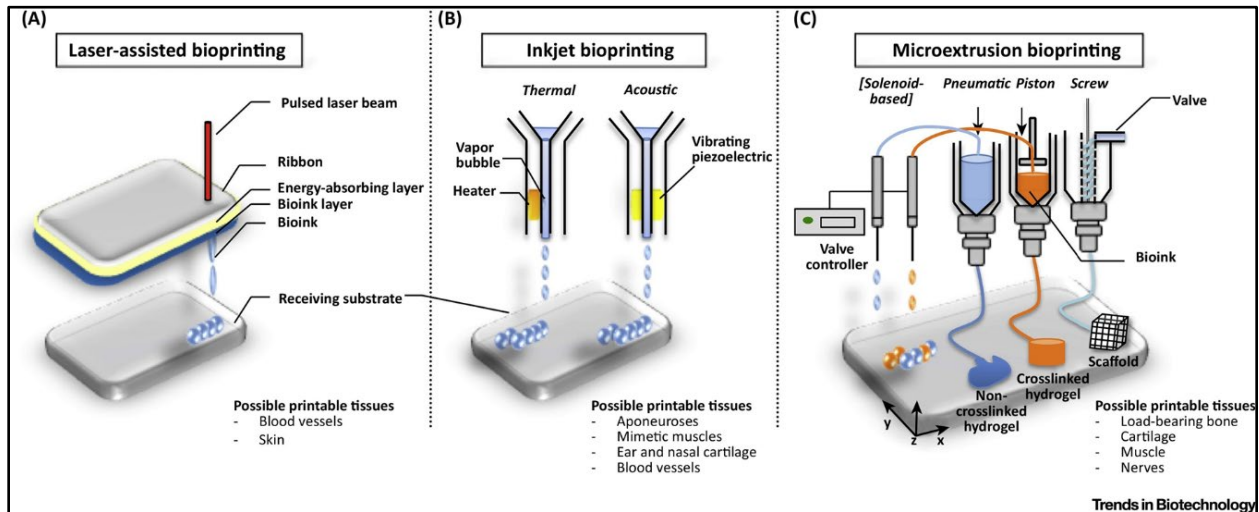
Figure 26 Schematics of the three main bioprinting methods: a. Laser-assisted, b. Inkjet, and c. Microextrusion [191]

In extrusion bioprinting, material (bioink and cells) is dispensed through a nozzle (or syringe) using either pneumatic or mechanical pressure (i.e. plunger, screw, etc.). The nozzle moves in the x and z directions, while a stage moves in the y direction. This gives the user complete special control of the deposition [192]. Extrusion bioprinting is typically a continuous flow process; however, in some cases, discrete spots may be able to be deposited [173, 193]. The larger nozzle size of extrusion printers leads to less clogging than in inkjet printing [189]. This means that the potential to deposit higher densities of cells exists and that a wider range of bioinks with varying viscosities can be used.

Commercial extrusion bioprinters are exceedingly expensive (upwards of $200,000); thus, this technique is often overlooked in laboratory settings despite it being the most promising of the three major bioprinting technologies for clinical translation [190]. Most "hobby" 3D printers are extrusion printers, and they are extremely inexpensive and relatively open source now that the

original patents for this technology (FDM, fused deposition modeling) have expired. For this reason, there is potential for the cost to greatly decrease and implement all the advantages of this technique by converting an off-the-shelf printer to a bioprinter, like many have done for inkjet printing.

In addition to the cost and the ability to "Do it Yourself", extrusion bioprinting has many advantages over other techniques. Extrusion printing allows for greater deposition and printer speed, which can facilitate scalability in a timely manner [194]. Extrusion bioprinting can accommodate a wide variety of bioinks inks including cell aggregates [195-198], cell-laden hydrogels [199-202], micro-carriers [203], and decellularized matrix components [204], while other techniques are only capable of printing cell-laden hydrogels. Additionally, bioprinting at high cell densities is currently feasible only using extrusion bioprinting [194]. The extrusion bioprinting process is biocompatible with reasonably small process-induced cell damage and injury compared to other techniques [192]. Extrusion bioprinting is capable of producing anatomically correct porous constructs [205], which is challenging with other methods. Most importantly as mentioned earlier, from an implementation perspective, extrusion bioprinting techniques are easy to implement and can be used by those with limited exposure to the technology.

The major disadvantage of extrusion bioprinting is the limited resolution. The minimum feature size is generally well over 100 μm [206]. This resolution is considerably lower than other techniques [207]. Inkjet and laser-based bioprinting can achieve resolutions of 50 μm and 5 μm, respectively [208].

Notable work on bioprinting using extrusion techniques has been performed by several groups. Khalil et.al. spent time working on the extrusion bioprinting of 3D hydrogel scaffolds. In this study, rat heart endothelial cells were encapsulated in various hydrogel solutions, including

alginate, fibrin, and chitosan, and printed. Their minimum feature sizes were shown to be 250 μm [209]. Bertassoni et.al. showed direct-write bioprinting of cell-laden methacrylated gelatin hydrogels. This work involved printing HepG2 and NIH3T3 cells suspended in a methacrylated gelatin hydrogel using a commercial extrusion bioprinter (NovoGen MMX Bioprinter). They showed minimum feature sizes of 500 μm and their hydrogels needed ultraviolet exposure to set into defined patterns [210].

As discussed in the Introduction section, cell printing has been gaining considerable traction in the field of biology since the turn of the century. The technology that was first explored was inkjet printing technology due to the availability of the technique and its application in the printing of conducting and non-conducting polymers [174, 182]. Utilizing this technique cells were typically either suspended in a bioink material or printed onto "biopaper" [10, 211-213]. More recently, this field has progressed to newer, more cell-friendly techniques that are mostly used to create 3D grafts, scaffolds, and cell structures and cellular spheroids in regenerative medicine and associated research fields [214].

While most current research focuses on 3D cell laden structures, 2D cell printing can be a viable technique acting as an alternative to lithographic definition of cells, reducing the number of cultured cells and the number of steps required to define these cells in a biosensor device; thus, improving the placement of cells, enhancing sensitivity, imaging, and reducing experimental costs associated with any cell culture methodology.

Theoretical Background

Shear stress is of primary concern in the bioprinting process [215-217]. Moderate shear stress has been shown to influence stem cell differentiation, while excessive shear stress can cause cell rupture by disrupting the cell membrane [215, 216]. Excessive shear stresses caused by the

small diameter of the printer nozzle, the high speed of printing, and the high viscosity of some bioinks are easily generated during the printing process [218]. The level and distribution of shear stress in the nozzle itself are directly influenced by the printing parameters including the driving force, the printhead structure, and the rheological parameters of the bioink, as shown in Equation 1, where K is the consistency coefficient, l is the capillary length, n is the consistency index, P is the dispensing pressure, r radial position, and v is the velocity [217].

$$v = \frac{n}{1+n}\left(\frac{P}{2lK}\right)^{\frac{1}{n}}\left(R^{\frac{1+n}{n}} - r^{\frac{1+n}{n}}\right)$$ (1)

The extrusion bioprinting process can be a useful tool for studying cell injury models *in vitro,* as it is essential to understand how cells respond to process-induced mechanical stresses because they alter cell morphology and function [218].

A piezoelectric drop-on-demand printing computational fluid dynamics model simulation, as well as some experimental work was developed by Shi et.al. to study the shear stress in nozzles during printing [215]. Their experiments specifically examined the effect of the shear stress on cell viability and cell proliferation. Their simulations and experiments demonstrated two results that could translate to extrusion printing: (1) the backflow fluid pushed the fluid that entered from the inlet down along the wall, which increased the wall shear stress simultaneously, and (2) fluid viscosity and nozzle diameter have important effects on the value and breadth of the effect of shear stress. Overall, they found that both cell viability and cell proliferation were decreased with increased shear stress. Individually, shear stress seemed to have a greater impact on cell proliferation when compared to cell viability.
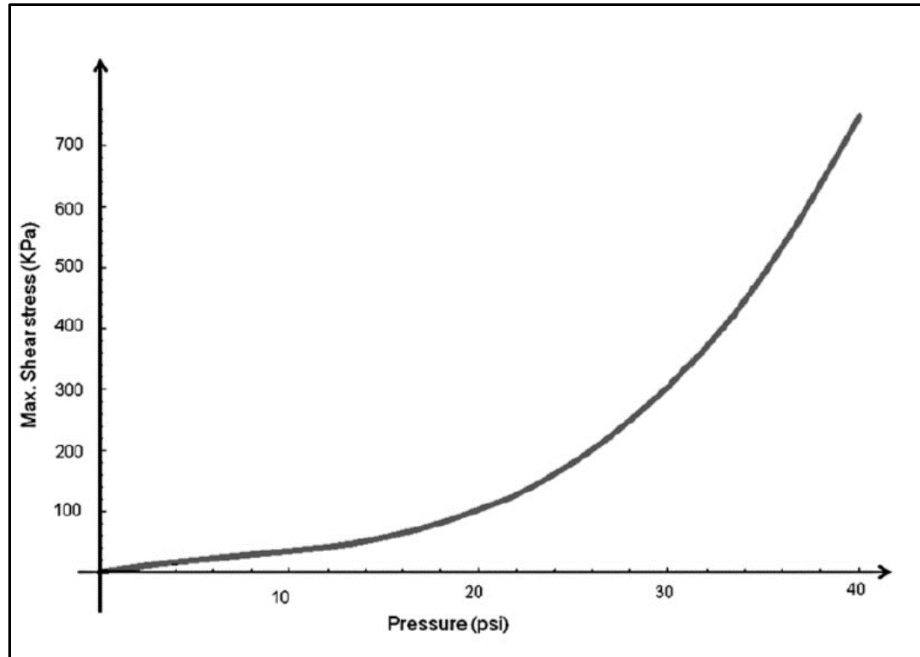
Figure 27 Model from Nair et. al. showing increased shear stress with increased pressure during the printing process.[218]

Wei Sun and collaborators out of Drexel University in Philadelphia have extensively studied extrusion bioprinting and its effects on cell viability, as well as determining optimal printing parameters. Nair et. al. from this group conducted a theoretical study with different printing process parameters to analyze and quantify how they impacted cell injury [218]. They also aimed to optimize parameters for printing viable cells.

A phenomenological model that correlated the percentage of live (P_L), injured (P_I), and dead (P_D) cells to the process parameters nozzle diameter (x_1) and pressure (x_2) (Equations 2-4), as well as an analytical formulation to predict the cell viability throughout the system as a function of the maximum shear stress in the system was developed.

$$E(P_L) = 0.8563 + 0.655x_1 - 0.0268x_2 + 0.0061x_1x_2 - 0.76x_1^2 + 0.000352x_2^2 \quad (2)$$

$$E(P_I) = 0.037 - 0.0469x_1 + 0.00297x_2 - 0.002754x_1x_2 - 0.00003488x_1^2 +$$

$$0.0283x_2^2 \quad (3)$$

$$E(P_D) = 0.099 - 0.561x_1 - 0.0242x_2 - 0.00496x_1x_2 + 0.665x_1^2 -$$

$$0.000321x_2^2 \qquad (4)$$

They found that the dispensing pressure had more of an effect on cell viability than the nozzle diameter. The relationship between dispensing pressure and shear stress is shown in Figure 27. In another study, Sun's group tried to determine suitable printing conditions for embryonic stem cells to achieve not only high cell viability, but also good printability [219]. Here the rheological properties of gelatin/alginate bioinks were evaluated to determine the gelation properties under different compositions, printing temperatures, and holding times. They determined that bioinks with longer gelation times resulted in poorer printability. Their live/dead assay showed that cell viability increased with increased printing temperatures and lower gelatin concentrations. Furthermore, they determined that there was an exponential relationship between embryonic stem cell viability and the induced shear stress, shown in Figure 28.
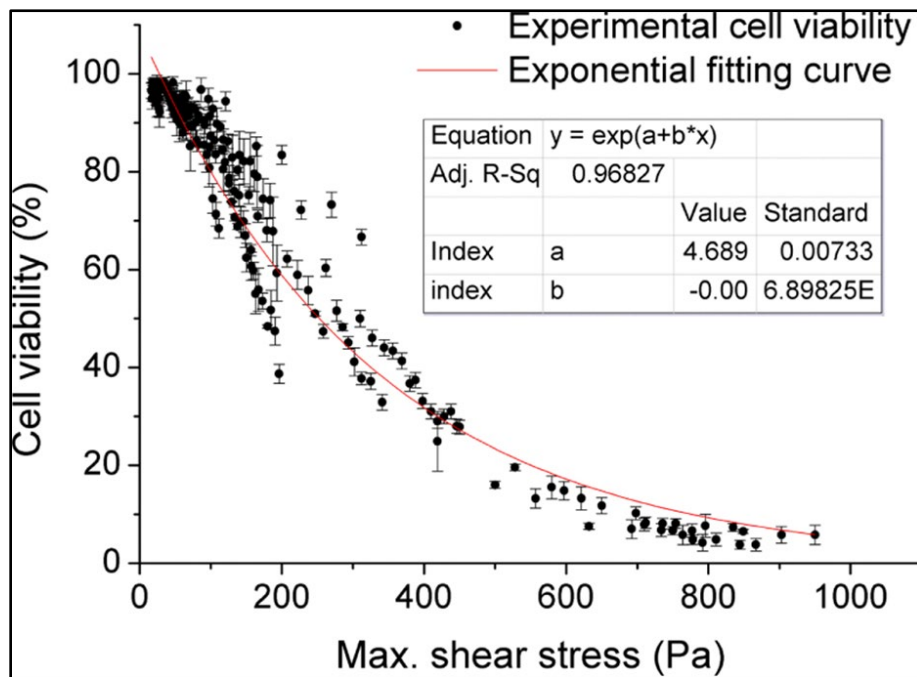
Figure 28 Exponential relationship between cell viability and induced shear stress [219]

Materials and Methods

Most extrusion-based cell printing relies on micro-dispensing units (commercial syringe-based extrusion bioprinters) that are used as designed or with minor alterations to their design. Such systems are not suited for depositing inks of different viscosities [220]. Micro-dispensing units still typically use conventional pneumatic extrusion processes, which require homogeneous bioinks to maintain a constant material flow rate [221]. Altering bioink functionality by introducing nanoparticles, cells, or biopolymers may induce inhomogeneities resulting in irregular material flow and nozzle clogging [221]. Additionally, they are expensive, with the cost of such systems ranging from $15,000 to upwards of $200,000 [222]. This expense makes bioprinting capabilities unobtainable for many research groups especially in low resource settings. Finally, micro-dispensing units are not user friendly. They require specialized training for use.

Semi-Sterile Rep-Rap 3D FDM Printer Conversion

The dramatic reduction in implementation costs for bioplotting resulted in the investigation of a cost-effective printer through the conversion of an off-the-shelf generic fused deposition modeling (FDM) 3D printer (approximately $150, plus $80 in additional parts) to an extrusion bioprinter was performed in a semi-sterile environment (Figure 29).
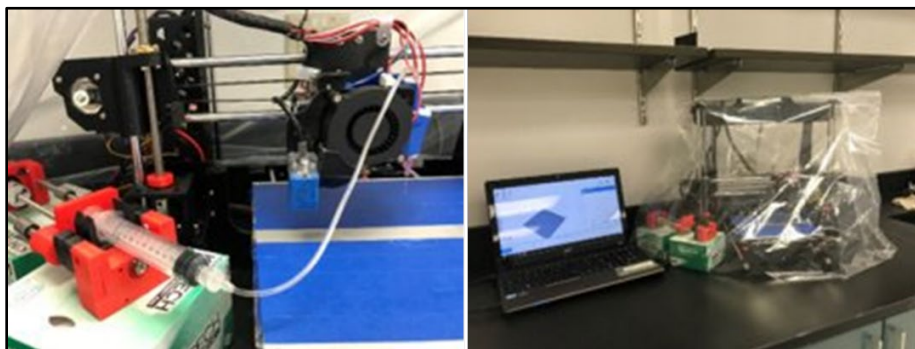
Figure 29 First homemade 3D bioprinter in the NBSS Lab.

Some preliminary design and experimental work on the printer development were performed by exchange students (Ms. Sandra Springer and Ms. Sarah Fremgen from Hochschule Kaiserslautern in Germany) with my guidance (and in collaboration with Dr. Frank Sommerhage, part-time Research Associate in our lab) that showed proof of concept results for droplet and cell printing. For the cell printing, HL-1 cells from Dr. James Hickman's lab were printed in a 3% w/v gelatin solution at a high concentration (actual concentration was not specified by Ms. Springer). Cells remained mostly viable, as shown in Figure 30. The size of the deposited dots was quite large (~1mm radius), and the process was performed under non-sterile conditions. Figure 31 shows 3% w/v gelatin dots colored with trypan blue for visibility printed with a 30-gauge flat needle. This image allows for better visualization of the relative size of dots printed with this RepRap printer.
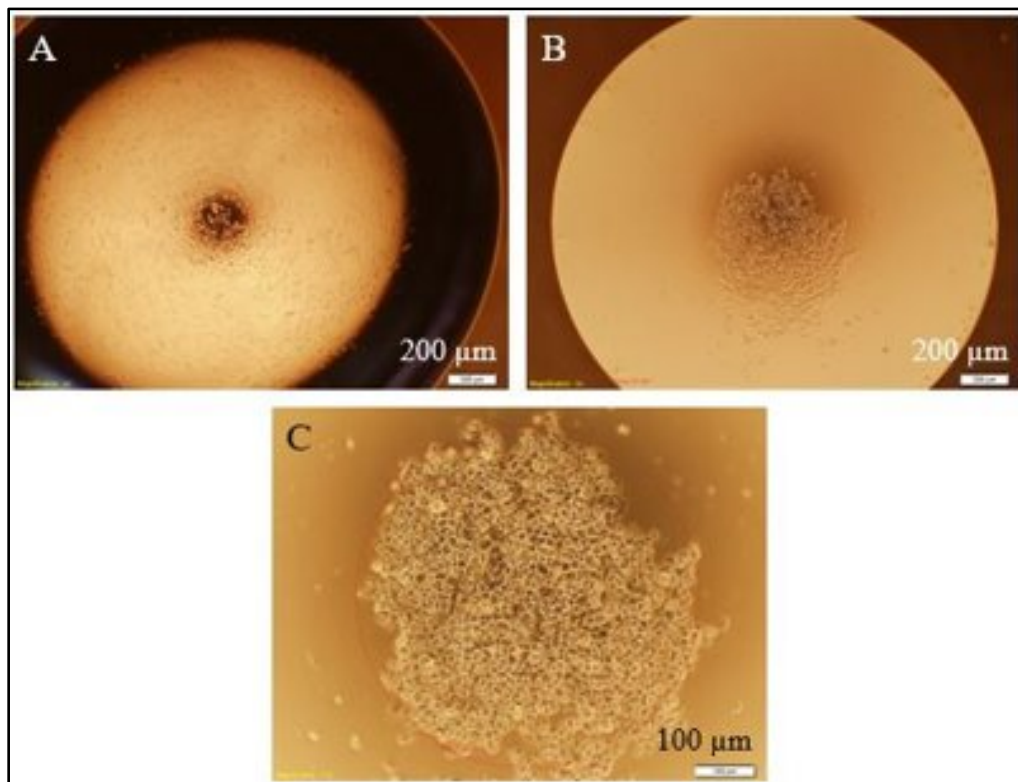
Figure 30 HL-1 cells printed with semi-sterile RepRap printer. a. Initial printed spot with radius of approximately 800 μm. b. Cells after 2 DIV. c. Zoomed in view of cells after 2 DIV.

The motion of the original 3D bioprinter was far from smooth, which often resulted in inaccurate droplet placement. Additionally, the large size and number of parts made the possibility of moving the printer to a sterile environment nearly impossible. As Figure 29 shows, the syringe pump is also quite sizable. This led to two specific issues during the printing process. The first issue was that the size and weight of the syringe pump meant that it could not be attached to the printer itself. Long tubing needed to be attached to the syringe for printing, which sometimes clogged. The second issue was that the pump often extruded more bioink than intended due to the extruder control limitations of the printer.
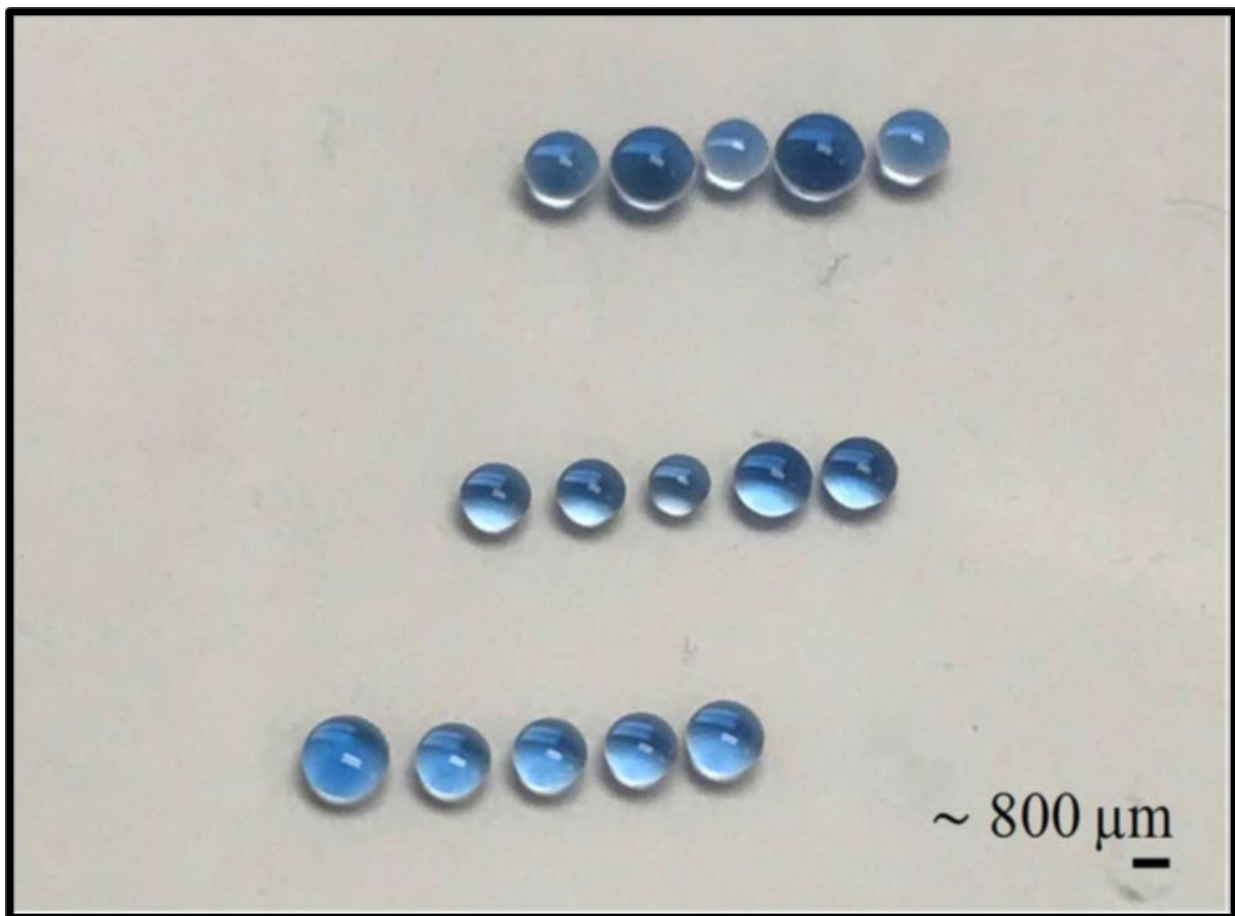
Figure 31 "Line of dots" produced by the first homemade extrusion bioprinter in the Rajaraman Lab. The dots had an average radius of about 1 mm.

Conversion of a Tronxy X1 FDM 3D Printer to a Bioprinter

The limitations of this first printer led to the purchase of a new FDM printer for conversion to a bioprinter. This new printer needed to be compact yet have a stage large enough to support a multiwell plate (128 mm x 85.5 mm x 20 mm) [223]. It also needed to be assembled, so that it could be built entirely inside of the biosafety cabinet to ensure sterility. A Tronxy X1 3D FDM Printer, shown in Figure 32, was selected, as it fit all these specifications.
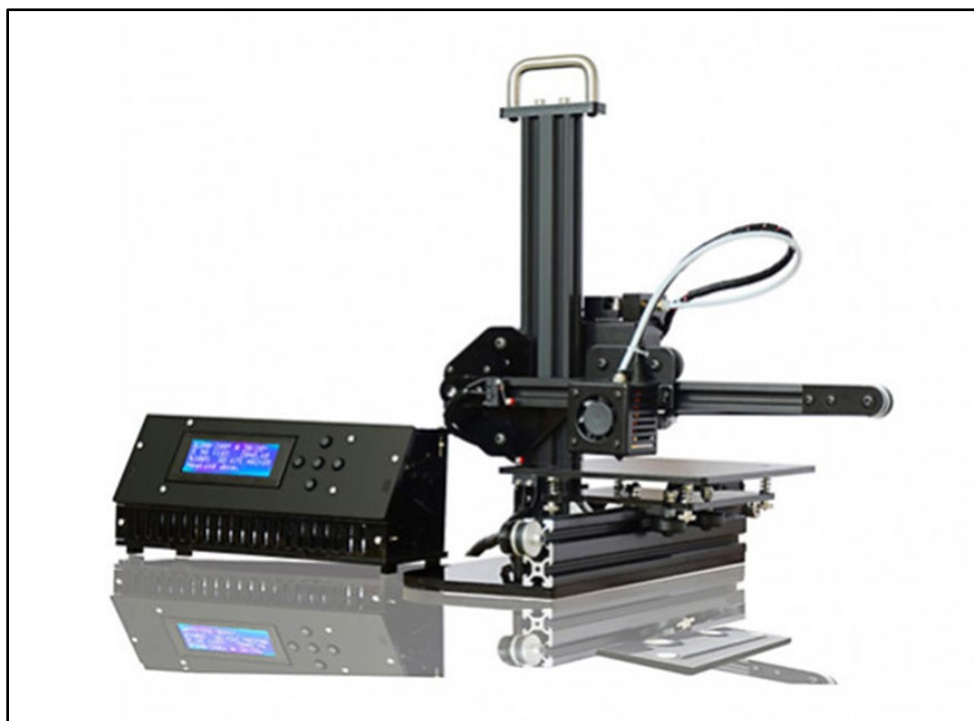
Figure 32 Tronxy X1 3D Printer.

The Tronxy X1 printer was fully assembled inside of a biosafety cabinet to ensure sterility from the onset. All components of the printer, as well as tools, were heavily sprayed with 70% isopropyl alcohol prior to introduction to the biosafety cabinet. The sterile environment of the biosafety cabinet needed to be maintained, as well. The polymer extruder was not affixed to the printer, as a custom-built syringe pump was to be attached in its place.
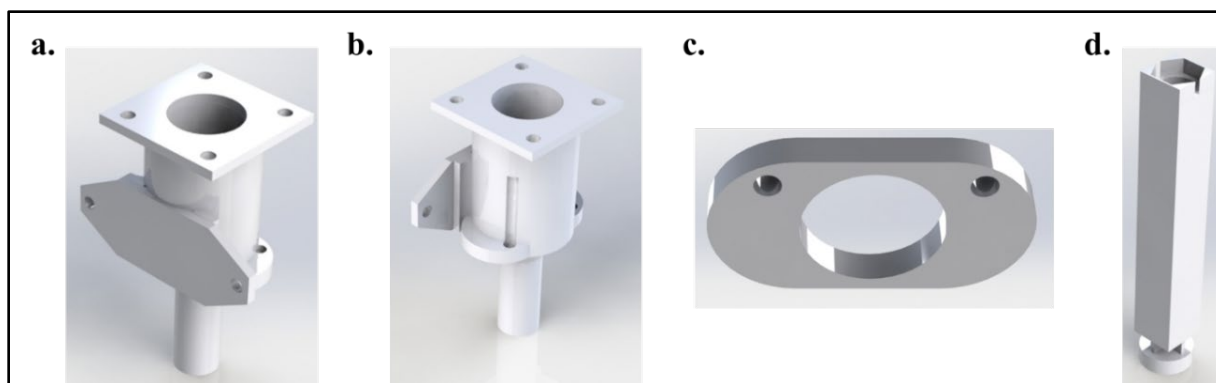
Figure 33 Syringe pump schematics. a. and b. Final syringe pump body design. Designed to fit directly onto the extruder plate of the Tronxy X1. c. Syringe holder designed to keep the syringe fixed to the syringe pump during printing. d. Syringe insert. Designed to fit rubber syringe gasket for improved performance. The M5 hex nut is glued to the insert to ensure perfectly coupled movement.

Custom Syringe Pump Design and Development

Measurements of the distance between the screws on the extruder-holder plate fixed to the printer arm were taken to design a syringe pump that could be fixed to the printer. This distance was 56.5 mm from center to center. The syringe pump was designed in SolidWorks and 3D printed on the back-converted RepRap FDM 3D printer in 1.75mm polylactic acid plastic in a rectilinear pattern with a 25% infill density at 35 mm/s with an extruder temperature of 200°C and a bed temperature of 60°C. The syringe pump was comprised of three parts: (1) the body (Figure 33A and B), (2) the syringe holder designed to keep the syringe fixed to the syringe pump during printing (Figure 33C), and (3) the syringe insert (Figure 33D).

Printer Micro-Nozzle Design and Fabrication

Cells were printed using 30-gauge dispensing needles, as well as 3D printed nozzles. The 3D printed micro-nozzles were designed with a flared output to reduce the physical stress on the cells [224], thus, decreasing the likelihood of cell death in the nozzle itself. The 3D printed nozzles were designed in SolidWorks. Outer nozzle dimensions were height of 16.4 mm and width of 6.25 mm at the top and 250 μm at the bottom. The inner nozzle dimensions are 4.25 mm top opening

with a height of 6.4 mm, followed by a tapered cone area with a height of 5 mm, followed by a 1 mm height by 100 μm cylinder, and finally another cone leading to the opening that starts with a width of 100 μm and ends with 250 μm opening and is 500 μm mm in height. This design is then printed on the Asiga DLP 3D Printer in High Temperature (FLAMHT01) resin from FormLabs (Somerville, MA). After printing, the nozzles were subjected to the post-print treatment described in Chapter 3 to increase biocompatibility. This treatment includes a six-minute wash in fresh IPA followed by a six-minute UV treatment followed by autoclaving. The micro-nozzle opening is rinsed with a syringe of IPA before and after each step to ensure that the opening is clear of any residual uncured resin.

<div align="center">Results and Discussion</div>

The Tronxy X1 3D printer was successful assembled inside of the biosafety cabinet (Figure 34); thus, making it sterile. After several iterations fixing some design flaws such as no room for screws on the pump body, blocked screw holes, and realizing that the syringe pump body size could be reduced, a successful print of the syringe pump was produced and subsequently installed on the 3D printer. A small screwdriver is needed to attach and detach the syringe holder before and after each use. This is also kept inside of the biosafety cabinet to maintain sterility.

Initial testing of the converted 3D printer required many test prints. While the focus remained on dots due to the nature of the sensor design and cell coupling to microsensors in our laboratory, several other patterns were explored. These patterns can be seen in Figure 35. During this phase of test, it was found that blanket coating of the plating surface with fibronectin to encourage cells to adhere to the surface caused full surface wetting upon droplet impact due to the hydrophilic nature of both the petri dish and the fibronectin [225].

Micro-nozzles made of high temperature resin were successfully printed and post-treated using the pre-determined steps in Chapter 3. The nozzles were designed to have 250 µm channel before the flared opening, as shown in Figure 36A. The actual results of the print are observed in Figure 36B. Due to the feature size limitations of the Asiga 3D printer, as well as the physical changes that occur in the resin during the post-print treatments, it was expected that the actual channel would translate to be less wide. The opening width was found to be 150 µm ± 11.42 µm (N=3) in the SEM image (Figure 36C), which is a deviation of 100 µm from the design dimensions. Additionally, the flared opening did not print at all. Instead, the opening is a single channel that averaged 150 µm wide. The channel prior to the flared opening was designed to be 100 µm, so there was a deviation of 50 µm from the design here. The remainder of the micro-nozzle dimensions printed as designed. Table 5 shows the full micronozzle dimensions.

Table 5 Design to printed micronozzle dimensions. Highlighted dimensions differ from design.

Dimension	Design	Device
Outer Nozzle height	16.4 mm	16.4 mm
Outer Nozzle width (top)	6.25 mm	6.25 mm
Outer Nozzle width (bottom)	250 µm	150 µm ± 11.42 µm
Inner Nozzle Opening (top)	4.25 mm	4.25 mm
Inner Nozzle height (top)	6.4 mm	6.4 mm
Tapered Cone height	5 mm	5 mm
Cylinder height	1 mm	1.5 mm
Cylinder width	100 µm	150 µm ± 11.42 µm
Cone height	500 µm	--
Cone width (bottom)	250 µm	--
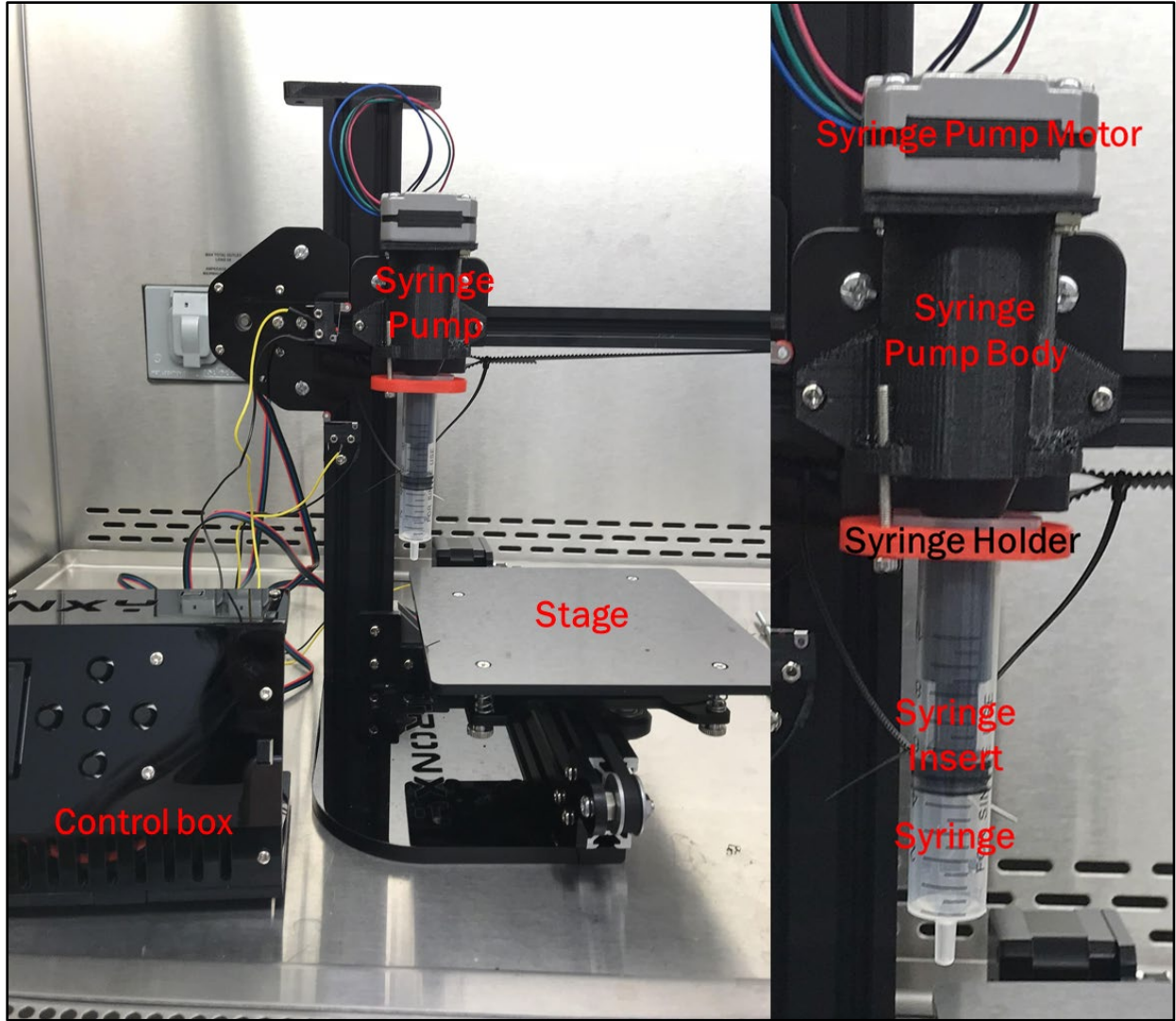
Figure 34 Fully converted Tronxy X1 3D printer. Left: wide view showing the entire set-up including the control box, stage, and syringe pump. Right: close-up of the syringe pump.
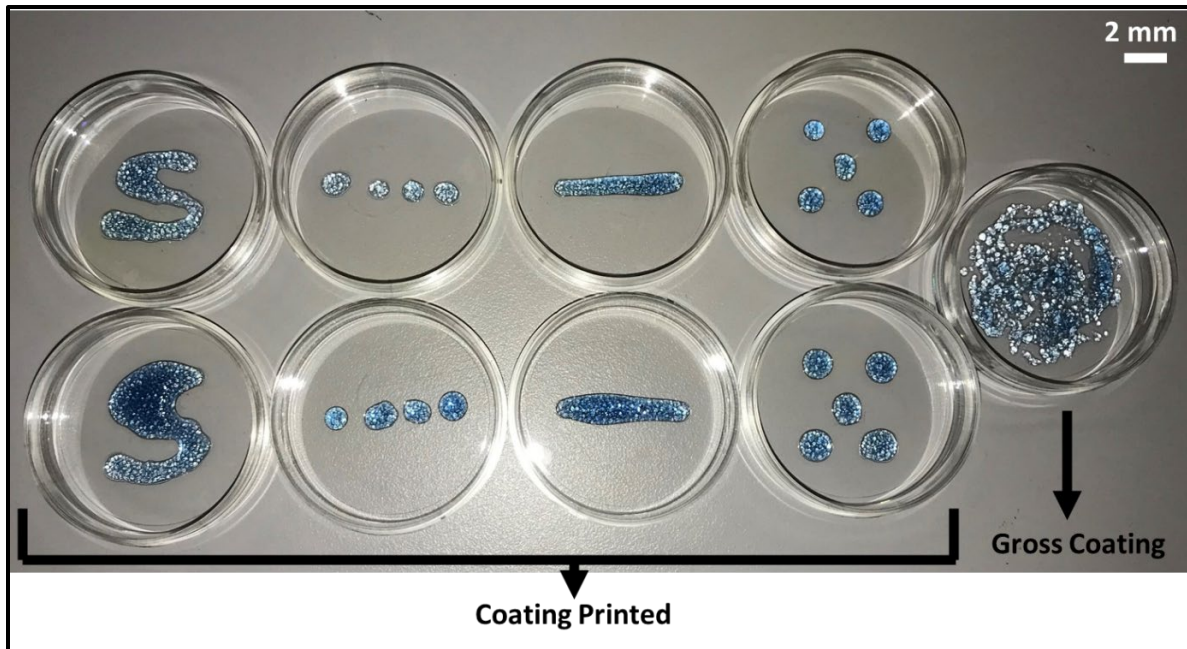
Figure 35 Cells were printed in a variety of patterns. Initially, the petri dishes were grossly coated with fibronectin. This resulted in full surface wetting due to the hydrophilic nature of both the petri dish and the fibronectin. To achieve the desired patterns, it was necessary to print the coating, as well. Printed patterns include dots, lines, and an s-shape.
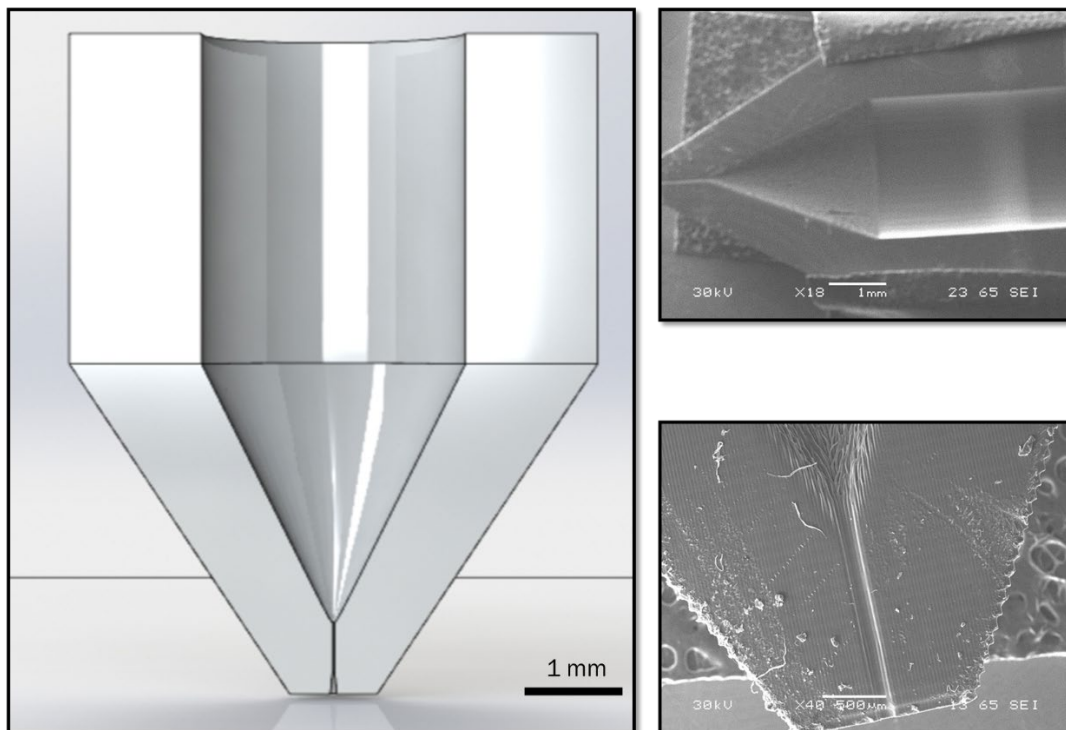
Figure 36 3D printed nozzle. a. SolidWorks schematic showing the intended design of the nozzle. b. SEM of the full nozzle. Scale bar is 1 mm. c. SEM of the nozzle outlet. Scale bar is 500 μm.

84
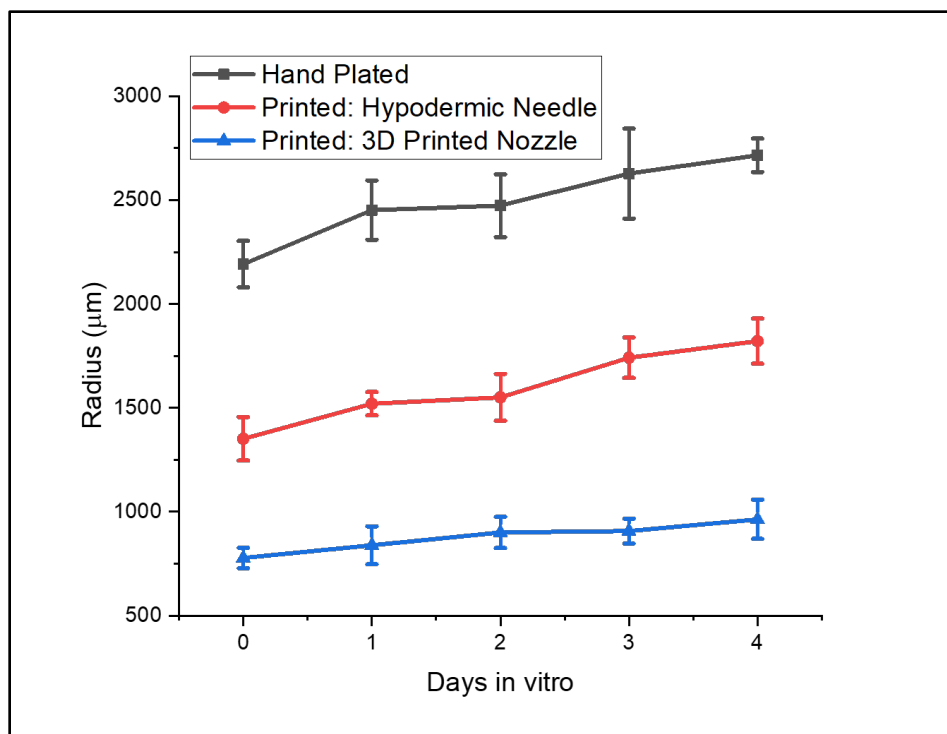
Figure 37 Comparison of sizes between spots that were hand plated, printed using a hypodermic needle, and printed using the 3D printed micronozzle. The 3D printed micronozzle provides the smallest spot sizes.

To demonstrate the effectiveness of the 3D printed micro-nozzles, it was necessary to ensure that the radius of printed spots was reduced. A detailed experiment was carried out to accomplish this task encompassing hand plating, hypodermic needle-based bioprinting and micro-nozzle-based bioprinting. Each group was plated in a separate 6-well plate for five days. Media was changed daily, and cells were imaged daily. Cell growth was monitored over the course of these five days, and a live/dead assay was performed on the fifth day to assess the viability of the HL-1 cells through confluency for each condition. The results followed the expected trends very well over the full assay of five days (Figure 37). The hand plated spots were consistently the largest. They had a radius of 2,192 µm ± 111 µm when initially plated and grew as expected over the course of the five days. The radius of the hand plated spots grew by 523 µm ± 81 µm over the course of five days. The spots printed with the hypodermic needle were the "intermediate" sized spots, with their average radius being approximately 1,351 µm ± 105 µm when printed and grew

as expected over the course of the five days. The radius of the spots printed with the hypodermic needle grew by 470 μm ± 56 μm. Finally, the spots printed with the 3D printed nozzle were the smallest of the three with their radius being approximately 775 μm ± 49 μm when initially printed. They also grew as expected over the course of the five days. The radius of the spots printed with the 3D printed nozzles grew by 188 μm ± 24 μm over the course of the five days. All three bioprinting conditions demonstrated excellent viability (Figure 38).
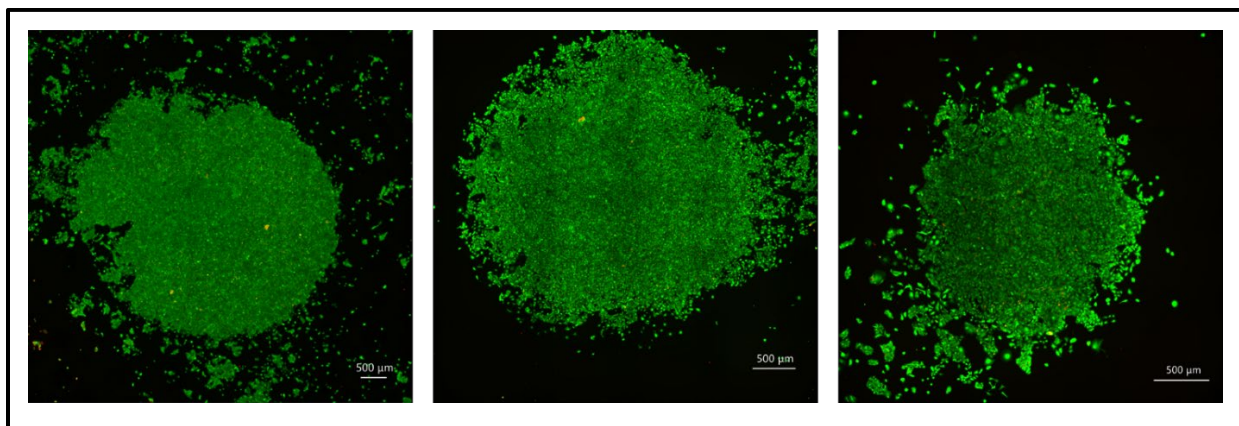
Figure 38 Live/Dead confocal images of the three plating conditions. Left: hand plated. Middle: printed using a hypodermic needle. Right: printed using the 3D printed nozzle. All three conditions showed similar viability, meaning that the printing process had little effect on the cells. All scale bars are 500 μm.

<u>Precision Cell Plating via Micro-Dispenser Device on an MEA</u>

As presented above, extrusion printed spots of sizes down to approximately 775 μm with the 3D printed printer micro-nozzles were achieved. These nozzles also demonstrated extremely good viability, as compared with both hand plating and cells printed with hypodermic needles as nozzles. By applying theoretical understanding of how shear stress impacts cell viability and optimizing printing speed, hydrogel viscosity, and micro-nozzle diameter, we were able to design our printer and adjust its parameters to minimize this shear stress, and thus increase cell viability. While these results are an improvement over other such 2D extrusion printing with cell-laden hydrogels, the resolution is still not low enough to allow for ideal cell-electrode coupling in devices

such as microelectrode arrays (MEAs) with individual electrodes sized at 30 µm and a pitch of 200 µm. While HL-1 cells are great for demonstration and materials testing purposes, the tissue chips community is moving rapidly toward human cells. These electrogenic cells, such as hiPSC-CMs and human motoneurons require vastly improved coupling methods with underlying analytical tools such as microelectrodes. Additionally, a typical HL-1 cell assay is 5 days *in vitro*, while most disease states and organ-chips need to be maintained and monitored a lot longer (months rather than days).

In this part of the chapter, droplets of media containing a small number of cells were placed onto protein-coated surfaces using a micro-dispenser device. This research was performed as a collaboration; thus, our cell printer was not used here due to its limited resolution. This approach introduces a method of precise, non-lithographic patterning of cells (more specifically electrogenic cells, human motoneurons and human cardiomyocytes provided by Prof. James Hickman) on precision nanomaterial enhanced microelectrodes (developed by my colleague in the group, Ms. Nilab Azim) to increase the probability of cell-electrode coupling, while reducing inaccuracies and expenses typically associated with cell plating [226]. The precision plating of cells using a micro-dispenser device was performed in collaboration with Dr. Frank Sommerhage and Prof. James Hickman's group at the NanoScience Technology Center in UCF.

Materials and Methods

Human electrogenic cells were cultured as described earlier [227]. In brief, human motoneurons (Neural Stem, Rockville, MD, USA) and human induced pluripotent stem cells (iPSCs) differentiated into cardiomyocytes (Cellular Dynamics International, Madison, WI, USA) were thawed and subsequently plated in a 60mm petri dish coated with 1 mL of laminin (Sigma

Aldrich, St. Louis, MO, USA) solution for motoneurons or 1 mL of fibronectin (Sigma Aldrich, St. Louis, MO, USA) for cardiomyocytes three to four days prior to the precision plating step.

Precision plating of the cells on an 8 x 8 Microelectrode Array with precision enhanced nano-porous platinum microelectrode coating (developed by my colleague Ms. Nilab Azim and the subject of an accepted paper [163]) was performed using a modified regenHU 3D Discovery Fluid Dispenser (regenHU Ltd., Villaz-St-Pierre, Switzerland) in a semi-sterile environment. The programs which controlled the plating patterns were designed with BioCAD (regenHU Ltd., Villaz-St-Pierre, Switzerland) or simple GCode. Cells were transferred into dispenser syringes at densities between 5×10^6 and 6×10^6 cells/mL (standard for both cell types). After precision plating, the surfaces were placed into an incubator for 20 to 30 minutes to allow the cells to adhere. For both motoneurons and cardiomyocytes, media with an antimicrobial (streptomycin) and an antibiotic (penicillin) was used.

Chemical and electrical stimulation, as well as daily spontaneous recordings, of the precision plated cells were performed to determine the specificity of precision plating. Chemical stimulation of cardiomyocytes was performed by adding norepinephrine (Sigma Aldrich, St. Louis, MO, USA) to the culture well in concentrations from 0 μM to 128 μM. Chemical stimulation of motoneurons was performed by adding glutamate (Sigma Aldrich, St. Louis, MO, USA) to the culture wells at concentrations from 0 mM to 4 mM. The electrophysiological activity of the cells was measured by interfacing the MEAs with the Axion MUSE system and AxIS software (Axion BioSystems, Atlanta, GA, USA). Cells were allowed to stabilize for five minutes, and then cellular activity was recorded for three minutes before and after each chemical stimulation step.

Human motoneurons were electrically stimulated using a biphasic pulse (-500 mV for 50 ms followed by 500 mV for 50 ms) in the Axion BioSystems AxIS software. Cells were allowed

to stabilize for five minutes prior to the experiment. Electrodes were selected for electrical stimulation based on the strong signal amplitudes (>5 μV) exhibited by the cells. The selected electrodes were stimulated within a three-minute recording window. This stimulation process was repeated three times and the data was analyzed and averaged.

Results and Discussion

Cellular electrophysiological activity of human motoneurons was measured regularly after approximately 14 days *in vitro* (DIV). The precision plated motoneurons produced a classic action potential with highlighted average, as shown in Figure 39, and demonstrated increased spike activity throughout their lifetime (Figure 40) [228]. Such classic action potential sequences were measured across several microelectrodes proving precision plating through micro-dispenser is as effective as normal hand plating. The cell cultures were maintained and showed successful spike activity for more than two months in culture (Figure 40).
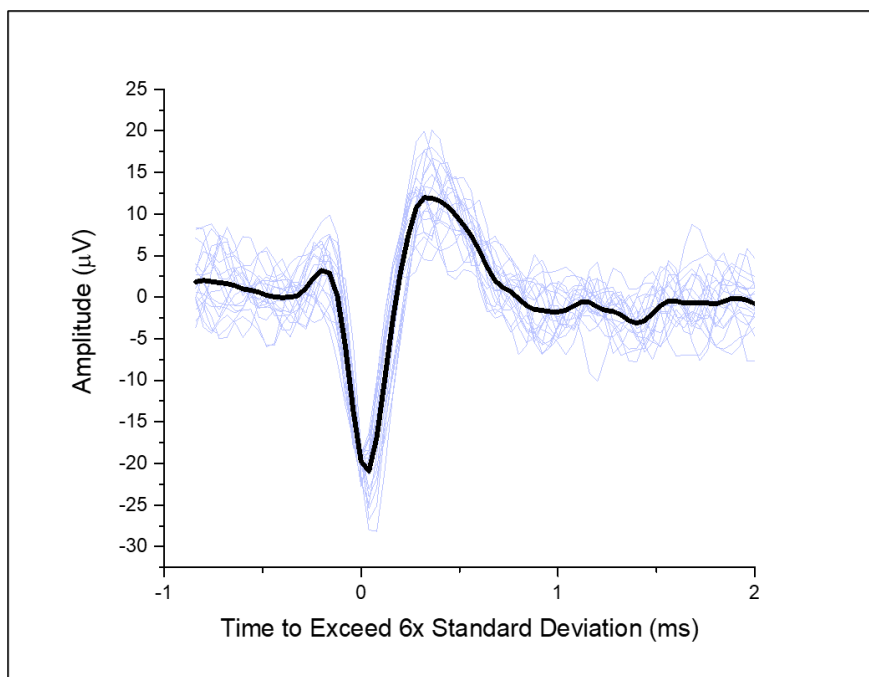
Figure 39 Example of a clearly repeating action potential for precision plated motoneurons recorded at DIV32 depicting a classic extracellular action potential signal.
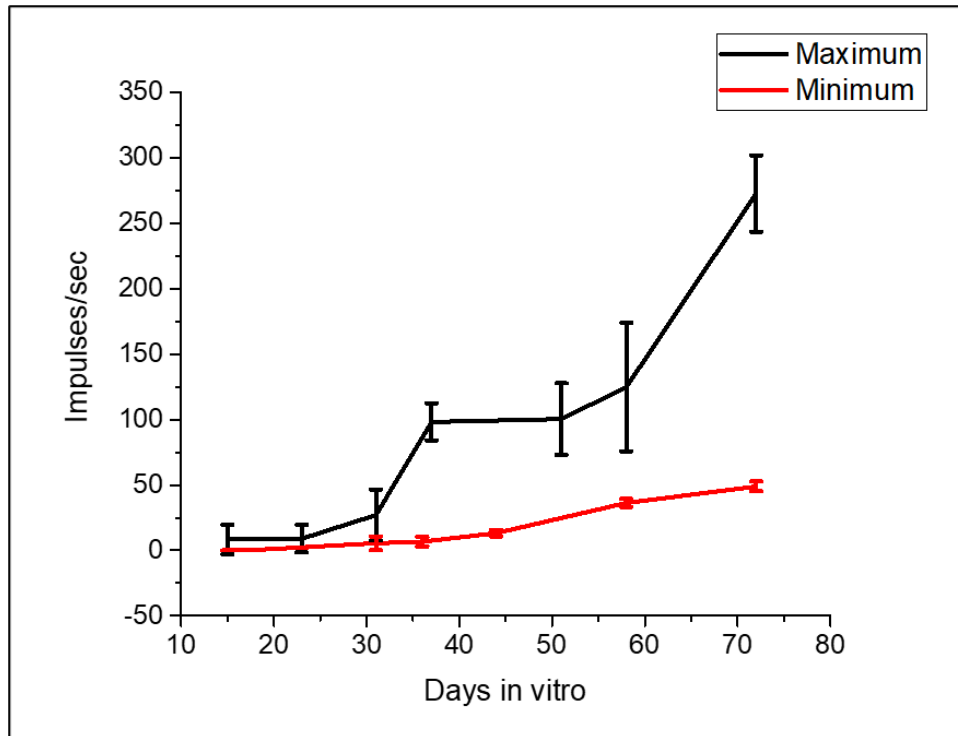
Figure 40 The cell cultures were successfully maintained in an in vitro setting for more than two months. The increased spike activity with error bars and the range of the precision plated cultures is demonstrated for their lifetime.

On the electrodes that were not precision plated, no neuronal activity was seen. This result demonstrates the power of the precision plating technique and the specificity to which human motoneurons can be coupled on specific electrodes. In addition to recording, the stimulation response data was post-processed using MATLAB and plotted in Origin, to show the specificity of the stimulation. Additionally, specific electrodes were electrically stimulated, eliciting a response on the stimulated electrodes with no elicited activity on the rest of the device, as shown in Figure 41. Other researchers such as Wagenaar et. al. showed similar stimulation results with hand plated neurons [229].
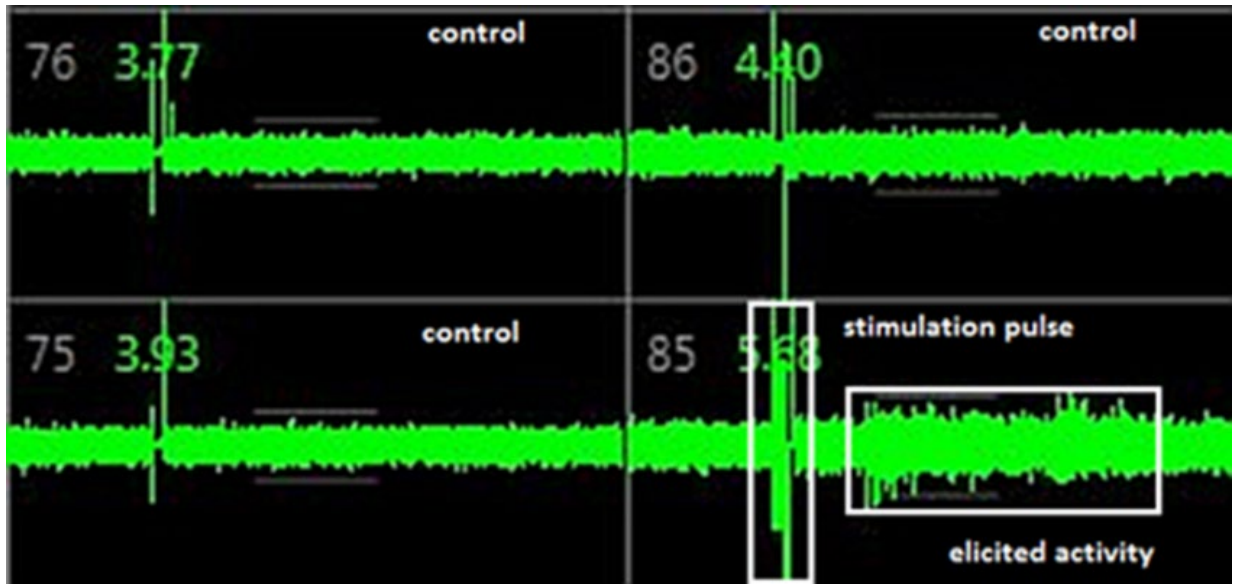
Figure 41 The stimulated electrode (85) elicited a response from the cells that were precision plated on it. The control electrodes (3 neighboring channels, 75, 76, and 86) showed some stimulation crosstalk, but the elicited response did not affect the neighboring channels, nor was there any response elicited in these channels.
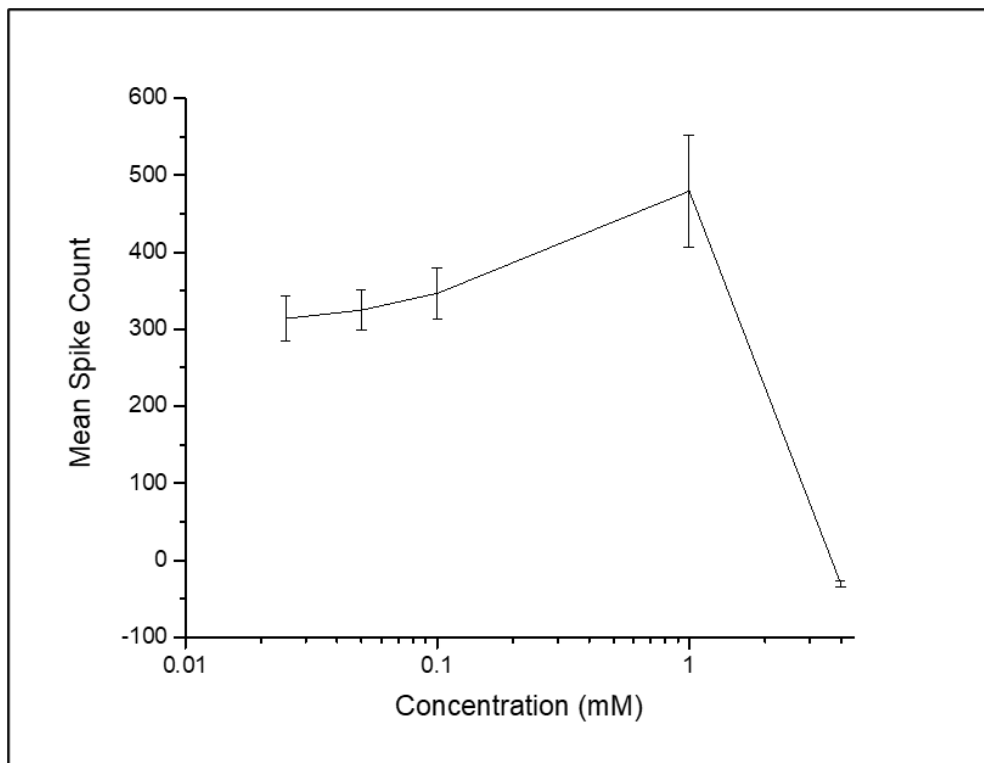
Figure 42 The mean spike count of precision plated human motoneurons chemically stimulated with glutamate is depicted as the normalized data from three active electrodes. The spike activity increases with increased concentrations of glutamate with peak activity observed at 1 mM. This is followed by a sharp decrease in spiking to zero, known as hormesis.

Chemical stimulation of motoneurons with glutamate showed a dose-dependent increase in spike activity peaking at about 1 mM (Figure 42). The observed activity dropped to 0 Hz when 4 mM of glutamate was added to the culture well. This follows the work of Jiang et. al., which showed that low levels of activation of receptors by glutamate engages the stress response pathways of the neurons, but excessive activation of the receptors by glutamate kills the nerve cells because of excitotoxicity [230].

Precision plating successfully allowed the human motoneurons to have localized growth on specific electrodes, while preserving their expected electrophysiological behavior during culture, as well as during stimulation. The electrical stimulation of specific electrodes was possible with minimal to no interference from surrounding electrodes and minimal stimulation effects on these electrodes. Precision plating offers a convenient method to yield significant results from small populations of motoneurons cultured in synaptic isolation on the same device.

For human cardiomyocytes, cellular activity was measured on a regular basis starting after 2DIV. The precision plated samples showed a classic cardiac signal with uniform beat periods, which varied from channel to channel due to the isolated populations. No signal was detected from electrodes that were not precision plated. Cardiomyocyte chemical stimulation depicted a steady decrease in cardiac action potential length with increasing concentrations of nor-epinephrine (Figure 43). Figure 43 also shows that the frequency (in beats per minute) increased with increasing concentrations of nor-epinephrine. The observed IC50 (concentration of an inhibitor where the response is reduced by half) of approximately 5 μM agrees with values reported in literature as depicted in the figure [231].
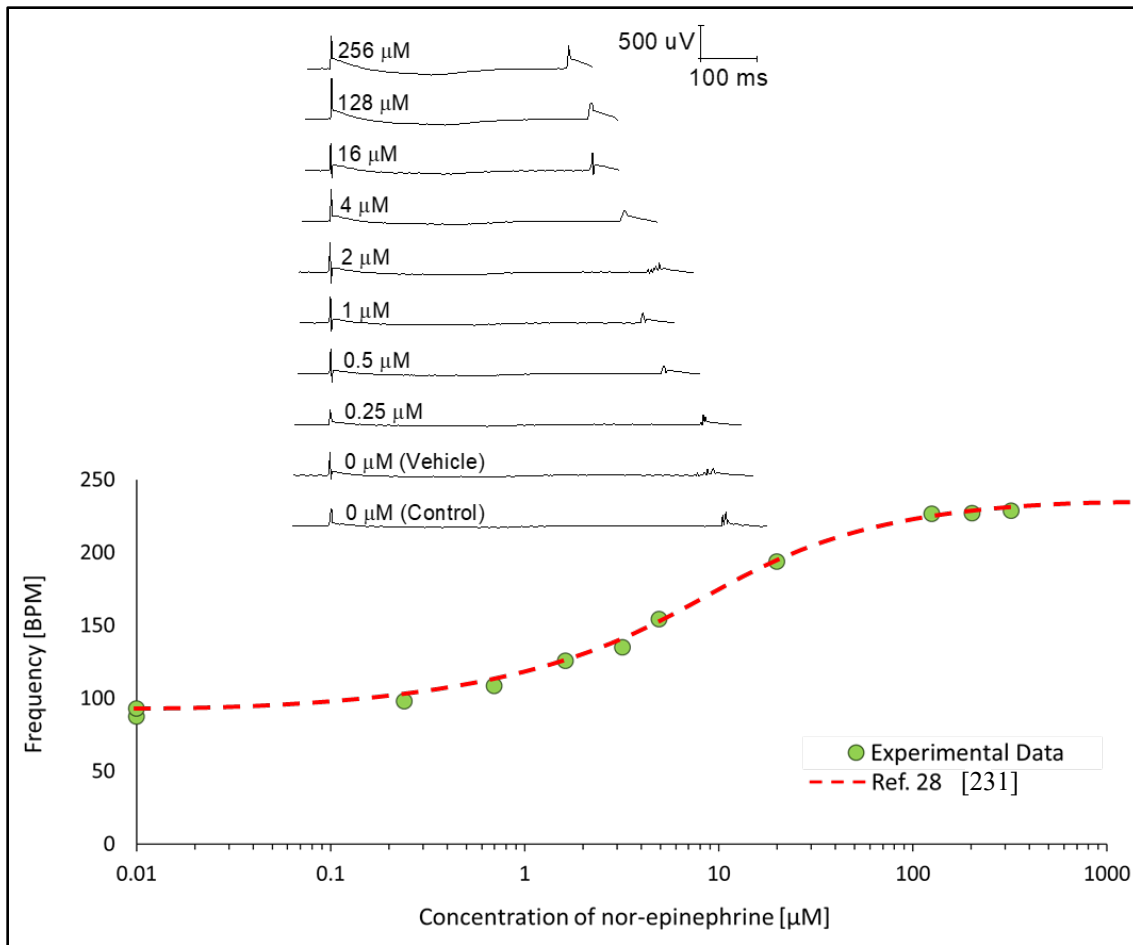
Figure 43 Cardiac dosing data – Top: Beat period reduction with varying concentrations. The beat period decreases with increasing concentrations of nor-epinephrine; Bottom: Beats per minute increase with increasing concentrations of nor-epinephrine in agreement with literature.

Precision plating allowed for small populations of cells to be placed precisely on and around a specific electrode, or a group of electrodes, as opposed to classic techniques, such as hand plating where cells tend to cover the entire surface area. As a result, precision plating is cost effective compared to standard plating, which becomes significant in the case of expensive human stem cells. The developed method becomes advantageous when optimizing for applications such as personalized medicine where the number of cells that can be isolated from a diseased patient is going to be limited and as a result maximal efficacy of plating of these cells is required. Figure 44 depicts "dot" pattern plating, as well as "semi-circle" pattern plated on a microelectrode and a grid

of electrodes, respectively. The "dot" pattern is intended to specifically cover one electrode with cells and was the focus of this study; however, the "semi-circle" pattern demonstrates the flexibility of this plating technique for future applications. Optically monitoring the "dot" pattern on a device over time shows the change, or blurring, of the pattern for up to 30DIV. The precision plated populations of motoneurons remained in nearly the same area for approximately 30 days, as shown in Figure 45; however, an increased spot-size from approximately 150 μm to 360 μm in diameter (N=3) indicated that the cells remained mobile and blurred the initial dot size. This indicated the growth and survival of a healthy human motoneuron culture throughout the lifetime of the cells.
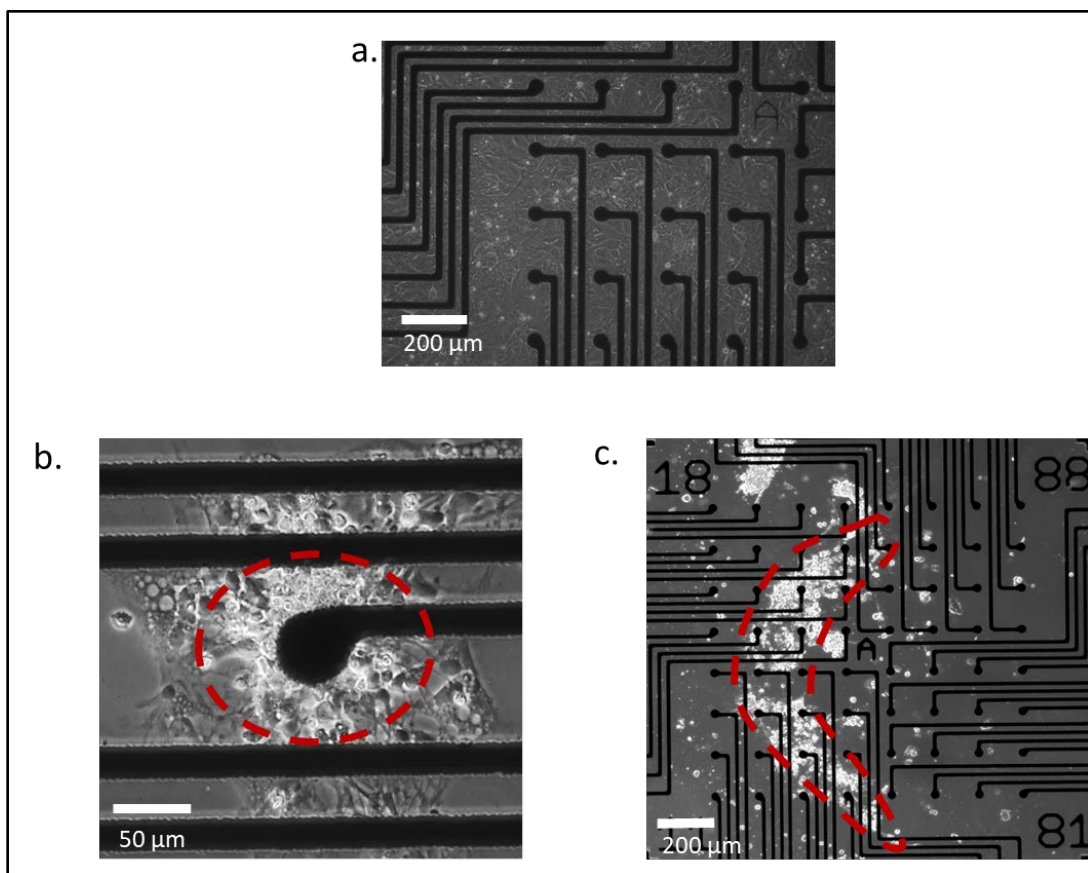
Figure 44 Hand plating versus precision plating of human motoneurons – a. Cells hand plated on a device show a confluent layer of cells. The cells are randomly distributed on the grid of microelectrodes; b. Cells precision plated in a spot right on top of an electrode. The cells are plated in a specific area. c. Cells precision plated in an arc pattern. The cells only appear in the designated area.
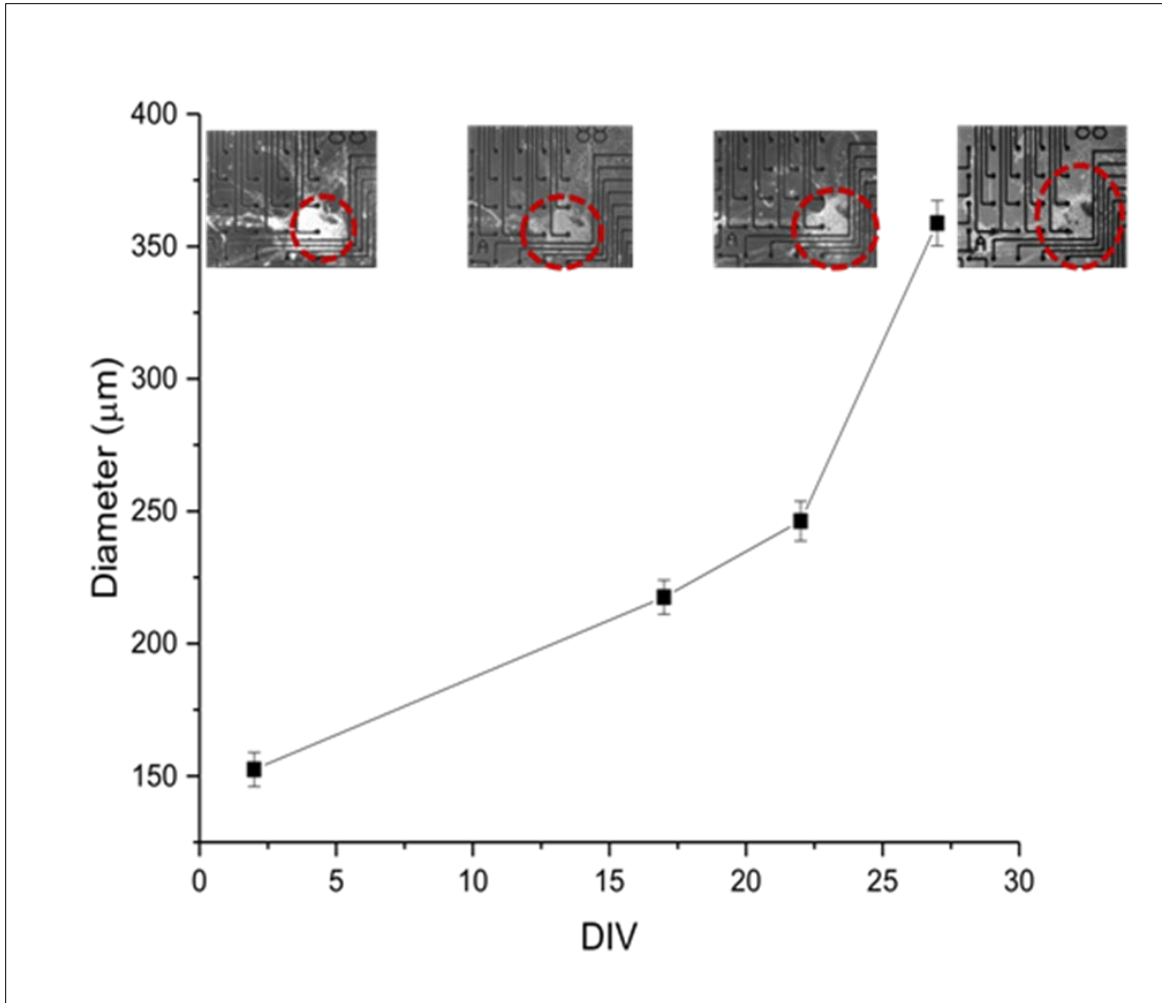
Figure 45 Tracking of a precision plated spot of human motoneurons over time. The spot size increased over time, which shows that the culture was healthy and growing. This observation held for N=3 experiments for approximately 30 days.

Summary

    Classic cell plating techniques are useful when an overall picture of electrogenic cellular activity is required for cells that are available aplenty. This precision plating technique developed here allows for an order of magnitude or more improved coupling with electrodes, passive recording responses for a long time (in excess of 2 months) as well as the study of electrical or chemical stimulation responses of small populations of cells (valuable cells such as human cells that are difficult to attain) on specific electrodes, or groups of electrodes. While the converted micro-dispenser used here was extremely effective and could selectively couple on to 30 µm

95

microelectrodes that are spaced 200 µm apart, the converted Tronxy X1 3D printer provides an excellent "do-it-yourself" solution for cell printing. Although the printing resolution is still limited to approximately 775 µm, it still provides better cell-electrode coupling than grossly plating a biosensor device in addition to improving specificity and reducing costs of cell culture. This resolution can be improved with higher resolution micro-nozzles. Moving forward such a technique will be invaluable to emerging areas such as personalized medicine and "patient on a chip".

CHAPTER 5: CELL-BASED BIOSENSOR PLATFORMS – nIDEs AND pIDEs

Adverse cardiac events are a major cause of late-stage drug development withdrawals. Improved *in vitro* systems for predicting cardiotoxicity are of great interest to prevent these events, improve heart-on-a-chip models, provide greater experimental control, improve specificity, and to reduce costs involved in the introduction of cardiac drugs into the marketplace. Additionally, retinal pigment epithelial cells serve as regulators in the eye. Through the expression and activity of specific proteins, this cell layer oversees the transport of nutrients and waste to and from the retina [232, 233]. The ability of the retinal pigment epithelium to properly express and activate these specific proteins becomes compromised with age and with other conditions that cause toxicity. This can lead to blindness. Such diseases of interest are Age-Related Macular Degeneration and Diabetic Retinopathy. Improved *in vitro* systems for studying the relationship between blindness and the retinal pigment epithelium is of great interest to many researchers.

Interdigitated electrodes (IDEs) affixed with a culture well provide a simple, suitable solution for *in vitro* analysis of cells because of their high sensitivity, ease of fabrication, and label-free, nondestructive analysis. Culturing cardiomyocytes onto these IDEs allows for the use of the IDE–cell combination in predictive toxicity assays. IDEs with smaller interdigitated distances allow for greater sensitivity, but typically require cleanroom fabrication. Here the definition of a simple IDE geometry on a printed nanostructured substrate, demonstrate a Cellular Index (CI) increase when compared to an IDE on a planar substrate is reported. The nanostructuring results in an increased sensitivity of each electrode gap width investigated. An additional measurement modality may be introduced for the first time to our knowledge through plasmonic resonance enhancement, thus a plasmonic interdigitated electrode (pIDE). The entire nanostructured IDE

(nIDE) is fabricated and assembled in a rapid nanofabrication environment; thus, allowing for iterative design changes and robust fabrication of devices. Both impedimetric and plasmonic modalities are combined and demonstrated together. Further sensitivities from individual sensing modalities have been isolated and studied separately.

Hypotheses and Publications

Several hypotheses are being evaluated in this chapter. The first hypothesis was that the interaction of the nanostructured PAN substrate with the electrodes should increase the sensitivity of the IDEs, and as a result, electrodes with a larger pitch should have the same performance as electrodes that are orders of magnitude smaller on standard, planar substrates. The second hypothesis was that the nanostructured PAN substrate layer can exhibit surface plasmon resonance. Finally, the third hypothesis evaluated was that through careful experimental design the individual contributions of each mode to the sensitivity enhancement can be determined: geometric, nanostructured surface, and plasmonic. In summary, through the combination of fabrication and measurement techniques the sensitivity of interdigitated electrode-based biosensors can be dramatically enhanced by several orders of magnitude.

Some of the work in this chapter has been previously published in Biosensors in 2018 [90] and IEEE JMEMS in 2020 [146], and will be presented at the 30th Anniversary World Congress on Biosensors in Busan, South Korea in July 2021.

Introduction

Drug-induced cardiotoxicity accounts for one-third of safety-based withdrawn pharmaceuticals, making it the number one cause of drug withdrawal, limitation, and development termination [14-16]. As of 2016, the Tufts Center for the Study of Drug Development estimates the cost of developing a new drug is on an average 2.89 billion US dollars [234]. Because of this

high cost, improved *in vitro* systems for predicting drug-induced toxicity are of great demand in the pharmaceutical industry to decrease late-stage drug attrition, advance rapid development, and reduce monetary loss [15, 16].

Interdigitated electrodes (IDEs), which are generally comprised of two individually addressable, interwoven, comb-like electrode structures, are one of the most favorable and widely used transducers as chemical and biological sensors because of their low cost, high sensitivity, and ease of fabrication [12]. By affixing a culture well to the IDE substrate, a biosensor can be easily fabricated. This allows for cells to be cultured onto the surface and assessed with label-free electrical and optical assays. A low-voltage signal induces a current between the IDEs. The cells on the electrodes at the bottom of the culture well impede this current, and a change in impedance results [14]. Measuring this impedance change across these electrodes gives an indirect measure of the number of cells in each culture well, as well as an assessment of the interaction between the cells and electrodes [15]. Cellular impedance measurements are useful for studying cell growth and drug interactions *in vitro* without the use of destructive labelling procedures with fluorescent, chemiluminescent, or radioactive chemicals [235]. Recently, these efforts are gaining industrial acceptance with efforts of collaboration between various electrode manufacturers to introduce rapid assays with uniform standards across industrial and academic testing laboratories for testing cardiotoxicity [236].

Electrochemical impedance spectroscopy (EIS) can be combined with surface plasmon resonance (SPR), as they are two of the most widely applied label-free monitoring methodologies for cell-based biosensors [90, 237]. They are both non-invasive and allow for continuous monitoring of cells over a long time; however, they are each based on different physical principles and provide different types of information about the cells [237]. A combination of EIS and SPR

measurements could provide a powerful means to monitor cells that overcomes the molecular specificity of each of the individual techniques. Such measurements are useful in monitoring cell growth, studying drug interactions, toxicity, safety, etc. all in a label-free fashion [12].

A nanoscale biosensor with thin, gold IDEs on a nanohole array substrate with dual-sensing capabilities has been realized. SPR is induced by illuminating the surface with light having a wavelength equivalent to the plasmonic resonance peak [238]. Exciting the surface plasmons while measuring the impedance of the biosensor simultaneously results in increased device sensitivity. These two simultaneous modes are further subdivided into geometric, surface conditioning, plasmonic and other considerations.

Predictive toxicity assays on IDEs based on human pluripotent stem cells may aid in predicting potential safety issues of drug candidates early in its development process, provide information about the mechanisms of drug-induced organ toxicity, reduce the reliance on animal testing, and increase the relevance of preclinical safety tests [15, 16, 236]. Human induced pluripotent stem cell (iPSC) differentiated cardiomyocytes are the ideal candidate for cardiotoxicity cell-based studies. They exhibit the molecular and functional properties of an intact human heart, and their electrical signatures can be monitored using non-destructive impedance sampling [15].

Several IDE and impedance-based biosensors exist, but many of them require the use of expensive commercial systems [13-20, 239] for data analysis and involve cost prohibitive cleanroom-based fabrication approaches for the IDE micro and nanostructuring [21]. These systems use densely packed electrodes, which cover much of the substrate surface and prohibit optical tracking of cells. Other approaches integrate microelectrode arrays with IDEs, which

allows for more comprehensive measurement at the cost of more complex fabrication processes [15].

Bioimpedance sensors offer an inexpensive, label-free solution for MEMS-based medical diagnostics and cell tissue research. Typically, interdigitated electrodes (IDE) are used where high sensitivity and high selectivity are desired. The output sensitivity and selectivity of an IDE is controlled through careful design of the active area, width, and spacing of the electrodes. Improved sensor impedance is achieved when the electrode spacing is comparable to the length of the biomolecule of interest (typically 1 nm to 100 nm) [11, 178, 240]. In addition, the concentration, growth, and alteration of the physiological state of cells during cultivation can be detected as impedance changes [241].

One of the goals for cell-based bioimpedance studies is to maximize the device sensitivity. "Circle-on-line" electrode array geometries are one way to improve the signal strength via greater electrode surface area, thus increasing sensitivity. Another way is through decreased electrode gaps. Most IDE biosensor studies have demonstrated a micron scale electrode gaps (minimum of 5 μm) [2, 3, 21, 92, 241-243]; however, some groups have demonstrated sub-micron electrode gaps (300 nm or 500 nm) fabricated through wet etching and hot embossing lithography (typically) for studying DNA [4, 244, 245]. Figure 46 shows some recent work with IDE biosensors [17, 246, 247].
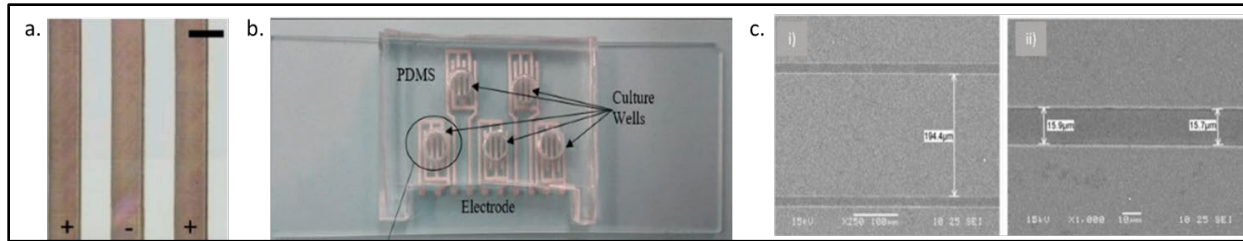
Figure 46 a. Indium tin oxide IDE on glass substrate fabricated via laser micromachining by Tandon et. al. Electrodes are 200 μm with 200 μm gaps. Scale bar is 200 μm. b. Screen printed silver/silver chloride IDE biosensors fabricated on a glass slide by Mansor et. al. Electrodes are 400 μm wide with gap widths of 300 μm, 400 μm, and 500 μm. c. Zinc oxide IDE on silicon substrates fabricated using conventional photolithography and etching techniques by Tasakaren et.al. Electrodes are approximately 200 μm apart and 16 μm wide.

Bioimpedance sensors are an active commercial area of research, as well. Several commercial systems for impedance-based biosensors exist; however, the cost is typically high, and the main one requires specific form factors for devices. ACEA Biosciences [248] produces several IDE-based systems (Figure 47) with "circle-on-line" electrodes of varying electrode gap widths from 10 μm to 100 nm. Their system is essentially a form-specific impedance sensor with a special software that converts impedance measurements to other useful metrics (cell index, beat period, etc.). Their system is label-free, has high sensitivity, and allows for cells to be followed in real time; however, the culture plates are not reusable, have transparency issues, are restricted to a fixed form factor and are expensive. The approximate cost of their basic system is $200,000 with the microsensor plates (Figure 47) costing $70 or more each, depending on the electrode gap width and other features.
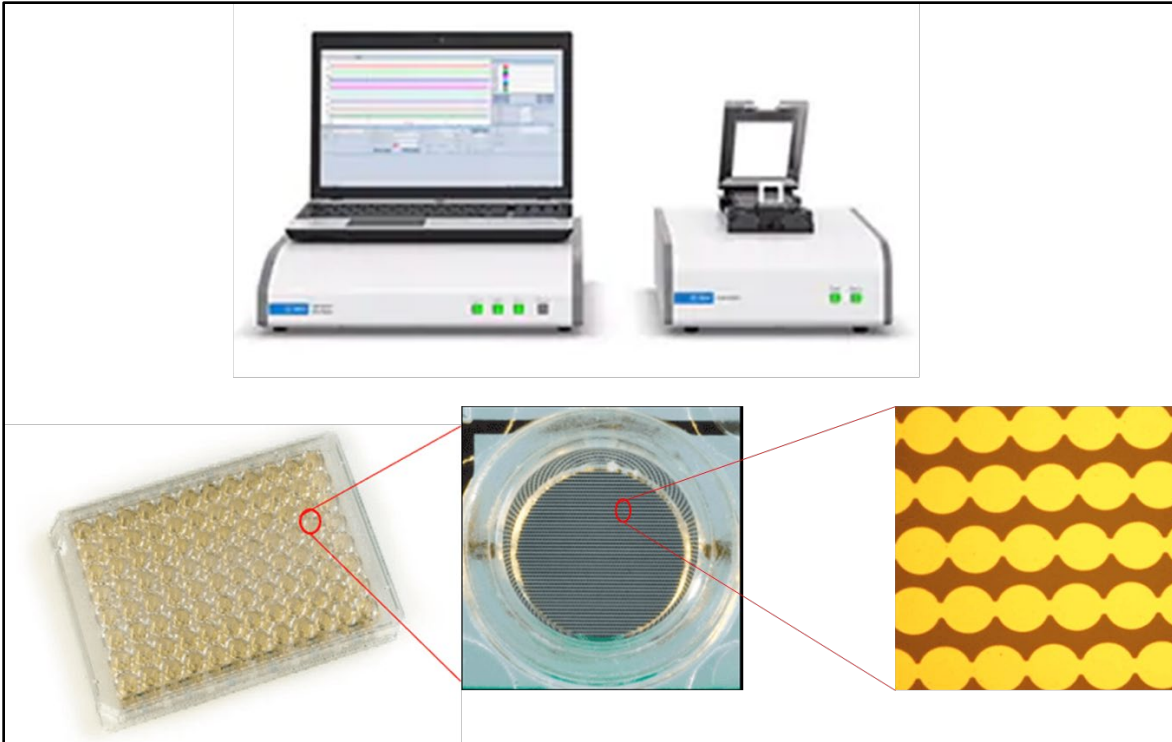
Figure 47 Top: One of ACEA Biosciences current systems. This system is designed specifically for cardiac cells and is featured in many of the cited papers within this chapter. Bottom: An example of one of the specially designed well plates required for using ACEA's systems.

Here a new impedance-based sensor that allows for long term *in vitro* cellular analysis with high fidelity is presented. IDEs are placed atop a nanostructured polyacrylonitrile (PAN) substrate, whose geometry is designed to maximize the interaction with the electrodes and cells. As a result, the device is fashioned as nanostructured Interdigitated Electrodes (nIDEs). Both the IDE and the nanostructured PAN substrate are fabricated utilizing the "Rapid Micro/Nanofabrication Approaches" presented in the previous chapters in this dissertation. This results in cost effectiveness, rapid translation from design to a fabricated device, utilization of direct write techniques, and the ability to reduce drug candidate testing times by an order of magnitude or more with dramatically increased sensitivity despite coarser geometries.

Theoretical Background

Here, some basic theory behind impedance and plasmonics is presented.
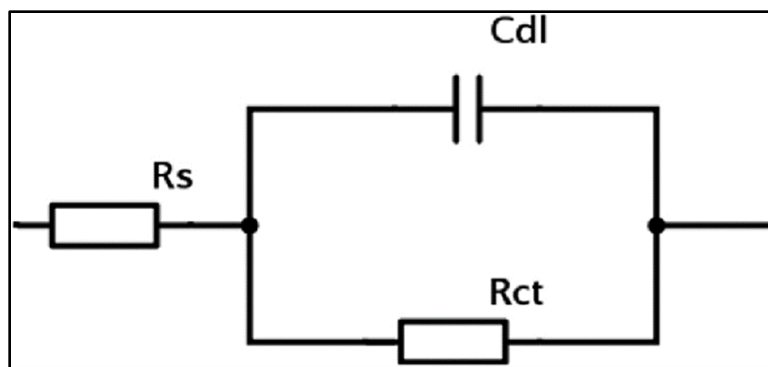
Figure 48 Simplified Randles circuit.

Impedance Theory

Impedance is the opposition of the flow of alternating current in a complex system when a voltage is applied. Impedance is essentially the representation of resistance in an AC system. Instead of just having a magnitude, it becomes complex and is comprised of both a magnitude and a phase, i.e. real and imaginary parts [239]. In biosensor research, we measure impedance by using electrochemical impedance spectroscopy (EIS). EIS allows for the study of the interface between an electrode and an electrolyte, which is typically cellular medium in the case of this type of research.

The simplest, but also most reasonable representation of EIS for the applications presented within this dissertation, is the simplified Randles' equivalent circuit [249-251]. This circuit, pictured in Figure 48, is comprised of three components: (1) a solution resistance (R_s), (2) a charge transfer resistance (R_{ct}), and (3) a double-layer capacitance (R_{dl}). The solution resistance is simply the resistance of the electrolyte. The charge transfer resistance is the resistance against the process of electron transfer from one phase to another, in this case between the electrode and electrolyte. Finally, the double-layer capacitance refers to the polarization of ionic charge at the surface of electrodes in EIS systems. The capacitance here is directly related to the electrode surface area

104

and the size of the ions. The double-layer capacitance increases with increased electrode surface area. The complex impedance of a simplified Randles' circuit is given in Equation 1 [249].

$$Z(\omega) = R_s + \frac{R_{ct}}{1 + R_{ct}C_{dl}i\omega} \tag{1}$$

The complex impedance can be further separated into its real and imaginary parts given by Equation 2 and Equation 3, respectively [249].

$$Z_{Re} = R_s + \frac{R_{ct}}{1 + \omega^2 R_{ct}^2 C_{dl}^2} \tag{2}$$

$$Z_{Im} = \frac{-i\omega C_{dl} R_{ct}^2}{1 + \omega^2 R_{ct}^2 C_{dl}^2} \tag{3}$$

When cells are cultured on the IDEs, they are added to culture dishes in suspension. At this point, the cells are spherical in shape. As the cells begin to reach the substrate, attachment sites begin to form, and the cells gradually transform from spherical to a flattened shape and the morphology becomes "spread out". This process generally takes two to four hours for most cultured cells [251]. The individual cells maintain this morphology until they divide, at which time they once again become rounded, furrow, and divide forming two cells. These two cells, termed daughter cells, spread out until another division occurs and the process continues. All these processes impact the double layer capacitance of the IDEs and hence changes to the impedance are observed.

Plasmonic Theory

Plasmonics is comprised of the science and applications of noble metal structures that can guide and manipulate visible light at the nanoscale. The optical properties of metals are partially determined by the resonant interaction between light and their surface free electrons at a metal-dielectric interface [252]. These longitudinal surface change density waves of conduction

electrons coupled to light are called surface plasmon polaritons (SPPs). To excite SPPs on a surface using light, additional momentum must be provided either by patterning a grating structure on the film or by evanescent coupling of light into the metal. Resonant excitations of these optical fields, also called surface plasmon resonances (SPRs), are sensitive to the dielectric materials that are in contact with the metallic surface [253]. SPRs in the visible/ near-infrared wavelength range are of interest because there is favorable optical confinement at these wavelengths [253].

Nanohole arrays exhibit peculiar and complex optical properties due to the presence of both localized and propagating plasmons, as well as their interacting effects [254]. The extinction spectrum of nanoholes in thin films contains one peak, called a transmission minimum, that corresponds to the grating-coupling SPR for the bonding mode [254]. Transmission of normally incident light through nanohole arrays is enhanced at the wavelengths that satisfy the SPR conditions given by [252, 255]:

$$\lambda_{SP}(i,j) = \frac{P}{\sqrt{i^2+j^2}} \sqrt{\frac{\varepsilon_{Au}\varepsilon_d}{\varepsilon_{Au}+\varepsilon_d}} \tag{4}$$

Here, P is the periodicity of the nanohole array, i and j are integers, ε_{Au} is the permittivity of gold (or whatever metal is used), and ε_d is the permittivity of the substrate adjacent to the metal. Effective coupling of light energy by designing nanohole arrays as per Equation 4 and defining metal layers of precise thickness can elicit a plasmonic signature in IDEs which has been extensively studied in this chapter for cell-based biosensing applications.

<u>Materials and Methods</u>

This section contains the materials and methods used throughout this chapter.
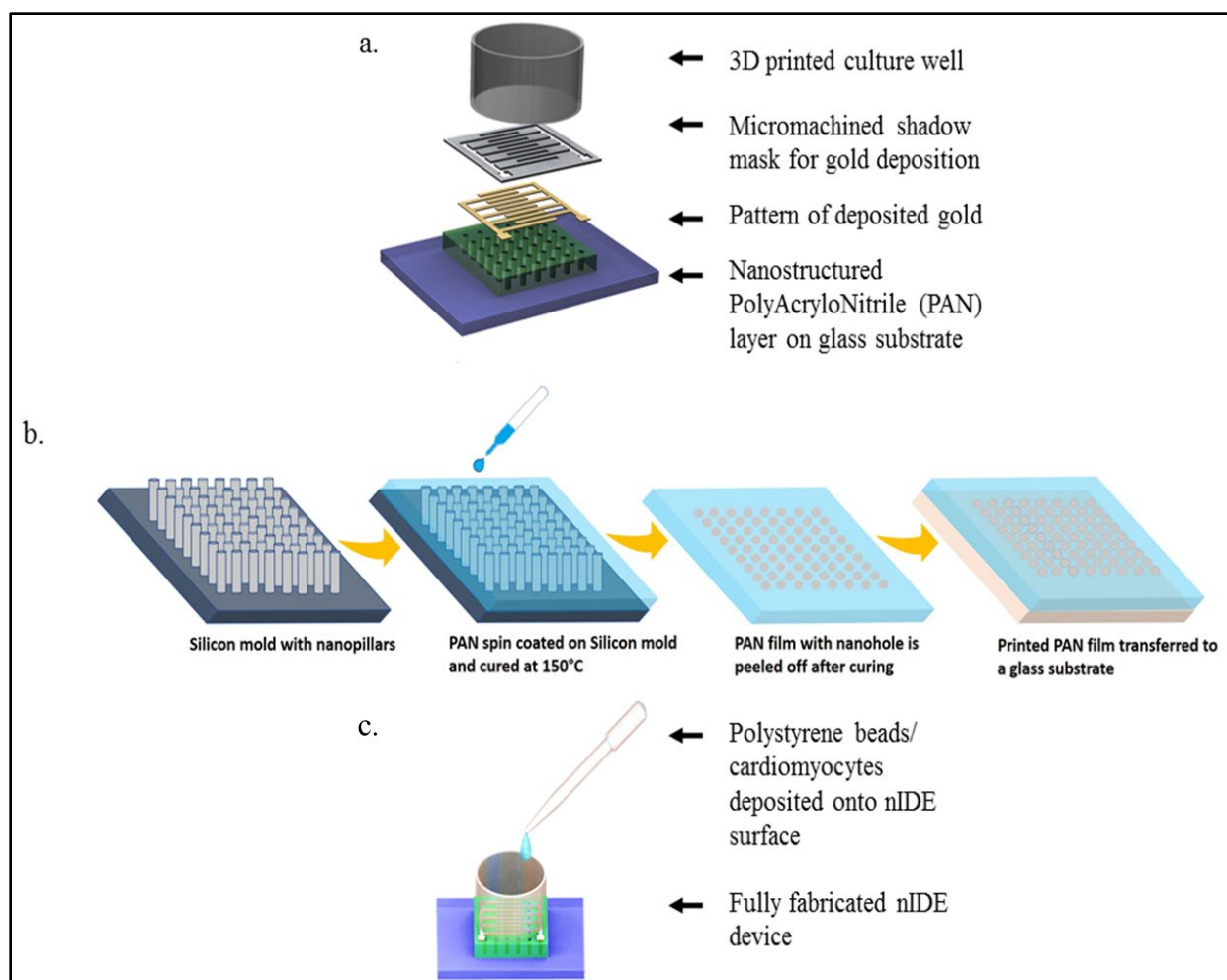
Figure 49 a. Schematic of nIDE device: A nanostructured polyacrylonitrile (PAN) layer is affixed to a glass substrate. A gold Interdigitated Electrode (IDE) structure is then patterned on top using a shadow mask. Finally, a 3D printed culture well coated with PDMS is attached to enable the IDE to be used with biological specimens. b. Process flow for spin-on nanoimprinting (SNAP) fabrication of PAN nanostructures. c. Fully assembled device being plated with polystyrene beads/ cardiomyocytes.

Design of the nIDEs/pIDEs

SolidWorks (Dassault Systems, Waltham, MA, USA) was used to design the interdigitated electrodes and the culture wells. A schematic of the nIDE device and its components are depicted in Figure 49a-c. The gold IDEs are designed to be 800 μm wide and 1 mm long with a pitch of either 1 mm, 250 μm, 100 μm, 64 μm, 10 μm, or 7 μm and a thickness of 30 nm, which gives a peak resonance wavelength between 620 nm and 750 nm [256]. The resonance peak red shifts as the thickness of the gold increases. At times, there were issues with the e-beam shutter that led to

some thickness variation. Additionally, the Thermionics e-gun power supply and controller were upgraded which seemed to consistently deposit a thickness to approximately 50 nm on the devices. The nanostructured chip is comprised of a 5 mm by 5 mm nanomachined PAN layer of 10 μm thickness with 50 nm nanoholes with a pitch of 200 nm. The fully assembled chip is designed to be 10 mm by 10 mm.

The pitch of the electrodes was varied for each experiment. Initially, we focused on 1 mm IDEs as our tool optimized to fabricate shadow masks at the time was the micromill which was not optimized for micrometer feature sizes in 2018. As a result, the shadow masking was switched to the laser micromachining tool. After optimizing the laser micromachining tool discussed in Chapter 2, we were able to fabricate a much wider variety of shadow mask pitches, so the natural progression of sizes came from starting at 1 mm and halving the value in succession. This led to the use of the 250 μm, 64 μm, and 7 μm pitched electrodes. From these results, we were able to determine that relating sizes by a factor of 10 would allow for more straightforward hypothesis formation and result comparison. This led to the use of 1 mm, 100 μm, and 10 μm pitched electrodes.

Fabrication of the Nanostructured Substrates

The PAN nanostructures and planar PAN substrates used in this work were fabricated by Kowsik Sambath Kumar in Dr. Jayan Thomas' Laboratory.

Typical methods for the fabrication of nanostructures include methods like photolithography [257], e-beam lithography [258], and focused ion beam lithography [259]. Even though these methods offer high quality nanostructures, they involve tedious procedures, long processing time, limited scalability, and high cost. To achieve scalability, bottom-up approaches like self-assembly have been used, but they are limited to select materials, and pattern versatility

cannot be easily achieved using this approach. Sacrificial anodic aluminum oxide (AAO) templates for developing nanostructures are also widely used [260] for fabricating nanostructures; however, the sacrificial nature of AAO and the required use of strong chemical etchants places a serious limitation on this method. Several unconventional lithographic methods have been developed to circumvent the limitations posed by conventional lithographic techniques. Among these techniques, nanoimprinting lithography (NIL) [261] has attracted considerable attention. In NIL technique, many nanostructures can be replicated using an inexpensive NIL machine from a master mold. The feature size depends on the mold used to print the nanostructures. These nanostructures, pictured in Figure 50, can subsequently be used as substrates for various applications, including interdigitated electrodes.
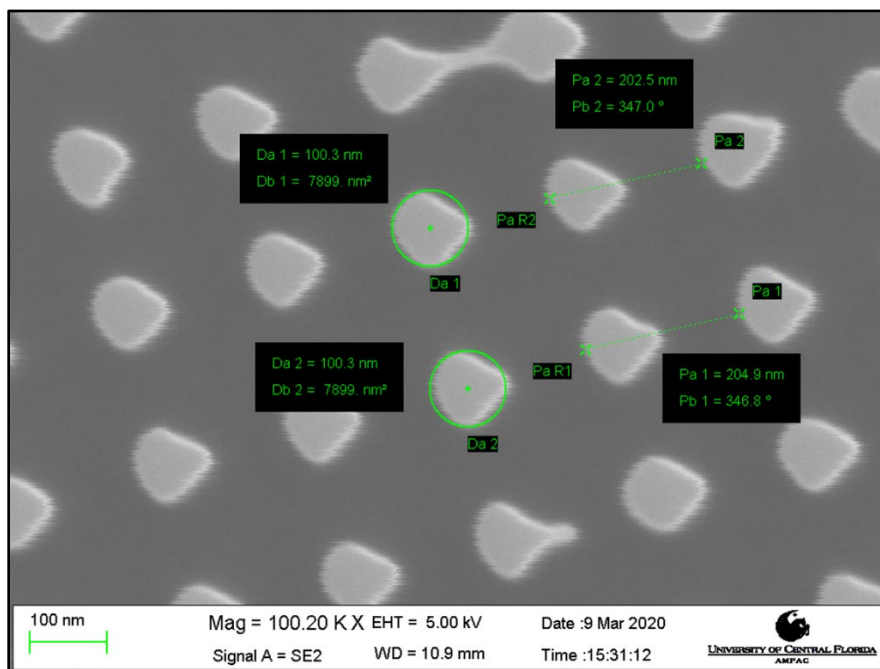
Figure 50 SEM of the mold used to fabricate the nanostructures.

Recently, the Thomas group developed a spin-on nanoimprinting process (SNAP), shown in Figure 49b, to make nanostructures rapidly [262-264]. A polymer solution is prepared by dissolving 8 wt.% of polyacrylonitrile (PAN, M_w=150,000) in dimethylformamide and heated at

150 °C for 5 minutes. The PAN solution was then cooled and spin-coated on a pre-made Si mold with the inverse of the pattern to be printed. The PAN film was subsequently peeled-off from the mold, transferred to a glass substrate, and cured at 250°C. SNAP technique does not need high temperature, pressure, or any other force during the printing process. We have successfully developed nanoholes as small as 50 nm on PAN films to make IDEs. The silicon mold fabrication is a one-time event and several 100s of nanostructures can be printed using the SNAP process from the same master mold without any degradation [263].

Investigation of the Uniformity of the E-beam

Since thickness of the metal film deposited onto the nanostructured substrate is a key factor in the device's plasmonic performance, it was decided to investigate the uniformity of the e-beam deposition. Standard sized microscope cover slips (22 mm x 22 mm x 1 mm) from Fisher Scientific were placed on the 14 cm diameter sample holder to entirely cover the holder. A 30 nm gold metal film as indicated by the quartz crystal monitor on the system was deposited onto the glass cover slips using electron beam evaporation (Thermionics, Hayward, CA). Kapton® tape was affixed to the center of each slide to create a step for thickness measurement. Thickness of the deposited metal was measured using a Dektak3 surface profilometer (Veeco, Plainview, NY).

Fabrication of the nIDEs/pIDEs

The initial 1 mm pitch IDE shadow masks were fabricated using the IDE designs by micromilling. A 90-degree T-8 Mill Tool (150 µm - 250 µm diameter; T-Tech, Peachtree Corners, GA, USA) was spun at 55,000 rpm in a T-Tech J5 Quick Circuit Prototyping Systems to micromill through an 80 µm thick stainless-steel sheet (Trinity Brand Industries, Countryside, Il, USA).

All subsequent shadow masks were fabricated on 12.5 µm Kapton® (DuPont, Wilmington, DE) using 355 nm UV light at 50 Hz from a multimodal laser micromachining tool (QuikLaze

50ST2, New Wave Research, Portland, OR). Masks were fabricated using two passes: the first to cut through the Kapton®, and the second to ensure that the shadow mask had smooth edges.

The shadow masks were affixed to the 5 mm by 5 mm squares of nanomachined PAN atop a glass carrier substrate using Kapton® tape. A metal film comprising of 30 nm to 50 nm of gold (depending on whether the new or old e-beam system was used) was deposited onto the nanostructured PAN/glass substrate (Figure 49a) using electron beam evaporation (Thermionics Laboratory Inc., Hayward, California, USA) to metallize the interdigitated electrodes. The shadow mask was released carefully after the metallization step to reduce the damage to the underlying nanostructures.

Initially, to package the nIDE device, a 3D printed (Form2, FormLabs, Somerville, MA, USA) culture well (10 mm inner diameter, 10 mm tall) was dip coated with polydimethylsiloxane (PDMS) in its entirety to improve biocompatibility of the printed resin material [265], and attached to the substrate using biocompatible 353ND epoxy (Epotek, Billerica, MA, USA) [266]. After determining that post-printing treatments could improve the biocompatibility of the 3D printer resin, culture wells were subsequently fabricated out of FormLabs High Temperature Resin (FLHTAM01) (FormLabs, Somerville, MA) and 3D printed in an Asiga MAX UV27 DLP (digital light processing) printer (Asiga, Sydney, Australia). After printing these culture wells were rinsed with IPA for 6 minutes, then UV cured for 6 minutes, and autoclaved for one hour. These culture wells were subsequently affixed on to the PAN/glass substrates using biocompatible 353ND epoxy (Epoxy Technology, Billerica, MA).

Lead wires of sanded copper were subsequently attached to the contact pads using an E2101 electrically conductive silver epoxy (Epotek, Billerica, MA, USA). The silver epoxy was then covered with 353ND epoxy to ensure that the wires remained attached for the entire culture.

Polystyrene Bead Assay

Prior to the cardiomyocyte assay, polystyrene (PS) latex beads of 1.1 μm particle size and concentration of 0.1 mg/ml in De-Ionized (DI) water (Sigma Aldrich, St. Louis, MO, USA) were used to emulate a cell-like material (Figure 49c). The aqueous suspension of PS latex beads was diluted with DI water in a ratio of 1:10 and the diluted solution was uploaded into a syringe and transferred to the culture well of the IDE device. The impedance measurements, using a frequency sweep from 10 Hz to 10 MHz, were performed on an IDE fabricated on a PAN nanomachined layer with a nanohole diameter of 50 nm and a pitch of 200 nm using a BODE Impedance Analyzer (Omicron Labs, Klaus, Austria). The reported impedance values are an average of two devices (N=2).

Cell Culture

The protocols for the different cell cultures used in this chapter are described in this section.

iCell Cardiomyocytes

Human induced pluripotent stem cell (iPSC) differentiated cardiomyocytes (iCell Cardiomyocytes[2], Cellular Dynamics, Madison, WI, USA) were used for cell studies. The iPSC cardiomyocytes were kept frozen in liquid nitrogen until they were cultured according to the manufacturer's directions. To ensure that the cells adhere to the surface, the IDE devices were coated with 5 μL of 1:20 fibronectin (Sigma Aldrich, St. Louis, MO, USA) and Dulbecco's Phosphate-Buffered Saline (DPBS) without Calcium and Magnesium (Gibco, Waltham, MA, USA) solution and placed in an incubator (37°C with 5% CO_2) for one hour. Cells were thawed and counted to determine the density. This task was performed by mixing 100 μL of cells suspended in media with 0.4% Trypan Blue (Fisher Scientific, Waltham, MA, USA). A droplet of 100 μL of this solution was subsequently applied to a glass hemocytometer and placed under a

10X microscope objective of a Nikon TE200 Inverted Fluorescence Microscope (Nikon, Tokyo, Japan) for observations. Live, unstained cells were counted in each of four sets of sixteen squares. The cell counts from each of the four sets of squares was averaged and multiplied by 10,000 and then multiplied by 5 to correct for the 1:5 dilution from the Trypan Blue addition. The fibronectin was aspirated, and the thawed cells were plated onto the nIDE surfaces (N=8) and two 6-well plates (control Polystyrene Plates from Corning Inc., Corning, NY, USA) and incubated for one hour (at 37°C with 7% CO_2). A measured droplet of 300 µL of iCell Cardiomyocytes maintenance medium (Cellular Dynamics, Madison, WI, USA) was subsequently added to each of the eight culture wells and the controls. Full media changes occurred every other day. Eight nIDE devices were densely plated with iCell cardiomyocytes with an average cell count of 310,500 cells per culture well. Each of the two 6-well plates (controls, N=12 wells) were plated with an average cell count of 50,000 cells per well for the experiment that used these cells.

iCell Retinal Pigment Epithelial Cells

IDEs and nIDEs were prepared for cell culture by coating with 5 µL of 1:20 fibronectin (Sigma Aldrich, St. Louis, MO) and incubated for 1 hour. To thaw the cells 25 mL of medium were warmed to room temperature. From this solution, 8 mL of medium were transferred into a sterile 15 mL centrifuge tube. The cryovial containing the cells was thawed in a 37°C water bath for 3 minutes. The cells were then transferred to the centrifuge tube containing the 8 mL of medium and the cryovial was rinsed with 1 mL of medium, which was then also transferred to the centrifuge tube. The cells were centrifuged at 300 x g (~1,000 rpm) for 5 minutes. The supernatant is aspirated and discarded. The cells were then resuspended by adding 2 mL of medium to the centrifuge tube and gently mixing with the pipettor. A selected quantity of 50,000 cells were cultured onto each device. Media was exchanged every 2 days.

HL-1 Cells

HL-1 cells were passaged from T75 flasks and resuspended according to the protocol in Chapter 3. A selected quantity of 50,000 cells were seeded onto each IDE device and medium was exchanged daily.

Biocompatibility Assay

After one day *in vitro* (DIV01), nanostructured PAN was placed in the 6-well plate that was plated with approximately 50,000 cardiomyocytes. Biocompatibility studies were performed in the 6-well plates at DIV07 (days *in vitro*) to ensure that the nanostructured PAN surface was suitably compatible with the iCell cardiomyocyte cell line. This study was performed using the Promega Cell-Titer Glo Luminescent Cell Viability Assay Kit (Promega, Waltham, MA, USA). A volume of reagent measuring 0.5 mL, was added to each culture well and mixed for two minutes to induce lysis. The 6-well plate was incubated at room temperature for ten minutes to stabilize the subsequent measurement of a luminescent signal. Luminescence was recorded using a Tecan Infinite Pro 200 plate reader (Tecan, Männedorf, Switzerland) with the emission wavelength set at 500 nm, the excitation wavelength set at 365 nm, and an integration time of 10 seconds. The background and control measurements with only media in the culture well and media with cells in the culture well, respectively, were performed in addition to the nanopatterned PAN measurements.

Impedance Measurements

Electric cell-substrate impedance sensing (ECIS) was used to characterize the electrochemical properties of the cell-substrate interface. A low-voltage signal is applied to the nIDEs, which forms ionic currents in the cell culture medium. When cells are located on the nIDEs, these ionic currents are affected by the number, morphology, and adhesion of these cells [18].

Impedance will gradually increase during the normal cell growth and proliferation process; thus, as more cells become attached to the nIDEs, an increase in electrical impedance is expected.

For the impedance measurement, a full spectrum of the frequency range from 10 Hz to 10 MHz, with an AC voltage perturbation of 20 mV, were scanned using BODE 100 impedance measurement station (Omicron Labs, Klaus, Austria) Figure 51a. Impedance was normalized using the cell index (CI) calculation [20, 239], which is represented in Equation 5, where ΔZ is the change in real part of impedance from day to day and Z_o is the background impedance on the nIDE.

$$CI = \Delta Z / Z_o \tag{5}$$

Since drug-induced cardiotoxicity is of great interest with these biosensors, impedance measurements were additionally performed on the nIDEs with cultured iPSC cardiomyocytes utilizing different concentrations of norepinephrine (Sigma Aldrich, St. Louis, MO, USA) as a model drug compound. Concentrations of norepinephrine ranging from 0 μM to 250 μM were introduced to the culture well and impedance was measured to detect any changes due to the addition of the model drug. Cell index results from the model drug experiments were further normalized by using the percent cell index (%CI) [20, 239], represented in Equation 6, where CI_o is the cell index with no norepinephrine and CI_c is the cell index for a specific concentration of norepinephrine.

$$\%CI = CI_c \,/\, CI_o \times 100 \tag{6}$$

Normalization of cell index calculations is an established calculation for such assays with IDE based approaches and this task was performed to compare our approach with others in this space.
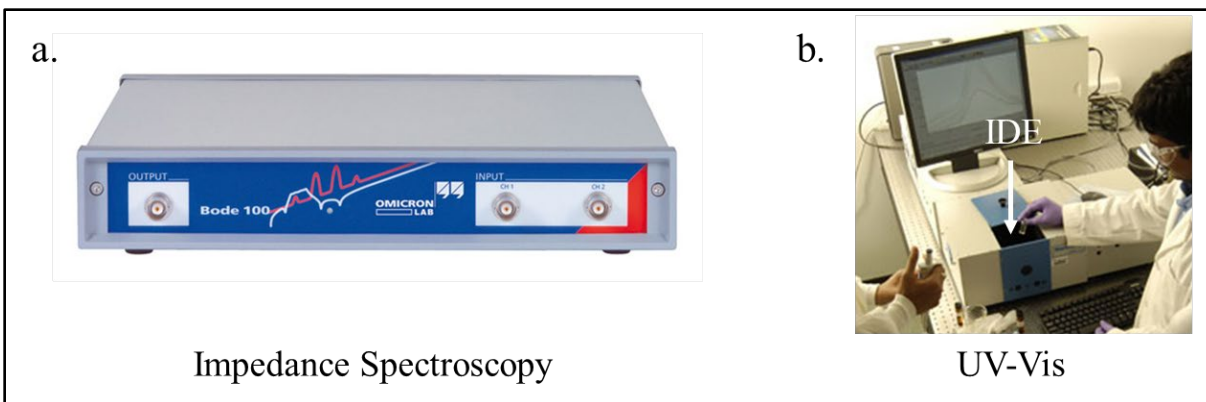
Figure 51 a. Bode 100 impedance sensor schematic. The IDE device is attached via alligator clips to the output and channel 2 to allow for a series through impedance measurement. b. Agilent Cary 300 UV-Vis spectrometer used for plasmonic peak measurements. Device is attached to a pinhole card and placed inside the chamber to determine peak. The pinhole is shifted to multiple locations to allow for more comprehensive characterization.

UV-Vis Measurements

UV-Vis spectroscopy measurements were performed using an Agilent Cary 300 (Agilent, Santa Clara, CA) UV-Vis Spectrometer (Figure 51b). Absorbance spectra of IDEs and nIDEs both with and without cells were measured using a solid sample pinhole card positioned over one of the gold electrodes. A planar PAN substrate on glass was used as the reference. Scans were performed with a spectral bandwidth of 300 nm to 850 nm with an averaging time of 0.1 seconds (standard for the program). Each scan was performed three times (N=3 measurements) and data was averaged for presentation.

Light and Dark Impedance Measurements

Dark impedance measurements were performed in a completely dark room, apart from the light from a fully dimmed laptop screen needed to perform the measurements. Light impedance measurements were performed in a normally lit lab with fluorescent lighting. Laser impedance measurements were performed in a completely dark room, except for the dimmed laptop screen and the focused laser light. Laser wavelengths used included 450 nm blue, 532 nm green, 625 nm red (all manufactured by Beam of Light Technologies, Clackamas, OR), and 650 nm red (OnPoint

Lasers Ltd., Minneapolis, MN). All impedance settings used follow those provided in the prior section.

<u>Imaging</u>

Images of the nIDEs were obtained with both a Nikon TS2 inverted microscope (Nikon, Tokyo, Japan) and a Keyence BZ-X800 All-in-One Confocal Microscope (Keyence, Tokyo, Japan). Imaging of the nanostructures was performed using a Zeiss Ultra-55 FEG SEM (Oberkochen, Germany) and an Anasys NanoIR AFM (Bruker, Billerica, MA). Live/Dead fluorescence imaging was also performed using the Keyence BZ-X800 All-in-One Confocal Microscope with the GFP and Texas Red filters. Cells were fluorescently stained using an Invitrogen Live/Dead Cell Imaging Kit (Invitrogen, Carlsbad, CA) and allowed to incubate in the dark at room temperature. Following this incubation time, the fluorescent stains were aspirated, and the cells were immediately imaged.

<div align="center">

Results and Discussion
</div>

This section presents the results and discussion from a series of nIDE/pIDE experiments that build on one another.

<u>1 mm nIDE vs. IDE</u>

To ensure that the suitable thickness of gold was consistently deposited on the nanostructured substrates due to the sensitivity of the SPR generation to thickness of the gold, we performed a test of the consistency of the electron beam deposition. Figure 52 shows the results of this test. The center of the sample plate gives the desired thickness of 30 nm, while a deviation from the desired thickness is seen in the outer areas of the sample plate. The thickness of gold deposited ranged from 30 nm in the center from ~22-23 nm at the outer edges of the sample holder.
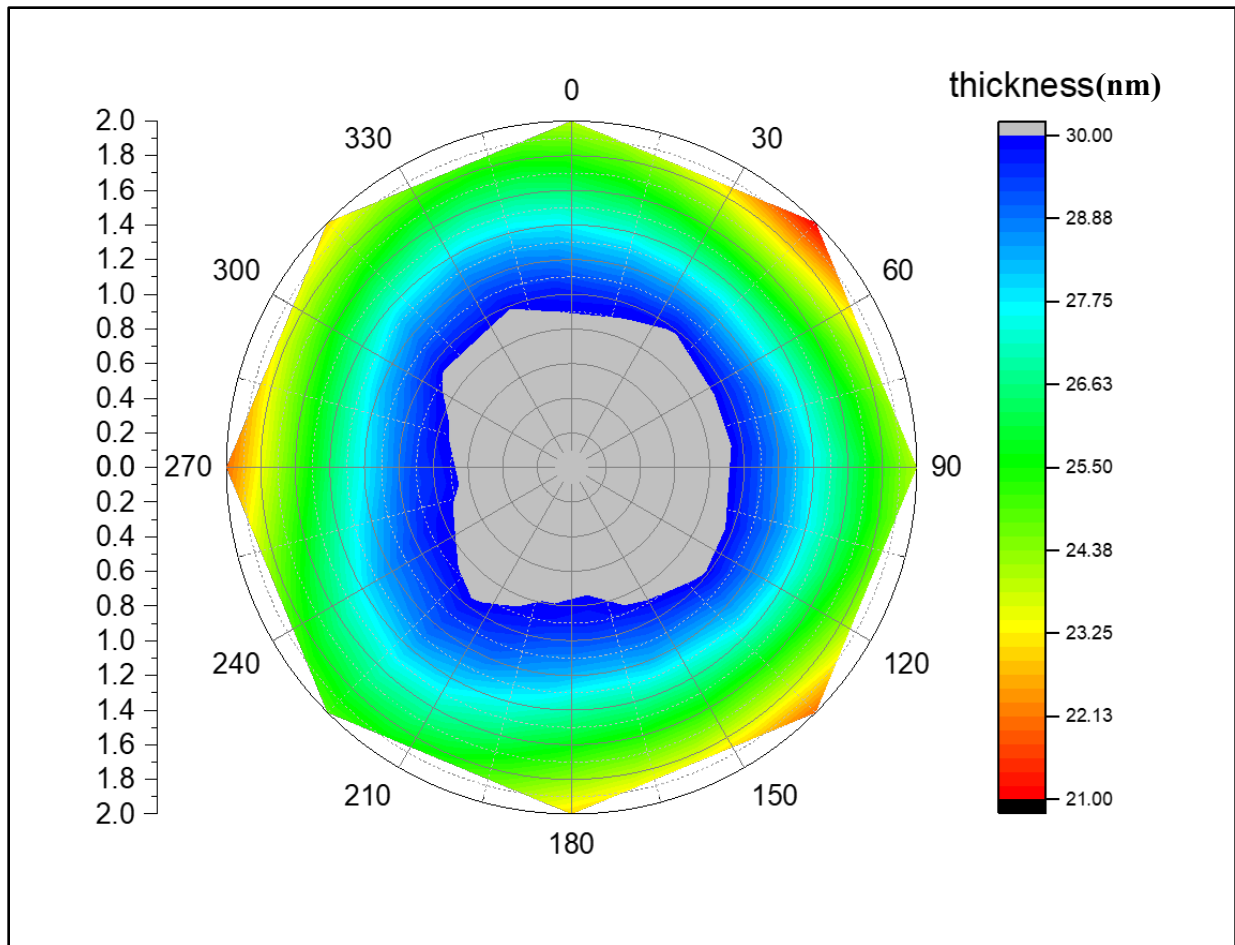
Figure 52 Measured thickness of metalized glass cover slides with steps. The middle of the substrate holder gives the desired thickness, while the outer half gives slightly thinner samples with thicknesses ranging from 20 nm to 26 nm.

Nanostructured IDEs (nIDEs) were successfully fabricated on the nanostructured PAN substrates. The nanostructures on the PAN substrate remained defined after the deposition of the gold IDE structure, as shown in Figure 53a. These SEM micrographs clearly depict the nanostructured PAN with repeatable "nanoholes" of approximately 50 nm in diameter and the mm-scale gold electrodes defined on top of these "nanoholes". The gold IDE structures measured within 99.37% of the designed dimensions representing an excellent translation from design. Fully assembled devices, as shown in Figure 53b, remained intact throughout the entire life cycle of the cardiomyocytes (DIV18).

Human iPSC cardiomyocytes were successfully cultured onto the nIDEs as depicted in a sample image in Figure 53c. One can clearly observe a mat of cells on top of the IDEs in the images collected with transmitted light microscopy. The cell viability assay confirmed that the nanostructured PAN substrate was cytocompatible for cell culture with iCell Cardiomyocytes[2]. The other components of the nIDE (gold, PDMS, and 353ND epoxy), have previously been established to be cytocompatible with cardiomyocytes [265, 266]. Fluorescence levels were well above the background fluorescence, which indicates that most of the cultured cells were viable, as shown in Figure 53d. Quantitatively, the nanostructured PAN and control wells (N=6 for both types), both showed a fluorescence of nearly 40,000 RFU with a low standard deviation of approximately 3000 RFU, which depicts excellent cytocompatibility performance (97.01% ± 2.15% of the control) with iCell Cardiomyocytes[2].
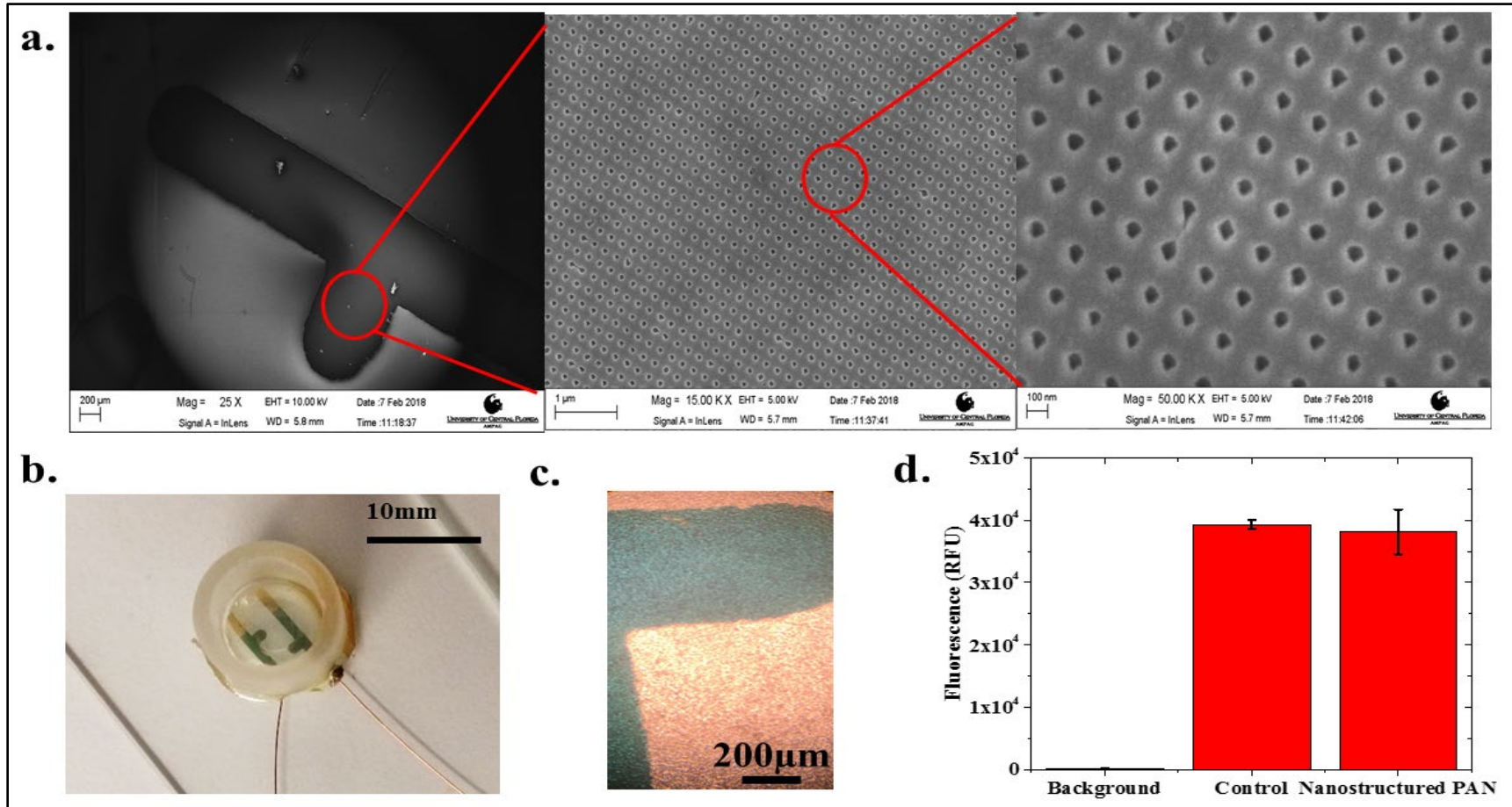
Figure 53 a. SEM image of electrodes deposited on top of the nanostructured PAN layer with zoomed in SEM images of the printed 50 nm PAN nanohole structures. Scales from left to right are 250 μm, 1 μm, and 180 nm, respectively. b. Completed nIDE device with culture well and wires attached. c. Human iPSC Cardiomyocytes cultured on 1 mm pitch nIDE at DIV01. The cardiomyocytes completely cover the surface of the IDE. d. Biocompatibility assay results - The nanostructured PAN substrate shows similar (97.01% ± 2.15%) biocompatibility (N=6) to control samples comprised of just cells in a 6-well plate.
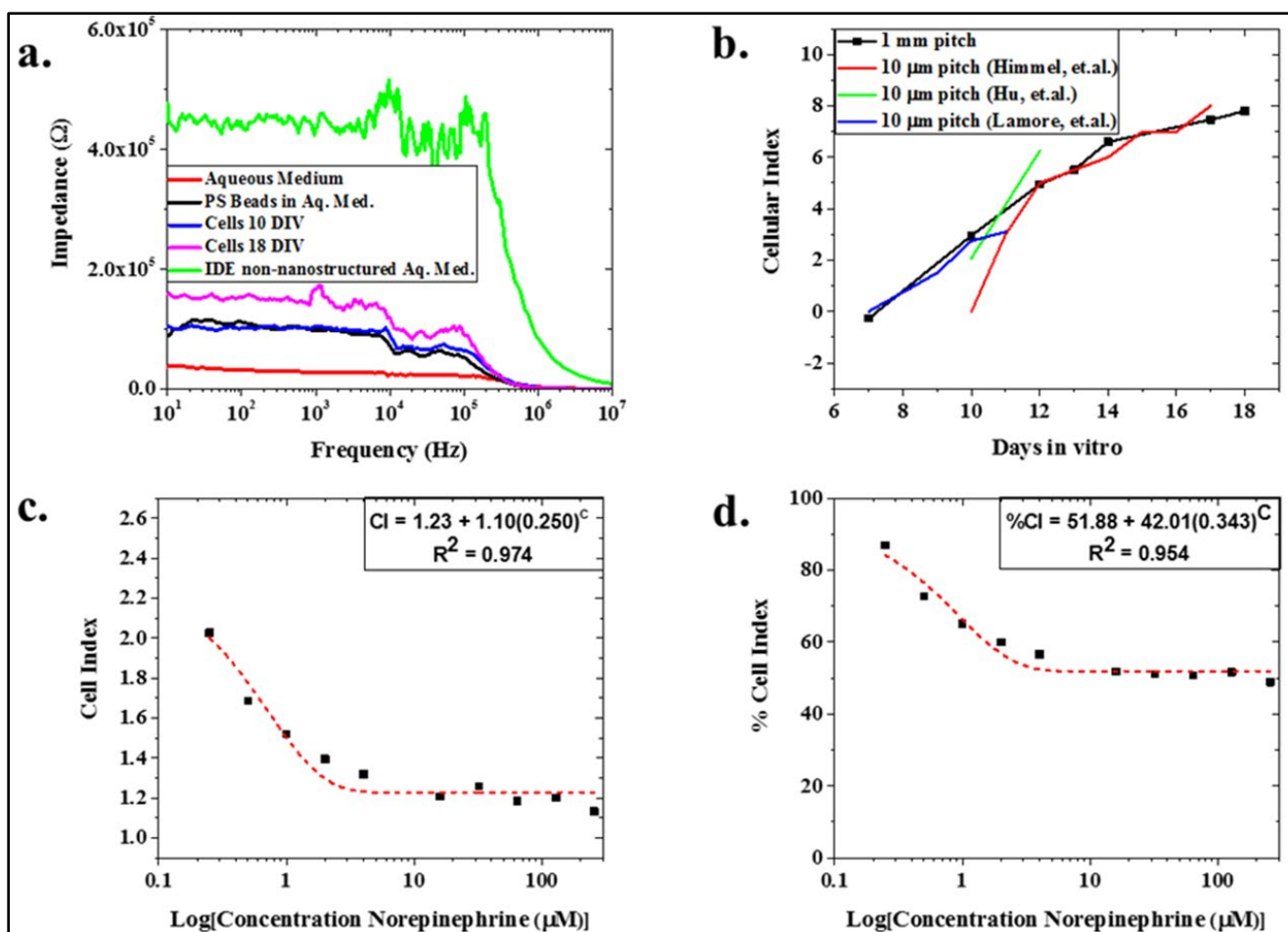
Figure 54 a. Representative full spectrum impedance measurements - The nIDEs with cardiomyocytes cultured on them show an increased impedance from the nIDEs that only have an aqueous medium. In addition, as the cells proliferate an increase in impedance is observed. b. Variation of the Cellular Index (CI) of the cells cultured on the nIDEs for 18 days: it was observed that the CI of the nIDEs increased over time as expected because the cell coverage of the nIDE increases over time. The calculated mean value of N=8 wells of nIDEs is represented by the square bullet point. A comparison to the data from Himmel et. al. tracks the CI changes observed in our assay. Since our IDE pitch is 100X the pitch demonstrated by the IDE from Himmel, we believe the presence of the nanostructures result in improvement in device sensitivity. c. CI and d. %CI for norepinephrine experiment: Mean values for N=6 is depicted with a square bullet point. The CI and %CI both show an exponential decrease, with excellent fits given by their R^2 values of 0.974 and 0.954, respectively, as the concentration of norepinephrine increases because the cells are dying due to the dosage of the drug. This causes a departure from the impedance of the nIDE with no norepinephrine added.

Figure 54a depicts an example of the raw, full spectrum impedance data for polystyrene beads, iCell Cardiomyocytes[2] (average value of N=8 at two specific days: DIV10 and DIV18), and aqueous media clearly delineating the three analytes. Further, this figure shows that the impedance of the nIDEs with cells (110.19 kΩ at 1 kHz for DIV10 and 243.21 kΩ at 1kHz for DIV18) and polystyrene beads (96.53 kΩ at 1 kHz) were higher than the nIDE with just aqueous medium (27.37 kΩ at 1 kHz), which follows expected trends due to the modification of the ionic currents due to the presence of cells and the PS beads [14]. In addition, Figure 54a demonstrates a decrease in impedance from an IDE without a nanostructured substrate to that of the nanostructured IDE, both in aqueous media. Looking closely at the ECIS for the two sample DIV measurements (N=8), they demonstrated an increase in impedance as the days *in vitro* increased. The cell index also demonstrated an increase as the days *in vitro* increased (Figure 54b). This is an expected result as reported by Himmel, et. al. The morphological changes in the cells leads to an increased impedance as the cell coverage increases; and the cell coverage will inherently increase as the cells grow over time [14, 267]. This result held until the assay was terminated at DIV18. To our knowledge, we are the first to report this result with 1 mm pitch nIDEs over a period of 18 days with human cardiomyocytes and a similar trend using a commercial system with 10 µm pitch IDEs on a glass substrate fabricated with a complex photolithographic technique involving several steps [267] is reported by Himmel, Hu et. al., and Lamore et. al. [14, 16, 268] Our devices are 100X larger than these three other studies but report similar CI increases from cell growth (CI=1.1 on DIV10 increasing to CI equal to approximately 7-8 on DIV17). It is believed the comparable performance is due to the nanoscale structure patterned onto the substrate of the nIDEs. As a result, we believe that the nIDE shows an increased sensitivity compared to commercial IDE systems, which have an electrode gap that is 100X smaller. It is believed that this increase in sensitivity is due to the

increased electrode surface area provided by the nanoholes. When surface area increases, capacitance increases; thus, impedance decreases giving greater sensitivity [92, 231, 243, 269], as shown in Equation 7, where C is the capacitance, ε_o is the vacuum permittivity, ε_r is the relative permittivity of the electrolyte, A is surface area of the electrode, d is electrode gap, and Z is impedance.

$$C = (\varepsilon_o \, \varepsilon_r \, A) / d \propto 1 / Z \tag{7}$$

The model drug experiment with norepinephrine showed a decrease in both cell index (from CI=2.34 at 0 µM of norepinephrine to CI=1.13 at 256 µM norepinephrine) (Figure 54c) and percent cell index (86.91% at 0 µM of norepinephrine to 48.88% at 256 µm norepinephrine) (Figure 49d) with increasing concentrations of norepinephrine (mean of N=7). Both the CI and %CI for norepinephrine addition demonstrate exponential behavior with excellent fits of 0.974 and 0.954, respectively. This is expected because as the cardiomyocytes are exposed to higher concentrations of norepinephrine, more cells are expected to die from the exposure [231]. As a result, there was less active cellular coverage, which lowers the impedance, CI, and %CI.
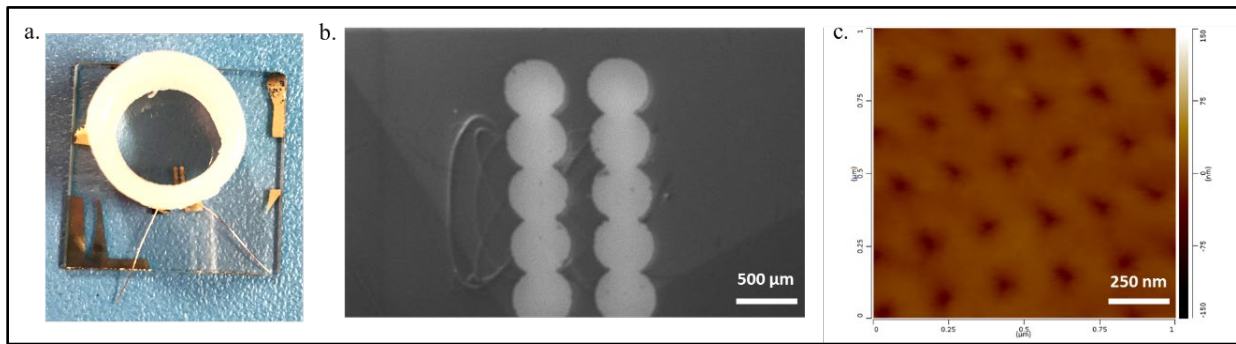
Figure 55 Fabricated device images: a. Fully packaged nIDE device with culture well and wires attached. b. SEM of gold IDEs on the nanostructured PAN substrate. c. AFM of an electrode. The nanoholes remain visible after gold deposition, which provides an increased electrode surface area.

<u>Plasmonic Resonance of the Nanostructured Substrate</u>

A fully packaged IDE with a culture well and wires attached is shown in Figure 55a. Figure 55b shows an SEM image of the gold electrodes on the nanostructured PAN surface and Figure 55c shows an AFM image of the electrode to show that the integrity of the nanostructures remains after repeated use of the mold. Impedance values measured at 1 kHz were converted to cell index (CI) and showed a trend of increasing CI and improved sensitivity for smaller gaps (Figure 56). Additionally, the CI of the IDEs on the nanostructured substrate was approximately 100-1000X greater than that of the IDEs on the non-nanostructured substrate. This indicates enhanced sensitivity due to the nanostructuring. UV-Vis measurements showed a 12 nm to 22 nm red-shift in the plasmonic peak of the devices with the addition of cells (Figure 57). Variation in peak intensity and shift can potentially be attributed to the thickness of gold, number of cells, and cell-nanostructure interactions demonstrating possibilities for cellular and sub-cellular manipulation. Figure 58 shows the retinal pigment epithelial cells growing on the 250 µm nanostructured IDE surface at DIV04. This expected growth helps confirm the biocompatibility of these PAN nanostructures for retinal pigment epithelial cells.
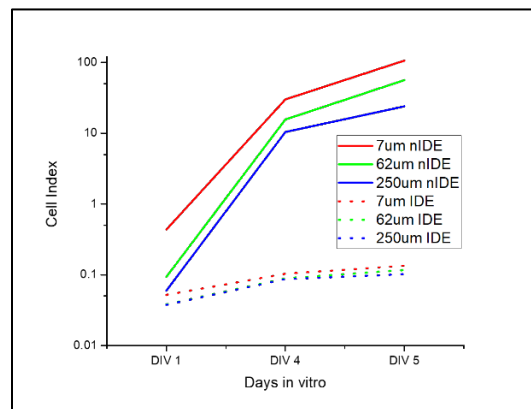
Figure 56 Average cellular index (CI=[Z$_o$-Z$_c$]/Z$_o$) for N=3 devices showing an increase in CI for nanostructured versus standard IDEs. CI is a tool for normalizing the impedance, as every device will not be identical. CI results follow the expected pattern of smaller electrode gaps having larger cellular indices. This indicates that smaller electrode gaps, as well as the presence of nanostructures allow for greater device sensitivity.
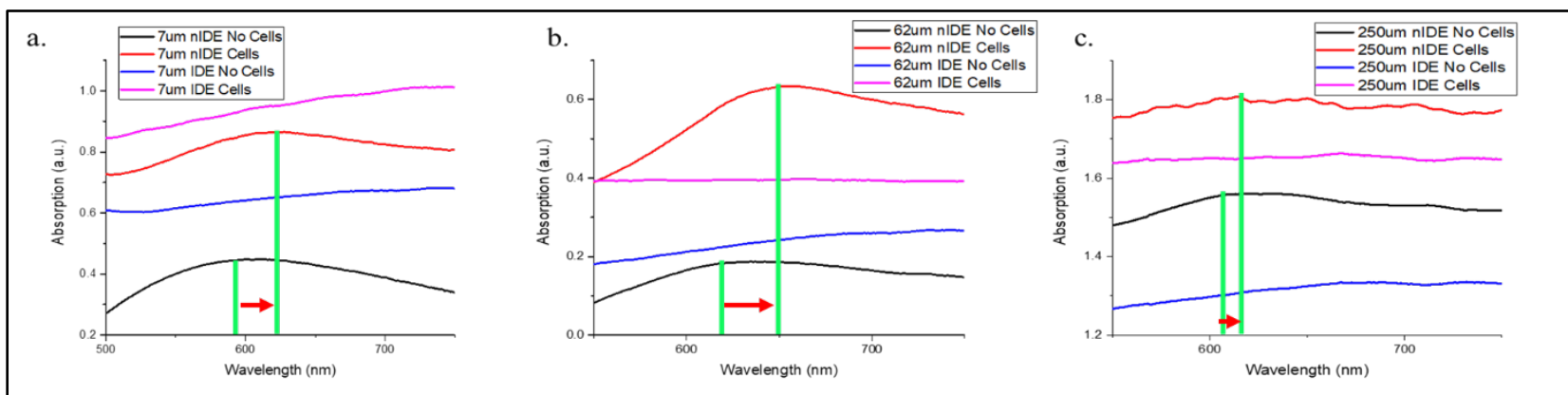
Figure 57 UV-Vis measurements for the devices. All nIDE devices show a red shift in the plasmonic peak, as indicated, with the addition of cells, as expected. The standard IDEs show no plasmonic peak. Variations in the plasmonic peaks are expected due to varying thickness the gold electrodes, as well as the cell-electrode interactions. a. 7 µm, b. 62 µm, and c. 250 µm electrode gap width
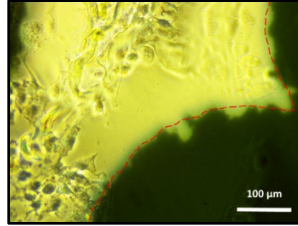
Figure 58 Human retinal pigment epithelial cells (DIV04) cultured onto a 250 μm electrode gap nanostructured IDE device. The cells grew on the devices, as expected, thus demonstrating good biocompatibility with the device materials.

Individual Contributions of Enhancement Modes

For the remainder of the experiments, HL-1 cells were used. They combine the quick mat-like growth of the retinal pigment epithelial cells with the electrophysiological characteristics of iCell cardiomyocytes. Figure 59a shows a schematic depicting the different enhancement modes that were hypothesized and studied, while Figure 59b shows HL-1 cells growing on an IDE at DIV03 showing typical mat-like growth. Impedance values were converted to CI (cellular index), which is a method to normalize impedance as we have discussed before in this chapter [90] and show a clear trend of increasing CI and improved sensitivity for smaller electrode gap widths or pitches.
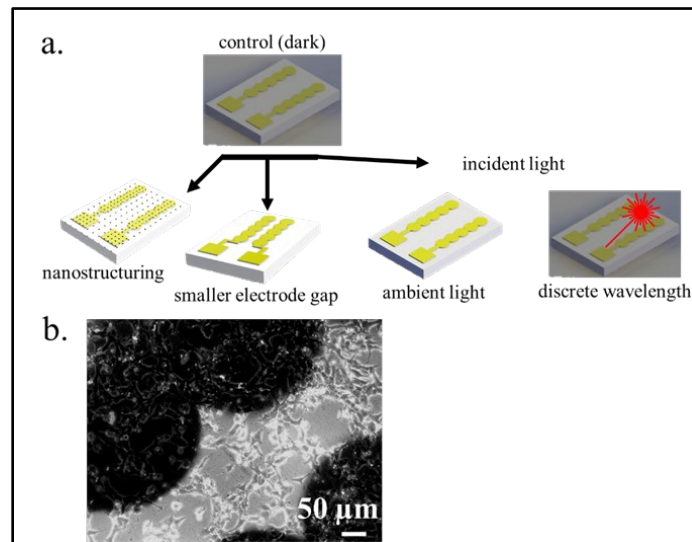
Figure 59 a. IDE sensitivity can be increased via nanostructuring of the substrate, designing smaller electrode gap widths, or probing with incident light of a wavelength equal to that of the plasmonic resonance peak. b. HL-1 cells on an IDE at 3 DIV. Cells show typical mat-like growth that is expected with this cell type.

126
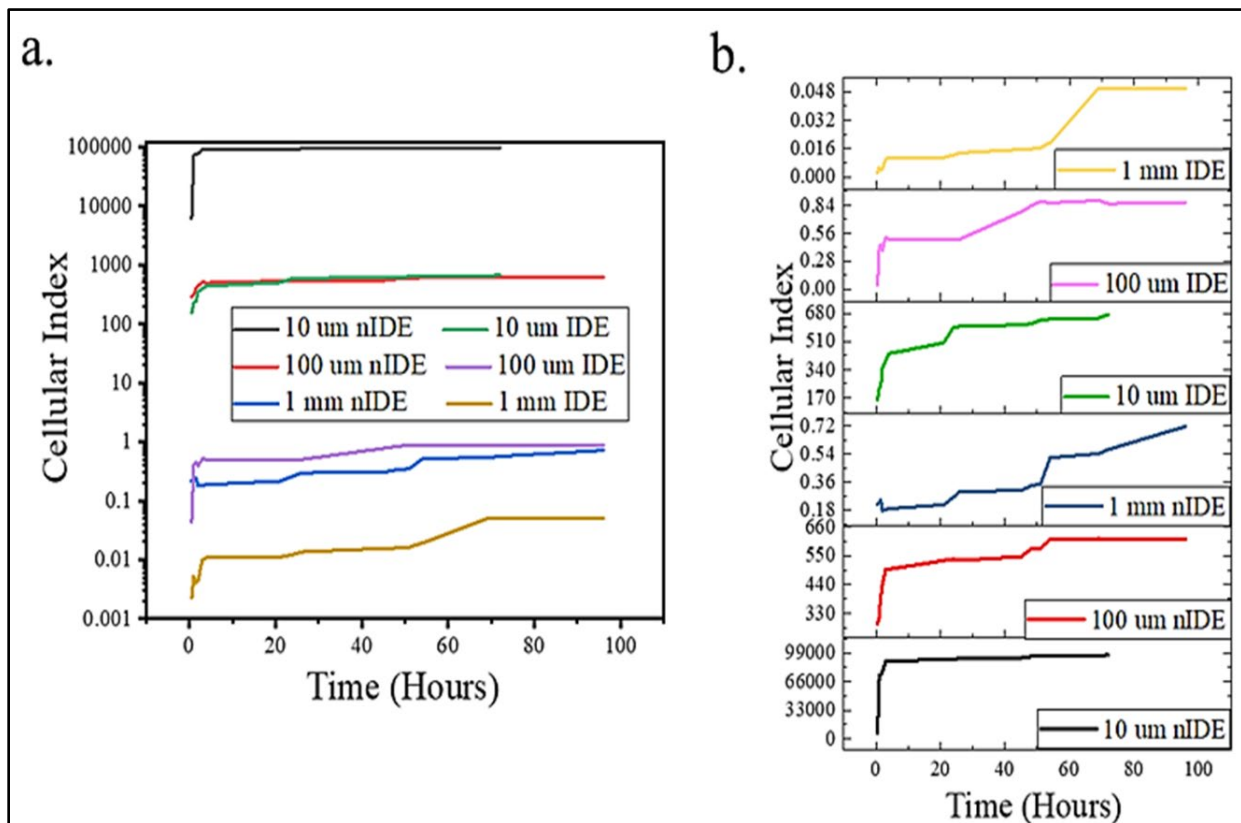
Figure 60 Cellular index measurements a. Cellular index (CI) measurements: decreased electrode gap width and the presence of nanostructures on the substrate cause an increase in the cellular index. b. Comparison of the various device measurements. All graphs are an average of N=3 devices.

This depicts the geometric trend with a calculated dramatic enhancement of 137,499X for the design extremities (Figure 60a). The CI for the IDEs cultured on the nanostructured surface reaches a maximum of 144.59X when compared to IDEs on the planar PAN at 5 DIV. Several orders of magnitude enhanced sensitivity from geometric and nanostructuring modes of the electrodes is observed (Figure 60b). The increased surface areas due to nanostructuring are calculated as 68.3%, 45.5%, and 21.3% for 10 μm, 100 μm, and 1 mm electrode gap widths, respectively. Since the measurements were all performed in ambient light, it was hypothesized that fluorescent lighting might have an emission peak near that of the plasmonic resonance peak for 30 nm gold nanostructures (approximately 720 nm), which it does [270]. To isolate this mode,

impedance measurements were performed in the dark for one of the designs (1 mm IDEs on nanostructured and planar substrates). An increase in CI for the dark measurements was elicited, but not to the same magnitude as that of the measurements performed in ambient light, resulting in a maximum of 6X (Figure 61a). We suspect that further enhancement would be observed if the incident light were of a discrete wavelength, as supported by the reflectivity measurement in Figure 61b. Individual contributions to the enhanced sensitivity from all three modes is further depicted in Figure 61c for a subset of the designs.
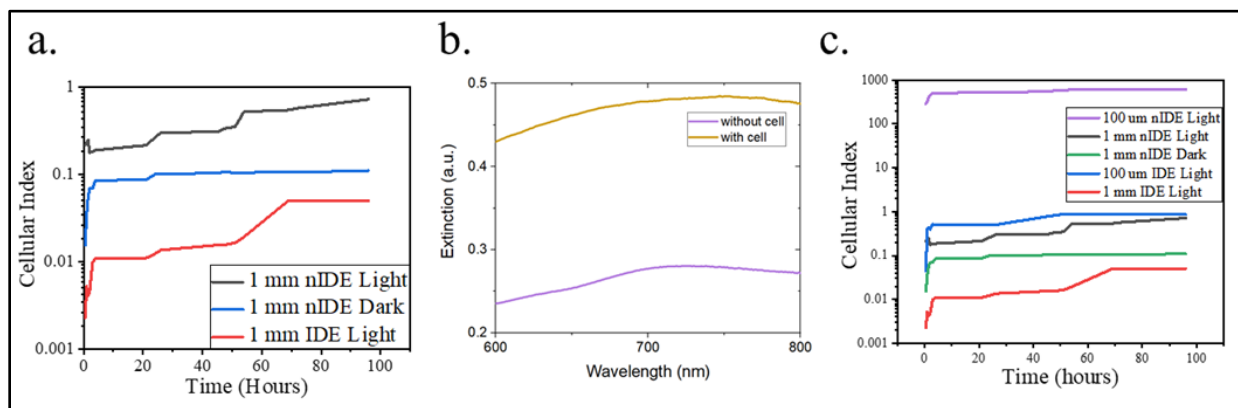
Figure 61 a. 1 mm cellular index measurements. The cellular index for the dark measurement falls between the IDE and nIDE performed in ambient light. This means that the fluorescent lighting is likely inducing surface plasmon resonance and causing an increase in impedance. b. The reflectivity measurement performed here shows the extinction of the nanohole substrate with and without cells. A 30 nm shift of the peak due to the change of the surface refractive index from the presence of the cells on the nanohole structures can be seen. This is an important characteristic of plasmonics. c. Comparison of different enhancements. Sensitivity can be increased by substrate nanostructuring, decreasing electrode gap width, introducing the proper wavelength of light, or a combination of these as desired in various cell-based biosensing assays.

To further examine the enhancement contribution from SPR elicitation with lasers in the range of 650-720nm, discrete wavelengths of incident light were tested. Figure 62a shows the difference between the cellular indices of the IDEs and pIDEs procured in the dark. The CI of the pIDE is higher than that of the IDE, as expected from prior experiments. Figure 62b compares the enhancement from each of the laser wavelengths when compared to the dark pIDE measurement. It is clear that as the laser wavelength nears the plasmonic peak of 720 nm [146], the sensitivity enhancement factor for CI is increased. Comparing this to the data in Figure 61 shows that by

choosing a wavelength close to the plasmonic peak, the CI can be increased by two orders of magnitude over that of diffuse incident light exposure, or three orders of magnitude of no light exposure.
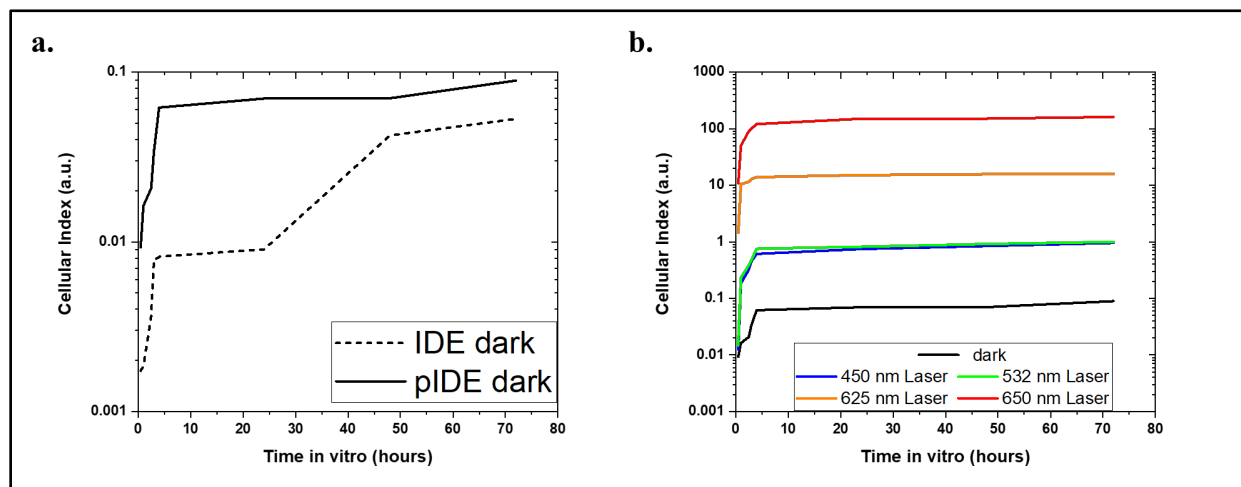
Figure 62 a. 1 mm cellular index measurements. The cellular index for the pIDE exceeds that of the IDE, as expected from previous work shown in this chapter. b. Comparison of enhancement due to different laser wavelengths. The 450 nm blue and 532 nm green lasers increase the cellular index when focused on the pIDE, but not much more than unfocused ambient light, as shown in Figure 12a. The 635 nm red laser increases the cellular index further, but the 650 nm laser demonstrates the greatest enhancement of cellular index likely due to its proximity to the plasmonic peak of the substrate.

Figure 63a shows cells growing on a pIDE electrode prior to termination of DIV05. Figure 63b and c show live/dead images of cells on an IDE and a pIDE, respectively. Here the green cells (fluorescing at 488 nm due to dye uptake) are alive, while the red cells (fluorescing at 570 nm due to dye uptake) are dead. Clearly, the cells remained largely viable over the course of the five-day assay. Some cell morphology change is expected due to phototoxicity from the various laser experiments [271]. Table 5 provides the maximum sensitivity enhancement in CI observed for each of the enhancement modes. While decreasing the electrode gap width provides the most dramatic sensitivity enhancement, it also becomes more and more difficult to produce microelectrodes as the pitch is reduced below 10μm. Therefore, combining these enhancement modes provides the greatest advantage. By producing the small (by the fabrication methods presented within this dissertation) electrode gap widths on nanostructured substrates and

measuring the impedance in a dark room while shining a discrete wavelength of laser light onto the electrode surface in order to produce surface plasmon resonance, one is able to take advantage of all of the sensitivity enhancement modes depicted in this chapter to achieve a highly sensitive benchtop fabricated plasmonic interdigitated electrode.
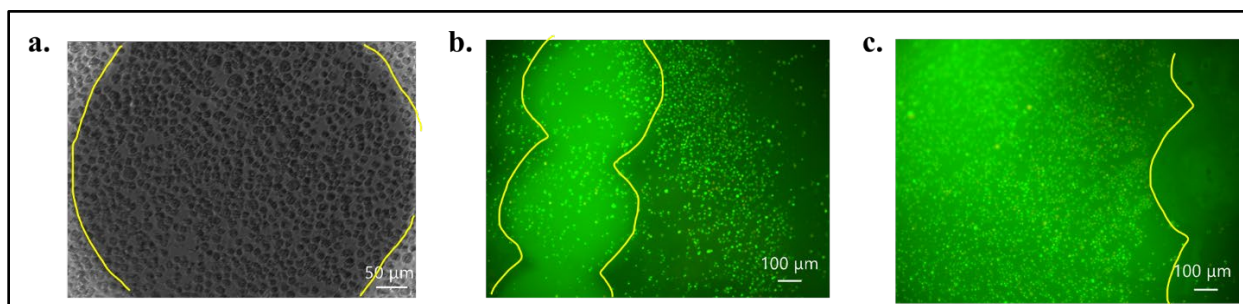
Figure 63 Optical Images of Cells on IDEs/pIDEs. a. Phase contrast image of HL-1 cells on pIDE electrode at DIV05. b. Live/Dead image of HL-1 cells on an IDE at DIV05. Most cells are living (green), while only a few cells are dead (red). c. Live/Dead image of HL-1 cells on a pIDE at DIV05. As with the IDE, most of the cells are living (green), while few are dead (red).

Table 6 Maximum enhancement for each enhancement mode of the pIDEs

Mode	Maximum Sensitivity Enhancement
Geometric	137,499X
Nanostructuring	144.59X
Ambient Lighting	6X
Discrete Laser Wavelength	1804.92X

Conclusions

This study reports for the first time the development of IDEs patterned onto nanostructured PAN substrates using rapid micro/nanofabrication technologies. The resulting nanostructured

IDEs (or nIDEs) demonstrated excellent design to device (99.37% translation of design features) and biocompatibility of 97.01% ± 2.15% with respect to iCell cardiomyocytes[2] control. The nIDEs were developed as a tool for rapid screening of toxins with an impedance metric and they demonstrated an impedance (110.19 kΩ at 1 kHz for DIV10 and 243.21 kΩ at 1 kHz for DIV18) that was higher than the IDEs with just an aqueous medium (27.37 kΩ at 1 kHz) which was used as a control. In addition, the nIDEs with cells showed increased impedance as evidenced by a Cell Index (CI) increase from 0 to 7.7 with increasing days *in vitro* of cell culturing. This result is as predicted because impedance should increase as cell coverage increases because of the cell-electrode interaction. Long term cell culture (18 days) was demonstrated with iCell Cardiomyocytes[2], and most significantly, an improvement in device performance when fabricated on nanostructured substrates (100X larger electrode gaps than commercial systems) was demonstrated through cellular index calculations. Finally, the cardiotoxicity testing utility of our devices was successfully demonstrated with the expected response of decreased cellular index from 2.34 to 1.13 in response to increased concentrations of a model drug, norepinephrine.

Additionally, it was demonstrated through UV-Vis spectroscopy that the nanostructured substrate exhibits a plasmonic peak. This means that an additional plasmonic resonance sensing mode can be activated by exposing the nIDE surface to the correct wavelength of light (and hence a pIDE). It was subsequently shown that the sensitivity of micron and millimeter scale IDEs can be enhanced via three individual alterations: two physical, and one optical: (1) increasing microelectrode surface area through fabrication on a nanostructured substrate; (2) decreasing the electrode gap width; and (3) probing the electrode surface with specific wavelengths of light. These modes can be tailored to specific cell based biosensing applications or combined to achieve greater device sensitivity.

CHAPTER 6: CONCLUSIONS & FUTURE WORK

Conclusions

In this dissertation, the development of several novel methods of patterning inorganic and organic materials and biocompatibility approaches for HL-1 cells and 3D printed materials, as well as the subsequent application of these methods to the development of biosensors and lab-on-a-chip devices, specifically Interdigitated Electrodes (IDEs), on non-traditional plasmonic polymer substrates as well as the deployment of these methods to enhance precision cellular placement on traditional glass MEA substrates has been presented. It was hypothesized that a combination of facile microfabrication techniques and patterning technologies on traditional and non-traditional substrates would increase the sensitivity and selectivity of sensor platforms such as these by several orders of magnitude, and even potentially introduce new modalities for cell-based biosensing. This was demonstrated using pIDEs where minimum enhancement of 6X was observed via exposure to incident ambient light alone not to mention 6 orders of improved sensitivity enhancements by combining multiple modalities. The biological functionality of these new IDEs was demonstrated through the use of a variety of cell cultures: cardiac, stem cell, and endothelial cells to study the growth, proliferation, modes of increasing sensitivity, and response to various compounds *in vitro* (outside the body).

Future Work

Given the results of this dissertation research, a gateway for a wide array of future work, has been opened and these expected directions are provided below.

Laser Micromachining

Laser micromachining has been utilized for a wide variety of two-dimensional materials in our laboratory. The natural progression of exploring the utility of this fabrication technique would

be to attempt to micromachine non-planar materials. Additionally, further decreasing the spot sizes that can be machined is paramount. Such an exploration would be particularly beneficial if processes can be reduced to the nanoscale widths.

Extrusion Bioprinting

The spot sizes able to be printed are still larger than ideal. The aim to get spots down to 100 μm will continue in future work on this aspect of the dissertation. Further exploring 3D printed micro-nozzles is a viable solution to reducing spot sizes, as well as looking into surface functionalization to decrease the drop contact diameter. Additionally, branching out from 2D cellular structures to 3D cellular constructs could potentially be explored, as cellular scaffolds are of great interest in the bioprinting field.

nIDE/pIDE

Probing a cell laden pIDE with the correct wavelength of laser light, cell layers can be encouraged to lift from the substrate surface, which could be interesting to the tissue engineering application of the plasmonic IDE. Further low-level laser/LED light could optically stimulate the cells. Potential probing of the pIDE with a low-power infrared laser for an extended period (approximately 40 minutes or more) to determine if tissue lifting occurs could be explored. This could be useful for tissue origami applications. Such plasmonic-based stimulation could provide a brand-new way for non-invasive cellular stimulation technologies.

pMEA

Full development and testing of a pMEA needs to be explored. The nanostructured substrates need to become more uniform to ensure that we can interface them with our modified Axion MUSE system. A realistic insulation solution needs to be found. This solution could be something as simple as an adhesive (e.g. Medco/Polyethylene Terephthalate (PET) layer). This is

an example of a solution that can first be laser micromachined to have openings in the appropriate areas for the electrodes and then carefully adhered to the pMEA surface. Another solution could be parylene deposition and suitable laser ablation. We had initially intended to try this along with SiO_2 but were unable to do so due to extenuating circumstances due to COVID-19 since UCF does not have a parylene deposition system. We had planned to go to UF or Georgia Tech to perform these experiments. SiO_2 is notoriously difficult to ablate, so perhaps a different material would produce better results. Additional electrodes could be added outside of the nanostructured area to allow for comparison with a planar substrate on the same device.

APPENDIX A:
OTHER RESEARCH PERFORMED DURING PH.D.

Development of a Plasmonic Microelectrode Array (pMEA)

Introduction

Microelectrode array (MEA) biosensors have been the standard in electrogenic cell measurements since the 1970s [272]. Electrogenic cells, such as cardiomyocytes and neurons, generate momentary changes in potential across the cell membrane. These changes in potential are called action potentials and can be thought of as electrical pulses. These electrical pulses can be recorded by the means of microelectrodes. MEA sensors involve a layer of patterned insulation atop a layer of patterned metal on a substrate, such as a glass or polymer wafer. While this technology has proliferated the marketplace, several issues with their microfabrication still exist. One such example is that the fabrication technology for most MEAs is silicon or glass-based; thus, it is highly reliant on expensive cleanroom-based processes, such as photolithography and chemical etching, which require advanced know-how [243, 272-276]. Alternative fabrication techniques for micro- and nanostructuring that allow for the same sensitivity, feature sizes and functionalities as cleanroom fabricated MEAs on a variety of substrates are required. Another such example is that impedance-based measurements using MEAs are time consuming, as each electrode must be measured individually. While this is not necessarily an issue for simple device characterization tasks, one could not perform such measurements on a cell laden device quickly and accurately enough to maintain the proper environment for ideal cell viability (humidity, temperature, etc.) [276].

Commercial MEA systems that allow for more comprehensive device measurements exist [214], but typically require biosensor devices to be of specific form factors; thus, the ability to fashion a device to needed specifications would be necessary for less tedious measurement processes. Axion BioSystems [277] makes a commercial form factor-specific MEA system. Their

proprietary software allows for the automatic application of filters for specific electrophysiological phenomenon and stimulation. Axion offers MEAs in a high throughput format of a multi-well plate. Multichannel Systems [278] also manufactures commercial MEA systems and typically in a low throughput, research scale, single well format. Their systems allow for the use of MEAs with varying number of electrodes. These systems are non-form specific to a point, label-free, high sensitivity, and allow for cells to be followed in real time. However, addition of other modalities of sensing are important in these systems and are just beginning to be evaluated.

In this appendix chapter, we present the development of a plasmonic microelectrode array (pMEA). Our lab has successfully used non-cleanroom-based techniques to fabricate a variety of MEAs in the past few years [145, 147, 148, 165]; however, the ability to reduce the signal-to-noise ratio (SNR) of the electrodes to enhance sensitivity and developing other modalities of sensing are under evaluation. In this appendix, we explored the preliminary processing-based integration of plasmonics with MEA technologies.

Hypothesis

One of the challenges for the plasmonic architectures we have demonstrated in the previous chapters is the fragile nanostructures. It is hypothesized that through careful metallization and insulation choices and processing conditions along with the use of facile microfabrication technologies discussed in the previous chapters, the integrity of the nanostructures can be preserved.

Additionally, it is hypothesized that by combining the nanostructured PAN substrate with an MEA, a reduction in SNR can be achieved; thus, giving the pMEA a greater device sensitivity. Also, by probing the device with light, a surface plasmon resonance can be induced, which introduces an additional sensing modality.

137

Materials and Methods

Shadow masks were designed in SolidWorks (Dassault Systems, Velizy-Villacoublay, France). Shadow masks were subsequently fabricated via laser micromachining on 12.5 µm thick Kapton® using the UV setting at 50 Hz and a 50 µm by 50 µm spot size.

Gold microelectrodes of approximately 50 nm thickness were deposited onto the nanostructured substrates using electron beam evaporation. Silicon dioxide (SiO_2) was subsequently deposited using electron beam evaporation atop the gold electrodes layer as an insulation layer. The SiO_2 insulation layer deposited was approximately 300 nm thick. The SiO_2 insulation layer was subsequently ablated using the green and UV settings to expose the electrodes. These test conditions for micro-ablation of the SiO_2 layer are shown in Table 6.

Table 7 pMEA laser ablation test conditions

		pMEA SiO_2 Insulation Laser Ablation Tests			
Sample	Electrode	Objective	Spot Size	Wavelength	Energy Density
1	1	10X	50 µm^2	532 nm	0.027 mJ/µm^2
	2	10X	50 µm^2	532 nm	0.0054 mJ/µm^2
	3	10X	50 µm^2	532 nm	0.0044 mJ/µm^2
	4	10X	50 µm^2	532 nm	0.0031 mJ/µm^2
	5	10X	50 µm^2	532 nm	0.0022 mJ/µm^2
2	1	50X	25 µm^2	355 nm	0.0088 mJ/µm^2
	2	50X	25 µm^2	355 nm	0.0044 mJ/µm^2
	3	50X	25 µm^2	355 nm	0.0018 mJ/µm^2
3	1	10X	45 µm^2	532 nm	0.0029 mJ/µm^2
	2	10X	45 µm^2	532 nm	0.0024 mJ/µm^2
	3	10X	45 µm^2	532 nm	0.0019 mJ/µm^2
	4	10X	45 µm^2	532 nm	0.0014 mJ/µm^2

Ablated electrodes were then imaged using the Keyence BZ-X800 All-in-One Confocal Microscope (Tokyo, Japan) in the standard brightfield imaging modality. Select electrodes were

also examined via the AFM (nanoIR2, Anasys, Billerica, MA) in both tapping and contact mode in order to characterize the micro-ablation.

Results and Discussion

The pMEA consists of 100 µm on a side microelectrodes (square size) with a 400 µm pitch, as shown in Figure 64a. In this test design 16 electrodes were arranged in a 4x4 array. The contacts were designed to be rather large (1 mm x 0.5 mm) to interface with our modified Axion MUSE system.
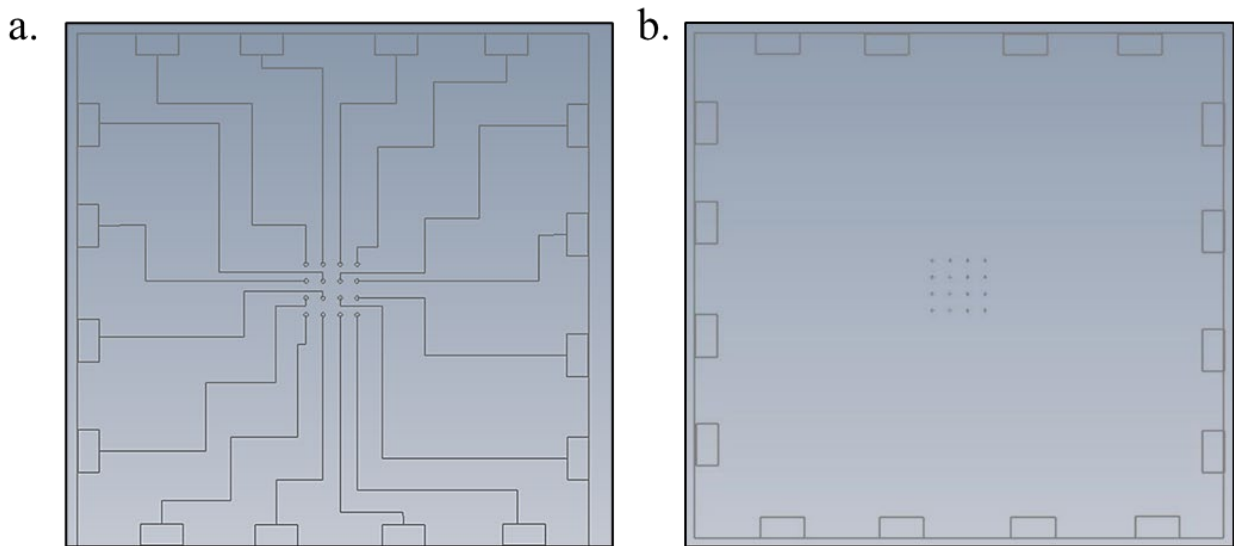
Figure 64 Schematic of a. pMEA design and b. pMEA insulation ablation mask.

Figure 64b shows the schematic for the pMEA insulation shadow mask. This shadow mask is aligned over the electrodes during laser micromachining of the insulation to ensure that only the electrodes area is ablated.

Due to an issue with the silicon mold for the fabrication of the spin on nanostructures, the effective nanostructure chip area was reduced from 5 mm x 5 mm to 4 mm x 4 mm. The initial metallization and SiO_2 ablation tests were performed with this chip size. The metallized pMEA

structure was smaller than the glass slide onto which the PAN and the PAN nanostructures are immobilized (Figure 65), as the glass slides used by the Thomas group vary each time. This condition would need to be consistent over time to interface effectively with the modified Axion MUSE during pMEA fabrication.
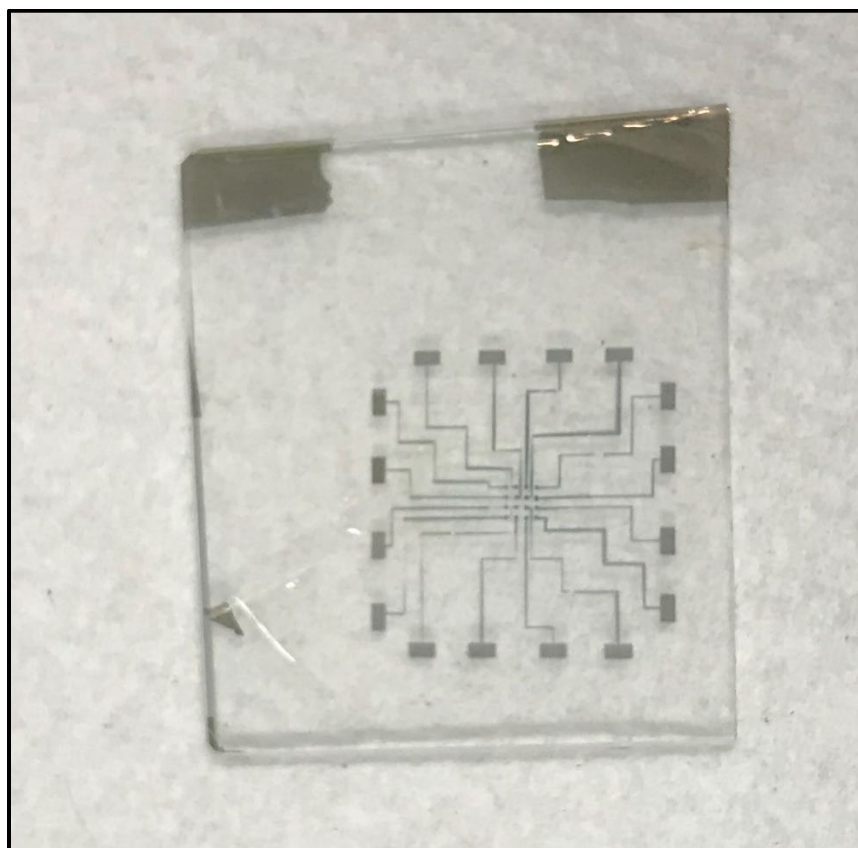
Figure 65 Metallized pMEA. This is one of the first iterations, so some shadowing can be seen from the shadow mask.

After gold deposition as depicted in the photo micrograph in Figure 65, silicon dioxide was deposited as an insulation layer. The deposition rate of SiO_2 in the e-beam was not able to be maintained at a constant rate, so the thickness and the surface roughness of the deposited materials needed to be tested. Additionally, it was necessary to determine whether the SiO_2 filled in the nanostructures. Figure 66 shows an AFM of a pMEA electrode with gold and silicon dioxide. The SiO_2 deposited evenly despite the rather uncontrollable deposition rate suggested by the quartz

crystal during deposition; however, the nanostructures became filled during the deposition process which is clear from this AFM image. This filling could invalidate the nanostructure and hence the fabrication of the pMEA microelectrodes. As a result, this first attempt was not successful and alternate insulate layers (e.g. atomic layer deposition, aluminum oxide, parylene etc.) need to be considered for the pMEA process.
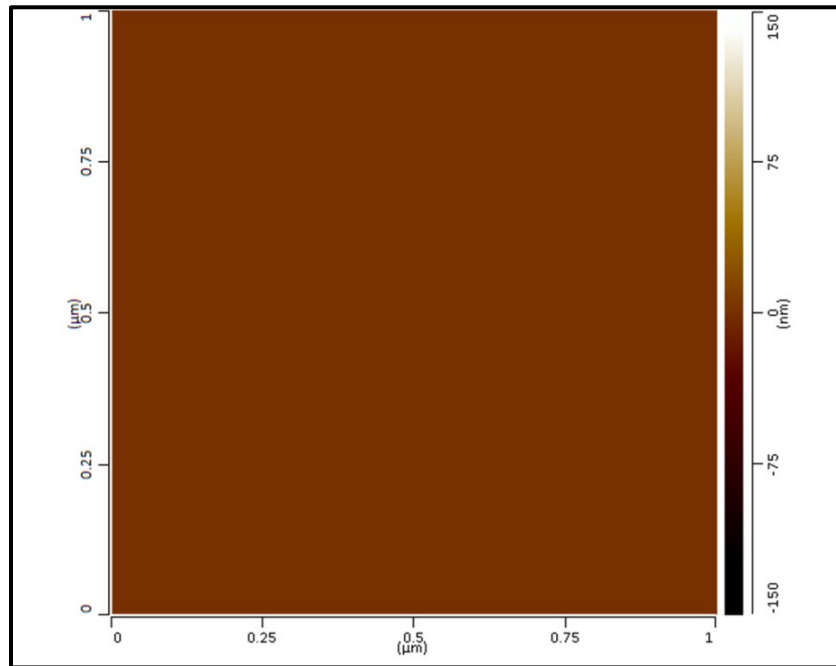
Figure 66 AFM of a pMEA electrode with SiO₂ insulation. The SiO₂ filled the nanostructures resulting in a completely smooth surface.
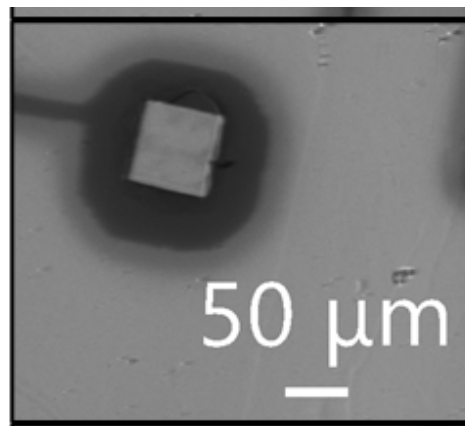
Figure 67 Example of an ablated electrode.

Figure 67 shows the one of the series of micrographs captures for the laser ablation of the silicon dioxide insulation layer as per the conditions provided in Table 6. From this micrograph, one can see that the laser micromachining conditions resulted in the entirety of gold being removed from the electrode surface along with the SiO_2 insulation layer at even the lowest energy density. All the other images taken for the microelectrode definition look similar or worse with the ablation of the entire structure.

Conclusions

Shadow masks for a pMEA device and for the laser ablation of insulation were successfully designed in CAD software. These shadow masks were successfully laser micromachined to allow for gold deposition. Insulation definition using e-beam evaporation of SiO_2 was attempted, followed by the laser micro-ablation of the SiO_2 insulation. A variety of low-power conditions were tested in the laser micromachining process to attempt to preserve the integrity of the nanostructured PAN layer. Despite our best efforts, laser micromachining of SiO_2 does not seem to be a viable insulation solution for the realization of pMEAs.

Makerspace Microfabrication of a Stainless-Steel 3D Microneedle Electrode Array (3D MEA) on a Glass Substrate for Simultaneous Optical & Electrical Probing of Electrogenic Cells

NBSS REU student Paola M. Morales Carvajal designed and fabricated a stainless-steel 3D MEA on a glass substrate with the guidance of lab members Avra Kundu and Chuck Didier. This paper has been accepted to RSC Advances and will be published in December 2020 [94].

After the 3D MEA had been fabricated, the ability of the device to capture electrophysiological activity needed to be determined in order to test the device from design to biological data generation. Figure 68 shows the device and the results of biological data capture.

Figure 68a and Figure 68b shows the fully packaged 3D MEA device interfacing with the Axion BioSystems MUSE electrophysiology system. Figure 68c shows the noise from one of the 3D MEA electrodes. Figure 68d shows HL-1 cells (plated and maintained per the protocol in Chapter 3) on the 3D MEA at 2 DIV. Figure 68e shows the cardiac beats as they appear in a screen capture from the AxIS software on the Axion MUSE, while Figure 68f provides a post-processed, averaged plot of repeatable single beats from the HL-1 cells cultured on the 3D MEA.
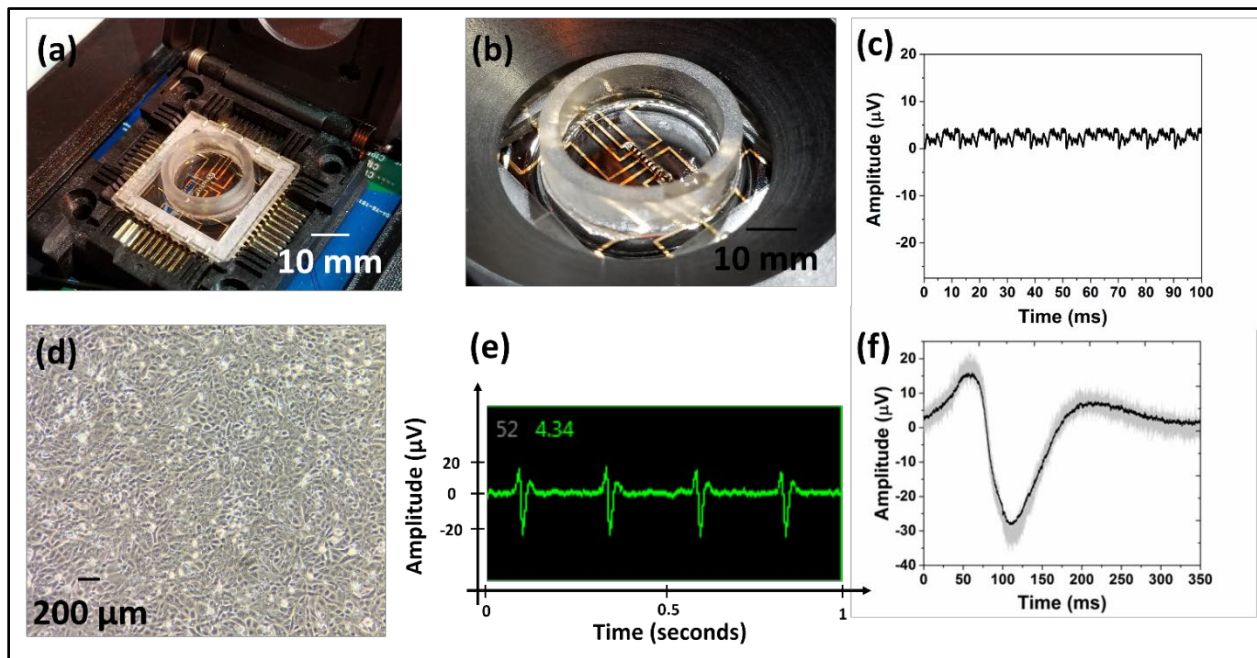
Figure 68 3D MEA device: a. and b. The fully packaged 3D MEA device interfacing with the Axion MUSE. c. Representative noise plot of one of the microelectrodes of the 3D MEA. d. HL-1 cells after 2 DIV. e. Cardiac beats as they appear on the AxIS software. f. Post-processed, averaged plot of repeatable single cardiac beats from HL-1 cells cultured on the 3D MEA.

APPENDIX B:
MATLAB CODES

Plotting Axion Raw Data

Axion MUSE files are output in raw data file form. MATLAB is the best tool to plot and

analyze this raw data. The MATLAB code for this data plotting is denoted below:

```
Data=AxisFile('FILENAME.raw').DataSets.LoadData, ('C2','34',[0 90]); %Loads the first 90
seconds of data for electrode 34
[t,v]=AllData{3,2,3,4}.GetTimeVoltageVector; %Get time and voltage vectors
plot(t,v) %Plot the voltage vs time data
```

```
AllData=AxisFile('NeuralDemoData_SpikeFile.spk').DataSets.LoadData; %Loads spike data
spikes=AllData{2,8,4,4}(1:5).GetVoltageVector; %Get the voltage data from the first 5 spikes of
electrode 44
time=AllData{2,8,4,4}(1).GetTimeVector; %Get the time vector from the first spike
plot_time=time-repmat(time(1),size(time)); %Shift the time vector back so it starts from zero
plot(plot_time,spikes); %Plot the 5 spike waveforms overlaid
```

Plotting Raw Impedance Data

Raw impedance data from the BODE 100 is comprised of hundreds of data points. Using

MATLAB to directly plot this data simplifies the process. The MATLAB code for this data

plotting is denoted below:

```
imp=dlmread('DATA.txt'); %Load real impedance data file
x1 = imp(:,1);
y1 = imp(:,2);
Re = 200:10:300; %4700:100:44000;
Rct = 15000; %100:100:5000;
Cdl = 0.0020*10^-8; %10^-9:10^-8:10^-6;
freq = 100:100:10^7; %Set frequency range
for k=1:1:length(Re)
Z(:,k) = Re(k) + 1.;
RealZ = real(Z);
ImagZ = imag(Z);
% AngleZ = phase(Z)
% DegreeZ = 180.*AngleZ./pi
end
figure (1)
plot(x1,y1,freq,RealZ)
set(gca, 'XScale', 'log')
```

APPENDIX C:
COPYRIGHT PERMISSIONS FOR CHAPTER 3, FIGURE 1

American Society for Cell Biology - License Terms and Conditions

This is a License Agreement between Cacie Hart ("You") and American Society for Cell Biology ("Publisher") provided by Copyright Clearance Center ("CCC"). The license consists of your order details, the terms and conditions provided by American Society for Cell Biology, and the CCC terms and conditions.

All payments must be made in full to CCC.

Order Date	18-Oct-2020	Type of Use	Republish in a thesis/dissertation
Order license ID	1071016-1	Publisher	American Society for Cell Biology
ISSN	1939-4586	Portion	Chart/graph/table/figure

LICENSED CONTENT

Publication Title	Molecular Biology of the Cell (Online)	Country	United States of America
Author/Editor	American Society for Cell Biology.	Rightsholder	American Society for Cell Biology
Date	01/01/1992	Publication Type	e-journal
Language	English		

REQUEST DETAILS

Portion Type	Chart/graph/table/figure	Distribution	Worldwide
Number of charts / graphs / tables / figures requested	1	Translation	Original language of publication
Format (select all that apply)	Electronic	Copies for the disabled?	No
Who will republish the content?	Academic institution	Minor editing privileges?	No
Duration of Use	Life of current edition	Incidental promotional use?	No
Lifetime Unit Quantity	Up to 499	Currency	USD
Rights Requested	Main product		

NEW WORK DETAILS

Title	Development of Facile Microfabrication Technologies for the Fabrication and Characterization of Multimodal Impedimetric, Plasmonic, and Electrophysiological Biosensors	Institution name	University of Central Florida
		Expected presentation date	2020-11-20

Instructor name	Cacie Hart

ADDITIONAL DETAILS

Order reference number	N/A	The requesting person / organization to appear on the license	Cacie Hart

REUSE CONTENT DETAILS

Title, description or numeric reference of the portion(s)	Figure 1	Title of the article/chapter the portion is from	N/A
Editor of portion(s)	N/A	Author of portion(s)	American Society for Cell Biology.
Volume of serial or monograph	N/A	Issue, if republishing an article from a serial	N/A
Page or page range of portion	N/A	Publication date of portion	1992-01-01

CCC Republication Terms and Conditions

the Order Confirmation, the license is automatically revoked and is null and void, as if it had never been issued, if complete payment for the license is not received on a timely basis either from User directly or through a payment agent, such as a credit card company.

3.3. Unless otherwise provided in the Order Confirmation, any grant of rights to User (i) is "one-time" (including the editions and product family specified in the license), (ii) is non-exclusive and non-transferable and (iii) is subject to any and all limitations and restrictions (such as, but not limited to, limitations on duration of use or circulation) included in the Order Confirmation or invoice and/or in these terms and conditions. Upon completion of the licensed use, User shall either secure a new permission for further use of the Work(s) or immediately cease any new use of the Work(s) and shall render inaccessible (such as by deleting or by removing or severing links or other locators) any further copies of the Work (except for copies printed on paper in accordance with this license and still in User's stock at the end of such period).

3.4. In the event that the material for which a republication license is sought includes third party materials (such as photographs, illustrations, graphs, inserts and similar materials) which are identified in such material as having been used by permission, User is responsible for identifying, and seeking separate licenses (under this Service or otherwise) for, any of such third party materials; without a separate license, such third party materials may not be used.

3.5. Use of proper copyright notice for a Work is required as a condition of any license granted under the Service. Unless otherwise provided in the Order Confirmation, a proper copyright notice will read substantially as follows: "Republished with permission of [Rightsholder's name], from [Work's title, author, volume, edition number and year of copyright]; permission conveyed through Copyright Clearance Center, Inc. " Such notice must be provided in a reasonably legible font size and must be placed either immediately adjacent to the Work as used (for example, as part of a by-line or footnote but not as a separate electronic link) or in the place where substantially all other credits or notices for the new work containing the republished Work are located. Failure to include the required notice results in loss to the Rightsholder and CCC, and the User shall be liable to pay liquidated damages for each such failure equal to twice the use fee specified in the Order Confirmation, in addition to the use fee itself and any other fees and charges specified.

3.6. User may only make alterations to the Work if and as expressly set forth in the Order Confirmation. No Work may be used in any way that is defamatory, violates the rights of third parties (including such third parties' rights of copyright, privacy, publicity, or other tangible or intangible property), or is otherwise illegal, sexually explicit or obscene. In addition, User may not conjoin a Work with any other material that may result in damage to the reputation of the Rightsholder. User agrees to inform CCC if it becomes aware of any infringement of any rights in a Work and to cooperate with any reasonable request of CCC or the Rightsholder in connection therewith.

4. Indemnity. User hereby indemnifies and agrees to defend the Rightsholder and CCC, and their respective employees and directors, against all claims, liability, damages, costs and expenses, including legal fees and expenses, arising out of any use of a Work beyond the scope of the rights granted herein, or any use of a Work which has been altered in any unauthorized way by User, including claims of defamation or infringement of rights of copyright, publicity, privacy or other tangible or intangible property.

5. Limitation of Liability. UNDER NO CIRCUMSTANCES WILL CCC OR THE RIGHTSHOLDER BE LIABLE FOR ANY DIRECT, INDIRECT, CONSEQUENTIAL OR INCIDENTAL DAMAGES (INCLUDING WITHOUT LIMITATION DAMAGES FOR LOSS OF BUSINESS PROFITS OR INFORMATION, OR FOR BUSINESS INTERRUPTION) ARISING OUT OF THE USE OR INABILITY TO USE A WORK, EVEN IF ONE OF THEM HAS BEEN ADVISED OF THE POSSIBILITY OF SUCH DAMAGES. In any event, the total liability of the Rightsholder and CCC (including their respective employees and directors) shall not exceed the total amount actually paid by User for this license. User assumes full liability for the actions and omissions of its principals, employees, agents, affiliates, successors and assigns.

6.
Limited Warranties. THE WORK(S) AND RIGHT(S) ARE PROVIDED "AS IS". CCC HAS THE RIGHT TO GRANT TO USER THE RIGHTS GRANTED IN THE ORDER CONFIRMATION DOCUMENT. CCC AND THE RIGHTSHOLDER DISCLAIM ALL

OTHER WARRANTIES RELATING TO THE WORK(S) AND RIGHT(S), EITHER EXPRESS OR IMPLIED, INCLUDING WITHOUT LIMITATION IMPLIED WARRANTIES OF MERCHANTABILITY OR FITNESS FOR A PARTICULAR PURPOSE. ADDITIONAL RIGHTS MAY BE REQUIRED TO USE ILLUSTRATIONS, GRAPHS, PHOTOGRAPHS, ABSTRACTS, INSERTS OR OTHER PORTIONS OF THE WORK (AS OPPOSED TO THE ENTIRE WORK) IN A MANNER CONTEMPLATED BY USER; USER UNDERSTANDS AND AGREES THAT NEITHER CCC NOR THE RIGHTSHOLDER MAY HAVE SUCH ADDITIONAL RIGHTS TO GRANT.

7. Effect of Breach. Any failure by User to pay any amount when due, or any use by User of a Work beyond the scope of the license set forth in the Order Confirmation and/or these terms and conditions, shall be a material breach of the license created by the Order Confirmation and these terms and conditions. Any breach not cured within 30 days of written notice thereof shall result in immediate termination of such license without further notice. Any unauthorized (but licensable) use of a Work that is terminated immediately upon notice thereof may be liquidated by payment of the Rightsholder's ordinary license price therefor; any unauthorized (and unlicensable) use that is not terminated immediately for any reason (including, for example, because materials containing the Work cannot reasonably be recalled) will be subject to all remedies available at law or in equity, but in no event to a payment of less than three times the Rightsholder's ordinary license price for the most closely analogous licensable use plus Rightsholder's and/or CCC's costs and expenses incurred in collecting such payment.

8. Miscellaneous.

   8.1. User acknowledges that CCC may, from time to time, make changes or additions to the Service or to these terms and conditions, and CCC reserves the right to send notice to the User by electronic mail or otherwise for the purposes of notifying User of such changes or additions; provided that any such changes or additions shall not apply to permissions already secured and paid for.

   8.2. Use of User-related information collected through the Service is governed by CCC's privacy policy, available online here:https://marketplace.copyright.com/rs-ui-web/mp/privacy-policy

   8.3. The licensing transaction described in the Order Confirmation is personal to User. Therefore, User may not assign or transfer to any other person (whether a natural person or an organization of any kind) the license created by the Order Confirmation and these terms and conditions or any rights granted hereunder; provided, however, that User may assign such license in its entirety on written notice to CCC in the event of a transfer of all or substantially all of User's rights in the new material which includes the Work(s) licensed under this Service.

   8.4. No amendment or waiver of any terms is binding unless set forth in writing and signed by the parties. The Rightsholder and CCC hereby object to any terms contained in any writing prepared by the User or its principals, employees, agents or affiliates and purporting to govern or otherwise relate to the licensing transaction described in the Order Confirmation, which terms are in any way inconsistent with any terms set forth in the Order Confirmation and/or in these terms and conditions or CCC's standard operating procedures, whether such writing is prepared prior to, simultaneously with or subsequent to the Order Confirmation, and whether such writing appears on a copy of the Order Confirmation or in a separate instrument.

   8.5. The licensing transaction described in the Order Confirmation document shall be governed by and construed under the law of the State of New York, USA, without regard to the principles thereof of conflicts of law. Any case, controversy, suit, action, or proceeding arising out of, in connection with, or related to such licensing transaction shall be brought, at CCC's sole discretion, in any federal or state court located in the County of New York, State of New York, USA, or in any federal or state court whose geographical jurisdiction covers the location of the Rightsholder set forth in the Order Confirmation. The parties expressly submit to the personal jurisdiction and venue of each such federal or state court.If you have any comments or questions about the Service or Copyright Clearance Center, please contact us at 978-750-8400 or send an e-mail to support@copyright.com.

v 1.1

APPENDIX D:
COPYRIGHT PERMISSIONS FOR CHAPTER 3, FIGURE 2

WOLTERS KLUWER HEALTH, INC. LICENSE
TERMS AND CONDITIONS

Oct 22, 2020

This Agreement between Ms. Cacie Hart ("You") and Wolters Kluwer Health, Inc. ("Wolters Kluwer Health, Inc.") consists of your license details and the terms and conditions provided by Wolters Kluwer Health, Inc. and Copyright Clearance Center.

License Number	4932090758101
License date	Oct 18, 2020
Licensed Content Publisher	Wolters Kluwer Health, Inc.
Licensed Content Publication	Circulation Research
Licensed Content Title	Human Embryonic Stem Cells Develop Into Multiple Types of Cardiac Myocytes
Licensed Content Author	Jia-Qiang He, Yue Ma, Youngsook Lee, et al
Licensed Content Date	Jun 5, 2003
Licensed Content Volume	93
Licensed Content Issue	1
Type of Use	Dissertation/Thesis
Requestor type	University/College
Sponsorship	No Sponsorship
Format	Electronic
Will this be posted on a password protected website?	No
Portion	Figures/tables/illustrations
Number of figures/tables/illustrations	1
Author of this Wolters Kluwer article	No
Will you be translating?	No
Intend to modify/adapt the content	No
Title	Development of Facile Microfabrication Technologies for the Fabrication and Characterization of Multimodal Impedimetric, Plasmonic, and Electrophysiological Biosensors
Institution name	University of Central Florida
Expected presentation date	Nov 2020
Portions	Figure 4
Requestor Location	Ms. Cacie Hart 3206 Everett St
	APOPKA, FL 32703 United States Attn: Ms. Cacie Hart
Publisher Tax ID	13-2932696
Total	0.00 USD
Terms and Conditions	

Wolters Kluwer Health Inc. Terms and Conditions

1. **Duration of License:** Permission is granted for a one time use only. Rights herein do not apply to future reproductions, editions, revisions, or other derivative works. This permission shall be effective as of the date of execution by the parties for the maximum period of 12 months and should be renewed after the term expires.
   i. When content is to be republished in a book or journal the validity of this agreement should be the life of the book edition or journal issue.
   ii. When content is licensed for use on a website, Internet, Intranet, or any publicly accessible site (not including a journal or book), you agree to remove the material from such site after 12 months, or request to renew your permission license.
2. **Credit Line:** A credit line must be prominently placed and include: For book content: the author(s), title of book, edition, copyright holder, year of publication; For journal content: the author(s), titles of article, title of journal, volume number, issue number, inclusive pages and website URL to the journal page; If a journal is published by a learned society the credit line must include the details of that society.
3. **Warranties:** The requestor warrants that the material shall not be used in any manner which may be considered derogatory to the title, content, authors of the material, or to Wolters Kluwer Health, Inc.
4. **Indemnity:** You hereby indemnify and hold harmless Wolters Kluwer Health, Inc. and its respective officers, directors, employees and agents, from and against any and all claims, costs, proceeding or demands arising out of your unauthorized use of the Licensed Material.
5. **Geographical Scope:** Permission granted is non-exclusive and is valid throughout the world in the English language and the languages specified in the license.
6. **Copy of Content:** Wolters Kluwer Health, Inc. cannot supply the requestor with the original artwork, high-resolution images, electronic files or a clean copy of content.
7. **Validity:** Permission is valid if the borrowed material is original to a Wolters Kluwer Health, Inc. imprint (J.B Lippincott, Lippincott-Raven Publishers, Williams & Wilkins, Lea & Febiger, Harwal, Rapid Science, Little Brown & Company, Harper & Row Medical, American Journal of Nursing Co, and Urban & Schwarzenberg - English Language, Raven Press, Paul Hoeber, Springhouse, Ovid), and the Anatomical Chart Company.
8. **Third Party Material:** This permission does not apply to content that is credited to publications other than Wolters Kluwer Health, Inc. or its Societies. For images credited to non-Wolters Kluwer Health, Inc. books or journals, you must obtain permission from the source referenced in the figure or table legend or credit line before making any use of the image(s), table(s) or other content.
9. **Adaptations:** Adaptations are protected by copyright. For images that have been adapted, permission must be sought from the rightsholder of the original material and the rightsholder of the adapted material.
10. **Modifications:** Wolters Kluwer Health, Inc. material is not permitted to be modified or adapted without written approval from Wolters Kluwer Health, Inc. with the exception of text size or color. The adaptation should be credited as follows: Adapted with permission from Wolters Kluwer Health, Inc.: [the author(s), title of book, edition, copyright holder, year of publication] or [the author(s), titles of article, title of journal, volume number, issue number, inclusive pages and website URL to the journal page].
11. **Full Text Articles:** Republication of full articles in English is prohibited.
12. **Branding and Marketing:** No drug name, trade name, drug logo, or trade logo can be included on the same page as material borrowed from Diseases of the Colon & Rectum, Plastic Reconstructive Surgery, Obstetrics & Gynecology (The Green Journal), Critical Care Medicine, Pediatric Critical Care Medicine, the American Heart Association publications and the American Academy of Neurology publications.
13. **Open Access:** Unless you are publishing content under the same Creative Commons license, the following statement must be added when reprinting material in Open Access journals: "The Creative Commons license does not apply to this content. Use of the material in any format is prohibited without written permission from the publisher, Wolters Kluwer Health, Inc. Please contact permissions@lww.com for further information."
14. **Translations:** The following disclaimer must appear on all translated copies: Wolters Kluwer Health, Inc. and its Societies take no responsibility for the accuracy of the translation from the published English original and are not liable for any errors which may occur.
15. **Published Ahead of Print (PAP):** Articles in the PAP stage of publication can be cited using the online publication date and the unique DOI number.
    i. Disclaimer: Articles appearing in the PAP section have been peer-reviewed and accepted for publication in the relevant journal and posted online before print publication. Articles appearing as PAP may contain statements, opinions, and information that have errors in facts, figures, or interpretation. Any final changes in manuscripts will be made at the time of print publication and will be reflected in the final electronic version of the issue. Accordingly, Wolters Kluwer Health, Inc., the editors, authors and their respective employees are not responsible or liable for the use of any such inaccurate or misleading data, opinion or information contained in the articles in this section.
16. **Termination of Contract:** Wolters Kluwer Health, Inc. must be notified within 90 days of the original license date if you opt not to use the requested material.
17. **Waived Permission Fee:** Permission fees that have been waived are not subject to future waivers, including similar requests or renewing a license.

18. Contingent on payment: You may exercise these rights licensed immediately upon issuance of the license, however until full payment is received either by the publisher or our authorized vendor, this license is not valid. If full payment is not received on a timely basis, then any license preliminarily granted shall be deemed automatically revoked and shall be void as if never granted. Further, in the event that you breach any of these terms and conditions or any of Wolters Kluwer Health, Inc.'s other billing and payment terms and conditions, the license is automatically revoked and shall be void as if never granted. Use of materials as described in a revoked license, as well as any use of the materials beyond the scope of an unrevoked license, may constitute copyright infringement and publisher reserves the right to take any and all action to protect its copyright in the materials.

19. STM Signatories Only: Any permission granted for a particular edition will apply to subsequent editions and for editions in other languages, provided such editions are for the work as a whole in situ and do not involve the separate exploitation of the permitted illustrations or excerpts. Please view: STM Permissions Guidelines

20. Warranties and Obligations: LICENSOR further represents and warrants that, to the best of its knowledge and belief, LICENSEE's contemplated use of the Content as represented to LICENSOR does not infringe any valid rights to any third party.

21. Breach: If LICENSEE fails to comply with any provisions of this agreement, LICENSOR may serve written notice of breach of LICENSEE and, unless such breach is fully cured within fifteen (15) days from the receipt of notice by LICENSEE, LICENSOR may thereupon, at its option, serve notice of cancellation on LICENSEE, whereupon this Agreement shall immediately terminate.

22. Assignment: License conveyed hereunder by the LICENSOR shall not be assigned or granted in any manner conveyed to any third party by the LICENSEE without the consent in writing to the LICENSOR.

23. Governing Law: The laws of The State of New York shall govern interpretation of this Agreement and all rights and liabilities arising hereunder.

24. Unlawful: If any provision of this Agreement shall be found unlawful or otherwise legally unenforceable, all other conditions and provisions of this Agreement shall remain in full force and effect.

For Copyright Clearance Center / RightsLink Only:

1. Service Description for Content Services: Subject to these terms of use, any terms set forth on the particular order, and payment of the applicable fee, you may make the following uses of the ordered materials:
    i. Content Rental: You may access and view a single electronic copy of the materials ordered for the time period designated at the time the order is placed. Access to the materials will be provided through a dedicated content viewer or other portal, and access will be discontinued upon expiration of the designated time period. An order for Content Rental does not include any rights to print, download, save, create additional copies, to distribute or to reuse in any way the full text or parts of the materials.
    ii. Content Purchase: You may access and download a single electronic copy of the materials ordered. Copies will be provided by email or by such other means as publisher may make available from time to time. An order for Content Purchase does not include any rights to create additional copies or to distribute copies of the materials

Other Terms and Conditions:
v1.18

Questions? customercare@copyright.com or +1-855-239-3415 (toll free in the US) or +1-978-646-2777.

APPENDIX E:
COPYRIGHT PERMISSIONS FOR CHAPTER 3, FIGURE 3

APPENDIX F:
COPYRIGHT PERMISSIONS FOR CHAPTER 4, FIGURE 1

ELSEVIER LICENSE
TERMS AND CONDITIONS

This Agreement between Ms. Cacie Hart ("You") and Elsevier ("Elsevier") consists of your license details and the terms and conditions provided by Elsevier and Copyright Clearance Center.

License Number	4932071435726
License date	Oct 18, 2020
Licensed Content Publisher	Elsevier
Licensed Content Publication	Trends in Biotechnology
Licensed Content Title	Advances in Bioprinting Technologies for Craniofacial Reconstruction
Licensed Content Author	Dafydd O. Visscher,Elisabet Farré-Guasch,Marco N. Helder,Susan Gibbs,Tymour Forouzanfar,Paul P. van Zuijlen,Jan Wolff
Licensed Content Date	Sep 1, 2016
Licensed Content Volume	34
Licensed Content Issue	9
Licensed Content Pages	11
Start Page	700
End Page	710
Type of Use	reuse in a thesis/dissertation
Portion	figures/tables/illustrations
Number of figures/tables/illustrations	1
Format	electronic
Are you the author of this Elsevier article?	No
Will you be translating?	No
Title	Development of Facile Microfabrication Technologies for the Fabrication and Characterization of Multimodal Impedimetric, Plasmonic, and Electrophysiological Biosensors
Institution name	University of Central Florida
Expected presentation date	Nov 2020
Portions	Figure 2
Requestor Location	Ms. Cacie Hart 3206 Everett St APOPKA, FL 32703 United States Attn: Ms. Cacie Hart
Publisher Tax ID	98-0397604
Total	0.00 USD

Terms and Conditions

INTRODUCTION

1. The publisher for this copyrighted material is Elsevier. By clicking "accept" in connection with completing this licensing transaction, you agree that the following terms and conditions apply to this transaction (along with the Billing and Payment terms and conditions established by Copyright Clearance Center, Inc. ("CCC"), at the time that you opened your Rightslink account and that are available at any time at http://myaccount.copyright.com).

GENERAL TERMS

2. Elsevier hereby grants you permission to reproduce the aforementioned material subject to the terms and conditions indicated.

3. Acknowledgement: If any part of the material to be used (for example, figures) has appeared in our publication with credit or acknowledgement to another source, permission must also be sought from that source. If such permission is not obtained then that material may not be included in your publication/copies. Suitable acknowledgement to the source must be made, either as a footnote or in a reference list at the end of your publication, as follows:

"Reprinted from Publication title, Vol /edition number, Author(s), Title of article / title of chapter, Pages No., Copyright (Year), with permission from Elsevier [OR APPLICABLE SOCIETY COPYRIGHT OWNER]." Also Lancet special credit - "Reprinted from The Lancet, Vol. number, Author(s), Title of article, Pages No., Copyright (Year), with permission from Elsevier."

4. Reproduction of this material is confined to the purpose and/or media for which permission is hereby given.

5. Altering/Modifying Material: Not Permitted. However figures and illustrations may be altered/adapted minimally to serve your work. Any other abbreviations, additions, deletions and/or any other alterations shall be made only with prior written authorization of Elsevier Ltd. (Please contact Elsevier's permissions helpdesk here). No modifications can be made to any Lancet figures/tables and they must be reproduced in full.

6. If the permission fee for the requested use of our material is waived in this instance, please be advised that your future requests for Elsevier materials may attract a fee.

7. Reservation of Rights: Publisher reserves all rights not specifically granted in the combination of (i) the license details provided by you and accepted in the course of this licensing transaction, (ii) these terms and conditions and (iii) CCC's Billing and Payment terms and conditions.

8. License Contingent Upon Payment: While you may exercise the rights licensed immediately upon issuance of the license at the end of the licensing process for the transaction, provided that you have disclosed complete and accurate details of your proposed use, no license is finally effective unless and until full payment is received from you (either by publisher or by CCC) as provided in CCC's Billing and Payment terms and conditions. If full payment is not received on a timely basis, then any license preliminarily granted shall be deemed automatically revoked and shall be void as if never granted. Further, in the event that you breach any of these terms and conditions or any of CCC's Billing and Payment terms and conditions, the license is automatically revoked and shall be void as if never granted. Use of materials as described in a revoked license, as well as any use of the materials beyond the scope of an unrevoked license, may constitute copyright infringement and publisher reserves the right to take any and all action to protect its copyright in the materials.

9. Warranties: Publisher makes no representations or warranties with respect to the licensed material.

10. Indemnity: You hereby indemnify and agree to hold harmless publisher and CCC, and their respective officers, directors, employees and agents, from and against any and all claims arising out of your use of the licensed material other than as specifically authorized pursuant to this license.

11. No Transfer of License: This license is personal to you and may not be sublicensed, assigned, or transferred by you to any other person without publisher's written permission.

12. No Amendment Except in Writing: This license may not be amended except in a writing signed by both parties (or, in the case of publisher, by CCC on publisher's behalf).

13. Objection to Contrary Terms: Publisher hereby objects to any terms contained in any purchase order, acknowledgment, check endorsement or other writing prepared by you, which terms are inconsistent with these terms and conditions or CCC's Billing and Payment terms and conditions. These terms and conditions, together with CCC's Billing and Payment terms and conditions (which are incorporated herein), comprise the entire agreement between you and publisher (and CCC) concerning this licensing transaction. In the event of any conflict between your obligations established by these terms and conditions and those established by CCC's Billing and Payment terms and conditions, these terms and conditions shall control.

14. Revocation: Elsevier or Copyright Clearance Center may deny the permissions described in this License at their sole discretion, for any reason or no reason, with a full refund payable to you. Notice of such denial will be made using the contact information provided by you. Failure to receive such notice will not alter or invalidate the denial. In no event will Elsevier or Copyright Clearance Center be responsible or liable for any costs, expenses or damage incurred by you as a result of a denial of your permission request, other than a refund of the amount(s) paid by you to Elsevier and/or Copyright Clearance Center for denied permissions.

LIMITED LICENSE

The following terms and conditions apply only to specific license types:

15. Translation: This permission is granted for non-exclusive world English rights only unless your license was granted for translation rights. If you licensed translation rights you may only translate this content into the languages you requested. A professional translator must perform all translations and reproduce the content word for word preserving the integrity of the article.

16. Posting licensed content on any Website: The following terms and conditions apply as follows: Licensing material from an Elsevier journal: All content posted to the web site must maintain the copyright information line on the bottom of each image; A hyper-text must be included to the Homepage of the journal from which you are licensing at http://www.sciencedirect.com/science/journal/xxxxx or the Elsevier homepage for books at http://www.elsevier.com; Central Storage: This license does not include permission for a scanned version of the material to be stored in a central repository such as that provided by Heron/XanEdu.

Licensing material from an Elsevier book: A hyper-text link must be included to the Elsevier homepage at http://www.elsevier.com . All content posted to the web site must maintain the copyright information line on the bottom of each image.

Posting licensed content on Electronic reserve: In addition to the above the following clauses are applicable: The web site must

be password-protected and made available only to bona fide students registered on a relevant course. This permission is granted for 1 year only. You may obtain a new license for future website posting.

17. For journal authors: the following clauses are applicable in addition to the above:

Preprints:

A preprint is an author's own write-up of research results and analysis, it has not been peer-reviewed, nor has it had any other value added to it by a publisher (such as formatting, copyright, technical enhancement etc.).

Authors can share their preprints anywhere at any time. Preprints should not be added to or enhanced in any way in order to appear more like, or to substitute for, the final versions of articles however authors can update their preprints on arXiv or RePEc with their Accepted Author Manuscript (see below).

If accepted for publication, we encourage authors to link from the preprint to their formal publication via its DOI. Millions of researchers have access to the formal publications on ScienceDirect, and so links will help users to find, access, cite and use the best available version. Please note that Cell Press, The Lancet and some society-owned have different preprint policies. Information on these policies is available on the journal homepage.

Accepted Author Manuscripts: An accepted author manuscript is the manuscript of an article that has been accepted for publication and which typically includes author-incorporated changes suggested during submission, peer review and editor-author communications.

Authors can share their accepted author manuscript:

- Immediately
  - via their non-commercial person homepage or blog
  - by updating a preprint in arXiv or RePEc with the accepted manuscript
  - via their research institute or institutional repository for internal institutional uses or as part of an invitation-only research collaboration work-group
  - directly by providing copies to their students or to research collaborators for their personal use
  - for private scholarly sharing as part of an invitation-only work group on commercial sites with which Elsevier has an agreement
- After the embargo period
  - via non-commercial hosting platforms such as their institutional repository
  - via commercial sites with which Elsevier has an agreement

In all cases accepted manuscripts should:

- link to the formal publication via its DOI
- bear a CC-BY-NC-ND license - this is easy to do
- if aggregated with other manuscripts, for example in a repository or other site, be shared in alignment with our hosting policy not be added to or enhanced in any way to appear more like, or to substitute for, the published journal article.

Published journal article (JPA): A published journal article (PJA) is the definitive final record of published research that appears or will appear in the journal and embodies all value-adding publishing activities including peer review co-ordination, copy-editing, formatting, (if relevant) pagination and online enrichment.

Policies for sharing publishing journal articles differ for subscription and gold open access articles:

Subscription Articles: If you are an author, please share a link to your article rather than the full-text. Millions of researchers have access to the formal publications on ScienceDirect, and so links will help your users to find, access, cite, and use the best available version.

Theses and dissertations which contain embedded PJAs as part of the formal submission can be posted publicly by the awarding institution with DOI links back to the formal publications on ScienceDirect.

If you are affiliated with a library that subscribes to ScienceDirect you have additional private sharing rights for others' research accessed under that agreement. This includes use for classroom teaching and internal training at the institution (including use in course packs and courseware programs), and inclusion of the article for grant funding purposes.

Gold Open Access Articles: May be shared according to the author-selected end-user license and should contain a CrossMark logo, the end user license, and a DOI link to the formal publication on ScienceDirect.

Please refer to Elsevier's posting policy for further information.

18. For book authors the following clauses are applicable in addition to the above: Authors are permitted to place a brief summary of their work online only. You are not allowed to download and post the published electronic version of your chapter, nor may you scan the printed edition to create an electronic version. **Posting to a repository:** Authors are permitted to post a summary of their chapter only in their institution's repository.

19. **Thesis/Dissertation:** If your license is for use in a thesis/dissertation your thesis may be submitted to your institution in either print or electronic form. Should your thesis be published commercially, please reapply for permission. These requirements include permission for the Library and Archives of Canada to supply single copies, on demand, of the complete thesis and include permission for Proquest/UMI to supply single copies, on demand, of the complete thesis. Should your thesis be published commercially, please reapply for permission. Theses and dissertations which contain embedded PJAs as part of the formal submission can be posted publicly by the awarding institution with DOI links back to the formal publications on ScienceDirect.

APPENDIX G:
COPYRIGHT PERMISSIONS FOR CHAPTER 4, FIGURE 2

IOP Publishing, Ltd - License Terms and Conditions

Order Date	18-Oct-2020	Type of Use	Republish in a thesis/dissertation
Order license ID	1071015-1		
ISSN	1758-5090	Publisher	IOP Publishing
		Portion	Chart/graph/table/figure

LICENSED CONTENT

Publication Title	Biofabrication	Country	United Kingdom of Great Britain and Northern Ireland
Author/Editor	Institute of Physics (Great Britain)		
Date	01/01/2009	Rightsholder	IOP Publishing, Ltd
Language	English	Publication Type	e-Journal
		URL	http://iopscience.iop.org/1758-5090

REQUEST DETAILS

Portion Type	Chart/graph/table/figure	Distribution	Worldwide
Number of charts / graphs / tables / figures requested	1	Translation	Original language of publication
		Copies for the disabled?	No
Format (select all that apply)	Electronic	Minor editing privileges?	No
Who will republish the content?	Academic institution	Incidental promotional use?	No
Duration of Use	Life of current edition	Currency	USD
Lifetime Unit Quantity	Up to 499		
Rights Requested	Main product		

NEW WORK DETAILS

Title	Development of Facile Microfabrication Technologies for the Fabrication and Characterization of Multimodal Impedimetric, Plasmonic, and Electrophysiological Biosensors	Institution name	University of Central Florida
		Expected presentation date	2020-11-20

Instructor name	Cacie Hart

ADDITIONAL DETAILS

Order reference number	N/A	The requesting person / organization to appear on the license	Cacie Hart

REUSE CONTENT DETAILS

Title, description or numeric reference of the portion(s)	Figure 8	Title of the article/chapter the portion is from	N/A
Editor of portion(s)	N/A	Author of portion(s)	Institute of Physics (Great Britain)
Volume of serial or monograph	N/A	Issue, if republishing an article from a serial	N/A
Page or page range of portion	N/A	Publication date of portion	2009-01-01

PUBLISHER TERMS AND CONDITIONS

These special terms and conditions are in addition to the standard terms and conditions for CCC's Republication Service and, together with those standard terms and conditions, govern the use of the Works. As the User you will make all reasonable efforts to contact the author(s) of the article which the Work is to be reused from, to seek consent for your intended use. Contacting one author who is acting expressly as authorised agent for their co-author(s) is acceptable. User will reproduce the following wording prominently alongside the Work: the source of the Work, including author, article title, title of journal, volume number, issue number (if relevant), page range (or first page if this is the only information available) and date of first publication. This information can be contained in a footnote or reference note; and a link back to the article (via DOI); and if practicable, and IN ALL CASES for new works published under any of the Creative Commons licences, the words "© IOP Publishing. Reproduced with permission. All rights reserved" Without the express permission of the author(s) and the Rightsholder of the article from which the Work is to be reused, User shall not use it in any way which, in the opinion of the Rightsholder, could: (i) distort or alter the author(s)' original intention(s) and meaning; (ii) be prejudicial to the honour or reputation of the author(s); and/or (iii) imply endorsement by the author(s) and/or the Rightsholder. This licence does not apply to any article which is credited to another source and which does not have the copyright line '© IOP Publishing Ltd'. User must check the copyright line of the article from which the Work is to be reused to check that IOP Publishing Ltd has all the necessary rights to be able to grant permission. User is solely responsible for identifying and obtaining separate licences and permissions from the copyright owner for reuse of any such third party material/figures which the Rightsholder is not the copyright owner of. The Rightsholder shall not reimburse any fees which User pays for a republication license for such third party content. This licence does not apply to any material/figure which is credited to another source in the Rightsholder's publication or has been obtained from a third party. User must check the Version of Record of the article from which the Work is to be reused, to check whether any of the material in the Work is third party material. Third party citations and/or copyright notices and/or permissions statements may not be included in any other version of the article from which the Work is to be reused and so cannot be relied upon by the User. User is solely responsible for identifying and obtaining separate licences and permissions from the copyright owner for reuse of any such third party material/figures where the Rightsholder is not the copyright owner. The Rightsholder shall not reimburse any fees which User pays for a republication license for such third party content. User and CCC acknowledge that the Rightsholder may, from time to time, make changes or additions to these special terms and conditions without express notification, provided that these shall not apply to permissions already secured and paid for by User prior to such change or addition. User acknowledges that the Rightsholder (which includes companies within its group and third parties for whom it publishes its titles) may make use of personal data collected through the service in the course of their business. If User is the author of the Work, User may automatically have the right to reuse it under the rights granted back when User transferred the copyright in the article to the Rightsholder. User should check the copyright form and the relevant author rights policy to check whether permission is required. If User is the author of the Work and does require permission for proposed reuse of the Work, User should select 'Author of requested content' as the Requestor Type. The Rightsholder shall not reimburse any fees which User pays for a republication license. If User is

164

the author of the article which User wishes to reuse in User's thesis or dissertation, the republication licence covers the right to include the Accepted Manuscript version (not the Version of Record) of the article. User must include citation details and, for online use, a link to the Version of Record of the article on the Rightsholder's website. User may need to obtain separate permission for any third party content included within the article. User must check this with the copyright owner of such third party content. User may not include the article in a thesis or dissertation which is published by ProQuest. Any other commercial use of User's thesis or dissertation containing the article would also need to be expressly notified in writing to the Rightsholder at the time of request and would require separate written permission from the Rightsholder. User does not need to request permission for Work which has been published under a CC BY licence. User must check the Version of Record of the CC BY article from which the Work is to be reused, to check whether any of the material in the Work is third party material and so not published under the CC BY licence. User is solely responsible for identifying and obtaining separate licences and permissions from the copyright owner for reuse of any such third party material/figures. The Rightsholder shall not reimburse any fees which User pays for such licences and permissions. As well as CCC, the Rightsholder shall have the right to bring any legal action that it deems necessary to enforce its rights should it consider that the Work infringes those rights in any way. For STM Signatories ONLY (as agreed as part of the STM Guidelines) Any licence granted for a particular edition of a Work will apply also to subsequent editions of it and for editions in other languages, provided such editions are for the Work as a whole in situ and do not involve the separate exploitation of the permitted illustrations or excerpts.

CCC Republication Terms and Conditions

1. Description of Service; Defined Terms. This Republication License enables the User to obtain licenses for republication of one or more copyrighted works as described in detail on the relevant Order Confirmation (the "Work(s)"). Copyright Clearance Center, Inc. ("CCC") grants licenses through the Service on behalf of the rightsholder identified on the Order Confirmation (the "Rightsholder"). "Republication", as used herein, generally means the inclusion of a Work, in whole or in part, in a new work or works, also as described on the Order Confirmation. "User", as used herein, means the person or entity making such republication.

2. The terms set forth in the relevant Order Confirmation, and any terms set by the Rightsholder with respect to a particular Work, govern the terms of use of Works in connection with the Service. By using the Service, the person transacting for a republication license on behalf of the User represents and warrants that he/she/it (a) has been duly authorized by the User to accept, and hereby does accept, all such terms and conditions on behalf of User, and (b) shall inform User of all such terms and conditions. In the event such person is a "freelancer" or other third party independent of User and CCC, such party shall be deemed jointly a "User" for purposes of these terms and conditions. In any event, User shall be deemed to have accepted and agreed to all such terms and conditions if User republishes the Work in any fashion.

3. Scope of License; Limitations and Obligations.

   3.1. All Works and all rights therein, including copyright rights, remain the sole and exclusive property of the Rightsholder. The license created by the exchange of an Order Confirmation (and/or any invoice) and payment by User of the full amount set forth on that document includes only those rights expressly set forth in the Order Confirmation and in these terms and conditions, and conveys no other rights in the Work(s) to User. All rights not expressly granted are hereby reserved.

   3.2. General Payment Terms: You may pay by credit card or through an account with us payable at the end of the month. If you and we agree that you may establish a standing account with CCC, then the following terms apply: Remit Payment to: Copyright Clearance Center, 29118 Network Place, Chicago, IL 60673-1291. Payments Due: Invoices are payable upon their delivery to you (or upon our notice to you that they are available to you for downloading). After 30 days, outstanding amounts will be subject to a service charge of 1-1/2% per month or, if less, the maximum rate allowed by applicable law. Unless otherwise specifically set forth in the Order Confirmation or in a separate written agreement signed by CCC, invoices are due and payable on "net 30" terms. While User may exercise the rights licensed immediately upon issuance of the Order Confirmation, the license is automatically revoked and is null and void, as if it had never been issued, if complete payment for the license is not received on a timely basis either from User directly or through a payment agent, such as a credit card company.

   3.3.
   Unless otherwise provided in the Order Confirmation, any grant of rights to User (i) is "one-time" (including

165

the editions and product family specified in the license), (ii) is non-exclusive and non-transferable and (iii) is subject to any and all limitations and restrictions (such as, but not limited to, limitations on duration of use or circulation) included in the Order Confirmation or invoice and/or in these terms and conditions. Upon completion of the licensed use, User shall either secure a new permission for further use of the Work(s) or immediately cease any new use of the Work(s) and shall render inaccessible (such as by deleting or by removing or severing links or other locators) any further copies of the Work (except for copies printed on paper in accordance with this license and still in User's stock at the end of such period).

3.4. In the event that the material for which a republication license is sought includes third party materials (such as photographs, illustrations, graphs, inserts and similar materials) which are identified in such material as having been used by permission, User is responsible for identifying, and seeking separate licenses (under this Service or otherwise) for, any of such third party materials; without a separate license, such third party materials may not be used.

3.5. Use of proper copyright notice for a Work is required as a condition of any license granted under the Service. Unless otherwise provided in the Order Confirmation, a proper copyright notice will read substantially as follows: "Republished with permission of [Rightsholder's name], from [Work's title, author, volume, edition number and year of copyright]; permission conveyed through Copyright Clearance Center, Inc. " Such notice must be provided in a reasonably legible font size and must be placed either immediately adjacent to the Work as used (for example, as part of a by-line or footnote but not as a separate electronic link) or in the place where substantially all other credits or notices for the new work containing the republished Work are located. Failure to include the required notice results in loss to the Rightsholder and CCC, and the User shall be liable to pay liquidated damages for each such failure equal to twice the use fee specified in the Order Confirmation, in addition to the use fee itself and any other fees and charges specified.

3.6. User may only make alterations to the Work if and as expressly set forth in the Order Confirmation. No Work may be used in any way that is defamatory, violates the rights of third parties (including such third parties' rights of copyright, privacy, publicity, or other tangible or intangible property), or is otherwise illegal, sexually explicit or obscene. In addition, User may not conjoin a Work with any other material that may result in damage to the reputation of the Rightsholder. User agrees to inform CCC if it becomes aware of any infringement of any rights in a Work and to cooperate with any reasonable request of CCC or the Rightsholder in connection therewith.

4. Indemnity. User hereby indemnifies and agrees to defend the Rightsholder and CCC, and their respective employees and directors, against all claims, liability, damages, costs and expenses, including legal fees and expenses, arising out of any use of a Work beyond the scope of the rights granted herein, or any use of a Work which has been altered in any unauthorized way by User, including claims of defamation or infringement of rights of copyright, publicity, privacy or other tangible or intangible property.

5. Limitation of Liability. UNDER NO CIRCUMSTANCES WILL CCC OR THE RIGHTSHOLDER BE LIABLE FOR ANY DIRECT, INDIRECT, CONSEQUENTIAL OR INCIDENTAL DAMAGES (INCLUDING WITHOUT LIMITATION DAMAGES FOR LOSS OF BUSINESS PROFITS OR INFORMATION, OR FOR BUSINESS INTERRUPTION) ARISING OUT OF THE USE OR INABILITY TO USE A WORK, EVEN IF ONE OF THEM HAS BEEN ADVISED OF THE POSSIBILITY OF SUCH DAMAGES. In any event, the total liability of the Rightsholder and CCC (including their respective employees and directors) shall not exceed the total amount actually paid by User for this license. User assumes full liability for the actions and omissions of its principals, employees, agents, affiliates, successors and assigns.

6.
Limited Warranties. THE WORK(S) AND RIGHT(S) ARE PROVIDED "AS IS". CCC HAS THE RIGHT TO GRANT TO USER THE RIGHTS GRANTED IN THE ORDER CONFIRMATION DOCUMENT. CCC AND THE RIGHTSHOLDER DISCLAIM ALL OTHER WARRANTIES RELATING TO THE WORK(S) AND RIGHT(S), EITHER EXPRESS OR IMPLIED, INCLUDING WITHOUT LIMITATION IMPLIED WARRANTIES OF MERCHANTABILITY OR FITNESS FOR A PARTICULAR PURPOSE. ADDITIONAL RIGHTS MAY BE REQUIRED TO USE ILLUSTRATIONS, GRAPHS, PHOTOGRAPHS, ABSTRACTS, INSERTS OR OTHER PORTIONS OF THE WORK (AS OPPOSED TO THE ENTIRE WORK) IN A MANNER CONTEMPLATED BY USER; USER UNDERSTANDS AND AGREES THAT NEITHER CCC NOR THE RIGHTSHOLDER MAY HAVE SUCH ADDITIONAL RIGHTS TO GRANT.

7. Effect of Breach. Any failure by User to pay any amount when due, or any use by User of a Work beyond the scope of the license set forth in the Order Confirmation and/or these terms and conditions, shall be a material breach of the license created by the Order Confirmation and these terms and conditions. Any breach not cured within 30 days of written notice thereof shall result in immediate termination of such license without further notice. Any unauthorized (but licensable) use of a Work that is terminated immediately upon notice thereof may be liquidated by payment of the Rightsholder's ordinary license price therefor; any unauthorized (and unlicensable) use that is not terminated immediately for any reason (including, for example, because materials containing the Work cannot reasonably be recalled) will be subject to all remedies available at law or in equity, but in no event to a payment of less than three times the Rightsholder's ordinary license price for the most closely analogous licensable use plus Rightsholder's and/or CCC's costs and expenses incurred in collecting such payment.

8. Miscellaneous.

   8.1. User acknowledges that CCC may, from time to time, make changes or additions to the Service or to these terms and conditions, and CCC reserves the right to send notice to the User by electronic mail or otherwise for the purposes of notifying User of such changes or additions; provided that any such changes or additions shall not apply to permissions already secured and paid for.

   8.2. Use of User-related information collected through the Service is governed by CCC's privacy policy, available online here:https://marketplace.copyright.com/rs-ui-web/mp/privacy-policy

   8.3. The licensing transaction described in the Order Confirmation is personal to User. Therefore, User may not assign or transfer to any other person (whether a natural person or an organization of any kind) the license created by the Order Confirmation and these terms and conditions or any rights granted hereunder; provided, however, that User may assign such license in its entirety on written notice to CCC in the event of a transfer of all or substantially all of User's rights in the new material which includes the Work(s) licensed under this Service.

   8.4. No amendment or waiver of any terms is binding unless set forth in writing and signed by the parties. The Rightsholder and CCC hereby object to any terms contained in any writing prepared by the User or its principals, employees, agents or affiliates and purporting to govern or otherwise relate to the licensing transaction described in the Order Confirmation, which terms are in any way inconsistent with any terms set forth in the Order Confirmation and/or in these terms and conditions or CCC's standard operating procedures, whether such writing is prepared prior to, simultaneously with or subsequent to the Order Confirmation, and whether such writing appears on a copy of the Order Confirmation or in a separate instrument.

   8.5. The licensing transaction described in the Order Confirmation document shall be governed by and construed under the law of the State of New York, USA, without regard to the principles thereof of conflicts of law. Any case, controversy, suit, action, or proceeding arising out of, in connection with, or related to such licensing transaction shall be brought, at CCC's sole discretion, in any federal or state court located in the County of New York, State of New York, USA, or in any federal or state court whose geographical jurisdiction covers the location of the Rightsholder set forth in the Order Confirmation. The parties expressly submit to the personal jurisdiction and venue of each such federal or state court.If you have any comments or questions about the Service or Copyright Clearance Center, please contact us at 978-750-8400 or send an e-mail to support@copyright.com.

v 1.1

APPENDIX H:
COPYRIGHT PERMISSIONS FOR CHAPTER 4, FIGURE 3

JOHN WILEY AND SONS LICENSE
TERMS AND CONDITIONS

Oct 22, 2020

This Agreement between Ms. Cacie Hart ("You") and John Wiley and Sons ("John Wiley and Sons") consists of your license details and the terms and conditions provided by John Wiley and Sons and Copyright Clearance Center.

License Number	4932080383180
License date	Oct 18, 2020
Licensed Content Publisher	John Wiley and Sons
Licensed Content Publication	Biotechnology Journal
Licensed Content Title	Characterization of cell viability during bioprinting processes
Licensed Content Author	Wei Sun, Kenneth Barbee, Michele Marcolongo, et al
Licensed Content Date	Aug 14, 2009
Licensed Content Volume	4
Licensed Content Issue	8
Licensed Content Pages	10
Type of Use	Dissertation/Thesis
Requestor type	University/Academic
Format	Electronic
Portion	Figure/table
Number of figures/tables	1
Will you be translating?	No
Title	Development of Facile Microfabrication Technologies for the Fabrication and Characterization of Multimodal Impedimetric, Plasmonic, and Electrophysiological Biosensors
Institution name	University of Central Florida
Expected presentation date	Nov 2020
Portions	Figure 6
Requestor Location	Ms. Cacie Hart 3206 Everett St APOPKA, FL 32703 United States Attn: Ms. Cacie Hart
Publisher Tax ID	EU826007151
Total	0.00 USD
Terms and Conditions	

TERMS AND CONDITIONS

Terms and Conditions

- The failure of either party to enforce any term or condition of this Agreement shall not constitute a waiver of either party's right to enforce each and every term and condition of this Agreement. No breach under this agreement shall be deemed waived or excused by either party unless such waiver or consent is in writing signed by the party granting such waiver or consent. The waiver by or consent of a party to a breach of any provision of this Agreement shall not operate or be construed as a waiver of or consent to any other or subsequent breach by such other party.

- This Agreement may not be assigned (including by operation of law or otherwise) by you without WILEY's prior written consent.

- Any fee required for this permission shall be non-refundable after thirty (30) days from receipt by the CCC.

- These terms and conditions together with CCC's Billing and Payment terms and conditions (which are incorporated herein) form the entire agreement between you and WILEY concerning this licensing transaction and (in the absence of fraud) supersedes all prior agreements and representations of the parties, oral or written. This Agreement may not be amended except in writing signed by both parties. This Agreement shall be binding upon and inure to the benefit of the parties' successors, legal representatives, and authorized assigns.

- In the event of any conflict between your obligations established by these terms and conditions and those established by CCC's Billing and Payment terms and conditions, these terms and conditions shall prevail.

- WILEY expressly reserves all rights not specifically granted in the combination of (i) the license details provided by you and accepted in the course of this licensing transaction, (ii) these terms and conditions and (iii) CCC's Billing and Payment terms and conditions.

- This Agreement will be void if the Type of Use, Format, Circulation, or Requestor Type was misrepresented during the licensing process.

- This Agreement shall be governed by and construed in accordance with the laws of the State of New York, USA, without regards to such state's conflict of law rules. Any legal action, suit or proceeding arising out of or relating to these Terms and Conditions or the breach thereof shall be instituted in a court of competent jurisdiction in New York County in the State of New York in the United States of America and each party hereby consents and submits to the personal jurisdiction of such court, waives any objection to venue in such court and consents to service of process by registered or certified mail, return receipt requested, at the last known address of such party.

WILEY OPEN ACCESS TERMS AND CONDITIONS

Wiley Publishes Open Access Articles in fully Open Access Journals and in Subscription journals offering Online Open. Although most of the fully Open Access journals publish open access articles under the terms of the Creative Commons Attribution (CC BY) License only, the subscription journals and a few of the Open Access Journals offer a choice of Creative Commons Licenses. The license type is clearly identified on the article.

The Creative Commons Attribution License

The Creative Commons Attribution License (CC-BY) allows users to copy, distribute and transmit an article, adapt the article and make commercial use of the article. The CC-BY license permits commercial and non-

Creative Commons Attribution Non-Commercial License

The Creative Commons Attribution Non-Commercial (CC-BY-NC)License permits use, distribution and reproduction in any medium, provided the original work is properly cited and is not used for commercial purposes.(see below)

Creative Commons Attribution-Non-Commercial-NoDerivs License

The Creative Commons Attribution Non-Commercial-NoDerivs License (CC-BY-NC-ND) permits use, distribution and reproduction in any medium, provided the original work is properly cited, is not used for commercial purposes and no modifications or adaptations are made. (see below)

Use by commercial "for-profit" organizations

Use of Wiley Open Access articles for commercial, promotional, or marketing purposes requires further explicit permission from Wiley and will be subject to a fee.

Further details can be found on Wiley Online Library http://olabout.wiley.com/WileyCDA/Section/id-410895.html

Other Terms and Conditions:

APPENDIX I:
COPYRIGHT PERMISSIONS FOR AUTHOR'S PUBLISHED MATERIAL
INCLUDED WITHIN THIS DISSERTATION

The author's publications in *Biosensors* and *Micromachines* are MDPI journals, which are eligible for sharing under the Creative Commons license.

Investigation of the Enhanced Sensitivity of Interdigitated Electrodes for Cellular Biosensing With Geometric, Nanostructured Surface Area, and Surface Plasmon Resonance Modes

IEEE

Requesting permission to reuse content from an IEEE publication

Author: Cacie Hart

Publication: Microelectromechanical Systems, IEEE/ASME Journal of

Publisher: IEEE

Date: Oct. 2020

Copyright © 2020, IEEE

Precision Plating of Human Electrogenic Cells on Microelectrodes Enhanced With Precision Electrodeposited Nano-Porous Platinum for Cell-Based Biosensing Applications

IEEE

Requesting permission to reuse content from an IEEE publication

Author: Nilab Azim

Publication: Microelectromechanical Systems, IEEE/ASME Journal of

Publisher: IEEE

Date: Feb. 2019

Copyright © 2019, IEEE

Thesis / Dissertation Reuse

The IEEE does not require individuals working on a thesis to obtain a formal reuse license, however, you may print out this statement to be used as a permission grant:

Requirements to be followed when using any portion (e.g., figure, graph, table, or textual material) of an IEEE copyrighted paper in a thesis:

1) In the case of textual material (e.g., using short quotes or referring to the work within these papers) users must give full credit to the original source (author, paper, publication) followed by the IEEE copyright line © 2011 IEEE.
2) In the case of illustrations or tabular material, we require that the copyright line © [Year of original publication] IEEE appear prominently with each reprinted figure and/or table.
3) If a substantial portion of the original paper is to be used, and if you are not the senior author, also obtain the senior author's approval.

Requirements to be followed when using an entire IEEE copyrighted paper in a thesis:

1) The following IEEE copyright/ credit notice should be placed prominently in the references: © [year of original publication] IEEE. Reprinted, with permission, from [author names, paper title, IEEE publication title, and month/year of publication]
2) Only the accepted version of an IEEE copyrighted paper can be used when posting the paper or your thesis on-line.
3) In placing the thesis on the author's university website, please display the following message in a prominent place on the website: In reference to IEEE copyrighted material which is used with permission in this thesis, the IEEE does not endorse any of [university/educational entity's name goes here]'s products or services. Internal or personal use of this material is permitted. If interested in reprinting/republishing IEEE copyrighted material for advertising or promotional purposes or for creating new collective works for resale or redistribution, please go to http://www.ieee.org/publications_standards/publications/rights/rights_link.html to learn how to obtain a License from RightsLink.

If applicable, University Microfilms and/or ProQuest Library, or the Archives of Canada may supply single copies of the dissertation.

BACK — CLOSE WINDOW

REFERENCES

[1]   X. W. H. Wang, P.Dong, C. Wang, J. Wang, Y. Liu, and J. Chen, "Electrochemical
        Biosensor Based on Interdigitated Electrodes for Determination of Thyroid Stimulating
        Hormone," *International Journal of Electrochemical Science,* vol. 9, pp. 12-21, 2014.

[2]   P. Y. P. Adelyn *et al.*, "Transparent mask design and fabrication of interdigitated
        electrodes," in *2015 IEEE Regional Symposium on Micro and Nanoelectronics (RSM)*,
        19-21 Aug. 2015 2015, pp. 1-4, doi: 10.1109/RSM.2015.7355014.

[3]   A. Rivadeneyra, J. Fernández-Salmerón, J. Banqueri, J. A. López-Villanueva, L. F.
        Capitan-Vallvey, and A. J. Palma, "A novel electrode structure compared with
        interdigitated electrodes as capacitive sensor," *Sensors and Actuators B: Chemical,* vol.
        204, pp. 552-560, 2014/12/01/ 2014, doi: https://doi.org/10.1016/j.snb.2014.08.010.

[4]   H. Schift, R. W. Jaszewski, C. David, and J. Gobrecht, "Nanostructuring of polymers and
        fabrication of interdigitated electrodes by hot embossing lithography," *Microelectronic
        Engineering,* vol. 46, no. 1, pp. 121-124, 1999/05/01/ 1999, doi:
        https://doi.org/10.1016/S0167-9317(99)00030-1.

[5]   I. T. Ozbolat, K. K. Moncal, and H. Gudapati, "Evaluation of bioprinter technologies,"
        Additive Manufacturing, vol. 13, pp. 179-200, 2017/01/01/ 2017, doi:
        https://doi.org/10.1016/j.addma.2016.10.003.

[6]   J. M. Williams *et al.*, "Bone tissue engineering using polycaprolactone scaffolds
        fabricated via selective laser sintering," *Biomaterials,* vol. 26, no. 23, pp. 4817-4827,
        2005/08/01/ 2005, doi: https://doi.org/10.1016/j.biomaterials.2004.11.057.

[7]   Q. Hamid *et al.*, "Fabrication of three-dimensional scaffolds using precision extrusion deposition with an assisted cooling device," *Biofabrication,* vol. 3, no. 3, p. 034109, 2011/07/05 2011, doi: 10.1088/1758-5082/3/3/034109.

[8]   S. Tarafder, V. K. Balla, N. M. Davies, A. Bandyopadhyay, and S. Bose, "Microwave-sintered 3D printed tricalcium phosphate scaffolds for bone tissue engineering," (in eng), *J Tissue Eng Regen Med,* vol. 7, no. 8, pp. 631-641, 2013, doi: 10.1002/term.555.

[9]   S. A. Skoog, P. L. Goering, and R. J. Narayan, "Stereolithography in tissue engineering," (in eng), *J Mater Sci Mater Med,* vol. 25, no. 3, pp. 845-56, Mar 2014, doi: 10.1007/s10856-013-5107-y.

[10]   W. C. Wilson Jr. and T. Boland, "Cell and organ printing 1: Protein and cell printers," *The Anatomical Record Part A: Discoveries in Molecular, Cellular, and Evolutionary Biology,* vol. 272A, no. 2, pp. 491-496, 2003, doi: 10.1002/ar.a.10057.

[11]   P. Calvert, "Printing Cells," *Science,* vol. 318, no. 5848, pp. 208-209, 2007, doi: 10.1126/science.1144212.

[12]   N. S. Mazlan *et al.*, "Interdigitated electrodes as impedance and capacitance biosensors: A review," *AIP Conference Proceedings,* vol. 1885, no. 1, p. 020276, 2017, doi: 10.1063/1.5002470.

[13]   L. E. Delle *et al.*, "ScFv-modified graphene-coated IDE-arrays for 'label-free' screening of cardiovascular disease biomarkers in physiological saline," *Biosensors and Bioelectronics,* vol. 102, pp. 574-581, 2018/04/15/ 2018, doi: https://doi.org/10.1016/j.bios.2017.12.005.

[14]   H. M. Himmel, "Drug-induced functional cardiotoxicity screening in stem cell-derived human and mouse cardiomyocytes: Effects of reference compounds," *Journal of*

Pharmacological and Toxicological Methods, vol. 68, no. 1, pp. 97-111, 2013/07/01/ 2013, doi: https://doi.org/10.1016/j.vascn.2013.05.005.

[15] L. Guo *et al.*, "Estimating the Risk of Drug-Induced Proarrhythmia Using Human Induced Pluripotent Stem Cell–Derived Cardiomyocytes," *Toxicological Sciences,* vol. 123, no. 1, pp. 281-289, 2011, doi: 10.1093/toxsci/kfr158.

[16] N. Hu *et al.*, "High-performance beating pattern function of human induced pluripotent stem cell-derived cardiomyocyte-based biosensors for hERG inhibition recognition," *Biosensors and Bioelectronics,* vol. 67, pp. 146-153, 2015/05/15/ 2015, doi: https://doi.org/10.1016/j.bios.2014.07.080.

[17] N. Tandon *et al.*, "Surface-patterned electrode bioreactor for electrical stimulation," *Lab on a Chip,* 10.1039/B917743D vol. 10, no. 6, pp. 692-700, 2010, doi: 10.1039/B917743D.

[18] Y. Qiu, R. Liao, and X. Zhang, "Real-Time Monitoring Primary Cardiomyocyte Adhesion Based on Electrochemical Impedance Spectroscopy and Electrical Cell−Substrate Impedance Sensing," *Analytical Chemistry,* vol. 80, no. 4, pp. 990-996, 2008/02/01 2008, doi: 10.1021/ac701745c.

[19] T. Wang, N. Hu, J. Cao, J. Wu, K. Su, and P. Wang, "A cardiomyocyte-based biosensor for antiarrhythmic drug evaluation by simultaneously monitoring cell growth and beating," *Biosensors and Bioelectronics,* vol. 49, pp. 9-13, 2013/11/15/ 2013, doi: https://doi.org/10.1016/j.bios.2013.04.039.

[20] D. Krinke, H.-G. Jahnke, O. Pänke, and A. A. Robitzki, "A microelectrode-based sensor for label-free *in vitro* detection of ischemic effects on cardiomyocytes," *Biosensors and*

Bioelectronics, vol. 24, no. 9, pp. 2798-2803, 2009/05/15/ 2009, doi: https://doi.org/10.1016/j.bios.2009.02.006.

[21]   M. Contreras-Saenz, C. Hassard, R. Vargas-Chacon, J. L. Gordillo, and S. Camacho-Leon, *Maskless fabrication of a microfluidic device with interdigitated electrodes on PCB using laser ablation* (SPIE BiOS). SPIE, 2016.

[22]   F. Qian *et al.*, "Simultaneous electrical recording of cardiac electrophysiology and contraction on chip," *Lab on a Chip,* 10.1039/C7LC00210F vol. 17, no. 10, pp. 1732-1739, 2017, doi: 10.1039/C7LC00210F.

[23]   C. R. Hart, Swaminathan, "Multimodal Laser Micromachined Shadow Masks for Rapid Patterning of Sub-5um Organic and Inorganic Layers for Lab-on-a-Chip Applications," presented at the 22nd International Conference on Miniaturized Systems for Chemistry and Life Sciences (MicroTAS 2018), Kaohsiung, Taiwan, 2018.

[24]   C. Hart and S. Rajaraman, "Low-Power, Multimodal Laser Micromachining of Materials for Applications in sub-5 µm Shadow Masks and sub-10 µm Interdigitated Electrodes (IDEs) Fabrication," *Micromachines,* vol. 11, no. 2, 2020, doi: 10.3390/mi11020178.

[25]   G. Bloembergen, "Laser-material interactions, fundamentals and applications Laser Ablation: Mechanisms and Applications II," in *AIP Conf. Proc. JC Miller, DB Geohegan eds*, 1994, vol. 288.

[26]   J. Miller, "History, scope, and the future of laser ablation," in *Laser Ablation*: Springer, 1994, pp. 1-10.

[27]   Y. Kawamura, K. Toyoda, and S. Namba, "Effective deep ultraviolet photoetching of polymethyl methacrylate by an excimer laser," *Applied Physics Letters,* vol. 40, no. 5, pp. 374-375, 1982.

[28]   R. Srinivasan and V. Mayne-Banton, "Self-developing photoetching of poly (ethylene

terephthalate) films by far-ultraviolet excimer laser radiation," *Applied Physics Letters,*

vol. 41, no. 6, pp. 576-578, 1982.

[29]   J. P. K. Henning Klank, and Oliver Geschke, "CO2-laser micromachining and back-end

processing for rapid production of PMMA-based microfluidic systems," *Lab on a Chip,*

vol. 2, pp. 242-246, 2002.

[30]   R. J. M. R. Rox Anderson, Shinichi Watenabe, Thomas Flotte, George J. Hruza, adn

Jeffrey S. Dover, "Selective photothermolysis of cutaneous pigmentation by q-switched

Nd:YAG laser pulses at 1064, 532, and 355 nm," *Journal of Investigative Dermatology,*

vol. 93, pp. 28-32, 1989.

[31]   H. L. Y. Fan, Y. Yi, and I.G. Foulds, "Laser micromachined wax-covered plastic paper as

both sputter deposition shadow masks and deep-ultraviolet patterning masks for

polymethylmethacrylate-based microfluidic systems," *Journal of Micro/nanolithography,*

MEMS, and MOEMS, vol. 12, no. 4, p. 049701, 2013.

[32]   H.-L. C. Yu-Hsuan Hung, Yung-Chun Lee, "Excimer laser three-dimensional

micromachining based on image projection and the optical diffraction effect," *Applied*

Sciences, vol. 8, p. 1690, 2018.

[33]   R. D. Schaeffer, *Fundamentals of Laser Micromachining*. Boca Raton: CRC Press, 2012.

[34]   M. S. B. a. C. B. Arnold, "Fundamentals of Laser-Material Interaction and Application to

Multiscale Surface Modification," in *Laser Precision Microfabrication*, vol. 135, M. M.

K. Sugioka, and A. Pique Ed. Berlin: Springer, 2010.

[35]   N. H. Rizvi and P. Apte, "Developments in laser micro-machining techniques," *Journal of Materials Processing Technology,* vol. 127, no. 2, pp. 206-210, 2002/09/30/ 2002, doi: https://doi.org/10.1016/S0924-0136(02)00143-7.

[36]   C. B. A. a. A. Pique, "Laser Direct-Write Processing," *MRS Bulletin,* vol. 32, pp. 9-15, 2007.

[37]   P. R. Miller, R. Aggarwal, A. Doraiswamy, Y. J. Lin, Y.-S. Lee, and R. J. Narayan, "Laser micromachining for biomedical applications," *JOM,* vol. 61, no. 9, pp. 35-40, 2009/09/01 2009, doi: 10.1007/s11837-009-0130-7.

[38]   M. Gower, *Laser micromachining for manufacturing MEMS devices* (Micromachining and Microfabrication). SPIE, 2001.

[39]   U. S. V. Schutz, and A. Horn, "Thermodynamic investigations on the laser ablation rate of silicon over five fluence decades," *Physics Procedia,* Lasers in Manufacturing Conference 2013, pp. 640-649, 2013.

[40]   R. A. Bashir Ahmed Tahir, M.G.B. Ashiq, Afaq Ahmed, and M.A. Saeed, "Cutting of nonmetallic materials using Nd:YAG laser beam," *Chinese Physics B,* vol. 21, no. 4, p. 044201, 2012.

[41]   C. C. F. D. Petit, S. Johnstone, D. Wood, and R.P. Cowburn, "Nanometer scale patterning using focused ion beam milling," *Review of Scientific Instruments,* vol. 76, p. 026105, 2005.

[42]   T. E. d. G. David. J. Guckenberger, Alwin M.D. Wan, David J. Beebe, and Edmond W.K. Young, "Micromilling: a method for ultra-rapid prototyping of plastic microfluidic devices," *Lab on a Chip,* vol. 15, p. 2364, 2015.

[43]   H. G. Henri Jansen, Meint de Boer, Miko Elwenspoek, and Jan Fluitman, "A survey on the reactive ion etching of silicon in microtechnology," *Journal of Micromechanics and Microengineering,* vol. 6, p. 14, 1995.

[44]   P. H. Ivo Utke, and John Melngailis, "Gas-assisted focused electron beam and ion beam processing and fabrication," *Journal of Vacuum Science & Technology B,* vol. 26, p. 1197, 2008.

[45]   F. Karouta, "A practical approach to reactive ion etching," *Journal of Physics D: Applied Physics,* vol. 47, no. 3, p. 233501, 2014.

[46]   G. M. Peake *et al.*, "A micromachined, shadow-mask technology for the OMVPE fabrication of integrated optical structures," *Journal of Electronic Materials,* journal article vol. 29, no. 1, pp. 86-90, January 01 2000, doi: 10.1007/s11664-000-0100-x.

[47]   A. A. Tseng, "Recent developments in micromilling using focused ion beam technology," *Journal of Micromechanics and Microengineering,* vol. 14, p. R15, 2004.

[48]   A. A. Anbesh Jamwal, Nishant Gautam, Akhil Devarapalli, "Electro-Discharge Machining: Recent Developments and Trends," *IRJET,* vol. 5, no. 2, pp. 433-448, 2018.

[49]   S. K. a. A. Dvivedi, "On machining of hard and brittle materials using rotary too micro-ultrasonic drilling process," *Materials and Manufacturing Processes,* vol. 34, no. 7, pp. 736-748, 2019.

[50]   Z. L. Xiaochu Liu, Guilin Wen, Xuefeng Yuan, "Waterjet Machining and Research Developments: A Review," *International Journal of Advanced Manufacturing Technology,* vol. 102, no. 5-8, pp. 1257-1335, 2019.

[51]   A. G. A. Kumar, R. Kant, S.N. Akhtar, N. Tiwari, J. Ramkumar, and S. Bhattacharya, "Optimization of laser machining process for the preparation of photomasks and its

application to microsystems fabrication," *Journal of Micro/nanolithography, MEMS, and MOEMS,* vol. 12, no. 4, p. 041203, 2013.

[52]   H. M. J. Heo, M. Lee, "Laser micromachining of permalloy for fine metal mask," *International Journal of Precision Engineering and Manufacturing - Green Technology,* vol. 2, no. 3, pp. 225-230, 2015.

[53]   M. R. H. Knowles, G. Rutterford, D. Karnakis, and A. Ferguson, "Micro-machining of metals, ceramics and polymers using nanosecond lasers," *The International Journal of Advanced Manufacturing Technology,* vol. 33, no. 1, pp. 95-102, 2007/05/01 2007, doi: 10.1007/s00170-007-0967-2.

[54]   X. Liu, D. Du, and G. Mourou, "Laser ablation and micromachining with ultrashort laser pulses," *IEEE Journal of Quantum Electronics,* vol. 33, no. 10, pp. 1706-1716, 1997, doi: 10.1109/3.631270.

[55]   K. Oblov *et al.*, "Fabrication of Microhotplates Based on Laser Micromachining of Zirconium Oxide," *Physics Procedia,* vol. 72, pp. 485-489, 2015/01/01/ 2015, doi: https://doi.org/10.1016/j.phpro.2015.09.057.

[56]   R. Moser *et al.*, "Laser processing of gallium nitride-based light-emitting diodes with ultraviolet picosecond laser pulses," *Optical Engineering,* vol. 51, no. 11, p. 114301, 2012. [Online]. Available: https://doi.org/10.1117/1.OE.51.11.114301.

[57]   M. Apanius, P. B. Kaul, and A. R. Abramson, "Silicon shadow mask fabrication for patterned metal deposition with microscale dimensions using a novel corner compensation scheme," *Sensors and Actuators A: Physical,* vol. 140, no. 2, pp. 168-175, 2007/11/10/ 2007, doi: https://doi.org/10.1016/j.sna.2007.06.028.

[58]   P. Y. P. Adelyn *et al.*, "Transparent Mask Design and Fabrication of Interdigitated Electrodes," in *RSM2015 Proc.*, K. Terengganu, Malaysia, 2015.

[59]   Y. Fan, H. Li, Y. Yi, and I. G. Foulds, "Laser micromachined wax-covered plastic paper as both sputter deposition shadow masks and deep-ultraviolet patterning masks for polymethylmethacrylate-based microfluidic systems," *J. Micro/nano-litho, MEMS, MOEMS,* vol. 12, no. 4, p. 049701, 2013.

[60]   F. Alexander Jr., D. T. Price, and S. Bhansali, "Optimization of interdigitated electrode (IDE) arrays for impedance based evaluation of Hs 578T cancer cells," *J. Phys: Conf. Series,* vol. 224, no. 1, p. 012134, 2010.

[61]   A. Bratov *et al.*, "Three-dimensional interdigitated electrode array as a transducer for label-free biosensors," *Biosensors & Bioelectronics,* vol. 24, pp. 729-735, 2008.

[62]   K.-S. Chou and C.-H. Lee, "Fabrication of Silver Interdigitated Electrode by a Stamp Method," *Adv. Mat. Sci. Eng.,* vol. 2014, p. 5 pages, 2014.

[63]   J.-Y. Cheng, C.-W. Wei, K.-H. Hsu, and T.-H. Young, "Direct-write laser micromachining and universal surface modification of PMMA for device development," *Sensors and Actuators B: Chemical,* vol. 99, no. 1, pp. 186-196, 2004/04/15/ 2004, doi: https://doi.org/10.1016/j.snb.2003.10.022.

[64]   I. L. Y. Chung, J.-D. Kim, and K.-H. Kang, "Ablation drilling of invar alloy using ultrashort pulsed laser," *International Journal of Precision Engineering and Manufacturing,* vol. 10, no. 2, pp. 11-16, 2009/04/01 2009, doi: 10.1007/s12541-009-0021-4.

[65]   J. Ihlemann and K. Rubahn, "Excimer laser micro machining: fabrication and applications of dielectric masks," *Applied Surface Science,* vol. 154-155, pp. 587-592, 2000/02/01/ 2000, doi: https://doi.org/10.1016/S0169-4332(99)00464-X.

[66]   J. H. Lee, J. W. Yoon, I. G. Kim, J. S. Oh, H. J. Nam, and D. Y. Jung, "Fabrication of polydimethylsiloxane shadow masks for chemical solution deposition of CdS thin-film transistors," *Thin Solid Films,* vol. 516, no. 18, pp. 6492-6498, 2008/07/31/ 2008, doi: https://doi.org/10.1016/j.tsf.2008.02.041.

[67]   J. Li and G. K. Ananthasuresh, "A quality study on the excimer laser micromachining of electro-thermal-compliant micro devices," *Journal of Micromechanics and Microengineering,* vol. 11, no. 1, pp. 38-47, 2000/12/05 2000, doi: 10.1088/0960-1317/11/1/307.

[68]   N. C. Nayak, Y. C. Lam, C. Y. Yue, and A. T. Sinha, "CO2-laser micromachining of PMMA: the effect of polymer molecular weight," *Journal of Micromechanics and Microengineering,* vol. 18, no. 9, p. 095020, 2008/08/13 2008, doi: 10.1088/0960-1317/18/9/095020.

[69]   W. Pfleging, W. Bernauer, T. Hanemann, and M. Torge, "Rapid fabrication of microcomponents – UV-laser assisted prototyping, laser micro-machining of mold inserts and replication via photomolding," *Microsystem Technologies,* vol. 9, no. 1, pp. 67-74, 2002/11/01 2002, doi: 10.1007/s00542-002-0197-3.

[70]   G. Ricciardi, M. Cantello, F. Mariotti, P. Castelli, and P. Giacosa, "Micromachining with Excimer Laser," *CIRP Annals,* vol. 47, no. 1, pp. 145-148, 1998/01/01/ 1998, doi: https://doi.org/10.1016/S0007-8506(07)62804-2.

[71]	P. P. Shiu, G. K. Knopf, M. Ostojic, and S. Nikumb, "Rapid fabrication of tooling for microfluidic devices via laser micromachining and hot embossing," *Journal of Micromechanics and Microengineering,* vol. 18, no. 2, p. 025012, 2008/01/04 2008, doi: 10.1088/0960-1317/18/2/025012.

[72]	D. Teixidor, T. Thepsonthi, J. Ciurana, and T. Özel, "Nanosecond pulsed laser micromachining of PMMA-based microfluidic channels," *Journal of Manufacturing Processes,* vol. 14, no. 4, pp. 435-442, 2012/10/01/ 2012, doi: https://doi.org/10.1016/j.jmapro.2012.09.001.

[73]	D. Yuan and S. Das, "Experimental and theoretical analysis of direct-write laser micromachining of polymethyl methacrylate by CO2 laser ablation," *Journal of Applied Physics,* vol. 101, no. 2, p. 024901, 2007, doi: 10.1063/1.2409621.

[74]	D. Yang, V. Pankov, L. Zhao, and P. Patnaik, "Laser deposited high temperature thin film sensors for gas turbines," *Aircraft Engineering and Aerospace Technology,* vol. 92, no. 1, pp. 2-7, 2020, doi: 10.1108/AEAT-11-2018-0292.

[75]	A. Kumar *et al.*, "Optimization of laser machining process for the preparation of photomasks, and its application to microsystems fabrication," *J. Micro/nano-litho, MEMS, MOEMS,* vol. 12, no. 4, p. 041203, 2013.

[76]	H. Klank, J. P. Kutter, and O. Geschke, "CO2-laser micromachining and back-end processing for rapid production of PMMA-based microfluidic systems," *Lab Chip,* vol. 2, pp. 242-246, 2002.

[77]	R. Pethig, J. P. H. Burt, A. Parton, N. Rizvi, M. S. Talary, and J. A. Tame, "Development of biofactory-on-a-chip technology using excimer laser micromachining," *J. Micromech. Microeng.,* vol. 8, no. 2, pp. 57-63, 1998.

[78]   V. V. Kancharla and S. Chen, "Fabrication of biodegradable polymeric micro-devices using laser micromachining," *Biomed Microdevices,* vol. 4, no. 2, pp. 105-109, 2002.

[79]   S. B. Blickenstaff, T. R. Nelson, and A. M. Sarangan, "Techniques for shadow mask deposition of nonplanar dielectric layers," in *Proc. of the 16th Annual Meeting of the IEEE Lasers and Electro-Optics Society*, Tucson, AZ, USA, 2003.

[80]   J. Heo, H. Min, and M. Lee, "Laser micromchining of permalloy for fine metal mask," *International Journal of Precision Eng. & Manuf. Green Tech.,* vol. 2, no. 3, pp. 225-230, 2015.

[81]   J. T. C. Yeh, "Laser ablation of polymers," *Journal of Vacuum Science & Technology A,* vol. 4, p. 653, 1986.

[82]   V. V. K. a. S. Chen, "Fabrication of Biodegradable Polymeric Micro-devices using Laser Micromachining," *Biomedical Microdevices,* vol. 4, no. 2, pp. 105-109, 2002.

[83]   L. J. L. Patrick Lorazo, and Michel Meunier, "Thermodynamic pathways to melting, ablation, and solidification in absorbing solids under pulsed laser irradiation," *Physical Review B,* vol. 73, p. 134108, 2006.

[84]   N. B. B. Lukyanchuck, M. Himmelbauer, and N. Arnold, "UV-laser ablation of polyimide: from long to ultra-short laser pulses," *Nuclear Instruments and Methods in Physics Research B,* vol. 122, pp. 347-355, 1997.

[85]   D. Z. Yu Zhang, Jianjun Wu, Zhen He, and Xiong Deng, "A thermal model for nanosecond pulsed laser ablation of aluminum," *AIP Advances,* vol. 7, p. 075010, 2017.

[86]   R. DeHoff, *Thermodynamics in Materials Science*, Second ed. Boca Raton: CRC Press, 2006.

[87]   R. E. Taylor, *CINDAS Data Series on Materials Properties: Thermal Expansion of Solids*. ASM International, 1998.

[88]   N. S. Yeqing Wang, Getachew K. Befekadu, and Crystal L. Pasiliao, "Modeling pulsed laser ablation of aluminum with finite element analysis considering material moving front," *Inernational Journal of Heat and Mass Transfer,* vol. 113, pp. 1246-1253, 2017.

[89]   J. Cheng *et al.*, "A review of ultrafast laser materials micromachining," *Optics & Laser Technology,* vol. 46, pp. 88-102, 2013/03/01/ 2013, doi: https://doi.org/10.1016/j.optlastec.2012.06.037.

[90]   A. K. Cacie Hart, Kowsik Kumar, Sreekanth J. Varma, Jayan Thomas, and Swaminathan Rajaraman, "Rapid nanofabrication of nanostructured interdigitated electrodes (nIDEs) for long-term *in vitro* analysis of human induced pluripotent stem cell differentiated cardiomyocytes," *Biosensors,* vol. 8, p. 88, 2018.

[91]   H. H. a. Z. Guo, "Ultra-short pulsed laser PDMS thin-layer separation and micro-fabrication," *Journal of Micromechanics and Microengineering,* vol. 19, p. 055007, 2009.

[92]   F. Alexander, D. T. Price, and S. Bhansali, "Optimization of interdigitated electrode (IDE) arrays for impedance based evaluation of Hs 578T cancer cells," *Journal of Physics: Conference Series,* vol. 224, p. 012134, 2010/04/01 2010, doi: 10.1088/1742-6596/224/1/012134.

[93]   C. Hart, C. M. Didier, F. Sommerhage, and S. Rajaraman, "Biocompatibility of Blank, Post-Processed and Coated 3D Printed Resin Structures with Electrogenic Cells," *Biosensors,* vol. 10, no. 11, p. 152, 2020. [Online]. Available: https://www.mdpi.com/2079-6374/10/11/152.

[94]   P. C. A. Kundu, C. Didier, C. Hart, F. Sommerhage, and S. Rajaraman, "Makerspace Microfabrication of a Stainless Steel 3D Microneedle Electrode Array (3D MEA) on a Glass Substrate for Simultaneous Optical and Electrical Probing of Electrogenic Cells," *RSC Advances,* 2020.

[95]   A. K. P.M. Morales Carvajal, C. Didier, C. Hart, F. Sommerhage and S. Rajaraman, "Microfabrication and Assembly of a 3D Microelectrode Array (MEA) for Simultaneous Optical and Electrical Probing of an Electrogenic "Organ-on-a-Chip" Model," presented at the NanoFlorida 2019, Tampa, FL, November 2019, 2019.

[96]   N. Azim, C. Hart, F. Sommerhage, M. Aubin, J. J. Hickman, and S. Rajaraman, "Precision Plating of Human Electrogenic Cells on Microelectrodes Enhanced With Precision Electrodeposited Nano-Porous Platinum for Cell-Based Biosensing Applications," *Journal of Microelectromechanical Systems,* vol. 28, no. 1, pp. 50-62, 2019, doi: 10.1109/JMEMS.2018.2879577.

[97]   A. D. Gitler, P. Dhillon, and J. Shorter, "Neurodegenerative disease: models, mechanisms, and a new hope," *Disease Models & Mechanisms,* vol. 10, no. 5, pp. 499-502, 2017, doi: 10.1242/dmm.030205.

[98]   J.-Q. He, Y. Ma, Y. Lee, J. A. Thomson, and T. J. Kamp, "Human Embryonic Stem Cells Develop Into Multiple Types of Cardiac Myocytes," *Circulation Research,* vol. 93, no. 1, pp. 32-39, 2003, doi: doi:10.1161/01.RES.0000080317.92718.99.

[99]   "iCell Cardiomyocytes User Guide." (accessed 01 December 2017.

[100]   W. C. Claycomb *et al.*, "HL-1 cells: A cardiac muscle cell line that contracts and retains phenotypic characteristics of the adult cardiomyocyte," *Proceedings of the National Academy of Sciences,* vol. 95, no. 6, pp. 2979-2984, 1998, doi: 10.1073/pnas.95.6.2979.

[101] S. M. White, P. E. Constantin, and W. C. Claycomb, "Cardiac physiology at the cellular level: use of cultured HL-1 cardiomyocytes for studies of cardiac muscle cell structure and function," *American Journal of Physiology-Heart and Circulatory Physiology,* vol. 286, no. 3, pp. H823-H829, 2004, doi: 10.1152/ajpheart.00986.2003.

[102] A. K. Peter, M. A. Bjerke, and L. A. Leinwand, "Biology of the cardiac myocyte in heart disease," (in eng), *Mol Biol Cell,* vol. 27, no. 14, pp. 2149-2160, 2016, doi: 10.1091/mbc.E16-01-0038.

[103] B. X. E. Desbiolles, E. de Coulon, A. Bertsch, S. Rohr, and P. Renaud, "Intracellular Recording of Cardiomyocyte Action Potentials with Nanopatterned Volcano-Shaped Microelectrode Arrays," *Nano Letters,* vol. 19, no. 9, pp. 6173-6181, 2019/09/11 2019, doi: 10.1021/acs.nanolett.9b02209.

[104] S. P. Wells *et al.*, "Cardiomyocyte functional screening: interrogating comparative electrophysiology of high-throughput model cell systems," *American Journal of Physiology-Cell Physiology,* vol. 317, no. 6, pp. C1256-C1267, 2019/12/01 2019, doi: 10.1152/ajpcell.00306.2019.

[105] H. Waddell, S. Wells, C. Sim, E. Porrello, L. Delbridge, and J. Bell, "Microelectrode Array Screening of Different Cardiomyocyte Cultures Reveals Inherent Disparities in Cardiac Cell Electrophysiology," *Heart, Lung and Circulation,* vol. 28, p. S147, 2019, doi: 10.1016/j.hlc.2019.06.035.

[106] Z. C. Lin *et al.*, "Accurate nanoelectrode recording of human pluripotent stem cell-derived cardiomyocytes for assaying drugs and modeling disease," *Microsystems & Nanoengineering,* vol. 3, no. 1, p. 16080, 2017/03/13 2017, doi: 10.1038/micronano.2016.80.

[107] I. C. Marcu, A. Illaste, P. Heuking, M. E. Jaconi, and N. D. Ullrich, "Functional Characterization and Comparison of Intercellular Communication in Stem Cell-Derived Cardiomyocytes," *STEM CELLS,* vol. 33, no. 7, pp. 2208-2218, 2015/07/01 2015, doi: 10.1002/stem.2009.

[108] N. Milani-Nejad and P. M. L. Janssen, "Small and large animal models in cardiac contraction research: Advantages and disadvantages," *Pharmacology & Therapeutics,* vol. 141, no. 3, pp. 235-249, 2014/03/01/ 2014, doi: https://doi.org/10.1016/j.pharmthera.2013.10.007.

[109] P. Konopelski and M. Ufnal, "Electrocardiography in rats: a comparison to human," (in eng), *Physiol Res,* vol. 65, no. 5, pp. 717-725, 2016/11// 2016, doi: 10.33549/physiolres.933270.

[110] G. Hasenfuss, "Animal models of human cardiovascular disease, heart failure and hypertrophy," *Cardiovascular Research,* vol. 39, no. 1, pp. 60-76, 1998, doi: 10.1016/S0008-6363(98)00110-2.

[111] S. G. Marcela *et al.*, "Chronological and Morphological Study of Heart Development in the Rat," *The Anatomical Record,* vol. 295, no. 8, pp. 1267-1290, 2012/08/01 2012, doi: 10.1002/ar.22508.

[112] K. S. Louis and A. C. Siegel, "Cell Viability Analysis Using Trypan Blue: Manual and Automated Methods," in *Mammalian Cell Viability: Methods and Protocols*, M. J. Stoddart Ed. Totowa, NJ: Humana Press, 2011, pp. 7-12.

[113] R. Amin *et al.*, "3D-printed microfluidic devices," *Biofabrication,* vol. 8, no. 2, p. 022001, 2016/06/20 2016, doi: 10.1088/1758-5090/8/2/022001.

[114] A. K. Au, W. Huynh, L. F. Horowitz, and A. Folch, "3D-Printed Microfluidics," *Angewandte Chemie International Edition,* vol. 55, no. 12, pp. 3862-3881, 2016, doi: 10.1002/anie.201504382.

[115] N. Bhattacharjee, A. Urrios, S. Kang, and A. Folch, "The upcoming 3D-printing revolution in microfluidics," *Lab on a Chip,* 10.1039/C6LC00163G vol. 16, no. 10, pp. 1720-1742, 2016, doi: 10.1039/C6LC00163G.

[116] B. C. Gross, J. L. Erkal, S. Y. Lockwood, C. Chen, and D. M. Spence, "Evaluation of 3D Printing and Its Potential Impact on Biotechnology and the Chemical Sciences," *Analytical Chemistry,* vol. 86, no. 7, pp. 3240-3253, 2014/04/01 2014, doi: 10.1021/ac403397r.

[117] T. D. Ngo, A. Kashani, G. Imbalzano, K. T. Q. Nguyen, and D. Hui, "Additive manufacturing (3D printing): A review of materials, methods, applications and challenges," *Composites Part B: Engineering,* vol. 143, pp. 172-196, 2018/06/15/ 2018, doi: https://doi.org/10.1016/j.compositesb.2018.02.012.

[118] Y. Ni, R. Ji, K. Long, T. Bu, K. Chen, and S. Zhuang, "A review of 3D-printed sensors," *Applied Spectroscopy Reviews,* vol. 52, no. 7, pp. 623-652, 2017/08/09 2017, doi: 10.1080/05704928.2017.1287082.

[119] J. U. Pucci, B. R. Christophe, J. A. Sisti, and E. S. Connolly, "Three-dimensional printing: technologies, applications, and limitations in neurosurgery," *Biotechnology Advances,* vol. 35, no. 5, pp. 521-529, 2017/09/01/ 2017, doi: https://doi.org/10.1016/j.biotechadv.2017.05.007.

[120]   S. Waheed *et al.*, "3D printed microfluidic devices: enablers and barriers," *Lab on a Chip,* 10.1039/C6LC00284F vol. 16, no. 11, pp. 1993-2013, 2016, doi: 10.1039/C6LC00284F.

[121]   O. Moreno-Rivas, D. Hernández-Velázquez, V. Piazza, and S. Marquez, "Rapid prototyping of microfluidic devices by SL 3D printing and their biocompatibility study for cell culturing," *Materials Today: Proceedings,* vol. 13, pp. 436-445, 2019/01/01/ 2019, doi: https://doi.org/10.1016/j.matpr.2019.03.189.

[122]   G. Grigalevičiūtė, D. Baltriukienė, E. Balčiūnas, L. Jonušauskas, and M. Malinauskas, *Fabrication of flexible microporous 3D scaffolds via stereolithography and optimization of their biocompatibility* (SPIE OPTO). SPIE, 2018.

[123]   W. Asghar, Y.-T. Kim, A. Ilyas, J. Sankaran, Y. Wan, and S. M. Iqbal, "Synthesis of nano-textured biocompatible scaffolds from chicken eggshells," *Nanotechnology,* vol. 23, no. 47, p. 475601, 2012/10/30 2012, doi: 10.1088/0957-4484/23/47/475601.

[124]   E. Babaliari *et al.*, "Engineering Cell Adhesion and Orientation via Ultrafast Laser Fabricated Microstructured Substrates," (in eng), *Int J Mol Sci,* vol. 19, no. 7, p. 2053, 2018, doi: 10.3390/ijms19072053.

[125]   N. J. Shirtcliffe, R. Toon, and P. Roach, "Surface Treatments for Microfluidic Biocompatibility," in *Microfluidic Diagnostics: Methods and Protocols*, G. Jenkins and C. D. Mansfield Eds. Totowa, NJ: Humana Press, 2013, pp. 241-268.

[126]   T.-S. Jang, H.-D. Jung, H. M. Pan, W. T. Han, S. Chen, and J. Song, "3D printing of hydrogel composite systems: Recent advances in technology for tissue engineering," *2018,* hydrogel composites; 3D printing; tissue engineering vol. 4, no. 1, 2018-01-19 2018, doi: 10.18063/ijb.v4i1.126.

[127] H. M. P. Eric Luis, Swee Leong Sing, Anil Kumar Bastola, Guo Dong Goh, Guo Liang Goh, Heang Kuan Joel Tan, Ram Bajpai, Juha Song, and Wai Yee Yeong, "Silicone 3D Printing: Process Optimization, Product Biocompatibility, and Reliability of Silicone Meniscus Implants," *3D Printing and Additive Manufacturing,* vol. 6, no. 6, pp. 319-332, 2019, doi: 10.1089/3dp.2018.0226.

[128] E. Luis, H. M. Pan, S. L. Sing, R. Bajpai, J. Song, and W. Y. Yeong, "3D Direct Printing of Silicone Meniscus Implant Using a Novel Heat-Cured Extrusion-Based Printer," *Polymers,* vol. 12, no. 5, p. 1031, 2020. [Online]. Available: https://www.mdpi.com/2073-4360/12/5/1031.

[129] F. Alifui-Segbaya and R. George, "Biocompatibility of 3D-Printed Methacrylate for Hearing Devices," *Inventions,* vol. 3, no. 3, p. 52, 2018. [Online]. Available: https://www.mdpi.com/2411-5134/3/3/52.

[130] M. Carve and D. Wlodkowic, "3D-Printed Chips: Compatibility of Additive Manufacturing Photopolymeric Substrata with Biological Applications," *Micromachines,* vol. 9, no. 2, p. 91, 2018. [Online]. Available: https://www.mdpi.com/2072-666X/9/2/91.

[131] H. N. Chia and B. M. Wu, "Recent advances in 3D printing of biomaterials," *Journal of Biological Engineering,* vol. 9, no. 1, p. 4, 2015/03/01 2015, doi: 10.1186/s13036-015-0001-4.

[132] R. Gautam, R. D. Singh, V. P. Sharma, R. Siddhartha, P. Chand, and R. Kumar, "Biocompatibility of polymethylmethacrylate resins used in dentistry," *Journal of Biomedical Materials Research Part B: Applied Biomaterials,* vol. 100B, no. 5, pp. 1444-1450, 2012, doi: 10.1002/jbm.b.32673.

[133] C. Kurzmann *et al.*, "Evaluation of Resins for Stereolithographic 3D-Printed Surgical Guides: The Response of L929 Cells and Human Gingival Fibroblasts," *BioMed Research International,* vol. 2017, p. 11, 2017, Art no. 4057612, doi: 10.1155/2017/4057612.

[134] R. P. Rimington, A. J. Capel, D. J. Player, R. J. Bibb, S. D. R. Christie, and M. P. Lewis, "Feasibility and Biocompatibility of 3D-Printed Photopolymerized and Laser Sintered Polymers for Neuronal, Myogenic, and Hepatic Cell Types," *Macromolecular Bioscience,* vol. 18, no. 7, p. 1800113, 2018, doi: 10.1002/mabi.201800113.

[135] M. Schuster, C. Turecek, B. Kaiser, J. Stampfl, R. Liska, and F. Varga, "Evaluation of Biocompatible Photopolymers I: Photoreactivity and Mechanical Properties of Reactive Diluents," *Journal of Macromolecular Science, Part A,* vol. 44, no. 5, pp. 547-557, 2007/03/01 2007, doi: 10.1080/10601320701235958.

[136] M. Sharafeldin, A. Jones, and J. F. Rusling, "3D-Printed Biosensor Arrays for Medical Diagnostics," *Micromachines,* vol. 9, no. 8, p. 394, 2018. [Online]. Available: https://www.mdpi.com/2072-666X/9/8/394.

[137] S. Takenaga *et al.*, "Fabrication of biocompatible lab-on-chip devices for biomedical applications by means of a 3D-printing process," *physica status solidi (a),* vol. 212, no. 6, pp. 1347-1352, 2015, doi: 10.1002/pssa.201532053.

[138] F. Zhu, T. Friedrich, D. Nugegoda, J. Kaslin, and D. Wlodkowic, "Assessment of the biocompatibility of three-dimensional-printed polymers using multispecies toxicity tests," (in eng), *Biomicrofluidics,* vol. 9, no. 6, pp. 061103-061103, 2015, doi: 10.1063/1.4939031.

[139] F. Zhu, J. Skommer, T. Friedrich, J. Kaslin, and D. Wlodkowic, *3D printed polymers toxicity profiling: a caution for biodevice applications* (SPIE Micro+Nano Materials, Devices, and Applications). SPIE, 2015.

[140] FormLabs. "Clear Resin MSDS." https://formlabs-media.formlabs.com/datasheets/Safety_Data_Sheet_EN_-_Clear.pdf (accessed.

[141] FormLabs. "High Temp MSDS." https://formlabs-media.formlabs.com/datasheets/Safety_Data_Sheet_EN_-_High_Temp.pdf (accessed.

[142] FormLabs. "Flexible Resin MSDS." https://formlabs-media.formlabs.com/datasheets/Safety_Data_Sheet_EN_-_Flexible.pdf (accessed.

[143] FormLabs. "Dental LT Resin MSDS." https://formlabs-media.formlabs.com/datasheets/Safety_Data_Sheet_EN-EU_-_Dental_LT_Clear.pdf (accessed.

[144] P. d. Medical. "GR-10 MSDS." https://www.pro3dure.com/media/pdf/80/57/9e/GR-10guide-E.pdf (accessed.

[145] A. Kundu, C. Nattoo, S. Fremgen, S. Springer, T. Ausaf, and S. Rajaraman, "Optimization of makerspace microfabrication techniques and materials for the realization of planar, 3D printed microelectrode arrays in under four days," *RSC Advances,* 10.1039/C8RA09116A vol. 9, no. 16, pp. 8949-8963, 2019, doi: 10.1039/C8RA09116A.

[146] C. Hart, K. S. Kumar, J. Li, J. Thomas, and S. Rajaraman, "Investigation of the Enhanced Sensitivity of Interdigitated Electrodes for Cellular Biosensing With Geometric, Nanostructured Surface Area, and Surface Plasmon Resonance Modes," *Journal of*

Microelectromechanical Systems, vol. 29, no. 5, pp. 1109-1111, 2020, doi: 10.1109/JMEMS.2020.3012277.

[147]   C. M. Didier, A. Kundu, and S. Rajaraman, "Facile, Packaging Substrate-Agnostic, Microfabrication and Assembly of Scalable 3D Metal Microelectrode Arrays for *in Vitro* Organ-on-a-Chip and Cellular Disease Modeling," in *2019 20th International Conference on Solid-State Sensors, Actuators and Microsystems & Eurosensors XXXIII (TRANSDUCERS & EUROSENSORS XXXIII)*, 23-27 June 2019 2019, pp. 1686-1689, doi: 10.1109/TRANSDUCERS.2019.8808364.

[148]   A. Kundu, T. Ausaf, and S. Rajaraman, "3D Printing, Ink Casting and Micromachined Lamination (3D PICLµM): A Makerspace Approach to the Fabrication of Biological Microdevices," *Micromachines,* vol. 9, no. 2, p. 85, 2018. [Online]. Available: https://www.mdpi.com/2072-666X/9/2/85.

[149]   S. P. Lacour *et al.*, "Flexible and stretchable micro-electrodes for *in vitro* and *in vivo* neural interfaces," *Medical & Biological Engineering & Computing,* vol. 48, no. 10, pp. 945-954, 2010/10/01 2010, doi: 10.1007/s11517-010-0644-8.

[150]   D. K. Patel, A. H. Sakhaei, M. Layani, B. Zhang, Q. Ge, and S. Magdassi, "Highly Stretchable and UV Curable Elastomers for Digital Light Processing Based 3D Printing," *Advanced Materials,* vol. 29, no. 15, p. 1606000, 2017, doi: 10.1002/adma.201606000.

[151]   S. Sivashankar, S. Agambayev, K. Alamoudi, U. Buttner, N. Khashab, and K. N. Salama, "Compatibility analysis of 3D printer resin for biological applications," *Micro & Nano Letters*, vol. 11, no. 10*, pp. 654-659. [Online]. Available: https://digital-library.theiet.org/content/journals/10.1049/mnl.2016.0530

[152]   S. Sivashankar, S. Agambayev, U. Buttner, and K. N. Salama, "Characterization of solid UV curable 3D printer resins for biological applications," in *2016 IEEE 11th Annual International Conference on Nano/Micro Engineered and Molecular Systems (NEMS)*, 17-20 April 2016 2016, pp. 305-309, doi: 10.1109/NEMS.2016.7758255.

[153]   W. A. Rutala, M. M. Stiegel, and F. A. Sarubbi, "Decontamination of laboratory microbiological waste by steam sterilization," *Applied and Environmental Microbiology,* vol. 43, no. 6, pp. 1311-1316, 1982. [Online]. Available: https://aem.asm.org/content/aem/43/6/1311.full.pdf.

[154]   W.-M. Chan, P. E. Gloor, and A. E. Hamielec, "A kinetic model for olefin polymerization in high-pressure autoclave reactors," *AIChE Journal,* vol. 39, no. 1, pp. 111-126, 1993, doi: 10.1002/aic.690390112.

[155]   R. Durkan, Ouml, M. B. Zel, B. Bagis, and A. Usanmaz, "*In vitro* Comparison of Autoclave Polymerization on the Transverse Strength of Denture Base Resins," *Dental Materials Journal,* vol. 27, no. 4, pp. 640-642, 2008, doi: 10.4012/dmj.27.640.

[156]   B. G. Kwag and K. Y. Choi, "Effect of Initiator Characteristics on High-Pressure Ethylene Polymerization in Autoclave Reactors," (in English), *Ind. Eng. Chem. Res.,* vol. 33, no. 2, pp. 211-217, 1994, doi: 10.1021/ie00026a006.

[157]   E. Technology. "EPO-TEK 353ND." https://www.epotek.com/site/administrator/components/com_products/assets/files/Style_Uploads/MED-353ND.pdf (accessed.

[158]   Promega. "CellTiter-Glo Luminescent Cell Viability Assay Technical Bulletin." https://www.promega.com/-/media/files/resources/protocols/technical-bulletins/0/celltiter-glo-luminescent-cell-viability-assay-protocol.pdf?la=en (accessed.

[159]   D. A. Tipton and J. W. Lewis, "Effects of a hindered amine light stabilizer and a UV light absorber used in maxillofacial elastomers on human gingival epithelial cells and fibroblasts," (in eng), *J Prosthet Dent,* vol. 100, no. 3, pp. 220-31, Sep 2008, doi: 10.1016/s0022-3913(08)60182-1.

[160]   K. L. Van Landuyt *et al.*, "Evaluation of cell responses toward adhesives with different photoinitiating systems," *Dental Materials,* vol. 31, no. 8, pp. 916-927, 2015/08/01/ 2015, doi: https://doi.org/10.1016/j.dental.2015.04.016.

[161]   M. Popal, J. Volk, G. Leyhausen, and W. Geurtsen, "Cytotoxic and genotoxic potential of the type I photoinitiators BAPO and TPO on human oral keratinocytes and V79 fibroblasts," (in eng), *Dent Mater,* vol. 34, no. 12, pp. 1783-1796, Dec 2018, doi: 10.1016/j.dental.2018.09.015.

[162]   N. M. Al-Namnam, K. H. Kim, W. L. Chai, K. O. Ha, C. H. Siar, and W. C. Ngeow, "A biocompatibility study of injectable poly(caprolactone-trifumarate) for use as a bone substitute material," *Frontiers in Life Science,* vol. 8, no. 3, pp. 215-222, 2015/07/03 2015, doi: 10.1080/21553769.2015.1051240.

[163]   N. Azim *et al.*, "Fabrication and Characterization of a 3D Printed, MicroElectrodes Platform With Functionalized Electrospun Nano-Scaffolds and Spin Coated 3D Insulation Towards Multi- Functional Biosystems," *Journal of Microelectromechanical Systems,* vol. 28, no. 4, pp. 606-618, 2019, doi: 10.1109/JMEMS.2019.2913652.

[164]   K. Kadimisetty *et al.*, "Fully 3D printed integrated reactor array for point-of-care molecular diagnostics," *Biosensors and Bioelectronics,* vol. 109, pp. 156-163, 2018/06/30/ 2018, doi: https://doi.org/10.1016/j.bios.2018.03.009.

[165]   A. Kundu, T. Ausaf, P. Rajasekaran, and S. Rajaraman, "Multimodal Microfluidic Biosensor With Interdigitated Electrodes (IDE) And Microelectrode Array (MEA) For Bacterial Detection And Identification," in *2019 20th International Conference on Solid-State Sensors, Actuators and Microsystems & Eurosensors XXXIII (TRANSDUCERS & EUROSENSORS XXXIII)*, 23-27 June 2019 2019, pp. 1199-1202, doi: 10.1109/TRANSDUCERS.2019.8808696.

[166]   Y. Liu, E. Smela, N. M. Nelson, and P. Abshire, "Cell-lab on a chip: a CMOS-based microsystem for culturing and monitoring cells," in *The 26th Annual International Conference of the IEEE Engineering in Medicine and Biology Society*, 1-5 Sept. 2004 2004, vol. 1, pp. 2534-2537, doi: 10.1109/IEMBS.2004.1403729.

[167]   N. P. Macdonald *et al.*, "Assessment of biocompatibility of 3D printed photopolymers using zebrafish embryo toxicity assays," *Lab on a Chip,* 10.1039/C5LC01374G vol. 16, no. 2, pp. 291-297, 2016, doi: 10.1039/C5LC01374G.

[168]   Y. Zhao *et al.*, "JMEMS Letters An Adhesive and Corrosion-Resistant Biomarker Sensing Film for Biosmart Wearable Consumer Electronics," *Journal of Microelectromechanical Systems,* pp. 1-3, 2020, doi: 10.1109/JMEMS.2020.3012101.

[169]   W. Strober, "Trypan Blue Exclusion Test of Cell Viability," *Current Protocols in Immunology,* vol. 21, no. 1, pp. A.3B.1-A.3B.2, 1997, doi: 10.1002/0471142735.ima03bs21.

[170]   M. Eimre *et al.*, "Distinct organization of energy metabolism in HL-1 cardiac cell line and cardiomyocytes," *Biochimica et Biophysica Acta (BBA) - Bioenergetics,* vol. 1777, no. 6, pp. 514-524, 2008/06/01/ 2008, doi: https://doi.org/10.1016/j.bbabio.2008.03.019.

[171] C. Didier, A. Kundu, and S. Rajaraman, "Capabilities and limitations of 3D printed microserpentines and integrated 3D electrodes for stretchable and conformable biosensor applications," *Microsystems & Nanoengineering,* vol. 6, no. 1, p. 15, 2020/04/20 2020, doi: 10.1038/s41378-019-0129-3.

[172] A. K. Makoto Nakamura, Fumio Takagi, Akihiko Watanabe, Yuko Hiruma, Katsuhiro Ohuchi, Yasuhiko Iwasaki, Mikio Horie, Ikuo Morita, and Setsuo Takatani., "Biocompatible Inkjet Printing Technique for Designed Seeding of Individual Living Cells," *Tissue Engineering,* vol. 11, no. 11-12, pp. 1658-1666, 2005, doi: 10.1089/ten.2005.11.1658.

[173] G. Gao, Y. Huang, A. F. Schilling, K. Hubbell, and X. Cui, "Organ Bioprinting: Are We There Yet?," *Advanced Healthcare Materials,* vol. 7, no. 1, p. 1701018, 2018, doi: 10.1002/adhm.201701018.

[174] B. R. Ringeisen, C. M. Othon, J. A. Barron, D. Young, and B. J. Spargo, "Jet-based methods to print living cells," *Biotechnology Journal,* vol. 1, no. 9, pp. 930-948, 2006, doi: 10.1002/biot.200600058.

[175] E. A. Roth, T. Xu, M. Das, C. Gregory, J. J. Hickman, and T. Boland, "Inkjet printing for high-throughput cell patterning," *Biomaterials,* vol. 25, no. 17, pp. 3707-3715, 2004/08/01/ 2004, doi: https://doi.org/10.1016/j.biomaterials.2003.10.052.

[176] L. Zhao, K. C. Yan, R. Yao, F. Lin, and W. Sun, "Modeling on Microdroplet Formation for Cell Printing Based on Alternating Viscous-Inertial Force Jetting," *Journal of Manufacturing Science and Engineering,* vol. 139, no. 1, 2016, doi: 10.1115/1.4032768.

[177] A. Skardal and A. Atala, "Biomaterials for Integration with 3-D Bioprinting," *Annals of Biomedical Engineering,* vol. 43, no. 3, pp. 730-746, 2015/03/01 2015, doi: 10.1007/s10439-014-1207-1.

[178] L. Koch *et al.*, "Skin tissue generation by laser cell printing," *Biotechnology and Bioengineering,* vol. 109, no. 7, pp. 1855-1863, 2012, doi: 10.1002/bit.24455.

[179] B. Guillotin and F. Guillemot, "Cell patterning technologies for organotypic tissue fabrication," *Trends in Biotechnology,* vol. 29, no. 4, pp. 183-190, 2011/04/01/ 2011, doi: https://doi.org/10.1016/j.tibtech.2010.12.008.

[180] A. Faulkner-Jones, S. Greenhough, J. A King, J. Gardner, A. Courtney, and W. Shu, "Development of a valve-based cell printer for the formation of human embryonic stem cell spheroid aggregates," *Biofabrication,* vol. 5, no. 1, p. 015013, 2013/02/04 2013, doi: 10.1088/1758-5082/5/1/015013.

[181] T. Boland, T. Xu, B. Damon, and X. Cui, "Application of inkjet printing to tissue engineering," *Biotechnology Journal,* vol. 1, no. 9, pp. 910-917, 2006, doi: 10.1002/biot.200600081.

[182] T. Boland *et al.*, "Drop-on-demand printing of cells and materials for designer tissue constructs," *Materials Science and Engineering: C,* vol. 27, no. 3, pp. 372-376, 2007/04/01/ 2007, doi: https://doi.org/10.1016/j.msec.2006.05.047.

[183] D. Chahal, A. Ahmadi, and K. C. Cheung, "Improving piezoelectric cell printing accuracy and reliability through neutral buoyancy of suspensions," *Biotechnology and Bioengineering,* vol. 109, no. 11, pp. 2932-2940, 2012, doi: 10.1002/bit.24562.

[184]   X. Cui, T. Boland, D. D. D'Lima, and M. K. Lotz, "Thermal inkjet printing in tissue engineering and regenerative medicine," (in eng), *Recent Pat Drug Deliv Formul,* vol. 6, no. 2, pp. 149-155, 2012, doi: 10.2174/187221112800672949.

[185]   B. Derby, "Bioprinting: inkjet printing proteins and hybrid cell-containing materials and structures," *Journal of Materials Chemistry,* 10.1039/B807560C vol. 18, no. 47, pp. 5717-5721, 2008, doi: 10.1039/B807560C.

[186]   B. Lorber, W.-K. Hsiao, I. M. Hutchings, and K. R. Martin, "Adult rat retinal ganglion cells and glia can be printed by piezoelectric inkjet printing," *Biofabrication,* vol. 6, no. 1, p. 015001, 2013/12/17 2013, doi: 10.1088/1758-5082/6/1/015001.

[187]   J. A. Park *et al.*, "Freeform micropatterning of living cells into cell culture medium using direct inkjet printing," *Scientific Reports,* vol. 7, no. 1, p. 14610, 2017/11/03 2017, doi: 10.1038/s41598-017-14726-w.

[188]   R. E. Saunders, J. E. Gough, and B. Derby, "Delivery of human fibroblast cells by piezoelectric drop-on-demand inkjet printing," *Biomaterials,* vol. 29, no. 2, pp. 193-203, 2008/01/01/ 2008, doi: https://doi.org/10.1016/j.biomaterials.2007.09.032.

[189]   J. He, X. Zhao, J. Chang, and D. Li, "Microscale Electro-Hydrodynamic Cell Printing with High Viability," *Small,* vol. 13, no. 47, p. 1702626, 2017, doi: 10.1002/smll.201702626.

[190]   J. Jang, J. Y. Park, G. Gao, and D.-W. Cho, "Biomaterials-based 3D cell printing for next-generation therapeutics and diagnostics," *Biomaterials,* vol. 156, pp. 88-106, 2018/02/01/ 2018, doi: https://doi.org/10.1016/j.biomaterials.2017.11.030.

[191] D. O. Visscher *et al.*, "Advances in Bioprinting Technologies for Craniofacial
Reconstruction," *Trends in Biotechnology,* vol. 34, no. 9, pp. 700-710, 2016/09/01/ 2016,
doi: https://doi.org/10.1016/j.tibtech.2016.04.001.

[192] C. J. Ferris, K. G. Gilmore, G. G. Wallace, and M. in het Panhuis, "Biofabrication: an
overview of the approaches used for printing of living cells," *Applied Microbiology and
Biotechnology,* vol. 97, no. 10, pp. 4243-4258, 2013/05/01 2013, doi: 10.1007/s00253-
013-4853-6.

[193] A. U. Chen and O. A. Basaran, "A new method for significantly reducing drop radius
without reducing nozzle radius in drop-on-demand drop production," *Physics of Fluids,*
vol. 14, no. 1, pp. L1-L4, 2002/01/01 2001, doi: 10.1063/1.1427441.

[194] I. T. Ozbolat and M. Hospodiuk, "Current advances and future perspectives in extrusion-
based bioprinting," *Biomaterials,* vol. 76, pp. 321-343, 2016/01/01/ 2016, doi:
https://doi.org/10.1016/j.biomaterials.2015.10.076.

[195] T. Boland, V. Mironov, A. Gutowska, E. A. Roth, and R. R. Markwald, "Cell and organ
printing 2: Fusion of cell aggregates in three-dimensional gels," *The Anatomical Record
Part A: Discoveries in Molecular, Cellular, and Evolutionary Biology,* vol. 272A, no. 2,
pp. 497-502, 2003, doi: 10.1002/ar.a.10059.

[196] V. Mironov, R. P. Visconti, V. Kasyanov, G. Forgacs, C. J. Drake, and R. R. Markwald,
"Organ printing: Tissue spheroids as building blocks," *Biomaterials,* vol. 30, no. 12, pp.
2164-2174, 2009/04/01/ 2009, doi: https://doi.org/10.1016/j.biomaterials.2008.12.084.

[197] K. Jakab, C. Norotte, F. Marga, K. Murphy, G. Vunjak-Novakovic, and G. Forgacs,
"Tissue engineering by self-assembly and bio-printing of living cells," *Biofabrication,*
vol. 2, no. 2, p. 022001, 2010/06/01 2010, doi: 10.1088/1758-5082/2/2/022001.

[198] A. N. Mehesz *et al.*, "Scalable robotic biofabrication of tissue spheroids," *Biofabrication,* vol. 3, no. 2, p. 025002, 2011/05/12 2011, doi: 10.1088/1758-5082/3/2/025002.

[199] J. H. Y. Chung *et al.*, "Bio-ink properties and printability for extrusion printing living cells," *Biomaterials Science,* 10.1039/C3BM00012E vol. 1, no. 7, pp. 763-773, 2013, doi: 10.1039/C3BM00012E.

[200] S. Khalil and W. Sun, "Bioprinting Endothelial Cells With Alginate for 3D Tissue Constructs," *Journal of Biomechanical Engineering,* vol. 131, no. 11, 2009, doi: 10.1115/1.3128729.

[201] J. Malda *et al.*, "25th Anniversary Article: Engineering Hydrogels for Biofabrication," *Advanced Materials,* vol. 25, no. 36, pp. 5011-5028, 2013, doi: 10.1002/adma.201302042.

[202] S. V. Murphy, A. Skardal, and A. Atala, "Evaluation of hydrogels for bio-printing applications," *Journal of Biomedical Materials Research Part A,* vol. 101A, no. 1, pp. 272-284, 2013, doi: 10.1002/jbm.a.34326.

[203] R. Levato, J. Visser, J. A. Planell, E. Engel, J. Malda, and M. A. Mateos-Timoneda, "Biofabrication of tissue constructs by 3D bioprinting of cell-laden microcarriers," *Biofabrication,* vol. 6, no. 3, p. 035020, 2014/07/22 2014, doi: 10.1088/1758-5082/6/3/035020.

[204] F. Pati *et al.*, "Printing three-dimensional tissue analogues with decellularized extracellular matrix bioink," *Nature Communications,* vol. 5, no. 1, p. 3935, 2014/06/02 2014, doi: 10.1038/ncomms4935.

[205] M. Gou *et al.*, "Bio-inspired detoxification using 3D-printed hydrogel nanocomposites," *Nature Communications,* vol. 5, no. 1, p. 3774, 2014/05/08 2014, doi: 10.1038/ncomms4774.

[206] B. Duan, L. A. Hockaday, K. H. Kang, and J. T. Butcher, "3D Bioprinting of heterogeneous aortic valve conduits with alginate/gelatin hydrogels," *Journal of Biomedical Materials Research Part A,* vol. 101A, no. 5, pp. 1255-1264, 2013, doi: 10.1002/jbm.a.34420.

[207] A. B. Dababneh and I. T. Ozbolat, "Bioprinting Technology: A Current State-of-the-Art Review," *Journal of Manufacturing Science and Engineering,* vol. 136, no. 6, 2014, doi: 10.1115/1.4028512.

[208] S. Boularaoui, G. Al Hussein, K. A. Khan, N. Christoforou, and C. Stefanini, "An overview of extrusion-based bioprinting with a focus on induced shear stress and its effect on cell viability," *Bioprinting,* vol. 20, p. e00093, 2020/12/01/ 2020, doi: https://doi.org/10.1016/j.bprint.2020.e00093.

[209] S. Khalil and W. Sun, "Biopolymer deposition for freeform fabrication of hydrogel tissue constructs," *Materials Science and Engineering: C,* vol. 27, no. 3, pp. 469-478, 2007/04/01/ 2007, doi: https://doi.org/10.1016/j.msec.2006.05.023.

[210] L. E. Bertassoni *et al.*, "Direct-write bioprinting of cell-laden methacrylated gelatin hydrogels," *Biofabrication,* vol. 6, no. 2, p. 024105, 2014/04/03 2014, doi: 10.1088/1758-5082/6/2/024105.

[211] T. Xu, J. Jin, C. Gregory, J. J. Hickman, and T. Boland, "Inkjet printing of viable mammalian cells," *Biomaterials,* vol. 26, no. 1, pp. 93-99, 2005/01/01/ 2005, doi: https://doi.org/10.1016/j.biomaterials.2004.04.011.

[212] N. B. M. Fidaleo, M. Schulte, M.C. Flickinger, "Ink-Jet Printing of Gluconobacter oxydans: Micropatterned Coatings as High Surface-to-Volume Ratio Bio-Reactive Coatings," *Coatings,* vol. 4, pp. 1-17, 2014.

[213] F. Turcu, K. Tratsk-Nitz, S. Thanos, W. Schuhmann, and P. Heiduschka, "Ink-jet printing for micropattern generation of laminin for neuronal adhesion," *Journal of Neuroscience Methods,* vol. 131, no. 1, pp. 141-148, 2003/12/30/ 2003, doi: https://doi.org/10.1016/j.jneumeth.2003.08.001.

[214] "Axion Biosystems: Explore Life's Circuitry."

[215] J. Shi, B. Wu, S. Li, J. Song, B. Song, and W. F. Lu, "Shear stress analysis and its effects on cell viability and cell proliferation in drop-on-demand bioprinting," *Biomedical Physics & Engineering Express,* vol. 4, no. 4, p. 045028, 2018/06/13 2018, doi: 10.1088/2057-1976/aac946.

[216] A. Tirella and A. Ahluwalia, "The impact of fabrication parameters and substrate stiffness in direct writing of living constructs," *Biotechnology Progress,* vol. 28, no. 5, pp. 1315-1320, 2012, doi: 10.1002/btpr.1586.

[217] J. Snyder, A. Rin Son, Q. Hamid, C. Wang, Y. Lui, and W. Sun, "Mesenchymal stem cell printing and process regulated cell properties," *Biofabrication,* vol. 7, no. 4, p. 044106, 2015/12/22 2015, doi: 10.1088/1758-5090/7/4/044106.

[218] K. Nair *et al.*, "Characterization of cell viability during bioprinting processes," *Biotechnology Journal,* vol. 4, no. 8, pp. 1168-1177, 2009, doi: 10.1002/biot.200900004.

[219] L. Ouyang, R. Yao, Y. Zhao, and W. Sun, "Effect of bioink properties on printability and cell viability for 3D bioplotting of embryonic stem cells," *Biofabrication,* vol. 8, no. 3, p. 035020, 2016/09/16 2016, doi: 10.1088/1758-5090/8/3/035020.

[220] G. O. a. D. Juncker, "Multiplexed co-culture patterning in 2D and 3D using low-cost 3D printed monolithic pin-heads," presented at the 22nd International Conference on Miniaturized Systems for Chemistry and Life Sciences, Kaohsiung, Taiwan, 2018.

[221] P. Fisch, M. Holub, and M. Zenobi-Wong, "Improved accuracy and precision of bioprinting through progressive cavity pump-controlled extrusion," *bioRxiv,* p. 2020.01.23.915868, 2020, doi: 10.1101/2020.01.23.915868.

[222] D. Sher. "Top 15 Bioprinters." 3D Printing Industry. https://3dprintingindustry.com/news/top-10-bioprinters-55699/. (accessed.

[223] C. L. Sciences. "Microplate Dimensions for Corning Cell Culture Microplates." Corning. https://www.corning.com/catalog/cls/documents/drawings/MD_Microplate_Dimension_ Sheets_Multiple_Well.pdf (accessed 11/02/2020, 2020).

[224] N. Chaturvedi, Baban, N. S., Sofela, S. O., Orozaliev, A., Giakoumidis, N., Kim, J., Gunsalus, K. C., & Song, Y. A., "A single pressure pulse-actuated 3D-printed microfluidic tip for high throughput dispensing of C. elegans worms," presented at the 22nd International Conference on Miniaturized Systems for Chemistry and Life Sciences, MicroTAS 2018, Kaohsiung, Taiwain, November 11 -15, 2018.

[225] F. Grinnell and M. K. Feld, "Fibronectin adsorption on hydrophilic and hydrophobic surfaces detected by antibody binding and analyzed during cell adhesion in serum-containing medium," (in eng), *J Biol Chem,* vol. 257, no. 9, pp. 4888-93, May 10 1982.

[226] M. P. M. Thery, *Micropatterning in Cell Biology: Part A*. New York: Academic, 2014.

[227] C. Oleaga *et al.*, "Multi-Organ toxicity demonstration in a functional human *in vitro* system composed of four organs," *Scientific Reports,* vol. 6, no. 1, p. 20030, 2016/02/03 2016, doi: 10.1038/srep20030.

[228] F. Cotel, R. Exley, S. J. Cragg, and J.-F. Perrier, "Serotonin spillover onto the axon initial segment of motoneurons induces central fatigue by inhibiting action potential initiation," *Proceedings of the National Academy of Sciences,* vol. 110, no. 12, pp. 4774-4779, 2013, doi: 10.1073/pnas.1216150110.

[229] D. A. Wagenaar, J. Pine, and S. M. Potter, "Effective parameters for stimulation of dissociated cultures using multi-electrode arrays," *Journal of Neuroscience Methods,* vol. 138, no. 1, pp. 27-37, 2004/09/30/ 2004, doi: https://doi.org/10.1016/j.jneumeth.2004.03.005.

[230] X. Jiang, F. Tian, K. Mearow, P. Okagaki, and R. H. Lipsky, "The excitoprotective effect of N-methyl-d-aspartate receptors is mediated by a brain-derived neurotrophic factor autocrine loop in cultured hippocampal neurons," *Journal of Neurochemistry,* vol. 94, no. 3, pp. 713-722, 2005, doi: 10.1111/j.1471-4159.2005.03200.x.

[231] K. L. Williamson and K. J. Broadley, "Do both adrenaline and noradrenaline stimulate cardiac α-adrenoceptors to induce positive inotropy of rat atria?," *British Journal of Pharmacology,* vol. 98, no. 2, pp. 597-611, 1989, doi: 10.1111/j.1476-5381.1989.tb12634.x.

[232] R. Simó, M. Villarroel, L. Corraliza, C. Hernández, and M. Garcia-Ramírez, "The Retinal Pigment Epithelium: Something More than a Constituent of the Blood-Retinal Barrier—Implications for the Pathogenesis of Diabetic Retinopathy," *Journal of Biomedicine and Biotechnology,* vol. 2010, p. 190724, 2010/02/17 2010, doi: 10.1155/2010/190724.

[233] O. Strauss, "The Retinal Pigment Epithelium in Visual Function," *Physiological Reviews,* vol. 85, no. 3, pp. 845-881, 2005, doi: 10.1152/physrev.00021.2004.

[234] J. A. DiMasi, H. G. Grabowski, and R. W. Hansen, "Innovation in the pharmaceutical industry: New estimates of R&D costs," *Journal of Health Economics,* vol. 47, pp. 20-33, 2016/05/01/ 2016, doi: https://doi.org/10.1016/j.jhealeco.2016.01.012.

[235] J. Zhou *et al.*, "Assessment of cadmium-induced hepatotoxicity and protective effects of zinc against it using an improved cell-based biosensor," *Sensors and Actuators A: Physical,* vol. 199, pp. 156-164, 2013/09/01/ 2013, doi: https://doi.org/10.1016/j.sna.2013.05.006.

[236] D. Millard *et al.*, "Cross-Site Reliability of Human Induced Pluripotent stem cell-derived Cardiomyocyte Based Safety Assays Using Microelectrode Arrays: Results from a Blinded CiPA Pilot Study," *Toxicological Sciences,* vol. 164, no. 2, pp. 550-562, 2018, doi: 10.1093/toxsci/kfy110.

[237] S. Michaelis, J. Wegener, and R. Robelek, "Label-free monitoring of cell-based assays: Combining impedance analysis with SPR for multiparametric cell profiling," *Biosensors and Bioelectronics,* vol. 49, pp. 63-70, 2013/11/15/ 2013, doi: https://doi.org/10.1016/j.bios.2013.04.042.

[238] A. B. Dahlin, "Sensing applications based on plasmonic nanopores: The hole story," *Analyst,* 10.1039/C4AN02258K vol. 140, no. 14, pp. 4748-4759, 2015, doi: 10.1039/C4AN02258K.

[239] N. Hu *et al.*, "Comparison between ECIS and LAPS for establishing a cardiomyocyte-based biosensor," *Sensors and Actuators B: Chemical,* vol. 185, pp. 238-244, 2013/08/01/ 2013, doi: https://doi.org/10.1016/j.snb.2013.04.093.

[240] C. M. Othon, X. Wu, J. J. Anders, and B. R. Ringeisen, "Single-cell printing to form three-dimensional lines of olfactory ensheathing cells," *Biomedical Materials,* vol. 3, no. 3, p. 034101, 2008/08/08 2008, doi: 10.1088/1748-6041/3/3/034101.

[241] R. Ehret, W. Baumann, M. Brischwein, A. Schwinde, K. Stegbauer, and B. Wolf, "Monitoring of cellular behaviour by impedance measurements on interdigitated electrode structures," *Biosensors and Bioelectronics,* vol. 12, no. 1, pp. 29-41, 1997/01/01/ 1997, doi: https://doi.org/10.1016/0956-5663(96)89087-7.

[242] A. Bratov *et al.*, "Three-dimensional interdigitated electrode array as a transducer for label-free biosensors," *Biosensors and Bioelectronics,* vol. 24, no. 4, pp. 729-735, 2008/12/01/ 2008, doi: https://doi.org/10.1016/j.bios.2008.06.057.

[243] S. M. Radke and E. C. Alocilja, "Design and fabrication of a microimpedance biosensor for bacterial detection," *IEEE Sensors Journal,* vol. 4, no. 4, pp. 434-440, 2004, doi: 10.1109/JSEN.2004.830300.

[244] W. Laureyn *et al.*, "Nanoscaled interdigitated titanium electrodes for impedimetric biosensing," *Sensors and Actuators B: Chemical,* vol. 68, pp. 360-370, 08/01 2000, doi: 10.1016/S0925-4005(00)00489-5.

[245] S. Partel, S. Kasemann, P. Choleva, C. Dincer, J. Kieninger, and G. A. Urban, "Novel fabrication process for sub-micron interdigitated electrode arrays for highly sensitive electrochemical detection," *Sensors and Actuators B: Chemical,* vol. 205, pp. 193-198, 2014/12/15/ 2014, doi: https://doi.org/10.1016/j.snb.2014.08.065.

[246] A. F. M. Mansor, I. Ibrahim, A. A. Zainuddin, I. Voiculescu, and A. N. Nordin, "Modeling and development of screen-printed impedance biosensor for cytotoxicity

studies of lung carcinoma cells," *Medical & Biological Engineering & Computing,* vol. 56, no. 1, pp. 173-181, 2018/01/01 2018, doi: 10.1007/s11517-017-1756-1.

[247]   T. Tasakaren, M. K. M. Arshad, M. N. M. N, I. Letchumanan, M. F. M. Fathil, and C. Ibau, "Fabrication and Characterization of Aluminium Interdigitated Electrodes (IDE) Hybrid with Zinc Oxide (ZnO) Nanoparticles for Detection of Cardiac Troponin I (cTnI) Biomarker," in *2019 IEEE International Conference on Sensors and Nanotechnology*, 24-25 July 2019 2019, pp. 1-4, doi: 10.1109/SENSORSNANO44414.2019.8940039.

[248]   "ACEA Biosciences Inc." Agilent. https://www.aceabio.com/ (accessed.

[249]   "EIS Equivalent Circuits," in *Electrochemical Impedance Spectroscopy in PEM Fuel Cells: Fundamentals and Applications*, X.-Z. Yuan, C. Song, H. Wang, and J. Zhang Eds. London: Springer London, 2010, pp. 139-192.

[250]   X. Chen, Y. Shirai, M. Yanagida, and K. Miyano, "Effect of Light and Voltage on Electrochemical Impedance Spectroscopy of Perovskite Solar Cells: An Empirical Approach Based on Modified Randles Circuit," *The Journal of Physical Chemistry C,* vol. 123, no. 7, pp. 3968-3978, 2019/02/21 2019, doi: 10.1021/acs.jpcc.8b10712.

[251]   I. Giaever and C. R. Keese, "Use of Electric Fields to Monitor the Dynamical Aspect of Cell Behavior in Tissue Culture," *IEEE Transactions on Biomedical Engineering,* vol. BME-33, no. 2, pp. 242-247, 1986, doi: 10.1109/TBME.1986.325896.

[252]   J. Henzie, J. Lee, M. H. Lee, W. Hasan, and T. W. Odom, "Nanofabrication of Plasmonic Structures," *Annual Review of Physical Chemistry,* vol. 60, no. 1, pp. 147-165, 2009/05/01 2009, doi: 10.1146/annurev.physchem.040808.090352.

[253]   A. G. Brolo, "Plasmonics for future biosensors," *Nature Photonics,* vol. 6, no. 11, pp. 709-713, 2012/11/01 2012, doi: 10.1038/nphoton.2012.266.

[254] A. B. Dahlin *et al.*, "Electrochemical plasmonic sensors," *Analytical and Bioanalytical Chemistry,* vol. 402, no. 5, pp. 1773-1784, 2012/02/01 2012, doi: 10.1007/s00216-011-5404-6.

[255] A. G. Brolo, R. Gordon, B. Leathem, and K. L. Kavanagh, "Surface Plasmon Sensor Based on the Enhanced Light Transmission through Arrays of Nanoholes in Gold Films," *Langmuir,* vol. 20, no. 12, pp. 4813-4815, 2004/06/01 2004, doi: 10.1021/la0493621.

[256] U. Thi Phuong Lien *et al.*, "Scanning the plasmonic properties of a nanohole array with a single nanocrystal near-field probe," (in English), *Nanophotonics,* vol. 9, no. 4, pp. 793-801, 01 Apr. 2020 2020, doi: https://doi.org/10.1515/nanoph-2019-0409.

[257] H. Wang, Y. Wu, M. Wang, Y. Zhang, G. Li, and L. Zhang, "Fabrication and magnetotransport properties of ordered sub-100 nm pseudo-spin-valve element arrays," *Nanotechnology,* vol. 17, no. 6, pp. 1651-1654, 2006/02/27 2006, doi: 10.1088/0957-4484/17/6/019.

[258] M. Altissimo, "E-beam lithography for micro-/nanofabrication," *Biomicrofluidics,* vol. 4, no. 2, p. 026503, 2010, doi: 10.1063/1.3437589.

[259] M. Kovylina *et al.*, "Tuning exchange bias in Ni/FeF2 heterostructures using antidot arrays," *Applied Physics Letters,* vol. 95, no. 15, p. 152507, 2009, doi: 10.1063/1.3248306.

[260] S. Pal, S. Chandra, M.-H. Phan, P. Mukherjee, and H. Srikanth, "Carbon nanostraws: nanotubes filled with superparamagnetic nanoparticles," *Nanotechnology,* vol. 20, no. 48, p. 485604, 2009/10/30 2009, doi: 10.1088/0957-4484/20/48/485604.

[261] S. Y. Chou, P. R. Krauss, and P. J. Renstrom, "Imprint of sub-25 nm vias and trenches in polymers," *Applied Physics Letters,* vol. 67, no. 21, pp. 3114-3116, 1995, doi: 10.1063/1.114851.

[262] P. Chantharasupawong, L. Tetard, and J. Thomas, "Coupling Enhancement and Giant Rabi-Splitting in Large Arrays of Tunable Plexcitonic Substrates," *The Journal of Physical Chemistry C,* vol. 118, no. 41, pp. 23954-23962, 2014/10/16 2014, doi: 10.1021/jp506091k.

[263] B. Duong *et al.*, "Printed Sub-100 nm Polymer-Derived Ceramic Structures," *ACS Applied Materials & Interfaces,* vol. 5, no. 9, pp. 3894-3899, 2013/05/08 2013, doi: 10.1021/am400587z.

[264] B. Duong *et al.*, "Enhanced Magnetism in Highly Ordered Magnetite Nanoparticle-Filled Nanohole Arrays," *Small,* vol. 10, no. 14, pp. 2840-2848, 2014, doi: 10.1002/smll.201303809.

[265] S. L. Peterson, A. McDonald, P. L. Gourley, and D. Y. Sasaki, "Poly(dimethylsiloxane) thin films as biocompatible coatings for microfluidic devices: Cell culture and flow studies with glial cells," *Journal of Biomedical Materials Research Part A,* vol. 72A, no. 1, pp. 10-18, 2005, doi: 10.1002/jbm.a.30166.

[266] A. Sokolov, B. C. Hellerud, A. Pharo, E. A. Johannessen, and T. E. Mollnes, "Complement activation by candidate biomaterials of an implantable microfabricated medical device," *Journal of Biomedical Materials Research Part B: Applied Biomaterials,* vol. 98B, no. 2, pp. 323-329, 2011, doi: 10.1002/jbm.b.31855.

[267] "Application of Real-Time Cell Electronic Sensing (RT-CES) Technology to Cell-Based Assays," *ASSAY and Drug Development Technologies,* vol. 2, no. 4, pp. 363-372, 2004, doi: 10.1089/adt.2004.2.363.

[268] C. W. S. S.D. Lamore, M.F. Peters, "Cardiomyocyte Impedance Assays," in *Assay Guidance Manual*, A. G. G.S. Sittampalam, K. Brimacombe Ed. Bethesda, MD: Eli Lilly & Company and the National Center for Advancing Translational Sciences, 2015.

[269] J. Min and A. J. Baeumner, "Characterization and Optimization of Interdigitated Ultramicroelectrode Arrays as Electrochemical Biosensor Transducers," *Electroanalysis,* vol. 16, no. 9, pp. 724-729, 2004, doi: 10.1002/elan.200302872.

[270] F. Abdel-Rahman, B. Okeremgbo, F. Alhamadah, S. Jamadar, K. Anthony, and M. A. Saleh, "Caenorhabditis elegans as a model to study the impact of exposure to light emitting diode (LED) domestic lighting," *Journal of Environmental Science and Health, Part A,* vol. 52, no. 5, pp. 433-439, 2017/04/16 2017, doi: 10.1080/10934529.2016.1270676.

[271] J. Icha, M. Weber, J. C. Waters, and C. Norden, "Phototoxicity in live fluorescence microscopy, and how to avoid it," *BioEssays,* vol. 39, no. 8, p. 1700003, 2017, doi: https://doi.org/10.1002/bies.201700003.

[272] C. A. Thomas, P. A. Springer, G. E. Loeb, Y. Berwald-Netter, and L. M. Okun, "A miniature microelectrode array to monitor the bioelectric activity of cultured cells," *Experimental Cell Research,* vol. 74, no. 1, pp. 61-66, 1972/09/01/ 1972, doi: https://doi.org/10.1016/0014-4827(72)90481-8.

[273] U. Frey *et al.*, "Switch-Matrix-Based High-Density Microelectrode Array in CMOS Technology," *IEEE Journal of Solid-State Circuits,* vol. 45, no. 2, pp. 467-482, 2010, doi: 10.1109/JSSC.2009.2035196.

[274] C. D. James *et al.*, "Extracellular recordings from patterned neuronal networks using planar microelectrode arrays," *IEEE Transactions on Biomedical Engineering,* vol. 51, no. 9, pp. 1640-1648, 2004, doi: 10.1109/TBME.2004.827252.

[275] A. Stett *et al.*, "Biological application of microelectrode arrays in drug discovery and basic research," *Analytical and Bioanalytical Chemistry,* vol. 377, no. 3, pp. 486-495, 2003/10/01 2003, doi: 10.1007/s00216-003-2149-x.

[276] B. C. Wheeler and Y. Nam, "*In Vitro* Microelectrode Array Technology and Neural Recordings," vol. 39, no. 1, pp. 45-61, 2011-03-30 2011, doi: 10.1615/CritRevBiomedEng.v39.i1.40.

[277] "Axion Biosystems: Explore life's circuitry," ed: Axion Biosystems.

[278] "Multichannel Systems." Harvard Bioscience Inc. https://www.multichannelsystems.com (accessed.